Spring 2020

Probing the Interstellar Medium of Galaxies Using Gravitationally Lensed Sight Lines and the Relevant Atomic Physics

Frances Cashman

Probing the Interstellar Medium of Galaxies using Gravitationally Lensed Sight Lines and the Relevant Atomic Physics

by

Frances Cashman

Bachelor of Science
College of Charleston 1998

Submitted in Partial Fulfillment of the Requirements

for the Degree of Doctor of Philosophy in

Physics

College of Arts and Sciences

University of South Carolina

2020

Accepted by:

Varsha P. Kulkarni, Major Professor

Steven A. Rodney, Committee Member

Richard J. Creswick, Committee Member

Romauldas Kisielius, Committee Member

Cheryl L. Addy, Vice Provost and Dean of Graduate Studies

Dedication

This dissertation is dedicated to Joe and Lizetta. I love you both very much.

Acknowledgments

I would like to express my sincere gratitude to those those who helped make this work possible. First and foremost, I would like to thank my family: Joe and Lizetta, this work is only possible because of your love and support. I am also profoundly grateful to my advisor Dr. Varsha Kulkarni, who has been an instructive and patient advisor and always demonstrated unwavering encouragement and support. I would also like to thank the members of my dissertation committee for their time and valuable suggestions – Dr. Steven Rodney, Dr. Romas Kisielius, and Dr. Richard Creswick. Additionally, I would like to acknowledge my collaborators for the important contributions they made to this work and to my growth as a researcher – Dr. Romas Kisielius, Dr. Gary Ferland, the late Dr. Pavel Bogdanovich, Dr. Sebastian Lopez, Dr. Sara Ellison, Dr. Debopam Som, and Dr. Maria José Maureira.

I am deeply grateful for the love and support from my fellow graduate students and good friends Alyssa Loos, Saba Arash, Sara FitzGerald, and Suraj Poudel. You all mean the world to me and I am so grateful that we are always there for each other. I would also like to thank the present and former graduate students in our group for their friendship and encouragement, especially Debopam Som and Sean Morrison for helping shape my early years at USC. I learned so much from you both.

I would also like to acknowledge the support of the National Science Foundation, the South Carolina Space Grant Consortium, the National Aeronautics and Space Administration, and the National Optical Astronomy Observatory.

Abstract

Absorption spectroscopy of gravitationally lensed quasars (GLQs) enables study of spatial variations in the interstellar and/or circumgalactic medium (ISM, CGM) of foreground galaxies. In this work I present observations of 4 GLQs, each with two images separated by 0.8-3.0″, that show strong absorbers at redshifts $0.4 < z_{abs} < 1.3$ in their spectra, including some at the lens redshift. The H I Lyman lines were measured in five absorbers using *HST*-STIS, and metal lines with either the MagE spectrograph or the Sloan Digital Sky Survey. These data, combined with the literature, show no strong correlation between absolute values of differences in $N_{\rm H\,I}$, $N_{\rm Fe\,II}$, or [Fe/H] and sight line separations at absorber redshifts. The measured abundance gradients show a tentative anti-correlation with abundances at galaxy centers.

A study of the lens galaxy foreground to the doubly lensed quasar SBS 0909+532 reveals a large difference in H I and metal column densities between sight lines. Using archival *HST*-STIS and *Keck* HIRES spectra, $\log N_{\rm H\,I} \leq 18.18$ cm^{-2} and $\log N_{\rm H\,I} = 20.38 \pm 0.02$ cm^{-2} were measured, resulting in a 99% fractional difference in $\log N_{\rm H\,I}$ between sight lines, the highest for a lens galaxy in which H I has been measured. Supersolar values of $N_{\rm Fe\,II}/N_{\rm Mg\,II}$ for all but one component in the HIRES spectra suggests that Type Ia supernovae made a contribution to the chemical enrichment of the lens.

Additionally this work addresses how sensitively measurements of element abundances from astrophysical spectroscopy depend on the atomic data used. We created a compilation of the latest atomic data for resonant absorption lines at wavelengths longward of 911.753 Å (the H I Lyman limit), for key heavy elements (Z > 5) of

astrophysical interest. In particular, we focused on transitions observed in the Milky Way ISM, the CGM of the Milky Way and/or other galaxies, and the intergalactic medium.

Table of Contents

Dedication iii

Acknowledgments iv

Abstract v

List of Tables x

List of Figures xiii

Chapter 1 Introduction 1

1.1 The Chemical Enrichment of the ISM 2

1.2 The Physics of Spectral Line Formation 9

Chapter 2 Quasar Absorption Line Systems 28

2.1 Quasi-Stellar Objects 29

2.2 Absorption Lines in Quasar Spectra 30

2.3 Properties of Quasar Absorption Line Systems 33

2.4 Exploring Absorption Line Systems with Multiple Sight Lines 43

Chapter 3 A Sample of Doubly Lensed Quasars 47

3.1 GLQs as Probes of Foreground Absorption Systems 47

3.2 Observations and Data Reduction 50

3.3 Absorption Line and Column Density Measurements 60
3.4 Results 68
3.5 Discussion 87

Chapter 4 An in-depth Look at SBS 0909+532 AB 110
4.1 Introduction 110
4.2 Observations and Data Reduction 115
4.3 Absorption Line and Column Density Measurements 117
4.4 Results 123
4.5 Discussion 129

Chapter 5 Creating an Atomic Survey 140
5.1 Atomic Spectroscopy 140
5.2 General Terminology and Definitions 142
5.3 Comments and Assessment of Improved Data 144
5.4 Discussion 160

Chapter 6 Conclusions and Future Work 163
6.1 Galaxies Foreground to Gravitationally Lensed Quasars 163
6.2 Regarding SBS 0909+532 AB 165
6.3 Atomic Spectroscopy 166

Bibliography 168

Appendix A References Abbreviated in Table 5.1 187

Appendix B Data for key transitions 190

List of Tables

Table 1.1 Phases of the Milky Way Interstellar Medium 2

Table 1.2 Summary of the Curve of Growth 24

Table 2.1 Properties of Absorption Line Systems 35

Table 3.1 Sample of GLQ Targets Observed 51

Table 3.2 Parameters for Absorbers along the Sight Lines 52

Table 3.3 Summary of Observations for GLQ Sample 57

Table 3.4 Rest-frame H I Lyα, Lyβ equivalent widths for AB sight lines . . . 62

Table 3.5 H I column density measurements based on Voigt Profile Fitting . 62

Table 3.6 Voigt Profile Fitting Results for Ions in the $z = 1.0859$ Absorber toward Q1017-2046A 72

Table 3.7 Voigt Profile Fitting Results for Ions in the $z = 1.086$ Absorber toward Q1017-2046B 73

Table 3.8 Total Column Densities for the $z = 1.086$ Absorber toward Q1017-2046A and Q1017-2046B 74

Table 3.9 Metallicities for the $z = 1.086$ Absorber toward Q1017-2046A and B 74

Table 3.10 Voigt Profile Fitting Results for Ions in the $z = 1.086$ Absorber toward Q1017-2046A+B from unresolved *Keck* HIRES data 74

Table 3.11 Total Column Densities for the $z = 1.086$ Absorber toward Q1017-2046A+B from unresolved Keck HIRES data 75

Table 3.12 Voigt Profile Fitting Results for Ions in the $z = 0.6794$ Unresolved Absorber toward Q1054+2733A+B 76

Table 3.13 Total Column Densities for the $z = 0.6794$ Unresolved Absorber toward Q1054+2733A+B 76

Table 3.14 Metallicities for the $z = 0.6794$ Unresolved Absorber toward Q1054+2733A+B 76

Table 3.15 Voigt Profile Fitting Results for Ions in the $z = 1.2366$ Unresolved Absorber toward Q1349+1227 78

Table 3.16 Total Column Densities for the $z = 1.2366$ Unresolved Absorber toward Q1349+1227 79

Table 3.17 Metallicities for the $z = 1.2366$ Unresolved Absorber toward Q1349+1227 79

Table 3.18 Voigt Profile Fitting Results for Ions in the $z = 0.4799$ Absorber toward Q1355-2257A 82

Table 3.19 Voigt Profile Fitting Results for Ions in the $z = 0.4797$ Absorber toward Q1355-2257B 82

Table 3.20 Total Column Densities for the $z \sim 0.48$ Absorbers toward Q1355-2257A and Q1355-2257B 83

Table 3.21 Metallicities for the $z \sim 0.48$ absorbers toward Q1355-2257A and Q1355-2257B 83

Table 3.22 3σ Upper Limits for Ions in the $z = 0.7022$ Absorber toward Q1355-2257A 84

Table 3.23 3σ Metallicity Upper Limits for the $z = 0.7022$ Absorber toward Q1355-2257A 84

Table 3.24 Voigt Profile Fitting Results for Ions in the $z = 0.7022$ Absorber toward Q1355-2257B 84

Table 3.25 Metallicities for the $z = 0.7022$ Absorber toward Q1355-2257B . . 84

Table 3.26 Absorbers with H I and/or Fe II Column Density Measurements toward GLQs 109

Table 4.1 Physical characteristics of SBS 0909+532 AB 113

Table 4.2 Absorbers Along the Lines of Sight Towards SBS 0909+532 115

Table 4.3 Component column densities in the $z_{\rm lens} = 0.83$ galaxy towards SBS 0909+532 A 120

Table 4.4 Component column densities in the $z_{\rm lens} = 0.83$ galaxy towards SBS 0909+532 B 120

Table 4.5 Voigt Profile Fitting for Ions in the $z_{\rm abs} = 0.6116$ Mg IIabsorber toward SBS 0909+532 A 128

Table 4.6 Voigt Profile Fitting for Ions in the $z_{\rm abs} = 0.6114$ Mg IIabsorber toward SBS 0909+532 B 130

Table 4.7 Total Column Densities, Metallicities, and Gradients in the $z_{\rm lens} =$ 0.83 galaxy 139

Table 5.1 Line identifications, observed wavelengths $\lambda_{\rm vac}$ (Å), Ritz wavelengths $\lambda_{\rm Ritz}$ (Å), absorption oscillator strengths f and their accuracy grade for key transitions 159

Table 5.2 Statistical Analysis of Change in Oscillator Strength 162

List of Figures

Figure 1.1 The dynamic environment of a disk galaxy 1

Figure 1.2 The planetary nebula NGC 2392 4

Figure 1.3 Tree diagram of the four broad types of supernovae 5

Figure 1.4 Chemical enrichment of the ISM 6

Figure 1.5 Gas-phase abundance versus condensation temperature for the cool, diffuse cloud ζ Oph 8

Figure 1.6 A ray of light passing at an angle θ through a surface element dA into a solid angle $d\Omega$ from a point source 10

Figure 1.7 Equivalent width 13

Figure 1.8 A comparison of theoretical Voigt profiles for S II 1259.5 Å 20

Figure 1.9 Curve of growth for the H I Lyα line 24

Figure 1.10 Solar photospheric abundances presented in Asplund et al. (2009) versus atomic number 27

Figure 2.1 Combined absorption spectra resulting from intervening absorption line systems 32

Figure 2.2 Superposition of multiple intervening absorption line systems . . . 34

Figure 2.3 Isotropic 3D distribution of Lyα clouds at $z = 3$ 36

Figure 2.4 Number density $\mathrm{d}n/\mathrm{d}z$ of lines for different column density thresholds versus redshift 37

Figure 2.5 DLA metallicity as a function of redshift 39

Figure 2.6 Smooth metallicity evolution for DLAs versus redshift 40

Figure 2.7 The Column Density Distribution Function (CDDF) of Lyα forest, LLS, sub-DLA, and DLA lines in quasar spectra 42

Figure 2.8 Illustration of the geometry of a gravitational lens 44

Figure 3.1 *HST* or ground-based images of GLQ targets in V or I band . . . 53

Figure 3.2 Redshift scale for the lens galaxy, absorption line systems, and quasars 54

Figure 3.3 Velocity plots of Q1017-2046A and B near Lyα and Lyβ 63

Figure 3.4 Velocity plots of Q1054+2733A and B near Lyα 64

Figure 3.5 Velocity plots near Lyα and Lyβ for Q1349+1227A and B 65

Figure 3.6 Velocity plots near Lyα for Q1355-2257A and B for $z = 0.48183$. 66

Figure 3.7 Velocity plots near Lyα for Q1355-2257A and B for $z = 0.70721$. 67

Figure 3.8 Voigt profile fit for the $z = 1.086$ system toward Q1017-2046A . . 69

Figure 3.9 Voigt profile fit for the $z = 1.086$ system toward Q1017-2046B . . 70

Figure 3.10 Voigt profile fit for the $z = 1.086$ system from the Q1017-2046A+B Keck HIRES spectrum 71

Figure 3.11 Voigt profile fits for the $z = 0.6794$ system in the SDSS spectrum of Q1054+2733A+B 75

Figure 3.12 Voigt profile fits for the $z = 1.2366$ system in the SDSS spectrum of Q1349+1227A+B 77

Figure 3.13 Voigt profile fits for the $z = 0.4799$ system in the MagE spectrum of Q1355-2257A 80

Figure 3.14 Voigt profile fits for the $z = 0.4797$ system in the MagE spectrum of Q1355-2257B 81

Figure 3.15 Voigt profile fits for the $z = 0.7022$ system in the MagE spectrum of Q1355-2257B 83

Figure 3.16 Absolute values of the differences in log $N_{\rm H\,I}$, log $N_{\rm Fe\,II}$, and Fe abundances between GLQ sight lines vs. the transverse separation 96

Figure 3.17 Differences in log $N_{\rm H\,I}$, log $N_{\rm Fe\,II}$, and Fe abundances between GLQ sight lines vs. the transverse separation 98

Figure 3.18 Metal abundance gradient in dex/kpc vs. abundance at the galaxy center 100

Figure 3.19 Mass-metallicity relation for GLQ absorbers compared with the mean Fe abundance and expected trends 106

Figure 3.20 Mass-metallicity relation for GLQ absorbers compared with the Fe abundance inferred at the galaxy center and expected trends . 107

Figure 4.1 *HST* and *Chandra* images of SBS 0909+532 AB 114

Figure 4.2 H I Lyα line in the $z = 0.83$ lens galaxy in the *HST*-STIS spectrum of SBS 0909+532 AB 121

Figure 4.3 Velocity plots of potential metal lines in the UV spectrum of SBS 0909+532 B 122

Figure 4.4 Velocity plots for the metal lines in the $z \sim 0.83$ lens galaxy in the HIRES spectrum of SBS 0909+532 A 123

Figure 4.5 Velocity plots for the metal lines in the $z \sim 0.83$ lens galaxy in the HIRES spectrum of SBS 0909+532 B 124

Figure 4.6 Ionization modeling results for SBS 0909+532 AB 129

Figure 4.7 Voigt profile fits of the Mg II absorber detected along both lines of sight towards SBS 0909+532 AB 130

Figure 4.8 Fractional difference in log $N_{\rm H\,I}$, log $N_{\rm Fe\,II}$ for SBS 0909+532 AB 133

Figure 4.9 $N_{\rm Fe\,II}/N_{\rm Mg\,II}$ for individual components versus velocity offset from center of the lens 138

Figure 5.1 Updated and former values for oscillator strengths 161

Figure 5.2 Statistical breakdown of accuracy grades of the 576 transitions in Table 5.1 162

Chapter 1

Introduction

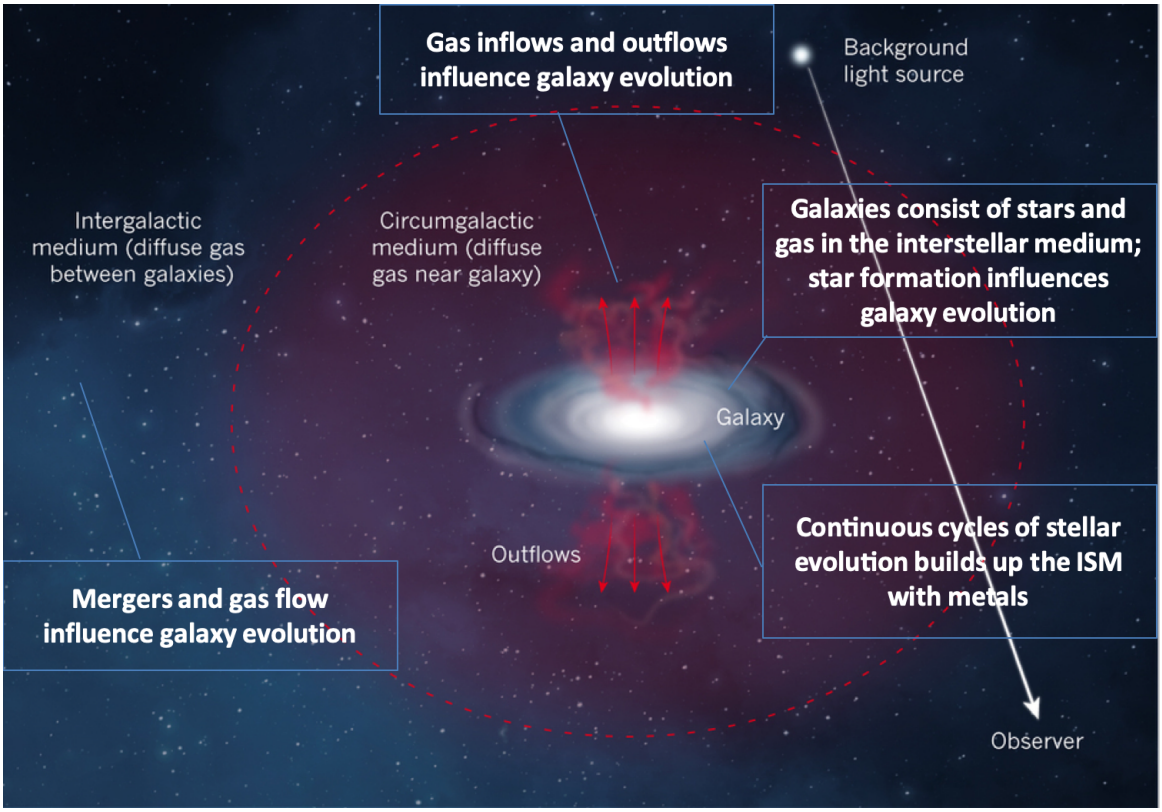

Figure 1.1 Illustration of the dynamic environment of a disk galaxy, which exchanges ISM gas with the CGM via gas outflows and inflows. The CGM, in turn, then exchanges gas with the IGM. Image adapted from M. Peeples of Space Telescope Science Institute.

As the main topic of this thesis concerns variations in chemical abundances in lensing galaxies and other line of sight absorption systems, it is prudent to discuss the chemical enrichment processes which are responsible for the features observed in the spectra of these systems. This is the topic of Section 1.1.

Additionally, this work discusses how atomic physics enables absorption line spectroscopy and that the accuracy of measurements depends sensitively on atomic data. All spectral measurements and calculations utilize either experimentally or theoretically determined atomic data such as transition probabilities, wavelengths, and energy levels. This is the topic of Chapter 5.

1.1 The Chemical Enrichment of the ISM

The Galactic interstellar medium (ISM) consists of a multitude of phases of matter. Within the disk of the Milky Way (MW) there exists both cold and warm neutral mediums. A warm ionized medium can be found in both the disk and the halo, whereas the hot ISM is typically found in the halo of the MW. Dense and cold molecular clouds can also be found throughout the MW. See Table 1.1 for a summary of the various mediums in the MW galaxy.

Table 1.1 Phases of the Milky Way Interstellar Medium

Phase	n (cm^{-3})	T (K)	Description
molecular clouds	$\sim 10^6$	~ 30	▪ cold, dense, and dusty ▪ associated with areas of star formation
cold neutral	∼50	∼100	▪ found in plane of MW
warm neutral	∼1	∼6000	▪ ∼50% of MW volume ▪ mainly in the disk of MW
warm ionized	$\sim 0.1 - 10^4$	$\sim 10^4$	▪ diffuse to denser gas in H II regions ▪ found in the disk and halo
hot	~ 0.001	$\sim 10^6$	▪ extremely hot and diffuse ▪ found in the halo

It is interesting to consider that if another distant civilization were studying the absorption lines the MW galaxy produced in the spectra of a background quasar, what would they see? Would their random sight line pierce the disk of our galaxy and allow them to characterize our entire galaxy based on whether they hit a cold or warm neutral medium? What if their sight line only intersected the hot ISM of the

halo? Absorption line spectroscopy is a powerful probe of the intergalactic medium (IGM), but when a sight line intercepts a distant absorption system, care has to be made to interpret the spectra correctly in order to identify the system. For example, it was long thought that elliptical galaxies were devoid of gas and that damped Lyman-alpha absorbers (discussed at length in Section 2.3) were exclusively associated with spiral galaxies. However, due to 21 cm surveys, it is now known that a large fraction of early-type galaxies are not gas poor, but can contain a large amount of neutral hydrogen as well as chemically enriched gas. Thus without complementary imaging, it can be difficult to determine what type of host galaxy a higher density absorption system might belong to. For example, in Chapter 4, we discuss our effort to explore variations in chemical abundances in a known elliptical galaxy. Using multiple sight lines through galaxies foreground to gravitationally lensed quasars (GLQs) allows us to deliver a more robust characterization of the galaxies as well as make a more confident description of their chemical enrichment history.

In order to ascertain the chemical enrichment history of a galaxy, we have to appreciate that the metals that are seen in galaxies are the result of very specific processes that have occurred in very specific environments. Understanding how and where metals are created is crucial to understanding how the ISM becomes enriched. There are three main ways that metals are produced: charged particle fusion, the s-process, and the r-process. Each of these processes contributes in some way to the chemical enrichment of the ISM.

Nearly all of the elements up to iron at Z = 30 are produced in the interiors of stars undergoing nuclear fusion, which is spurred on by its perpetual state of gravitational collapse. Lower mass stars with mass $\lesssim 8M_{\odot}$, this includes our Sun, spend their lives producing mainly helium (via the proton-proton chain) and carbon (via the triple alpha process), but are not massive enough to provide the pressure required to begin fusion of the carbon core. The core is supported by electron degeneracy pressure at

Figure 1.2 The planetary nebula NGC 2392. The expansion of gases is readily visible and the estimated distance across is $2000 - 4000$ ly. A white dwarf at the center is responsible for the beautiful colors seen from the ionized gas: nitrogen (red), hydrogen (green), oxygen (blue), and helium (violet). Image credit: NASA, ESA, Andrew Fruchter (STScI), and the ERO team (STScI + ST-ECF)

this point. Thermal pulsing persists as the hydrogen and helium shells burn out of phase with each other and these pulses are responsible for the ejection of the outer layers of the star. The remaining carbon core is called a white dwarf and its radiation ionizes the ejected outer layers, resulting in an extraordinarily beautiful display of color, see Figure 1.2 as an example. The ejection of the outer layers is one way that the ISM is enriched by these low mass stars.

Stars with mass $\gtrsim 8M_{\odot}$, on the other hand, will be able to reach a temperature that can initiate carbon fusion to create neon. There is a repeated cycle of core burning and core contraction which produces consecutively heavier elements until

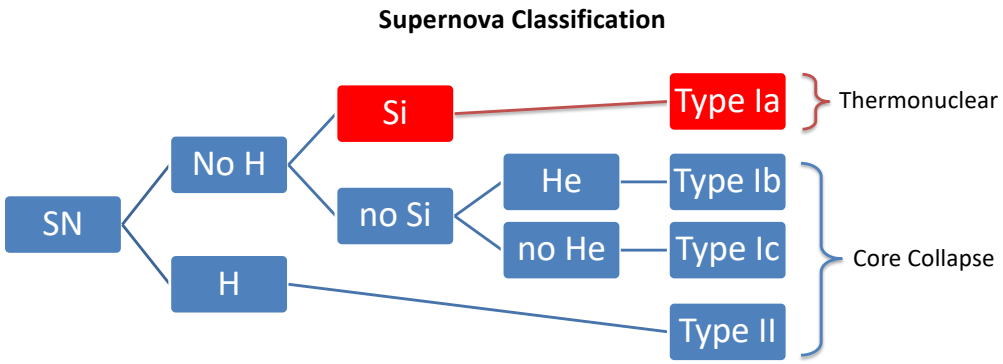

Figure 1.3 A tree diagram of the four broad types of supernovae (SNe), which are classified based on the presence of certain features in their optical spectra taken near maximum light. The broadest distinction separates the Type I from the Type II in that Type I do not show H absorption lines in their spectra. Type I SNe are further sub-divided based on the presence of Si and He in their spectra. Type Ia SNe contain a Si absorption line at $\lambda 6150$, whereas Type Ib show no Si but show He in emission. Type Ic show neither Si nor He lines. Type Ia SNe can be found anywhere and in any type of galaxy, Type Ib and Type Ic SNe generally occur for massive stars, similar to Type IIs. Type Ia SNe are the thermonuclear explosions of white dwarfs. Type II, Type Ib, and Type Ic SNe result from the core-collapse of massive stars.

an iron core begins to build up due to the rapid burning of silicon. A build up of iron spells the end of the road, as iron can only be fused to heavier elements at the expense of hydrostatic equilibrium since the nuclear reaction is endothermic. The core collapses and during the process of photo-disintegration, the iron core loses support from electron degeneracy pressure and collapses further. What happens next depends on the core mass. For a core with mass $\lesssim 3M_{\odot}$, this collapse will be stopped by the pressure of neutrons and the core becomes a neutron star. The sudden halt of the collapsing core produces a shock wave which gets sent back out through the onion layers of the star. This shock wave blows apart the star and the outer layers and the ejected gas are then strewn into the ISM. For a core of mass $\gtrsim 3M_{\odot}$, the contracting core is not stopped by neutron degeneracy pressure and it will collapse further to form a black hole. The supernova events are classified into two groups based on whether or not hydrogen absorption lines exist in their spectra. Figure 1.3 summarizes the different types of supernova. More specific details on the astrophysical processes that

occur during stellar evolution and during a supernova can be found in any astrophysics textbook but will not be discussed further in this work.

All end scenarios, (i.e., a planetary nebula, neutron star, or black hole) serve as conduits for the chemical enrichment of the ISM either through stellar winds or supernova explosions. The chemically enriched interstellar gas can then serve as a foundation for the next generation of stars. This repeats in a cyclical process that is illustrated in Figure 1.4.

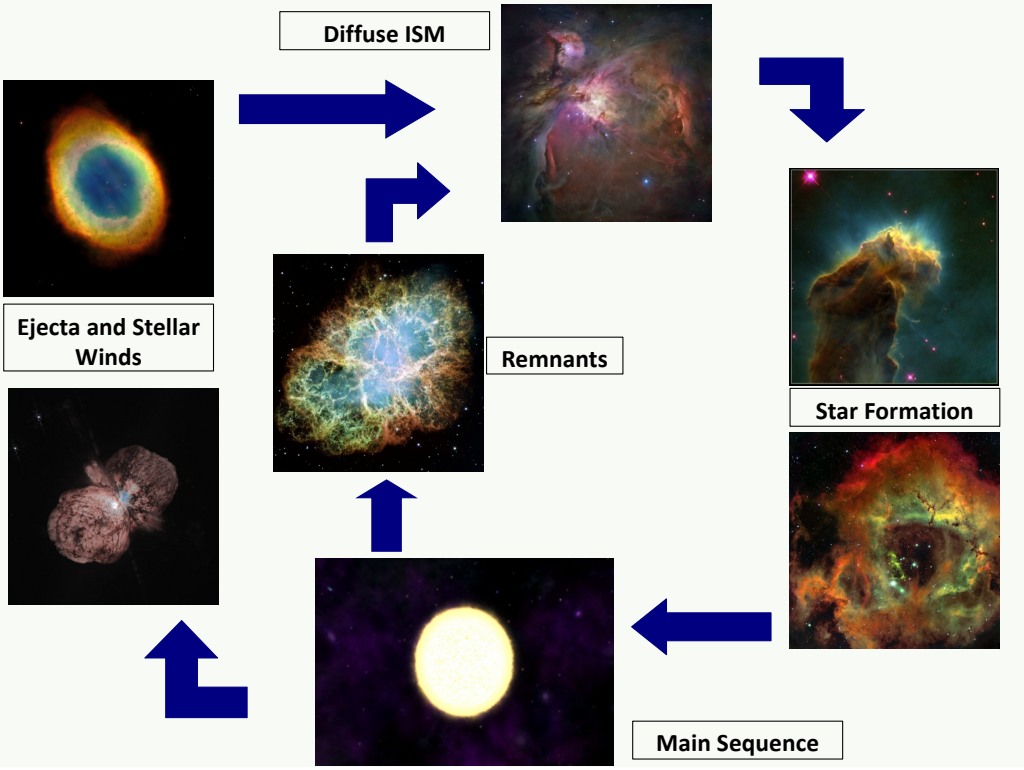

Figure 1.4 An illustration of how stellar evolution and the eventual production of stellar remnants in a galaxy are tied to the chemical enrichment of the ISM. Image credit: Debopam Som

The enrichment of the ISM by supernovae influences the chemical evolution of a galaxy significantly. Type II SNe produce more α-elements including C, O, Mg, Si, S, Ca, and Ar than they do Fe, resulting in a high [α/Fe] ratio (Type II SNe typically produce $\sim 0.1 M_{\odot}$ of Fe per event). A Type Ia SNe, on the other hand, can

produce a significant amount of Fe-peak elements, $\sim 0.8 M_{\odot}$ of Fe per event. Thus environments enriched by Type Ia SNe show lower [α/Fe] ratios. In the context of the work presented in Chapter 4, the enrichment of the ISM due to Type Ia SNe has been suggested to be directly responsible for the stalling of the chemical evolution of elliptical galaxies (e.g. Conroy et al. 2015; Zahedy et al. 2017) due to the injection of energy from Type Ia SNe and stellar winds from asymptotic giant branch (AGB) stars.

A problem that plagues astronomers when studying the chemical enrichment of the ISM is element depletion. The temperature of the ISM can vary depending on the type of medium present, see Table 1.1. Since elements have different condensation temperatures, it is possible that an element could have a significant presence in the medium but goes undetected because absorption line spectroscopy only measures gas phase abundances. Figure 1.5 from Savage & Sembach (1996) shows the depletion factors for elements abundant in the ISM of the interstellar cloud ζ Oph, plotting the gas phase abundance versus the condensation temperature. The elements with low condensation temperatures have ∼solar abundances. Elements with high condensation temperature show significant depletion onto dust grains. From the figure, it is clear that Fe depletes heavily into dust grains and thus is not a reliable metallicity indicator for the ISM, even though it is used extensively to determine the metallicity of stars. Elements such as Zn, S, and P are found to be relatively undepleted in the ISM, even for the warm medium. Thus for quasar absorption line spectroscopy different conventions are desired for metallicity than for those generally accepted in other fields. As will be presented in Chapter 3, Fe lines were the only lines available in the systems we studied, thus sight lines probing the ISM of these galaxies are likely not representative of the galaxy's true enrichment. Metallicity and measurement of absorption lines are discussed at greater length in Section 2.2.

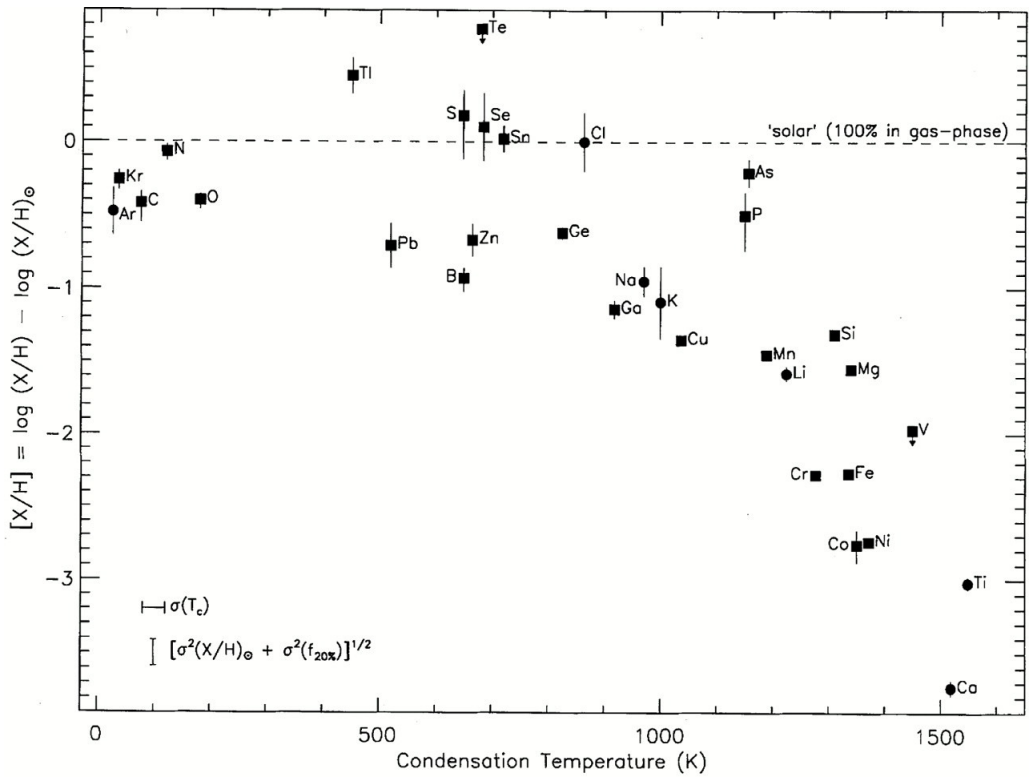

Figure 1.5 Gas-phase abundance versus condensation temperature for the cool, diffuse cloud ζ Oph from Savage & Sembach (1996). The filled squares are GHRS data and are supplemented by Copernicus and ground-based observations (the filled circles) for a few elements. The elements with low condensation temperatures have $\sim$solar abundances. Elements with high condensation temperature show significant depletion onto dust grains. C, N, O, S, Ar, Kr, and some heavy elements have depletion factors < 3, while P, Zn, and Ge have slightly larger depletion factors. The depletion factors for Ca, Ti, V, Cr, Fe, Co, and Ni are more than 100.

1.2 The Physics of Spectral Line Formation

The light observed from distant extragalactic sources such as quasars can be considered a point source of radiation. This light originates from a supermassive black hole accretion disk within that galaxy. In order to correctly interpret the spectral lines that we observe, it is important to understand how quantitative measurements, e.g., equivalent widths and thus column densities, ultimately descend from a fundamental observable called the optical depth.

1.2.1 The Optical Depth

In equation 1.1 below, $E_\lambda \, d\lambda$ is the amount of energy carried by a beam of light rays from a point source of radiation through a surface area element dA at an angle θ into a cone of solid angle $d\Omega$ over some amount of time dt (see Figure 1.6).

$$E_\lambda \, d\lambda = I_\lambda \, cos\theta \, dA \, d\Omega \, d\lambda \, dt \tag{1.1}$$

I_λ is the specific intensity of the beam in units of W m^{-3} sr^{-1}, or the energy per second per unit area per unit wavelength per unit solid angle. We consider the convention that the beam consists of parallel light rays and recognize that photons could be added to (by emission from the gaseous medium) or removed from (by absorption or scattering) the beam depending on the medium that the beam is traveling through. The absorption or scattering of photons from the beam by the medium will reduce the intensity, and this change in intensity dI_λ is proportional to several factors, i.e., its initial intensity I_λ, the density of the gas ρ, and the distance ds that the ray has traveled. The proportionality constant κ_λ, is called the absorption coefficient or opacity, and depends on the density, temperature, and make-up of the gaseous medium. More specifically, the opacity is the cross section per unit mass for absorbing photons, i.e., $\kappa_\lambda = n\sigma_\lambda$, where n is the number density of particles.

$$dI_\lambda = -\kappa_\lambda \, \rho \, I_\lambda \, ds = -n \, \sigma_\lambda \, I_\lambda \, ds \tag{1.2}$$

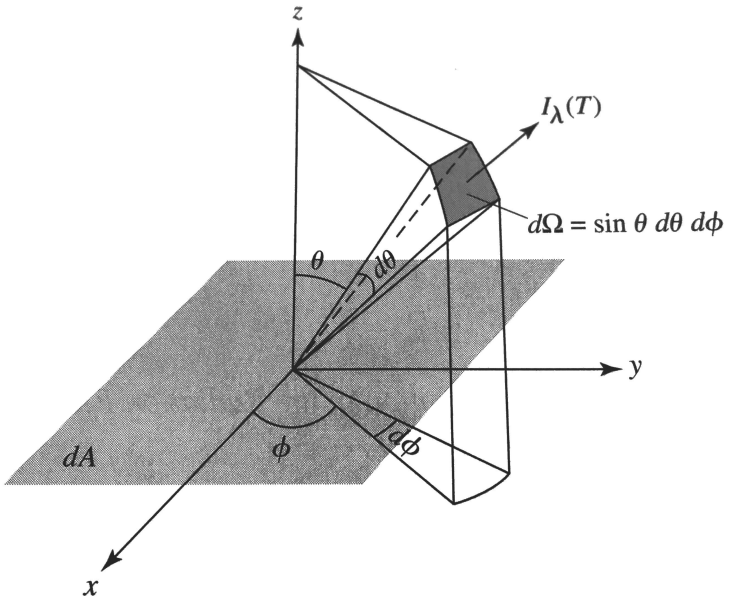

Figure 1.6 A ray of light passing at an angle θ through a surface element dA into a solid angle $d\Omega$ from a point source. The ray contains an amount of energy $E_\lambda\, d\lambda$ in the wavelength range $d\lambda$. (Carroll & Ostlie 2006)

The negative sign in the equation above reflects the convention that distance s increases in the direction the beam travels, therefore the intensity should decrease with distance due to increased absorption by photons. The optical depth τ_λ is defined as

$$\tau_\lambda = \int_0^s \kappa_\lambda\, \rho\, ds = \int_0^s n\sigma_\lambda\, ds, \tag{1.3}$$

and describes the wavelength dependence of opacity over a distance s, looking back along the path traveled by the photons.

Just as changes in intensity due to absorption could occur and these changes vary depending on the characteristics of the gas, the intensity can also change as a result of incident emission from its environment. If the beam enters a medium that is itself emitting photons then these photons may be added to the beam. The change in intensity in this case is also proportional to the density ρ of the gas and the distance traveled, but is independent of the value of the intensity I_λ of the beam. The

proportionality constant j_λ, or the emission coefficient, varies with the wavelength of the light (m s^{-3} sr^{-1}). This dependence makes sense since the energy of the incident photons depends on their wavelength, i.e. $E = hc/\lambda$. The change in intensity due to emission of photons is

$$dI_\lambda = j_\lambda \, \rho \, ds. \tag{1.4}$$

If we consider the more complete scenario that a beam is affected by both absorption and emission while traveling through a medium, then the change in intensity dI_λ is the sum of the two factors:

$$dI_\lambda = -\kappa_\lambda \rho \, I_\lambda \, ds + j_\lambda \rho \, ds. \tag{1.5}$$

Dividing the equation above by $\kappa_\lambda \rho \, ds$ and defining $j_\lambda / \kappa_\lambda \equiv S_\lambda$,

$$-\frac{1}{\kappa_\lambda \rho} \frac{dI_\lambda}{ds} = I_\lambda - S_\lambda, \tag{1.6}$$

where S_λ is the source function which characterizes how the original photons are replaced by photons from the surrounding medium, we obtain the radiative transfer equation. If we replace the term $-\kappa_\lambda \rho \, ds$, which is $d\tau_\lambda$, which we defined earlier, then another form of the transfer equation looks like

$$\frac{dI_\lambda}{d\tau_\lambda} = I_\lambda - S_\lambda. \tag{1.7}$$

This is a very important equation because lying within in it are the physical conditions of the line of sight environment.

To make meaningful interpretations of the spectral lines we observe, we can make simplifying assumptions about the transfer equation. Since we are interested in describing the properties of the intervening gas along the line of sight to quasars through the use of absorption lines, it is a reasonable assumption to recast the transfer equation for the case of pure absorption. Setting $S = 0$, making a slight rearrangement, and integrating both sides yields

$$\int_{I_{\lambda,0}}^{I_{\lambda,f}} \frac{dI_\lambda}{I_\lambda} = -\int_0^s \kappa_\lambda \, \rho \, ds. \tag{1.8}$$

$$I_{\lambda,f} = I_{\lambda,0}\, e^{-\tau_\lambda}. \tag{1.9}$$

Which is the result we would have obtained by simply integrating both sides of equation 1.2. This equation shows that the intensity falls off by a factor of $e^{-\tau_\lambda}$ as it travels through a gas. The fact that the intensity we receive depends on the composition, temperature, and density of the intervening material that the quasar's light travels through means that we can quantitatively characterize the absorbing gas that is observed along the line of sight to the quasar. Integrating the number density of particles along the line of sight gives a measurement of the number of particles in a thin "tube" of cross sectional area that is the length of the sight line. This measurement is called the column density and typically the cross sectional area is in units of cm^2, although it can be in other units as well.

$$N \equiv \int_0^s n\, ds. \tag{1.10}$$

Thus we can recast equation 1.4 as

$$\tau_\lambda = \int_0^s \kappa_\lambda\, \rho\, ds = \int_0^s n\sigma_\lambda\, ds = N\sigma_\lambda. \tag{1.11}$$

This makes the optical depth perhaps the most crucial observable because by measuring the absorption lines created by the different atoms, ions, and molecules we can then determine the column densities of the present chemical composition. Absorption line systems are characterized by their column densities, which are in turn used to determine the absorber's chemical abundance, or metallicity. The metallicity, or absolute abundance, is the convention used to describe how abundant elements heavier than hydrogen or helium, i.e., metals, are compared to the Sun.

$$\left[\frac{X}{\mathrm{H}}\right] = \log_{10}\left(\frac{N_X}{N_\mathrm{H}}\right)_\mathrm{abs} - \log_{10}\left(\frac{N_X}{N_\mathrm{H}}\right)_\odot \tag{1.12}$$

1.2.2 Equivalent Width

One way in which the optical depth is used to obtain column densities is by measuring the equivalent width of the spectral line. The equivalent width is the area

of a rectangular box with height equal to the value of the flat part of the spectrum (continuum) with the same area within the spectral line, see Figure 1.7. The region near the central wavelength λ_0 is the core of the line and the sides sloping upward to the continuum are the wings of the line.

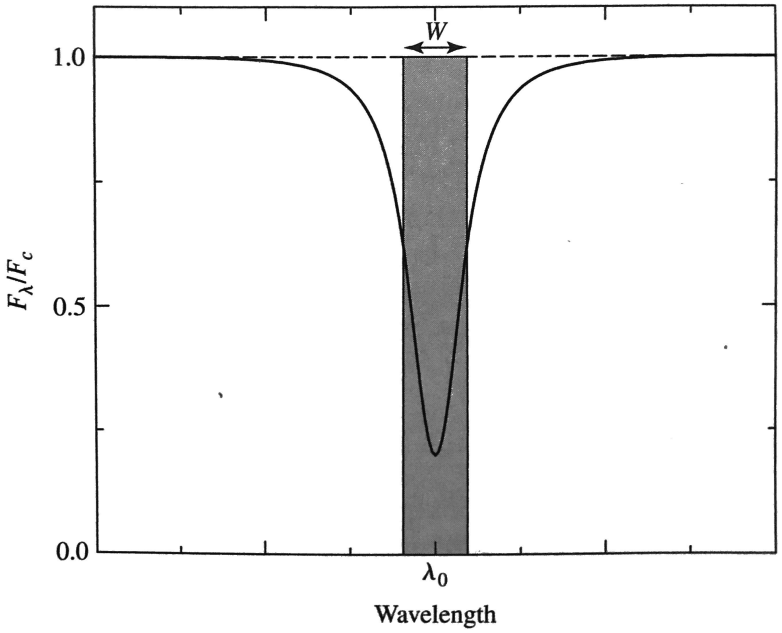

Figure 1.7 An optically thin spectral line of central wavelength λ_0 with normalized intensity F_λ/F_c on the y-axis. The shaded box of continuum height has the same area as the area within the spectral line. W, or the equivalent width is the width necessary to form that box. (Carroll & Ostlie 2006)

Integrating the depth of the line from one side of the spectral feature to the other gives the strength or equivalent width of the line.

$$W \equiv \int_0^\infty \frac{I_c - I_\lambda}{I_c}\, d_\lambda = \int_0^\infty (1 - e^{-\tau_\lambda})\, d_\lambda \tag{1.13}$$

It is important to point out that an equivalent width measured from a spectrum originating in an absorption system at redshift $z_{\rm abs}$ is the observed equivalent width ($W_{\rm obs}$), which has been stretched from the rest frame by a factor of $(1 + z_{\rm abs})$ due to the Hubble expansion of the Universe. The rest equivalent widths ($W_{\rm rest}$) can thus

be determined by dividing the observed equivalent widths by the factor $(1 + z_{\rm abs})$,

$$W_{\rm rest} = \frac{W_{\rm obs}}{(1 + z_{\rm abs})}. \tag{1.14}$$

An additional measurement of a spectral line that is useful is the full width at half maximum (FWHM or $\Delta\lambda_{1/2}$). This is the width of the spectral line at which the depth is equal to one-half of its entire value.

1.2.3 Line Broadening Processes

A spectral line is a combination of the total absorbed (or emitted, in the case of emission) radiation and thus represents a distribution of velocities within the gas. For an optically thin line, the opacity κ_λ of the absorption system is greatest at λ_0 and the core of the line is produced in the coolest region of this absorption system. The opacity then decreases going into the wings, which are formed at hotter regions of the system, and eventually merges with the continuum-producing region. This implies that the cooler the system, the sharper the absorption lines should be. However, spectral lines cannot be infinitely sharp. In fact, there are many factors that determine the width and shape of a spectral line including the amount of ions present (column density) and the turbulence and bulk motion of the gas. Each of these factors has a particular effect on the line profile.

The sections below discuss the two main mechanisms responsible for the broadening of spectral lines: natural broadening and Doppler broadening.

Natural Broadening

As mentioned above, if the system is very cool or even cold, then an optically thin absorption line can indeed be very narrow. A spectral line is the result of a photon being absorbed, and since an electron is in an excited state for only a brief amount of time, the energy associated with the transition has an inherent uncertainty which

varies inversely with the time available for a measurement, i.e.,

$$\Delta E \approx \frac{\hbar}{\Delta t}, \tag{1.15}$$

according to Heisenberg's uncertainty principle. Therefore any spectral line has a finite minimum width due solely to the uncertainty in the wavelength propagated from the uncertainty in the energy (and therefore lifetime) of the transition, without even considering other broadening mechanisms. The uncertainty in the wavelength inversely depends on both the lifetime of the electron in its initial state (Δt_i) and its final state (Δt_f) and is approximately

$$\Delta\lambda \approx \frac{\lambda^2}{2\pi c}\left(\frac{1}{\Delta t_i} + \frac{1}{\Delta t_f}\right). \tag{1.16}$$

Additionally, the FWHM (recall full width at half-maximum or $\Delta\lambda_{1/2}$) of the line shape or profile due to natural broadening is

$$\Delta\lambda_{1/2} = \frac{\lambda^2}{\pi c}\frac{1}{\Delta t_0}. \tag{1.17}$$

The variable Δt_0 is the average time that it takes for the transition to occur. The line profile that results from natural broadening is called a natural or Lorentzian profile and the line profile ϕ for resonant transitions to the ground state takes the form

$$\phi(\lambda) = \frac{1}{\pi}\frac{\gamma}{(\lambda - \lambda_0)^2 + \gamma^2}, \tag{1.18}$$

where γ is the rate of spontaneous decay, $A_{n,n'}$, of an atomic state n to to all lower energy levels n', and has the form

$$\gamma = \frac{\lambda^2}{4\pi c}\sum_{n'} A_{n,n'}. \tag{1.19}$$

Doppler Broadening

Assuming that the gas is in thermal equilibrium, each atom in the gas moves randomly with a distribution of speeds that can be described by the Maxwell-Boltzmann

distribution function

$$n_v\ dv = n\left(\frac{m}{2\pi kT}\right)^{3/2} e^{-mv^2/2kT} 4\pi v^2\ dv, \tag{1.20}$$

where n is the total number of particles per unit volume and n_v is the fraction of particles in that volume moving in the velocity range v to $v + dv$ (recalling equation 1.10 that $N = \int_0^s n\ ds$). The random motions of atoms in a gas depend on the temperature. The factor $\sqrt{2kT/m}$ is the most probable speed of the particles and is called the Doppler b-parameter (b, $b_{thermal}$, or b-value) and is derived from

$$\frac{1}{2}mv^2 = kT. \tag{1.21}$$

When photons are absorbed (or emitted in the case of emission) by the atoms in the absorption system, the wavelength of these photons experiences a non-relativistic Doppler shift equivalent to

$$\Delta\lambda = \pm\frac{v_r}{c}\lambda, \tag{1.22}$$

where v_r is the radial velocity, i.e., the velocity component that is either directly away from or toward the observer. Thus, we can estimate the contribution to the width of the spectral line due to Doppler broadening by using the most probable speed $b_{th} = \sqrt{2kT/m}$ as the velocity of the gas in equation 1.22,

$$\Delta\lambda \approx \frac{2\lambda}{c}\sqrt{\frac{2kT}{m}} = \frac{2\lambda}{c}\ b_{th}. \tag{1.23}$$

As with natural broadening, we can also express the Doppler broadening in terms of the FWHM of the line profile.

$$\Delta\lambda_{1/2} = \frac{2\lambda}{c}\sqrt{\frac{2kT\ \ln 2}{m}} = \frac{2\lambda}{c}\ b_{th}\sqrt{\ln 2} \tag{1.24}$$

Comparing the FWHM for natural broadening versus Doppler broadening, the line profile for natural broadening falls off much more slowly as the wavelength moves away from λ_0 than for Doppler broadening. The Doppler or thermal line profile is a

Gaussian and it falls off rapidly as the wavelength moves away from the line center λ_0. This rapid decrease in the Doppler line profile is due to the exponential term $e^{-mv^2/2kT}$ in the Maxwell-Boltzmann description of the distribution of speeds for the atoms in the gas. The fraction of atoms absorbing radiation between wavelengths λ and $\lambda + d\lambda$ is

$$\psi(\lambda)\, d\lambda = \frac{N(\lambda)\, d\lambda}{N_0} = \frac{1}{\sqrt{\pi}\Delta\lambda} \exp\left(-\frac{(\lambda - \lambda_0)^2}{\Delta\lambda^2}\right)\, d\lambda, \tag{1.25}$$

where $\Delta\lambda$ is the Doppler width defined in equation 1.23.

In addition to the thermal motions described so far in this section, some broadening of the spectral line can occur due to small or large-scale turbulent motions that are occurring in the absorption system. For the studies of absorption line systems discussed in this dissertation, the turbulent motions are small-scale motions occurring within the cloud. The broadening that results from this motion can be accounted for by defining an *effective* Doppler parameter b_{eff} which is the sum in quadrature of the individual thermal and turbulent b-values, as in

$$b_{eff} = \sqrt{b_{th}^2 + b_{turb}^2}, \tag{1.26}$$

where b_{turb} is the most probable turbulent speed. Thus equation 1.23 and 1.24 can be recast as

$$\Delta\lambda \approx \frac{2\lambda}{c}\sqrt{\frac{2kT}{m}} = \frac{2\lambda}{c} b_{eff}. \tag{1.27}$$

and

$$\Delta\lambda_{1/2} = \frac{2\lambda}{c}\sqrt{(b_{th}^2 + b_{turb}^2)\, \ln 2} = \frac{2\lambda}{c}\, b_{eff}\, \sqrt{\ln 2} \tag{1.28}$$

to include turbulence. The combined effect of turbulent and thermal motions is what is seen in the observed spectra and therefore to determine the temperature of the absorbing gas, it is necessary to separate b_{th} from b_{eff}. The effect of the b_{turb} term is the same for all ion species since it does not depend on mass. The temperature is then calculated by taking the ratio of the FWHM (equation 1.28) for two different lines of

different species, eliminating the b_{turb} and other common terms, and then solving for T, which is their shared variable. For example, the temperature of a component in an absorption line system that had evidence of both iron and silicon could be expressed as

$$T = \frac{m_{\rm Si}\, m_{\rm Fe}\, (b_{\rm Si}^2 - b_{\rm Fe}^2)}{(m_{\rm Fe} - m_{\rm Si})\, 2k}. \tag{1.29}$$

It is important to mention that the temperature calculation is typically not reliable unless the spectra is high-resolution and both lines are unblended. Jenkins et al. (2005) used this technique to determine the temperature of a Lyman-limit system at $z_{\rm abs} = 0.081$ along the line of sight to the bright quasar PHL 1811 at $z_{\rm QSO} = 0.192$ using spectra taken with the E140M grating of the Space Telescope Imaging Spectrograph (STIS) onboard the *Hubble Space Telescope*.

It also needs to be mentioned that this has all been discussed for a single component in an absorption system lying along the line of sight, but often an absorption line system consists of multiple components. Each of these components may have their own distinctive composition and kinematics. Thus each component is analyzed separately (the methods to do this will be described in the next section) to determine its b-value and the column density of whichever ions are present therein. A total column density is then found by adding the column densities of the individual components together. It is also possible that the absorption cloud undergoes bulk motions, in which the entire cloud or multiple components within the cloud move together with respect to the rest frame of the observer. In this case, it may be possible to explore the kinematics of the system. For example, if the cloud is experiencing radial infall, then in velocity space its components will be distributed over a range of velocities, or if the cloud components are distributed in a rotating disk then the result is a cluster of lines superimposed in velocity space.

A third type of broadening occurs when a neutral atom collides or has a close encounter with another atom and perturbs the orbitals of the atom. These effects

are called collisional broadening. When this happens on a large scale, i.e. when a large number of close encounters or collisions occur, the effect of the electric fields is called pressure broadening. For example, this is the primary broadening mechanism in the troposphere of the Earth's atmosphere. As this mechanism does not make a significant contribution to the broadening seen in low density quasar absorption line systems, the details will not be discussed further, but the resulting line profile is Lorentzian, as for natural broadening.

1.2.4 The Voigt Profile

In reality, the observed spectral line profile is a combination of independently produced profiles. The combination of the naturally broadened profile with the thermal Doppler broadened profile is called the Voigt profile and is mathematically represented by the convolution of these independent profiles.

$$\phi_{\text{Voigt}}(\lambda) = \phi_{\text{Natural}}(\lambda) \otimes \psi_{\text{Doppler}}(\lambda) \tag{1.30}$$

There is no simple analytic form but the convoluted profile can be expressed as the superposition of equations 1.18 and 1.25,

$$\phi_{\text{Voigt}}(\lambda) = \frac{1}{\pi^{3/2}\Delta\lambda} \int_{-\infty}^{\infty} \frac{\gamma}{(\lambda - \lambda_0)^2 + \gamma^2} \exp\left(-\frac{(\lambda - \lambda_0)^2}{\Delta\lambda^2}\right) \, d\lambda_0. \tag{1.31}$$

The absorption profile can then be written as

$$I_{\lambda,f} = I_{\lambda,0}\, e^{-\tau_\lambda} = I_{\lambda,0}\, e^{-N\sigma_\lambda \phi_{\text{Voigt}}(\lambda)} \tag{1.32}$$

where $\sigma_\lambda \phi_{Voigt}(\lambda)$ is the absorption cross section (from equation 1.11) recast in terms of the Voigt profile function. As mentioned earlier, the thermal Doppler profile falls off rapidly as the wavelength moves away from the line center (i.e., $\lambda - \lambda_0$) due to the exponential term $e^{-mv^2/2kT}$ in the Maxwell-Boltzmann description, whereas the natural profile falls off more slowly (via inverse square) for $\lambda - \lambda_0$. Equating equations 1.18 and 1.25 yields $(\lambda - \lambda_0) \times (\mathrm{c}/\lambda) \simeq 3b$, meaning that for a distance

away from line center $< (3b\lambda/c)$ the Gaussian thermal Doppler profile dominates. For a distance away from line center $> (3b\lambda/c)$ there is a transition to a Lorentzian natural profile in the wings. These profiles are frequently described as having Doppler cores and damping wings. Voigt profiles have predictable shapes for fixed b-values with different values of N and for fixed N with different b-values, see Figure 1.8.

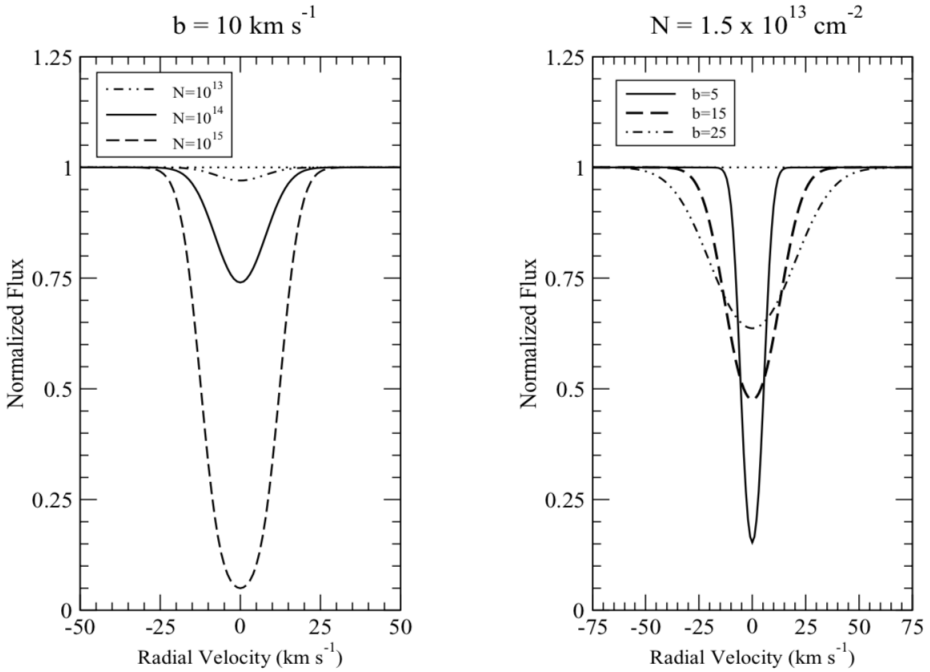

Figure 1.8 A comparison of theoretical Voigt profiles for the S II 1259.5 Å line with oscillator strength $f = 0.0166$. Left: Voigt profiles with $N(\mathrm{cm}^{-2}) = 10^{13}$, 10^{14}, 10^{15} with a fixed b-value of 10 km s^{-1}. Right: Voigt profile for the H I Lyα line with b-values (km s^{-1}) = 5, 15, 15 but with a fixed value of $N = 1.5 \times 10^{13}$ cm^{-2}. Image credit: Debopam Som

Additionally, the observed spectral profile is affected by the instrument that made the observations. The limitations of optics, detectors, and gratings impart some blurring to the absorptions lines and these combined effects are called the instrument spread function, or ISF. Thus the observed spectrum is an additional convolution of the Voigt profile and the ISF or

$$I_{\mathrm{observed}}(\lambda) = I_{\lambda,0}\, e^{-\tau_\lambda} \otimes \phi_{\mathrm{ISF}}(\lambda), \tag{1.33}$$

$$I_{\rm observed}(\lambda) = I_{\lambda,0}\, e^{-N\sigma_\lambda \phi_{\rm Voigt}} \otimes \phi_{\rm ISF}(\lambda). \tag{1.34}$$

The ISF for different telescopes and instruments is typically provided in the instrument manual and is determined from lab measurements of emission lines created from gas discharge lamps. Since these emission lines typically have very small natural widths, the ISF can be approximated as a Gaussian. By incorporating the ISF, computer programs (e.g., VPFIT[1], FITS6P[2] which fit via χ^2 minimizations) can extract column densities very accurately by fitting Voigt profiles to high resolution absorption profiles.

It should be discussed that the calculation of a spectral line also depends on the quantum mechanical specifics of how atoms absorb photons, and not just the abundance of the element. The simplest models to calculate a line profile assume that the source of the photons behaves as a blackbody and that the atoms foreground to the emitting region absorb photons from this continuous blackbody spectrum to form the absorption lines. Additionally, values for the density, temperature, and composition must be approximated where the line is formed. The temperature and density are important factors in the Boltzmann and Saha equations, which are used to determine the atomic states of excitation and ionization. These factors will also gauge the extent of the contribution that line broadening processes, such as Doppler and pressure broadening, are making to the line profile. The goal is to find the number of absorbing atoms per unit area (the column density N, as defined earlier) that have electrons in the correct orbital that are capable of absorbing a photon with a wavelength equivalent to the wavelength of the spectral line. The column density can then be determined by comparing the calculated profile to the observed line profiles. This process is typically done using computer programs (like the ones mentioned in the paragraph above) using χ^2 minimization statistics.

[1]https://people.ast.cam.ac.uk/∼rfc/

[2]https://astro.uchicago.edu/ dwelty/fits6p.txt

The transitions between the atomic orbitals, however, are not all equally likely to occur for a given ion and the calculation for the number of atoms involved in producing a spectral line needs to take this relative probability into account. For example, the transition from the n = 3 orbital to the ground state that produces an absorption line at $\lambda \simeq 2026$ Å is approximately two times more likely to occur than the Zn II 2062 Å transition from the n = 2 orbital to the ground state. The f-value, or oscillator strength gives the relative probability that an electron makes a transition between orbitals. Assuming electric-dipole transitions, the f-value depends on the vacuum wavelength $\lambda_{lu}(\text{Å}) = 10^8/(E_u - E_l)$ produced in the transition between energy levels, the statistical weight (as a function of the angular momentum J of the state involved) $g = 2J + 1$, and the transition probability A in s^{-1} (also known as the Einstein A coefficient). In equation form and numerically,

$$f_{lu} = \frac{g_u}{g_l} \frac{m_e c}{8\pi^2 e^2} \lambda_{lu}^2 A_{ul} = 1.49919 \times 10^{-16} \, \lambda_{lu}^2 \, \frac{g_u}{g_l} \, A_{ul}, \tag{1.35}$$

where m_e is the mass of the electron in grams, c is the speed of light in cm s^{-1}, and e is the charge of an electron in esu. For the Zn II λ2026 transition mentioned above, $f = 0.630$, whereas $f = 0.309$ for the λ2062 transition. There are other Zn II transitions, however, they have very low relative probabilities, e.g., $\lambda\lambda$986, 984, 949, and 938 with f-values = 0.00154, 0.00246, 0.00475, and 0.00183 respectively. The f-values for transitions from the same initial orbital add up to the number of electrons in the atom or ion, which means that the oscillator strength is the effective number of electrons per atom involved in the transition. The quantity fN, i.e., the oscillator strength multiplied by the number of absorbing atoms per unit area, will give the number of atoms that are participating in the transition in front of the emitting region per unit area (typically cm^{-2} for column densities).

1.2.5 Curve of Growth

The curve of growth (COG) method is another method that can be used to derive the column density N. It does not rely on fitting line profiles, but rather from measurements of the equivalent width W. Thus, the COG method is only reliable for unsaturated and unblended absorption lines. As was seen in Figure 1.8, the equivalent width W varies directly with the column density N. The relationship between W and N is interesting and satisfyingly predictable. For example, if the number of absorbing atoms is doubled, then twice as much light is removed from the spectrum and the equivalent width of the line is twice as large. This relationship, $W \propto N$, can be represented with a linear line on a plot of W vs. N. However, if the number of atoms increases to the point where the line bottoms out and becomes saturated, then any continued growth would occur in the wings of the line, since the center of the line has become optically thick. During this process, the value for N can increase significantly with very little change in W, thus on a graph the relationship would look like a flattening line. If the number of atoms were to increase further, pressure broadening would increase the equivalent width through widening wings, although W does not increase as steeply as it did at first. Figure 1.9 shows this proportional relationship in a logarithmic graph of W as a function of N.

Delving deeper into the three regions described above and presented in Figure 1.9, the behavior of the COG in these regions in terms of τ and N are summarized in Table 1.2.

1.2.6 The Apparent Optical Depth Method

So far, two methods have been described to derive column densities from spectra and each method has its advantages and disadvantages. The curve of growth method is effective as long as the lines are unblended and unsaturated. An advantage of the Voigt profile method is its ability to deal with blended lines provided the resolution

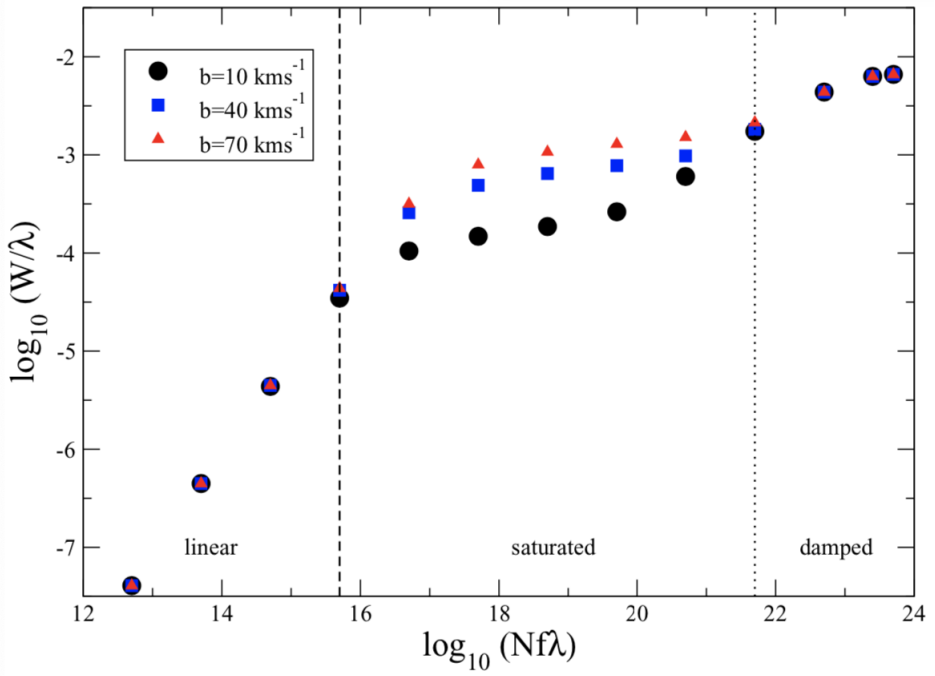

Figure 1.9 A curve of growth graph for the H I Lyα line for three different b-values: 10, 40, and 70 km s^{-1}. In the linear and damped portions of the COG the equivalent width is independent of the b-value. Note that there is relatively little change in W for saturated lines even as $\log_{10}(Nf\lambda)$ increases by two magnitudes. This makes determination of N challenging in this regime. Image credit: Debopam Som

Table 1.2 Summary of the Curve of Growth

Regime	Behavior of W	Notes
linear	$\propto N$ $W = N\sigma \int_{-\infty}^{\infty} \phi \, d\lambda = N\sigma$	. occurs for optically thin lines, $\tau \ll 1$. independent of b-value . $N = 1.13 \times 10^{20} \frac{W}{\lambda^2 f}$ cm^{-2} . W determines N for unblended lines
logarithmic (saturated)	$W \propto b\sqrt{\ln(N/b)}$	. occurs for saturated lines, $10 \lesssim \tau \lesssim 10^3$. growth sensitive to b-value . W not accurate measure of N
damped	$W = 2\sqrt{N\sigma\gamma}$	. optically thick, $\tau \gtrsim 10^4$. independent of b-value . exhibits damping wings, $\sigma \propto (\lambda - \lambda_0)^{-2}$

of the spectra is high enough. Here, I introduce another method, the apparent optical depth or AOD method, that is effective for unblended and unsaturated lines.

An underlying assumption of the AOD method is that the continuum background source of photons (e.g., a quasar) from which the absorption lines are formed from varies slowly with wavelength. Thus, we can reason that the continuum level is nearly constant across the absorption feature if the line width is small. This allows the initial intensity term $I_{\lambda,0}$ to be pulled out from equation 1.33 and it can be rewritten as

$$I_{\lambda,f}(\lambda) = I_{\lambda,0}\,[e^{-\tau_\lambda} \otimes \phi_{\rm ISF}(\lambda)]. \tag{1.36}$$

Inverting equation 1.36, dividing by $I_{\lambda,f}$, and then taking the natural logarithm of both sides, we can obtain an expression for an instrumentally blurred version of the *actual* optical depth which is defined as the *apparent* optical depth, $\tau_{\rm AOD}$,

$$\tau_{\rm AOD} = \ln\left(\frac{I_{\lambda,0}(\lambda)}{I_{\lambda,f}(\lambda)}\right) = \ln\left(\frac{1}{e^{-\tau_\lambda} \otimes \phi_{\rm ISF}(\lambda)}\right). \tag{1.37}$$

If the FWHM for $\phi_{\rm ISF}(\lambda)$ is much less than the FWHM for the line, then $\tau_{\rm AOD}$ is indeed a good approximation of the actual optical depth τ_λ. Thus, this method can be very accurate for well resolved lines. According to Savage & Sembach (1996) the AOD method can deliver column densities with uncertainties $\lesssim 10\%$ for moderately strong lines in medium-resolution spectra, however, it works best for non-saturated lines observed in high S/N spectra. In terms of column density, τ_{AOD} is

$$\tau_{AOD}(\lambda) = \frac{\pi e^2}{m_e c^2} f \lambda^2 N(\lambda). \tag{1.38}$$

The total column density is given by $N = \int N(\lambda)\, d\lambda$ in the interval from λ to $\lambda + d\lambda$.

Important! For all three of the described methods, it is vital to point out that the column density also depends inversely on the f-value. Therefore, uncertainties in the oscillator strength can translate into significant uncertainties in the column density independent of the S/N. Much effort and money are put into advancing telescopes and instrumentation, however, it is vain to do so if the high resolution spectral lines captured have f-value accuracies known only to 40%. It is imperative that the atomic data (i.e., energy levels and wavelengths, oscillator strengths, collisional data)

required to interpret spectra be advanced alongside telescopes and instrumentation for truly robust results. This is the subject of Chapter 5.

1.2.7 Element Abundances

After determining the column densities of the atoms and ions from the absorption lines present in a spectrum, the metallicity can be calculated to quantitatively characterize the chemical properties of the absorbing gas. The absolute abundance was defined earlier in Section 1.2.1 and was shown in equation 1.3. The equations for abundance and absolute abundance are both shown below for continuity.

Abundance of X relative to Y:

$$\left[\frac{X}{Y}\right] = \log_{10}\left(\frac{N_X}{N_Y}\right)_{\text{abs}} - \log_{10}\left(\frac{N_X}{N_Y}\right)_{\odot} \tag{1.39}$$

Absolute Abundance of X relative to Hydrogen:

$$\left[\frac{X}{H}\right] = \log_{10}\left(\frac{N_X}{N_H}\right)_{\text{abs}} - \log_{10}\left(\frac{N_X}{N_H}\right)_{\odot} \tag{1.40}$$

The terms $\log(X/Y)_{\odot}$ and $\log(X/H)_{\odot}$ use solar system abundances and for this work come from measurements of elemental abundances in the Sun's photosphere. Solar system abundances can also come from the composition of meteorites, however, all solar abundance data for this work is from the solar photosphere measurements of Asplund et al. (2009). A plot of this abundance data is shown in Figure 1.10 for reference.

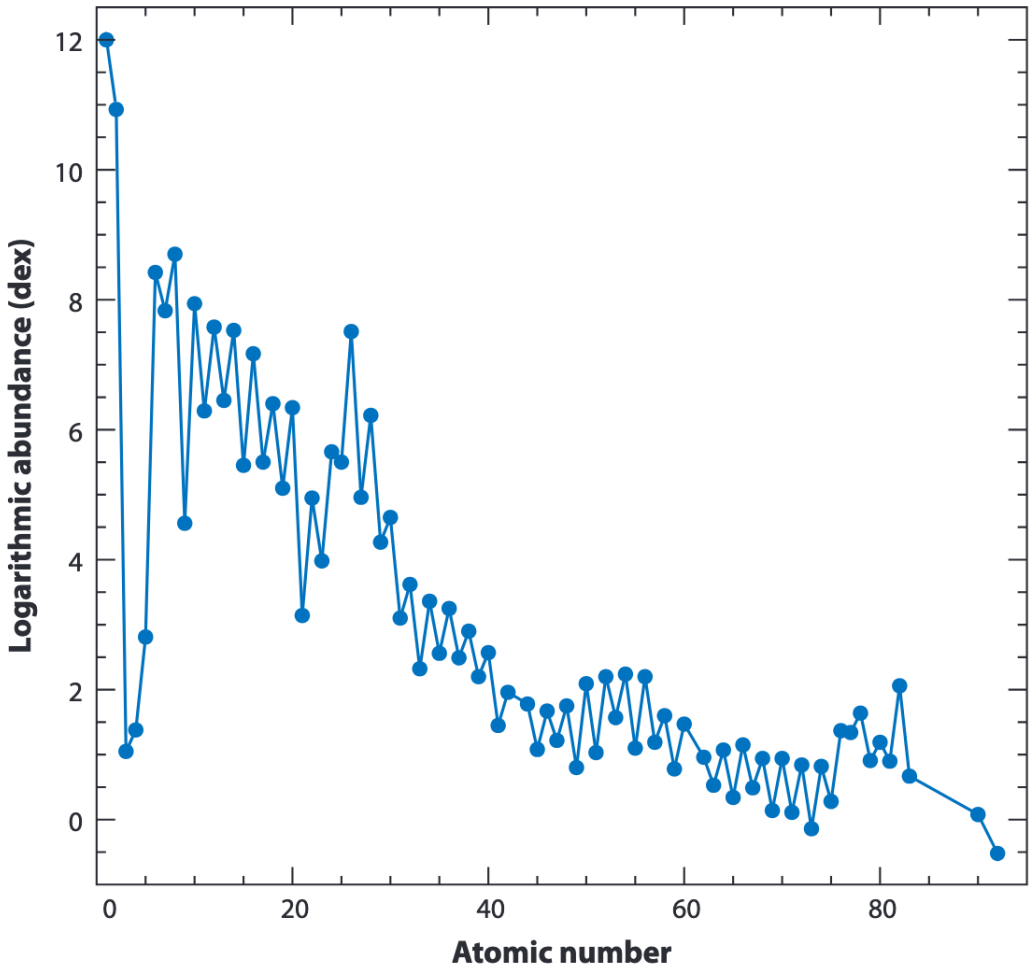

Figure 1.10 The solar photospheric abundances presented in Asplund et al. (2009) versus atomic number.

Chapter 2

Quasar Absorption Line Systems

The optical depth, equivalent width, and line broadening mechanisms discussed in Section 1.2 were introduced by way of descriptions of absorption line systems foreground to a background quasar. The absorption systems discussed in this work are all either absorbing regions associated with lens galaxies or are a type of Lyman Limit system (LLS) that was discovered along the line of sight to the lensed images of the quasars. What both of these absorption systems have in common is that they are very distant and are too dim to be studied through their continuum or line emission. However, quasar absorption line spectroscopy is a powerful flux-independent technique, i.e., independent of the absorber's flux, that can probe the gas in and around distant systems. Investigating the physical and chemical properties of the gas along multiple sight lines through these lensed systems is among the most accurate methods for studying the small-scale structure of the interstellar medium or ISM of these lensing galaxies and LLSs.

Section 2.1 discusses the origin of Quasi-stellar Objects or QSOs and why their intense energy output makes them ideal continuum sources for absorption line spectroscopy. Section 2.2 discusses the quasar spectrum and how an absorption system appears when superposed with a quasar's spectrum. Section 2.3 introduces the Lyman-alpha forest and the Lyman-limit systems. Section 2.4 introduces gravitational lensing and explains how using multiple sight lines towards gravitationally lensed quasars improves upon the traditional single sight line method.

2.1 Quasi-Stellar Objects

Radio astronomy took off after World World II when astronomers began noticing radio sources in the sky that turned out to be extragalactic in origin. These radio galaxies often displayed extended radio lobes and jets connected to the central portion of the galaxy. These findings were the first suggestion that galaxies could be active. The first quasar was stumbled upon in 1960. The discoverers, Thomas Matthews and Allan Sandage, were looking for the optical counterpart to a radio source named 3C 48 and unexpectedly found what appeared to be a 16th magnitude star with a spectrum unlike any they had ever seen. A few years later, another star-like object was found to be the optical counterpart for another radio source, 3C 273. This object also had a peculiar spectrum with broad emission lines that astronomers could not associate with any known element or molecule. These star-like objects were classified as quasi-stellar radio sources or QSRs, which morphed into the term quasars. The mystery of the unknown broad emission lines was solved by Maarten Schmidt, who recognized that the line pattern matched the Balmer lines of Hydrogen, but were redshifted to longer, and thus unrecognized wavelengths. Once astronomers realized that what seemed unfamiliar was actually familiar, they were able calculate redshifts for these objects using the Doppler shift equation and estimate their cosmological distances.

One of the distinguishing features of quasars when compared to stars is the excess of emitted ultraviolet light, making them appear blue, and most quasars have a negative color index $U - B < -0.4$. The blue color can be explained from a look at their spectral energy distribution, which indicates that quasars produce most of their energy at short wavelengths, thus a quasar's rest-frame spectrum has a profusion of high energy, short wavelength photons. The transitions associated with these shorter wavelengths are important for absorption line studies, e.g., H I λ1215 and λ1025, which are required to calculate robust absolute abundances. For higher red-

shift quasars ($z \gtrsim 2.3$ to bring H I λ1215 to the blue edge of the visible spectrum at 4000 Å), these lines are redshifted into the visible portion of the electromagnetic spectrum and may be observed from the ground. The currently accepted theory is that accreting super-massive black holes ($\sim 10^6 - 10^9 M_\odot$) are the central engines driving these luminous quasars. To date, over five hundred thousand quasars have been found with the Sloan Digital Sky Survey (SDSS; York et al. 2000), which only covers a fraction of the sky. This tells us that active galaxies are common. Another interesting discovery to emerge from cataloguing quasars is that the overwhelming majority of quasars are, in fact, radio-quiet. Thus, the term quasi-stellar object was introduced to distinguish between radio-loud quasars (QSRs) and radio-quiet quasars (QSOs). Presently, the term quasar and the abbreviation QSO are used for both types of objects and the distinction between radio-loud and radio-quiet is made as needed.

As interesting as quasars are in and of themselves, the focus here will shift to how quasars are an effective tool to probe the distant universe. Since they are so luminous, they are among the most distant objects in the universe that are visible, and as such, they offer a unique way to probe the intervening space along the line of sight from us to the quasar. It is useful to recall that the AOD method described in 1.2.6 relies on the assumption that the quasar continuum is predictable and slowly varying, which also facilitates the measurement of superposed absorption lines. The superposed absorption line spectra is the subject of Section 2.2.

2.2 Absorption Lines in Quasar Spectra

Imaging surveys have formed the foundation for our current interpretation of galaxy evolution. These surveys have shown that the global star formation rate in galaxies was much higher at $z > 1$ than what is seen in the local universe, and the major part of the stellar matter in galaxies was assembled at approximately $2 \lesssim z \lesssim 3$ (e.g., Madau & Dickinson et al. 2014). However, in order for a galaxy to be imaged,

it must be bright enough in emission. These imaging surveys are magnitude-limited, however, and so by design are flux-limited. A more representative view of distant galaxies is provided by studying the absorption lines in quasar spectra superposed by intervening foreground galaxies. Galaxies studied with the quasar absorption-line technique are sampled by gas cross section, independent of their brightness.

Due to their large redshift baseline, a quasar sight line often passes through multiple absorption systems such as diffuse intergalactic clouds, the ISM of a galaxy, or through the circumgalactic medium (CGM) of a galaxy, as illustrated in Figure 2.1. When the spectrum of a quasar is captured with a spectrometer, the spectrum is the cumulative spectrum of all the emission and absorption lines from all of the intervening material, where the absorption lines correspond to chemical elements and molecules present in the intervening systems. In the rest-frame of the absorber, an electron in an atom or ion will only absorb a photon if its energy is exactly equal to the difference between two energy levels within its electron cloud. As quasars produce a nearly continuous spectrum of photons, the absorption of a photon produces an absorption line at an observed wavelength equivalent to the rest-frame wavelength of the transition multiplied by $(1 + z)$,

$$\lambda_{\text{observed}} = \lambda_{\text{rest}} \times (1 + z_{\text{abs}}). \tag{2.1}$$

This is what makes it possible to observe multiple systems at different redshifts, as the absorption lines for successively distant systems are redshifted to longer wavelengths. It is even possible to observe multiple clouds within the target system at more or less the same redshift as they have different line of sight velocities. The ability to not only observe multiple systems, but also multiple components within a system independent of brightness is what makes quasar absorption line spectroscopy such a powerful observation method for observing distant galaxies.

When a quasar sight line passes through or near a galaxy, it may directly intersect the ISM of the galaxy, or perhaps intersect the halo or CGM of the galaxy, or it may

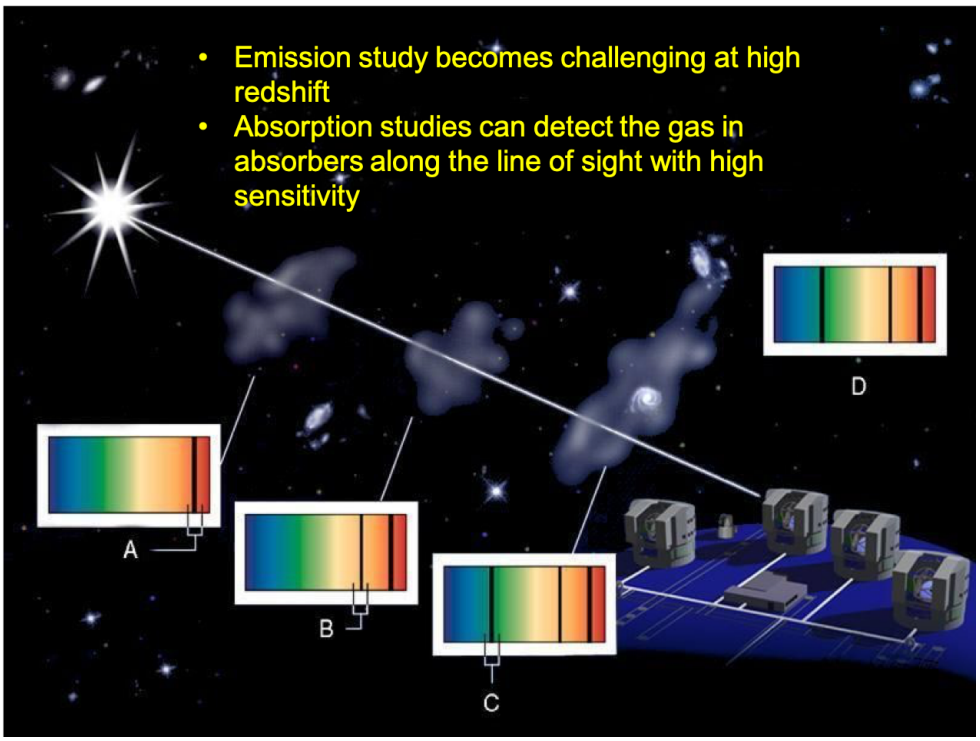

Figure 2.1 An illustration of the combined absorption spectra resulting from intervening absorption line systems along the line of sight from a bright background quasar to Earth. Spectrum A shows the strong absorption features associated with the absorbing gas of that systems. Spectrum B shows its absorption feature in addition to the feature from spectrum A. D is the cumulative spectrum including absorption lines from all intervening galaxies or intergalactic clouds (as seen in spectra A, B, C), where the lines correspond to chemical elements and molecules that are present in the intervening galaxies. Image adapted from Ed Janssen of *ESO*.

pass just outside the circumgalactic region through the intergalactic medium (IGM), see Figure 1.1. As mentioned above, studying the gas in and around galaxies is imperative to understanding how galaxies evolve. Measuring element abundances in the ISM is crucial to understanding the chemical composition of gas and understanding dust depletion, and additionally for very distant galaxies, the cosmic evolution of dust and stellar nucleosynthetic processes. Observing the CGM provides constraints on the effects of inflows and outflows in and out of galaxies. Measuring element abundances in the intergalactic medium reveals the physical conditions and processes influencing the diffuse cosmic web.

An illustrative example of a single sight line to a quasar and its corresponding spectrum is shown in Figure 2.2. There are several features of the spectrum that should be described, as they are common to most quasar spectra. The broad emission peak (at ∼4890 Å) corresponds to Hydrogen emission from the quasar itself. The portion of the spectrum to the left of this peak shows numerous absorption lines of varying width and depth which were created as light from the quasar passed through frequent Hydrogen absorption systems ranging in size from small intergalactic clouds to massive gas-rich spiral or elliptical galaxies. Neutral hydrogen (H I) atoms absorb photons of wavelength 1215.6701 Å to excite its ground state electron to the 1st excited state. The excitation from $n = 1$ to $n = 2$ corresponds to the Lyman-alpha (Lyα) line of the Lyman spectral series, of which it is the strongest member. So when looking at the continuous spectrum source through an intervening absorption system, photons of ∼1216 Å (in the rest frame of the absorbing system) are absorbed by the H I atoms in that system. Absorption lines result and in the most optically thick regions, the absorption feature is trough-like instead of appearing as narrow lines. This foreground section of the spectrum characterized by closely-spaced narrow Hydrogen absorption lines is called the Lyα forest. There is significant H I absorption at ∼4600 Å due to an intervening gas-rich galaxy, producing a line with a strong Doppler core and pronounced Lorentzian wings. The portion of the spectrum to the right of this peak shows narrow absorption lines which correspond to metal (Z > 2) absorption occurring in this same gas-rich galaxy.

2.3 Properties of Quasar Absorption Line Systems

The different absorbers encountered along the line of sight to the quasar are named for their identifying features. The absorbers are typically classified by their metal lines or by their neutral hydrogen column density ($N_{\rm H\,I}$). For example, C IV, Mg II, and Ca II absorbers are typically identified by their metal lines. A "damped"

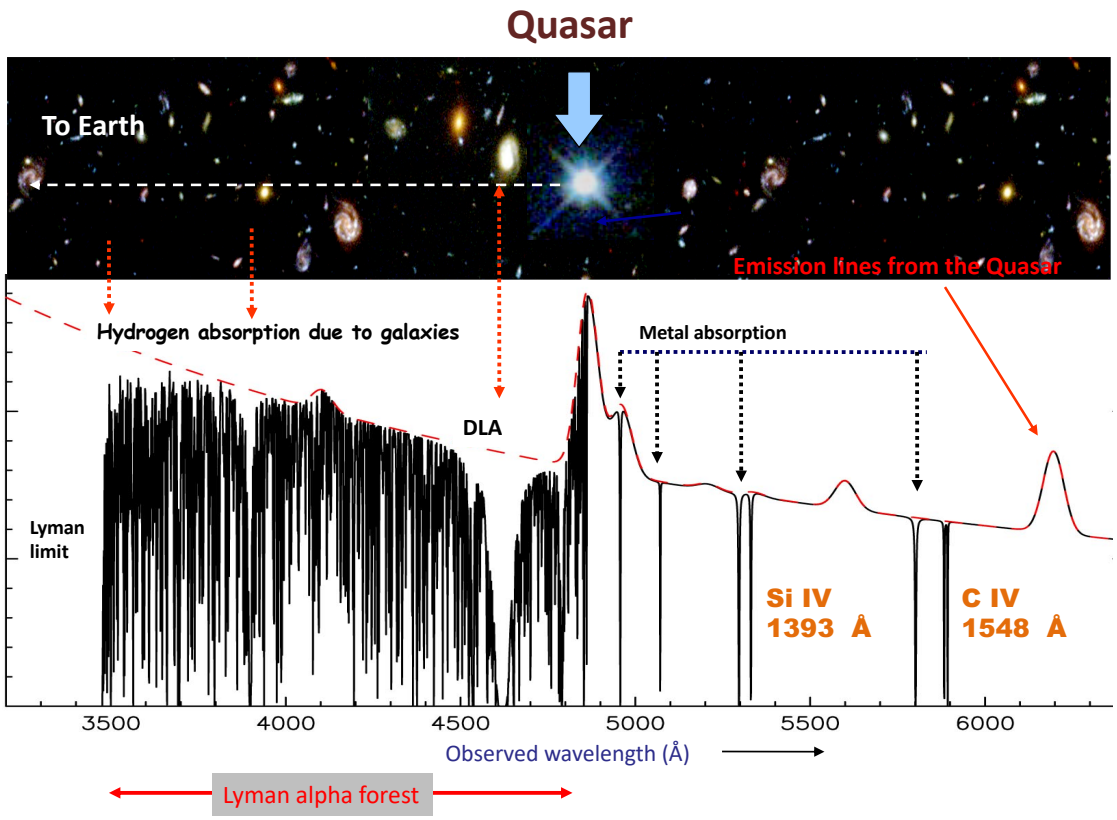

Figure 2.2 An illustration of how multiple intervening absorption line systems can superpose on a quasar's spectrum. The red dashed line traces the quasar continuum across a range of wavelengths. The broad emission peaks are associated with emission from the quasar itself. Each absorption feature is associated with an absorption system along the line of sight to the quasar. This figure was adapted from a version originally created by John Webb and was published in Pettini (2004).

Lyman alpha absorber (DLA), a sub-damped Lyman-alpha absorber (sub-DLA), Lyman Limit systems (LLS), and the Lyα forest are all identified by their H I properties. This classification is helpful because Hydrogen is the predominant element in the universe. DLAs ($N_{\rm H\,I} \geq 2 \times 10^{20}$ cm^{-2}) and sub-DLAs ($10^{19} \leq N_{\rm H\,I} < 2 \times 10^{20}$ cm^{-2}) dominate the mass density of neutral gas in the universe (see Prochaska, & Wolfe 2009, Zafar et al. 2013, Popping et al. 2014, Neeleman et al. 2016). The LLS begin at the upper boundary of the ionized forest systems with $17.2 \lesssim \log N_{\rm H\,I}$ (cm^{-2}) $\lesssim 19.0$. The narrow lines of the Lyα forest have are defined as absorption systems with $\log N_{\rm H\,I} < 17.2$ cm^{-2}.

The properties of metal line and H I absorbers are summarized in Table 2.1. Note that the origin and log $N_{\rm H\,I}$ of some of the systems is still not well understood. Those systems are marked with an asterisk (*) in the table. Each H I absorption system will be described in the sections following the table.

Table 2.1 Properties of Absorption Line Systems

Absorption System	log $N_{\rm H\,I}$	Feature	Source
C IV	> 14 cm^{-2*}	C IV 1548, 1551 Å	IGM/galaxy
Mg II	> 17 cm^{-2}	Mg II 2796, 2803 Å	Galaxy halo
Ca II	> 19 cm^{-2*}	Ca II 3934, 3969 Å	Dense gas*
Lyα forest	< 17.2 cm^{-2}	Lyα 1216 Å	IGM
Lyman limit	$\gtrsim 17.2$ cm^{-2}	Lyman limit at 912 Å	Galaxy halo
Sub-DLA	19$-$20.3 cm^{-2}	Weak Lyα damping wings	Halo* Galaxy*
DLA	≥ 20.3 cm^{-2}	Lyα damping wings	Galaxy

2.3.1 The Lyman Alpha Forest

The narrow H I lines shortward of the quasar's strong Lyα emission line are that of the Lyα forest. Each of these lines is produced by absorption from a different intergalactic cloud of hydrogen and helium that the quasar's continuum photons have intercepted on the way to Earth. These clouds are considered to be separate from intervening galaxies and are thought to be diffuse ($n_{\rm H\,I}/n_{\rm H} \sim 10^{-4}$), hot ($T \sim 4 \times 10^4$ K), and ionized. A typical column density for a Lyα cloud is $\sim 10^{-14}$ cm^{-2} and this low density is transparent to the ultraviolet background that permeates space. The fact that they are so diffuse, yet are also the most numerous of the absorbers according (see the column density distribution function in Figure 2.7 in Section 2.3.4) signifies how ubiquitous their presence is in the IGM, as the majority of the baryons in the Universe likely lie in the Lyα forest. Since sight lines through the Lyα forest are sight lines through the IGM, mapping the Lyα forest out to high redshifts can

show the evolution of the structure of the Universe, see Figure 2.3. The Lyα forest appears to be isotropic, i. e., uniform along sight lines in all directions.

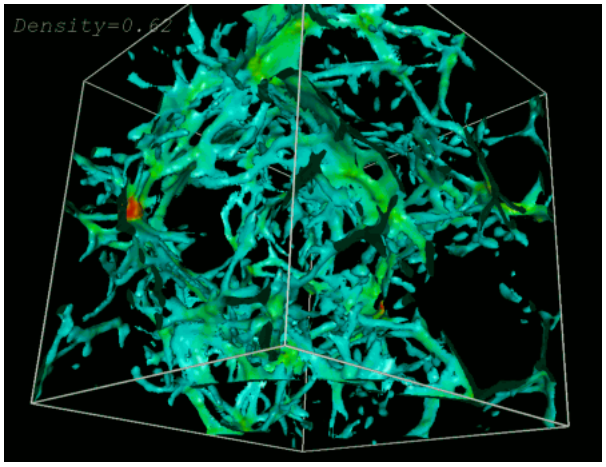

Figure 2.3 A simulation showing an isotropic 3D distribution of Lyα clouds at $z = 3$. The length of each side of the box is 30 million light-years. Image credit: J. Shalf, Y. Zhang (UIUC) et al., GCCC

There are significantly more Lyα forest lines in the spectra of distant quasars than there are in nearby ones, which suggests that the early universe had a denser web of hydrogen filaments and clouds. Figure 2.4 illustrates how the number density of Lyα clouds evolves as a function of redshift (Riediger et al. 1998).

The number of lines per unit redshift behaves approximately as a power law:

$$\frac{\mathrm{d}n}{\mathrm{d}z} \propto (1+z)^{\gamma}. \tag{2.2}$$

Riediger et al. (1998) found $\gamma \approx 2.6$ for $1.5 < z < 3$ and $\gamma \approx 0.6$ for $0 < z < 1.5$ for the log $N_{\mathrm{H\,I}}$, suggesting a strong pattern in the evolution of the number of Lyα clouds.

2.3.2 The Lyman Limit Systems (LLSs)

The LLSs begin at the upper boundary of the ionized forest systems with log $N_{\mathrm{H\,I}} \gtrsim 17.2$ cm^{-2}. Although DLAs and sub-DLAs are technically included in this

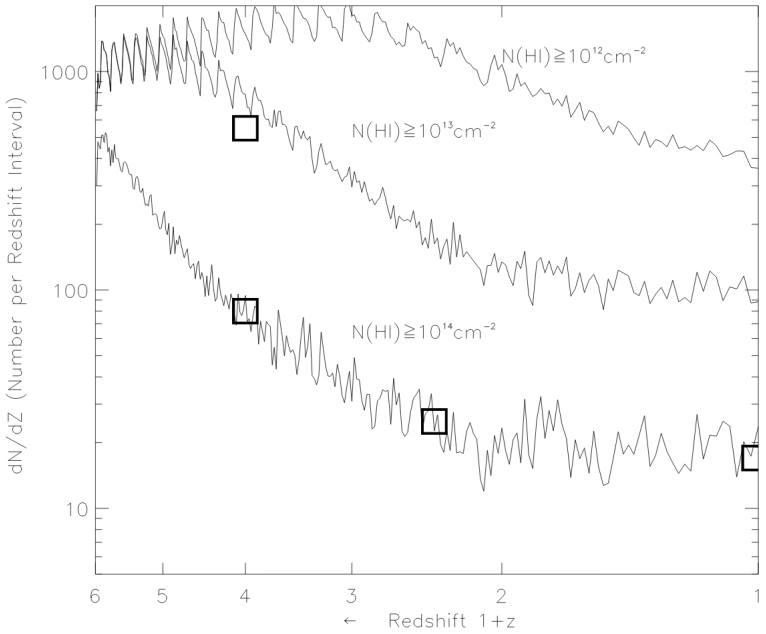

Figure 2.4 Model prediction from Riediger et al. (1998) of the number density $\mathrm{d}n/\mathrm{d}z$ of lines for different column density thresholds versus redshift, where log $N_{H\,I} \geq 12, 13, 14$. The higher density Lyα lines decline steeply until $z \sim 2$. The squares are observed data points from Rauch et al. (1997)

classification, they are categorized separately due to the significance that these higher density systems impart on our understanding of how galaxies evolve. Thus the scope of the discussion about LLSs in this section will focus on the moderately-sized LLSs that have an upper column density cap at log $N_{\mathrm{H\,I}} \lesssim 19.0$ cm^{-2}, where the sub-DLAs will then take over. The LLSs are named so because at $N_{\mathrm{H\,I}} = 17.2$ cm^{-2} a cloud becomes optically thick ($\tau = 1$) at ∼912 Å , which is the wavelength limit of the hydrogen Lyman series and ionization potential of H. Thus, the flux essentially drops to zero for wavelengths shortward of the Lyman limit. Although one of the major benefits to absorption line spectroscopy is being able to observe multiple systems, the Lyman limit can make spectroscopy more challenging for lower redshift systems as their absorption lines can be "wiped out" by the Lyman limit of a higher redshift system. As log $N_{\mathrm{H\,I}}$ increases for an absorption system, it is easy to imagine the systems becoming denser and thicker. An increasing density of H I atoms means

that a larger number of the atoms are protected from ionizing radiation, essentially shielding themselves through a process appropriately named self-shielding. Thus the LLSs have a higher neutral hydrogen fraction than the Lyα forest clouds. An intercepted LLS is believed to be intersecting the CGM of a galaxy, thus studying them is important for galaxy evolution studies, as the CGM exchanges material with the ISM of a galaxy. There are two defining exchanges which heavily influence a galaxy's evolution. The first is material flowing into or onto a galaxy from the IGM and/or CGM via primordial streams of colder, metal-poor gas. This inflow may increase star formation by providing material that can collapse and form into stars and have the effect of showing a lower metallicity value because of the diluting effect. The second exchange are outflows from the galaxy and its ISM to the CGM. These outflows can be due to many events including stellar winds, supernovae ejecting metal-rich gas, and/or ISM gas being tidally stripped due to gravitational interactions with nearby galaxies. A paper from Lehner et al. (2013) presented empirical results that support there being two distinct exchanging mechanisms between the ISM and CGM of a galaxy. They reported a metallicity bimodality in a sample of 28 LLSs and suggest that the lower metallicity LLSs were intercepting cold accretion streams and that the higher metallicity LLSs were probing regions significantly impacted by stellar winds, recycled outflows, and/or tidally stripped gas. Increasing observations and analysis in this manner of the number of LLSs will help to confirm if their small sample is representative of LLSs as a whole.

2.3.3 The Damped and sub-Damped Lyman Alpha Absorbers

The sub-DLA bracket picks up at log $N_{\rm H\,I} \gtrsim 19.0$ cm^{-2} and beyond log $N_{\rm H\,I} > 20.3$ cm^{-2} absorption systems are classified as DLAs. These high density neutral gas absorption systems are believed to be directly associated with galaxies and thus are vitally important for galaxy evolution studies. The distinction between DLAs and

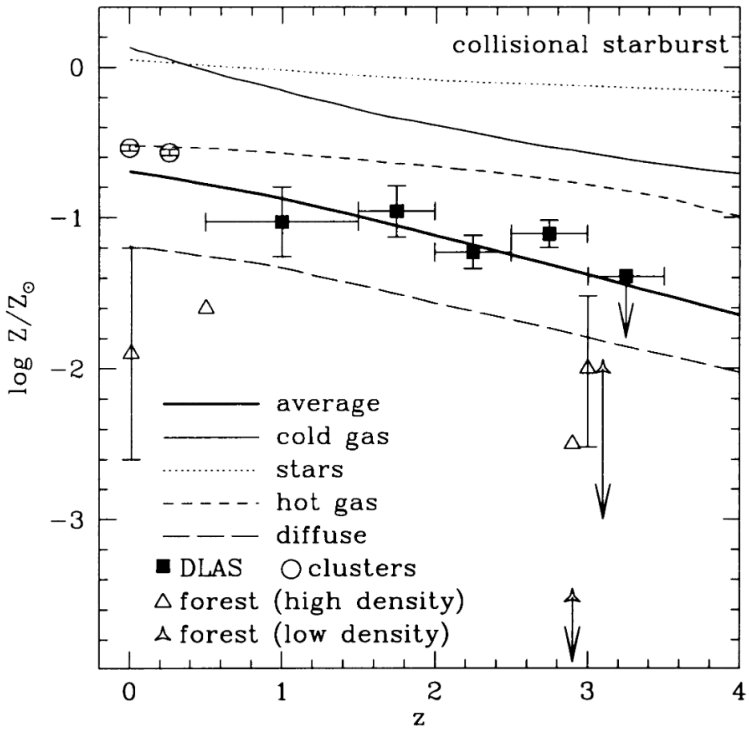

Figure 2.5 Metallicity as a function of redshift from Somerville et al. (2001). The square symbols are the metallicities of DLAs from the measurements of Zn ([Zn/H_{DLA}]) from Pettini et al. (1997b). The metallicities are well below the solar level even near $z = 0$.

sub-DLAs is not limited to the difference in log $N_{\rm H\,I}$, however, as they also differ in metallicity trends. Generally, DLAs are found to be metal-poor, whereas sub-DLAs are largely found to be more metal-rich. DLAs on average have a metallicity $\sim 0.2Z_{\odot}$ and are well below the predicted mean interstellar metallicity from models such as those from Pei et al. (1999) and Somerville et al. (2001), which predict that the mean interstellar metallicity should reach solar level at $z = 0$. Figure 2.5 shows an example model from Somerville et al. (2001).

More recently, our group (see Poudel et al. 2019) combined seven new abundance measurements with those previously published in the literature to estimate the $N_{\rm H\,I}$-weighted binned mean metallicity. The metallicity value of -1.51 ± 0.18 at $z = 4.8$ is in excellent agreement with the prediction from lower redshift DLAs, supporting the

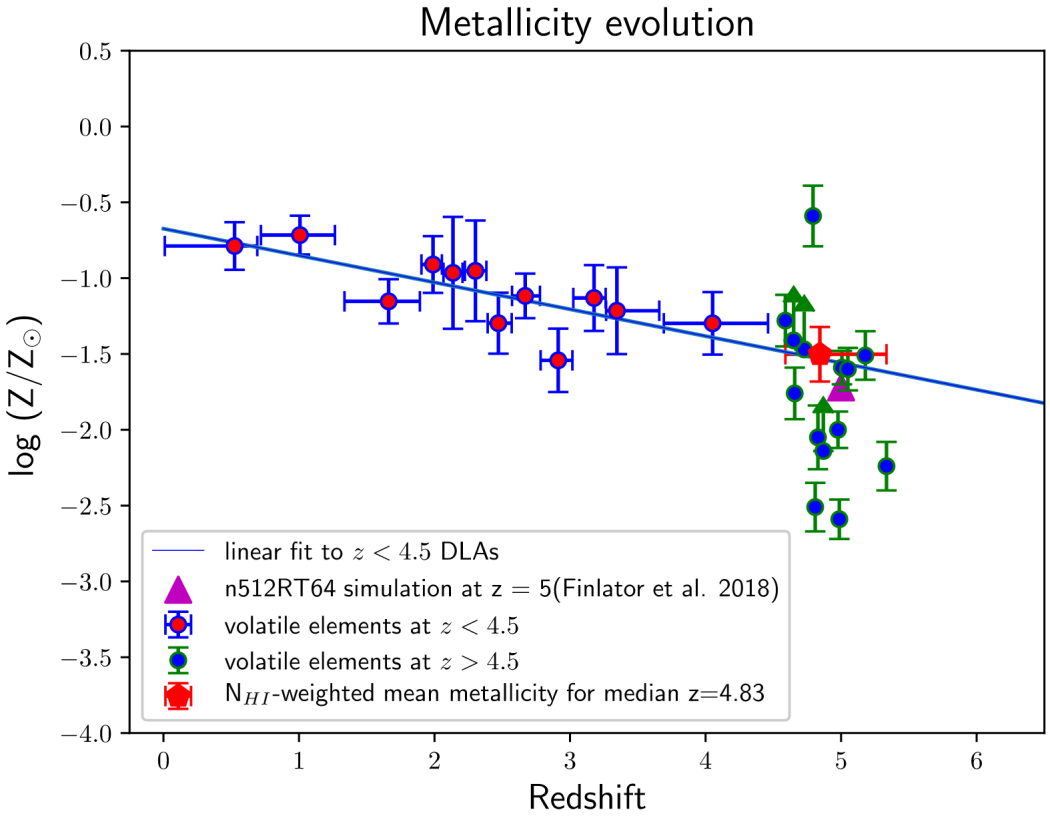

Figure 2.6 A smooth metallicity evolution for DLAs versus redshift from Poudel et al. (2019). The red dots with blue error bars are the binned log $N_{\rm H\,I}$-weighted mean metallicities of DLAs at $z < 4.5$ using volatile elements from the literature, with each bin containing 16 or 17 DLAs and the solid blue line showing the corresponding best fit. The blue dots with green error bars are the individual measurements for $z > 4.5$ absorbers also using volatile elements. The metallicities are well below the solar level even near $z = 0$.

interpretation that the metallicity evolution is smooth at $z \sim 5$, rather than showing a sudden decline at $z > 4.7$, as was reported in Rafelski et al. (2012, 2014). The results in those studies used metallicity measurements based on refractory elements (i.e., Fe, Si) which could have been affected by depletion, rather than volatile elements (i.e., S, O, Zn) which do not deplete into dust grains as readily in the ISM. These abundance measurements and their comparison with the literature can be seen in Figure 2.6.

Additionally, there have been multiple studies of chemical abundances for sub-DLAs based on Zn or S, in the redshift range from $0.6 \lesssim z \lesssim 1.5$. These have

shown that there is a difference between the chemical evolution of sub-DLAs versus DLAs (Péroux et al. 2006, Meiring et al. 2007, Meiring et al. 2008, Meiring et al. 2009a, Meiring et al. 2009b, Nestor et al. 2008, Dessauges-Zavadsky et al. 2009). At this lower redshift range, the sub-DLAs are more metal-rich and appear to be evolving faster than DLAs, which suggests that these absorbers could be forebearers of different populations of present day galaxies. The metal-rich sub-DLAs may have their origins in massive galaxies that happened to convert their reservoirs of gas into stars at an earlier stage then the DLAs did. Logically this makes sense, since massive stars experience shorter lifetimes, massive galaxies could analogously undergo star formation more rapidly.

2.3.4 The Column Density Distribution Function

As is probably already obvious from the extensive discussion of these absorption systems in the preceding sections, the rate of incidence of quasar absorption line systems is inversely proportional to the observed column density, i.e., the number of systems decreases as log $N_{\rm H\,I}$ increases. This trend can be expressed as a column density distribution function, or CDDF, and is shown in Figure 2.7 for a sample of quasar absorption line systems at $z \approx 2.8$. Formally, the CDDF for a particular redshift z is defined as the number of absorbers detected in m-number of quasar spectra over a total absorption distance $\Sigma_{i=1}^{m} \Delta X_i$ in a range from N to $N + \Delta N$.

$$f_{H\,I}(N, z)\, dN\, dX = \frac{n}{\Delta N\, \Sigma_{i=1}^{m} \Delta X_i} dN\, dX \tag{2.3}$$

The absorption distance $X(z)$ naturally depends on the cosmology used and is determined using the equation

$$\frac{dX}{dz} = \frac{(1+z)^2}{[\Omega_\lambda + \Omega_m (1+z)^3 + \Omega_r (1+z)^4 + (1-\Omega)(1+z)^2)]^{1/2}}. \tag{2.4}$$

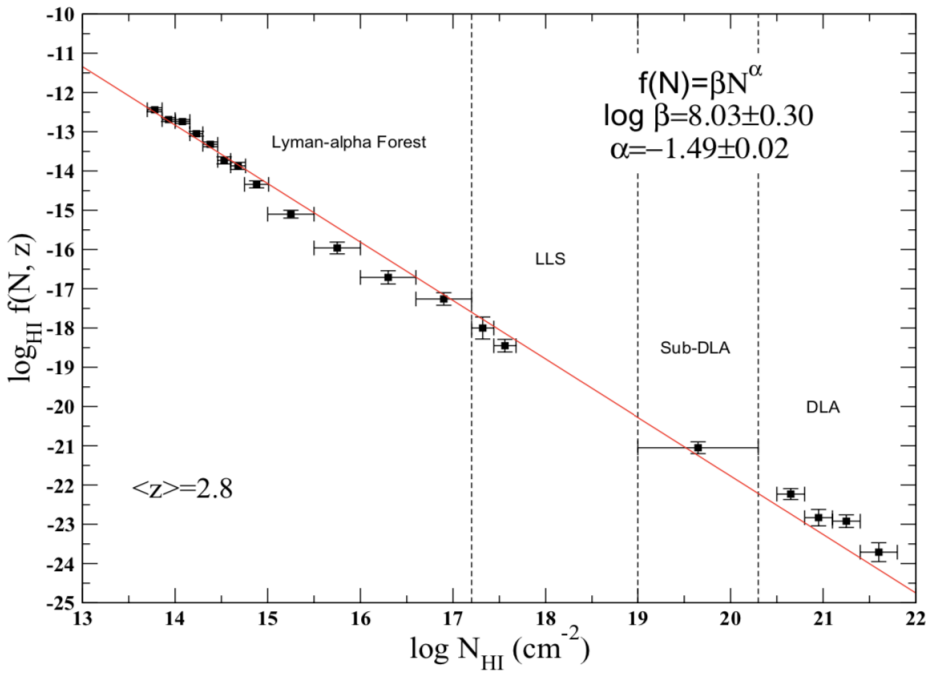

Figure 2.7 The Column Density Distribution Function (CDDF) of Lyα forest, LLS, sub-DLA, and DLA lines in quasar spectra. The sub-DLA data came from Péroux et al. (2003). The remaining data comes from Petitjean et al. (1993). Image credit: Debopam Som

The total number of absorbers at redshift z per redshift interval can be then estimated from the zeroth order moment of the CDDF,

$$\frac{dN}{dX} = \int_{Nmin}^{Nmax} f_{H\,I}(N, z)\, dN. \tag{2.5}$$

For the sample of quasar absorption line systems plotted in Figure 2.7, it is visually apparent that there are way fewer DLA and sub-DLAs than there are Lyα forest systems. A power law has been fit to the data with coefficients $\alpha = -1.49$ and $\beta = 8.03$. However the very nature of the distribution function itself introduces an issue with completeness. Since low redshift Lyα lines have shorter redshift path lengths $X(z)$, this decreases the probability that these lines are intercepted (Péroux et al. 2003). On top of this built-in issue, spectroscopy of low redshift Lyα lines is only obtainable using space-based observations because the Lyα spectral series lines are observed in the UV.

An improvement on the current understanding of the nature of these absorption systems is possible when we begin to study these systems along multiple sight lines through them. Section 2.4 discusses how using gravitationally lensed quasars allows an even deeper probe into the Lyα forest, the LLSs, and both DLAs and sub-DLAs. Our current understanding of the DLA and sub-DLA gas reservoirs had relied on one sight line which may or may not actually be characteristic of the galaxy. However, lensed quasars are rare objects, but advancing telescopes and instrumentation will eventually allow absorption line studies using bright background galaxies as probes of foreground systems. This advancement will offer a plethora of lensed targets and has been successfully implemented at low redshifts already, see Pettini et al. (2002) and Rubin et al. (2010) as examples.

2.4 Exploring Absorption Line Systems with Multiple Sight Lines

The first gravitationally lensed quasar, Q0957+561 at $z_{\rm QSO} = 1.41$, was discovered in 1979. Its double images are due to a supergiant elliptical galaxy (cD), producing images separated by $6\farcs15$.

Gravitational lensing can occur when the path of a ray of light from some source (e.g., a quasar, a galaxy, the cosmic microwave background) is deflected by the presence of matter. The geometry is analogous to the refraction of light by lenses in optics. Just as with optical lenses, a gravitational lens can magnify and increase the brightness of the object. For example, the two images of Q0142-100 that are formed by a gravitational lens have a difference in magnitude $\Delta m_V = 2.12$, due to one of the images being more gravitationally amplified than the other. Figure 2.8 shows how light from a source at S has its path deflected by an angle ϕ due to the presence of a large point mass M at position L. The angle ϕ is the angular deviation of a photon at closest approach to M,

$$\phi = \frac{4GM}{r_0 c^2} \text{rad}. \tag{2.6}$$

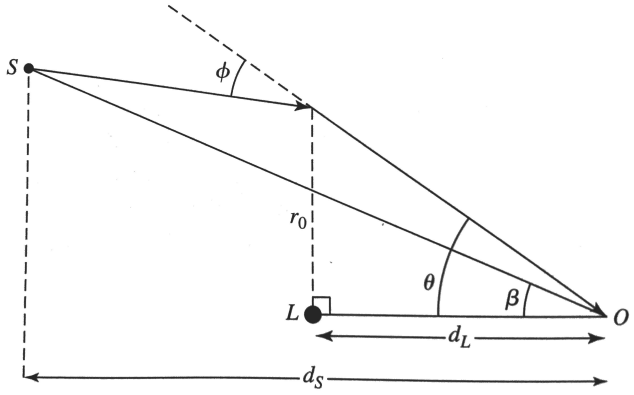

Figure 2.8 Illustration of the geometry of a gravitational lens. Light emanating from a source at S passes a distance $\sim r_0$, the distance of closest approach, from a point mass at position L. The observer at O views an image of the source at an angle of θ measured from the line of sight to L. Image credit: Carroll & Ostlie (2006)

Here and in future discussions of mass, as it pertains to multiply-imaged quasars and the lensing equations, a point mass is used even though in reality the lenses have mass profiles that extend beyond the Einstein radius.

If β is the angle between the line of sight to the lensing mass and the line of sight to the source, then the angles $\pm\theta$ are the solutions to the quadratic equation

$$\theta^2 - \beta\theta - \frac{4GM}{c^2}\left(\frac{d_{SL}}{d_S\, d_L}\right), \tag{2.7}$$

and the two images form on opposite sides of the lens. $D_{\rm S}$, $D_{\rm L}$, and $D_{\rm SL}$ denote the angular diameter distances (see equation 4.3 in Section 3.5.3 for a more detailed explanation of how angular diameter distances are calculated) between the observer and the source (quasar), the observer and the lens, and the source and the lens, respectively. The solutions θ_+ and θ_- can be measured on the sky and then used to solve for the mass of the lensing galaxy, M. For $\beta = \theta_+ + \theta_-$, the mass M is then

$$M = -\frac{\theta_+\theta_- c^2}{4G}\left(\frac{d_S\, d_L}{d_{SL}}\right). \tag{2.8}$$

In the rare instances that the lens galaxy lies directly in line with the quasar such that $\beta = 0$ in Figure 2.8, then the quasar will be imaged as an Einstein ring. In this

case, equation 2.7 can be solved for the sole value for θ, which is then the angular radius of the Einstein ring (θ_E), and is represented as

$$\theta_E = \sqrt{\frac{4GM}{c^2}\frac{d_{SL}}{d_S\, d_L}} \text{ rad.} \tag{2.9}$$

2.4.1 Improving on the Traditional Single Sight Line Method

Comparing the Lyα forest between closely spaced sight lines towards gravitationally lensed quasars is a good way to constrain the sizes of these intergalactic clouds. If absorption lines at the redshift of the lens are seen in both spectra, then it can be inferred that the foreground clouds are at least the size of the lensing galaxy. This can be achieved by seeing how well the absorption line equivalent widths are correlated between the spectra of the different sight lines and can confirm whether all lines of sight to the QSO are passing through the same absorbers, thus placing limits on absorber sizes and shapes. Monier et al. (1998) examined the intervening Lyα forest and metal-line absorbers toward the "Cloverleaf" quadruply lensed quasar (H1413+1143 at $z_{\rm QSO} = 2.54$) along its four individual sight lines using *HST*-FOS spectra. Their observations probed the Lyα forest systems on size scales of up to 4 kpc h^{-1} (for cosmology $H_0 = 100$ h km s^{-1} Mpc^{-1}, $q_0 = 0.5$) and metal-line systems on scales up to 6 h^{-1} kpc. On these small scales, they were able to show that the equivalent widths of Lyα forest lines were coherent along the four different lines of sight.

In addition to the Lyα forest, absorption spectroscopy of GLQs enables the study of spatial variations in the ISM and/or CGM of foreground galaxies. Traditional quasar absorption line studies probe only a single sight line through a generally unidentified galaxy. This makes it difficult to connect the absorber's properties to the host galaxy, as it is nearly impossible to capture the galaxy's properties with a single sight line. If the lens galaxy is seen in absorption (as well as other intervening absorbers), then one has multiple sight lines to characterize the galaxy and variations

therein. Lensed quasars are preferable to binary quasars because they have more closely spaced sight lines to the background quasars to probe small-scale structure in the ISM of the lens galaxy. If other absorbers exist between the lens and the background source, structures on scales from very small (less than a parsec) to large (several kiloparsecs or tens of kiloparsecs, depending on the location of the absorption line system) can also be probed. These systems will be magnified by gravitational lensing. Chapters 3 and 4 provide a detailed explanation on how we applied the technique of using lensed quasar absorption line spectroscopy to search for metallicity trends in lensing galaxies, as well as other absorption systems.

Chapter 3

A Sample of Doubly Lensed Quasars

Imaging surveys form the cornerstone of our current understanding of galaxy evolution. These surveys indicate that the global star formation rate (SFR) in galaxies was considerably higher at $z > 1$ than in the local universe, and that the bulk of the stellar matter in galaxies was assembled during $2 \lesssim z \lesssim 3$ (e.g., Madau & Dickinson 2014). However, the majority of these surveys are designed to be flux-limited. A flux-independent probe to study the evolution of the overall galaxy population is provided by absorption lines in quasar spectra superposed by intervening foreground galaxies, sampled simply by gas cross-section, independent of their brightness. Quasar absorption systems, especially the damped Lyman α absorbers (DLAs, defined as absorbers with H I column densities $\geq 2 \times 10^{20}$ cm^{-2}) and sub-DLAs (absorbers with $10^{19} \leq N_{\rm H\,I} < 2 \times 10^{20}$) allow detailed investigations of the interstellar medium (ISM) in distant galaxies and the circumgalactic medium (CGM) around them, and trace evolution of metals and dust (e.g., Wolfe et al. 1986; Péroux et al. 2003; Pettini 2006, Kulkarni et al. 2005, 2007, 2010; Prochaska et al. 2007; Rafelski et al. 2012; Som et al. 2013, 2015; Quiret et al. 2016). This quasar absorption-line technique can, in principle, give a more representative view of distant galaxies than magnitude-limited imaging surveys.

3.1 GLQs as Probes of Foreground Absorption Systems

Traditional quasar absorption line studies probe a single sight line through a generally unidentified galaxy. This represents two shortcomings: 1) it is difficult to

connect the absorber's properties to the galaxy host, and 2) it is difficult to capture the galaxy's properties with a single sight line. However, gravitationally lensed quasars (GLQs) can help to address both of these issues, since the lens galaxy may be seen in absorption (as well as other intervening absorbers), and one has multiple sight lines to characterize the galaxy and variations therein. Observations of multiple sight lines have been successfully used in the Milky Way (MW) and nearby galaxies. Indeed, the interstellar medium (ISM) within the MW and nearby galaxies shows structure over more than 8 orders of magnitude in spatial scale (e.g., Spangler 2001; McClure-Griffiths 2010). On small scales, the cold neutral gas (traced by Na I absorption lines) shows AU-scale variations caused by turbulence (e.g., Lauroesch et al. 2000; Andrews et al. 2001). At the same time, kpc-scale ISM structures such as supernova-driven bubbles are also evident. Such variations cannot be studied with absorption-line studies of single sight lines.

In principle, sight lines to binary quasars also offer multiple probes of foreground galaxies. However, most binary quasars typically have separations in the 15-200 kpc range (e.g. Hennawi et al. 2006, Ellison et al. 2007; Green et al. 2011). In this study, we focus on GLQs rather than binary quasars because GLQs allow us to build a sample of sight lines with close (<10 kpc) transverse separations. Past observations of different kinds of absorbers toward GLQs have enabled constraints on absorber sizes and kinematics, using coincident and anti-coincident absorption features in the separate sight-lines (e.g., Smette et al. 1992; Rauch et al. 1999, 2001, 2002; Churchill et al. 2003; Ellison et al. 2004; Lopez et al. 2005, 2007; Chen et al. 2014; Zahedy et al. 2016, 2017; Rubin et al. 2018b). Absorption studies of background galaxies and gravitationally lensed arcs are also becoming possible (e.g., Bordoloi et al. 2016, Rubin et al. 2018a, Lopez et al. 2018; Péroux et al. 2018). Closely separated sight lines to the background quasars or galaxies probe small-scale structure in the ISM of the lens galaxy. Furthermore, if other absorbers exist between the lens and

the background source, structures on scales from very small (less than a parsec) to large (several kpc or tens of kpc, depending on the absorber location) can be probed, magnified by gravitational lensing.

The most sensitive probe of H I absorption is the Lyα line, which lies in the UV for galaxies with $z < 1.6$. Given that most lensing galaxies are usually at $z \lesssim 1$, their H I absorption studies require UV spectroscopy, as do the studies of any other $z < 1.6$ absorbers along the GLQ sight lines. Absorption studies of the lensing galaxies are especially important since the analyses of the GLQ images allow determinations of the galaxy mass, which can be combined with the gas properties to determine abundance gradients, constrain the mass-metallicity relation etc. Studies of non-lens absorbers toward GLQs are more common, but have been conducted primarily for $z > 1.6$ absorbers using optical spectra. The UV coverage and high spatial resolution of the Hubble Space Telescope (HST) allow measurement of H I absorption in both lensing galaxies and other absorbers at $z < 1.6$ along the sight lines to closely separated GLQ images. With this in mind, we have obtained HST UV spectroscopy of 5 absorbers at $0.4 < z_{abs} < 1.3$ toward 4 GLQs. This is a unique dataset since UV spectra exist for only a handful of GLQs (Michalitsianos et al. 1997; Lopez et al. 2005; Monier et al. 2009; Zahedy et al. 2017). Here we report results from these observations, along with the analysis of metal absorption lines based on Magellan Echellette (MagE) and Sloan Digital Sky Survey (SDSS) spectra. Section 3.2 describes the observations and data reduction. Section 3.4 describes line measurements and column density determinations. Section 3.5 presents a discussion of our results for element abundances along the individual sight lines, the implications for abundance gradients, a search for trends in absorption property differences with sight line separations, and constraints on the total mass vs. metallicity relation for lens galaxy absorbers. Throughout this paper, we adopt the cosmological parameters $\Omega_m = 0.3$, $\Omega_\Lambda = 0.7$, and $H_0 = 70$ km s^{-1} Mpc^{-1}.

3.2 Observations and Data Reduction

Our targets consist of five absorbers with $0.4 < z_{\rm abs} < 1.3$ toward four GLQs. As mentioned in chapter 1, our main goal was to study absorption properties of the lens galaxies themselves. In some cases, the H I Lyα or Lyβ lines at the estimated lens redshifts could not be covered with STIS, but additional absorbers at other redshifts along the same sight lines could be covered. *HST* observations of these non-lens absorbers are also valuable given the paucity of GLQ absorbers at $z < 1.6$ with UV spectroscopy. At the time we designed our *HST* program, there were only 2 GLQs at similar angular separation that had been previously observed individually with *HST* in 2 separate programs, and only 1 of these had the absorber at the lens redshift.

3.2.1 Targets

Table 3.1 lists basic properties of the GLQs in our sample, i.e., the number of images, quasar redshift, lens redshift, angular separation between the images, and the transverse separation between the GLQ sight lines at the lens redshift. Table 3.2 lists key properties of the targeted absorbers in these sight lines, i.e., the absorber redshift, rest-frame equivalent widths of the Mg II λ2796 absorption line in each sight line, the transverse separation between the sight lines at the absorber redshift, and the impact parameters of the lensed quasar images from the lens galaxies. These GLQ sight lines with small angular separations allow us to probe small-scale structures. Figure 3.1 shows *HST* or ground-based images of each field. Figure 3.2 is a visual representation of the distance scale for the lenses, absorbers, and quasars with respect to their sight line separations.

The targets were selected from the CfA-Arizona Space Telescope LEns Survey (CASTLES; e.g., Lehár et al. 2000) and the SDSS Quasar Lens Search (SQLS), with the following considerations:

- known lens redshift (photometric or spectroscopic);

Table 3.1 Sample of GLQ Targets Observed

QSO	$N^a_{\rm im}$	$z_{\rm QSO}$	$z_{\rm lens}$	$\rm Mag_A$, $\rm Mag_B$	$\Delta\theta^b_{\rm AB}$ ($''$)	$l_{\rm AB,l}$ (kpc)^c
Q1017-2046	2	2.545	1.086	17.43, 19.58^d	0.85	6.9
Q1054+2733	2	1.452	0.230	17.21, 19.22^e	1.27	4.7
Q1349+1227	2	1.722	0.645	17.79, 19.30^e	3.0	20.7
Q1355-2257	2	1.373	0.48 or 0.70	17.61, 19.27^d	1.22	7.3 or 8.7^f

a: Number of lensed quasar images;
b: Angular separation between lensed quasar images;
c: Transverse separation between the GLQ sight lines at the lens redshift;
d: *HST* F555W band filter;
e: V band filter;
f: The separation between the sight lines in the lensing galaxy would be 7.3 kpc if the lens galaxy is at $z = 0.48$, or 8.7 kpc if the lens galaxy is at $z = 0.70$.

• presence of strong Mg II absorption ($W^{\rm rest}_{2796}$>0.5 Å) at coincident redshifts at the lens galaxy or other redshift $z_{\rm abs}$<$z_{\rm QSO}$ along multiple sight-lines based on existing ground-based spectroscopy, indicating the need for UV spectroscopy ($z_{\rm abs} < 1.6$);

• at least 2 adequately UV-bright lensed images (as judged by the STIS exposure-time calculator).

Given the Mg II equivalent widths, the sample absorbers are good candidates to be DLAs or sub-DLAs, due to the link between the strength of the Mg II absorption lines and the existence of a DLA/sub-DLA (e.g., Rao et al. 2006). This aspect of our sample selection strategy is important for metallicity determinations, since DLA/sub-DLAs enable accurate measurements of H I column densities and thus of metallicities. Thus, apart from requiring the presence of Mg II absorption, our survey is blind to the other galaxy properties. It is possible that stronger Mg II absorption tends to favor more luminous galaxies, in which case less luminous galaxies may be less likely to show Mg II absorption in sight lines separated by several kpc. On the other hand, some galaxies, despite being associated with strong Mg II absorption, are found to have low luminosity (e.g., Péroux et al. 2011a and references therein). It is still debated whether or not Mg II selection could introduce a metallicity bias

Table 3.2 Parameters for Absorbers along the Sight Lines

QSO	$z_{\rm abs}$	$W_A^{2796(a)}$ (Å)	$W_B^{2796(b)}$ (Å)	$l_{\rm AB,a}{}^{(c)}$ (kpc)	$r_A{}^{(d)}$ (kpc)	$r_B{}^{(e)}$ (kpc)
Q1017-2046	1.086	2.23 ± 0.01	1.29 ± 0.02	6.9	5.4	1.5
Q1054+2733	0.6794	0.77 ± 0.10	1.07 ± 0.19	1.9	...	...
Q1349+1227	1.2366	2.84 ± 0.12		5.8	...	...
Q1355-2257$^{(f)}$	0.4798	0.75 ± 0.02	0.55 ± 0.02	7.3	5.7	1.6
Q1355-2257$^{(g)}$	0.7022	< 0.06	0.62 ± 0.02	4.4 or 8.7	6.9	1.9

a: Rest equivalent width of the Mg II λ2796 absorption line in sight line A;
b: Rest equivalent width of the Mg II λ2796 absorption line in sight line B;
c: Transverse separation between the GLQ sight lines at the absorber redshift;
d: Impact parameter of image A from the galaxy, i.e. projected distance between the A sight line and the galaxy center (listed when the absorber is the lensing galaxy itself, i.e. $z_{\rm abs} = z_{\rm lens}$).
e: Impact parameter of image B from the galaxy, i.e. projected distance between the B sight line and the galaxy center (listed when the absorber is the lensing galaxy itself, i.e. $z_{\rm abs} = z_{\rm lens}$).
f: The separation between the sight lines in the absorbing galaxy at $z_{\rm abs} = 0.48$ would be 7.3 kpc whether the lens galaxy is at $z = 0.48$ or at $z = 0.70$. (See the text for more details.)
g: The separation between the sight lines in the absorbing galaxy at $z_{\rm abs} = 0.70$ would be 4.4 kpc if the lens galaxy is at $z = 0.48$, or 8.7 kpc if the lens galaxy is at $z = 0.70$. (See the text for more details.)

(e.g., Kulkarni et al. 2007, 2010; Dessauges-Zavadsky et al. 2009; Som et al. 2015; Berg et al. 2016). In any case, in this paper, we are using the dual lines of sight to look at differences within a galaxy. Our interest is in merely the relative values of the gas column densities and metallicities in the two sight lines, not the actual absolute values of these quantities. Therefore, we emphasize that any potential effect of Mg II selection is not relevant to the main goal of our program.

3.2.2 Past Observations

We now briefly review the properties of the GLQs studied in this work based on past observations. One of the most important properties is the redshift of the lens galaxy. Ideally, the lens galaxy redshifts for all the targets would come from the same

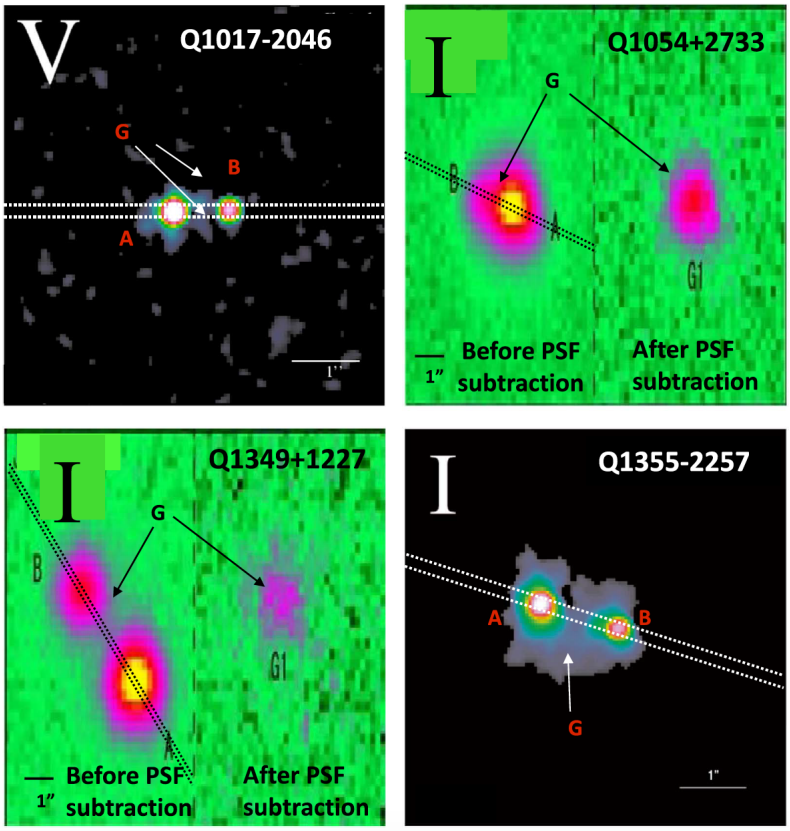

Figure 3.1 *HST* or ground-based images of our targets in V or I band, showing the gravitationally lensed images of the background quasar and the foreground lens galaxy (adopted from the CASTLES gravitational lens survey of Léhar et al. 2000 for Q1017-2046 and Q1355-2257, and from Kayo et al. 2010 for Q1054+2733 and Q1349+1227). Dashed lines show the STIS slit orientations used in our *HST* observations to efficiently observe the multiple sight-lines. For Q1054+2733 and Q1349+1227, the left half shows the quasar and faint lens galaxy images, while the right half shows the galaxy after subtracting the quasar images.

method. Unfortunately such a uniform procedure is not possible for our sample, since the different GLQs have been observed in different studies with different quality of observations and thus different degrees of reliability. We have therefore used our judgment and the quality of the data available for each object to decide on a case-by-case basis which redshift is likely to be more accurate.

Q1017-2046 was reported to be a gravitationally lensed quasar at $z = 2.545$ with an image separation of $0\farcs85$ (Surdej et al. 1997). The lens galaxy was not detected

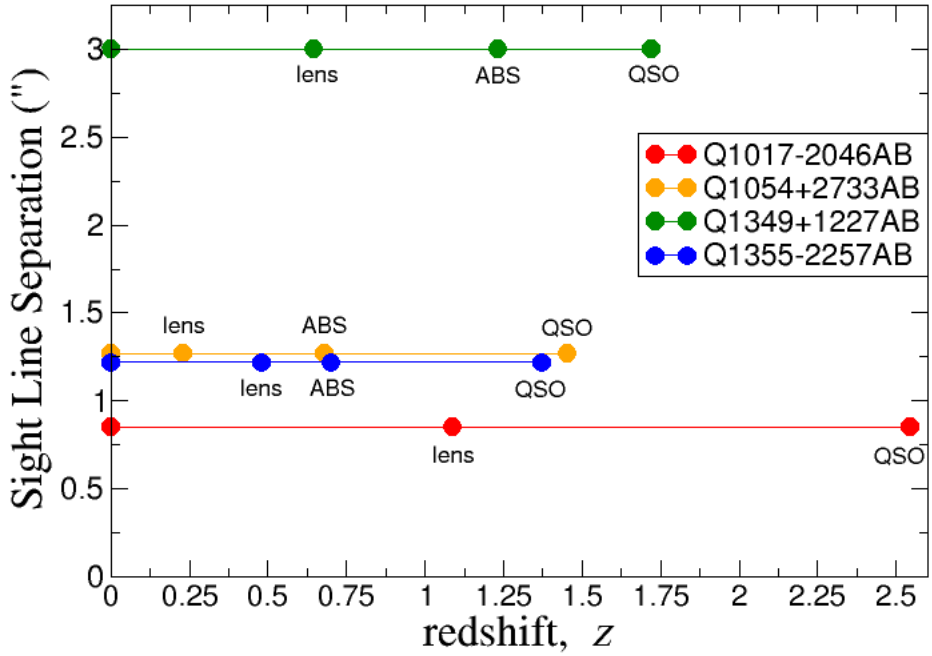

Figure 3.2 A visual representation of the redshift scale for the lens galaxy, absorption line systems, and background quasars with respect to their transverse separation. The colored line begins at the location of the observer ($z = 0$) and ends at the location of the quasar (QSO). The location of the lens is indicated, as well as the location of any other absorbers (ABS) along the line of sight (if they exist). For Q1355-2257 AB, it is unknown whether 0.48 or 0.70 is the lens. The scenario displayed is for $z_{lens} = 0.48$ and $z_{abs} = 0.70$.

in *HST* WFPC2 V and I band images of Remy et al. (1998), but was detected in *HST* NICMOS H-band images of Léhar et al. (2000). The redshift of the lens galaxy was estimated to be 0.78 from the available photometry (Kochanek et al. 2000), but was suggested to be 1.088 ± 0.001 based on the presence of strong Mg II absorption features in both sight lines (Ofek et al. 2006). Our data confirm the presence of absorption lines of H I and several metal ions in both sight lines in the range $z = 1.086 - 1.089$, and we adopt the redshift of the dominant metal component (1.086) as the lens redshift.

Q1054+2733 was discovered as a new gravitationally lensed quasar with an image separation of $1\farcs27$ in the SDSS by Kayo et al. (2010), who estimated the redshift of the lensing galaxy to be about 0.23, based on the galaxy photometry and the

Faber-Jackson relation. A strong Mg II absorber at $z = 0.68$ was detected in the sight lines of Q1054+2733A, B (Kayo et al. 2010, Rogerson & Hall 2012). Our *HST* STIS spectra do not cover the H I Lyman series lines for the $z = 0.23$ lens, but are targeted for the $z = 0.68$ absorber.

Q1349+1227 was shown to be a gravitationally lensed quasar with an image separation of $3\farcs00$ by Kayo et al. (2010), who reported the detection of a faint lens galaxy close to the faint quasar image, and estimated the redshift of the lensing galaxy to be about 0.63, based on the galaxy photometry and the Faber-Jackson relation. An Mg II and Fe II absorber was reported at $z = 1.24$ (Kayo et al. 2010; Quider et al. 2011). Our *HST* STIS spectra do cover the H I Lyα feature for the lens, but are very noisy due to the low continuum flux level caused by the presence of the Lyman break for the absorber at $z = 1.24$.

Q1355-2257 (CTQ 327) was shown to be gravitationally lensed with an image separation of $1\farcs22$ based on *HST* STIS images by Morgan et al. (2003). The lens galaxy was estimated to be an early-type galaxy with a redshift in the range of 0.4 to 0.6, on the basis of the galaxy photometry in I and K bands, and the Faber-Jackson relation by Morgan et al. (2003). Mg II absorption is detected at $z = 0.48$, and a tentative detection of a 4000 Å break at $z = 0.48$ has also been reported (Ofek et al. 2006). Eigenbrod et al. (2006) attempted to obtain a spectrum of the lensing galaxy from spatial deconvolution of the quasar spectra. However, they could not obtain the lens redshift securely owing to low S/N resulting from the close proximity ($< 0\farcs3$) of the galaxy to the quasar image B, and provided only a tentative estimate of 0.70. Eigenbrod et al. (2007) detect Mg II absorption at $z = 0.70$ in sight line B, but not A, and suggest $z = 0.70$ as the lens redshift. Chen et al. (2013) report X-ray observations of Q1355-2257, but detect no Fe K α emission in image A or B. Our data confirm the presence of H I and metal absorption in both sight lines at $z = 0.48$. We also confirm the detection of H I absorption at $z = 0.70$ in both sight lines, and

the detection of metal absorption in sight line B (but not sight line A) at $z = 0.70$. It is possible that the metal absorber at $z = 0.70$ is associated with a galaxy other than the lens galaxy whose Mg II cross-section is just not large enough to cover both sight lines. The presence of H I and metal absorption at $z = 0.48$ in both sight lines also makes it a potential candidate for the lens galaxy. In the analysis below, we determine the abundance gradients for both scenarios, considering the lens galaxy redshift to be (a) $z = 0.48$ and (b) $z = 0.70$.

3.2.3 *HST* Spectra

HST observations were carried out with the Space Telescope Imaging Spectrograph (STIS) with the goal of measuring the H I Lyα (and, in most cases, also Lyβ) lines in the absorbers of interest. STIS was chosen over COS in order to efficiently obtain spatially resolved long-slit spectra of the individual GLQ images. The two images for each GLQ were aligned along the cross-dispersion direction of the $52'' \times 0\farcs2$ STIS slit. The optimum slit orientations were calculated using the known RA and DEC separations of the lensed images, and ORIENT ranges of 2 degrees centered on the optimum value needed to line up both images in the slit were chosen. The G230L grating (which has a spectral resolution of $R \sim 500$) was used with the NUV-MAMA to cover the Lyα and Lyβ absorption lines. Figure 3.1 indicates the orientation of the *HST* STIS slit for our observations. Table 3.3 summarizes the observations.

Each GLQ pair was acquired with onboard target acquisition. No other brighter sources exist within the $5'' \times 5''$ aperture from the brighter quasar image in each pair of sight lines. For each orbit, two spectroscopic exposures were obtained, corresponding to two positions of a STIS-ALONG-SLIT dither pattern. A total of 4 dither patterns were employed, each with two positions separated by $1\farcs5$, $2\farcs0$, $2\farcs5$, or $3\farcs0$, so as to prevent the spectra of the lensed images in different orbits from falling on the same part of the detector.

Table 3.3 Summary of Observations for GLQ Sample

QSO	STIS UV setting	$t_{\rm exp}$ (s) $\times$ $n^a_{\rm exp}$	Optical setting	$t_{\rm exp}$(s)$\times$ $n^b_{\rm exp}$
Q1017-2046	G230L 2376	1104×4 (A,B)	Magellan MagE	2700×2 (A)
		1334×10 (A,B)		3600 ×2 (A)
				3600×2 (B)
Q1054+2733	G230L 2376	1143×2 (A,B)	SDSS	2700×3 (A,B)
Q1349+1227	G230L 2376	1133×1 (A,B)	SDSS	2700×3 (A,B)
		1134×1 A,B)		
Q1355-2257	G230L 2376	1132×1 (A,B)	Magellan MagE	2700×5 (A)
		1133×1 (A,B)		2700×1 (B)
		1368×2 (A,B)		3600×4 (B)
		1369×2 (A,B)		

Note: In the SDSS spectra, images A and B are unresolved.
a: Exposure time and number of individual exposures for *HST* STIS.
b: Exposure time and number of individual exposures for the optical spectra obtained with Magellan MagE or adopted from the SDSS.

The *HST* STIS spectra were first reduced using the `IRAF/STSDAS` task `CALSTIS`. The `CALSTIS` pipeline reduction consists of overscan subtraction, bias subtraction, cosmic ray rejection, linearity correction, dark subtraction, flat-fielding, processing of the contemporaneously obtained wavelength calibration data, wavelength calibration, flux calibration, and 2-D rectification. The reduced 2-dimensional data were examined to determine the locations of the two quasar images, and further processed using the `X1D` task to extract 1-dimensional spectra. The `X1D` task also performs background subtraction, charge transfer efficiency correction, conversion to heliocentric wavelengths, and absolute flux calibration. The extracted 1-dimensional spectra for the individual sub-exposure were co-added to calculate the combined spectra, including the flux uncertainties. Continuum fitting was performed with the `IRAF` task `CONTINUUM` using low-order cubic spline polynomial functions, and the continuum-normalized spectra were examined to measure the H I absorption lines.

While the low-resolution STIS spectra are adequate for measuring the H I Lyman absorption lines in our sample, they are not suitable for measurements of the much

narrower metal absorption lines. The metal lines were measured with either Magellan spectra or SDSS spectra. While the spectral resolution of our MagE data is moderate ($\sim$51 km s^{-1}), we note that the high S/N of these data makes them adequate for deriving reliable metal column densities. Indeed, a number of past studies of element abundances for quasar absorbers have been based on spectra with resolution comparable to or lower than our MagE spectra (e.g., 44 km s^{-1} for Keck ESI, 75 km s^{-1} for MMT Blue Channel). In cases where both high S/N medium-resolution spectra and high-resolution spectra are available for the same object, the column densities derived from the two sets of spectra are found to agree well (e.g., comparison of Keck ESI and HIRES results in Prochaska et al. 2007, and comparison of MMT blue channel and VLT UVES results in Péroux et al. 2006).

3.2.4 Magellan Spectra

The quasars Q1017-2046 and Q1355-2257 were observed using the Magellan Echellette (MagE) spectrograph on the Clay 6.5 meter Magellan telescope at the Las Campanas Observatory in March 2010, with the goal of measuring metal absorption lines (e.g., lines of Mg I, Mg II, Fe II). The excellent seeing ($0\farcs5-0\farcs7$) allowed observations with a $0\farcs7$ slit, giving a spectral resolution of $R \sim 5900$. Multiple exposures lasting 2700-3600 seconds each were taken separately for each of the quasar images. In each case, the slit was aligned with the parallactic angle in order to minimize chromatic slit losses, since the MagE spectrograph does not have an Atmospheric Dispersion Corrector. The spectrum of the fainter images thus contained some light from the brighter image. This was corrected for in the extraction as follows: Two Gaussians + a sky floor were fit simultaneously, with all parameters free. In a second fit, we tied the Gaussian positions and common width by a model that we obtained from fitting those measurements as a function of wavelength with a smooth polynomial. In the second double Gaussian fit only the amplitudes and the sky were free to vary. This

gave a much more robust fit. The (barely) resolved fluxes were the areas of the fitted Gaussians. More details of this procedure can be found in Lopez et al. (2005).

The MagE data were reduced using custom FORTRAN routines which interact with `MIDAS`[1] commands. The `MIDAS` task "IDENTIFY/ECHELLE" was used to calibrate the wavelengths using the 2D Th-Ar lamp spectrum. The wavelengths were converted to vacuum wavelengths and heliocentric corrections were calculated using "COMPUTE/BARYCORR". The calibrated Echelle orders were continuum-fitted individually using cubic spline polynomials. The normalized orders were then merged into a single spectrum.

3.2.5 Keck Spectra

For one of our GLQs (Q1017-2046), archival Keck HIRES spectra are available. Although these spectra are not spatially resolved, their higher spectral resolution makes them useful to obtain a sanity check on the metal column densities estimated from the MagE data. Extracted HIRES spectra for each order containing the lines of interest were downloaded from the Keck Observatory Archive and dispersion-corrected to a dispersion of 0.075 Å to align the exact starting wavelengths for the individual exposures of a given order. Continuum-fitting was performed with the `PyRAF` task "CONTINUUM" using spline polynomials of orders 2 to 5. The individual exposures for each order of interest were co-added using the PyRAF task "SCOMBINE" (three exposures for Mg II, four exposures for Fe II).

3.2.6 SDSS Spectra

For Q1054+2733 and Q1349+1227, we do not have MagE or HIRES data, and use spectra from the Sloan Digital Sky Survey (York et al. 2000), that were originally part of Data Release 7 (Abazajian et al. 2009) to examine the metal lines. These spectra

[1]See Ballester (1992) and http://www.eso.org/sci/software/esomidas/

are not resolved (as the lensed image separations for these GLQs are smaller than or equal to the SDSS fiber diameter), and thus do not allow metal line measurements in the individual sight lines. Nevertheless, the SDSS spectra still give a useful indication of the integrated metal line strengths. The spectra were split into multiple sections of $\sim 30 - 500$ Å to facilitate continuum fitting. The pieces were continuum-fitted with the `PyRAF` task "CONTINUUM". Spline polynomials of order $\sim 2 - 10$ were typically the best fit for both quasar spectra, as they resulted in the lowest root mean square (rms) residuals. The normalized split sections for each quasar were then combined into a single spectrum using the `PyRAF` task "SCOMBINE" for subsequent analysis.

3.3 Absorption Line and Column Density Measurements

The H I and metal lines were identified and measured in each sight line. Column densities were measured using the Voigt profile fitting software `VPFIT` (more information available at https://www.ast.cam.ac.uk/∼rfc/vpfit.html).

3.3.1 H I Lines

Table 3.4 lists the equivalent widths of the Lyα lines, and of the Lyβ lines where available. We note, however, that in some cases (e.g., Q1017A, B $z_{\rm abs} = 1.09$ and Q1355A $z_{\rm abs} = 0.70$), it is difficult to measure the Lyα and/or Lyβ equivalent widths accurately due to blends or the presence of nearby features (arising in metal lines, Lyα forest lines, and/or MW interstellar lines), and the presence of noise. It is thus not possible to reliably estimate the H I column densities from just the equivalent widths assuming a theoretical profile. We therefore estimate $N_{\rm H\,I}$ by fitting Voigt profiles, convolved with the instrumental profile, to the data. A procedure similar to that of Rao & Turnshek (2000) and Rao et al. (2006) was followed while estimating the H I column densities from the *HST* spectra. Voigt profile fitting was performed for the absorption lines of Lyα (and Lyβ where available and not severely affected by noise or

blending with other Lyα forest lines), including the convolution with the STIS G230L line spread function provided by the Space Telescope Science Institute. (Higher order Lyman lines were not available.) Given the low resolution of the G230L data, the relatively low S/N in some spectra, and the presence of other nearby lines, it is not meaningful to vary all three parameters (i.e., H I column density, Doppler b-value, and the redshift) while performing a Voigt profile fit to the Lyα and/or Lyβ lines in the absorbers of interest. Instead, the H I column density and redshift were allowed to vary and the Doppler b-value was fixed during the profile fits. (We note that the difference between the H I and metal-line redshifts is less than the velocity resolution of the G230L, and repeating the H I Voigt profile fits using the redshifts derived from the metal lines made $< 1\sigma$ difference to the H I column densities determined.) The fits were repeated for a variety of fixed b-values ranging from 15 km s^{-1} to the maximum value deemed possible given the Doppler b-values of the metal lines, if available, for the individual sight lines. The range of b-values explored varied between 15-30 and 15-87 km s^{-1}. If the $N_{\rm H\,I}$ values for the maximum and minimum b-values differed, the average of the two values was adopted as the $N_{\rm H\,I}$ value, and the sampling error in this average value was added in quadrature with the measurement uncertainties to obtain the total $N_{\rm H\,I}$ uncertainty. Table 3.5 lists the adopted $N_{\rm H\,I}$ values and uncertainties. For the $z_{\rm abs} = 0.70$ system toward Q1355-2257A (for which no metal lines are detected), we adopt the $N_{\rm H\,I}$ value (log $N_{\rm H\,I}$=18.20 $\pm$ 0.23) for b = 15 km s^{-1} and note that $N_{\rm H\,I}$ values within $\lesssim 1.5\sigma$ of this adopted value are obtained for a reasonable range of b-values (15-30 km s^{-1}). Figures. 3.3 $-$ 3.7 show the H I profile fits for the best-fit and $\pm1\sigma$ $N_{\rm H\,I}$ values. In cases where the $N_{\rm H\,I}$ values obtained for the minimum and maximum b-values differ by $\geq$ 0.02 dex, the fits for both sets of values are shown.

For the $z = 0.68$ absorber toward Q1054+2733B, the noisy STIS data barely show a weak Lyα line that is $\sim$1.2 resolution elements away (730 km s^{-1} away) from the

Table 3.4 Rest-frame H I Lyα, Lyβ equivalent widths for AB sight lines

GLQ	$z^{\rm A}_{\rm H\,I}$	$W^{\rm A}_{{\rm Ly}\alpha}$ (Å) $W^{\rm A}_{{\rm Ly}\beta}$	$z^{\rm B}_{\rm H\,I}$	$W^{\rm B}_{{\rm Ly}\alpha}$ (Å) $W^{\rm B}_{{\rm Ly}\beta}$
Q1017-2046	1.08803±0.00044	4.22[b]±0.79 1.92[b]±0.60	1.08714±0.00053	3.72[b]±0.77 0.82[b]±0.91
Q1054+2733	0.68153±0.00036	1.47±0.49 N/A	0.68350±0.00286	< 2.47[a] N/A
Q1349+1227	1.23750±0.00026	17.71±2.65 2.36±0.61	1.24022±0.00083	28.05±4.25 2.21±0.82
Q1355-2257	0.48169±0.00048	1.70±0.51 N/A	0.48128±0.00112	2.98±1.42 N/A
Q1355-2257	0.70721±0.00045	0.86[b]±0.28 N/A	0.70501±0.00067	2.19±0.84 N/A

a: 3σ upper limit
b: Equivalent width measurement affected by blends and/or noise.

Table 3.5 H I column density measurements based on Voigt Profile Fitting

GLQ	$z^{\rm A}_{\rm H\,I}$	log $N^{\rm A}_{\rm H\,I}$	$z^{\rm B}_{\rm H\,I}$	log $N^{\rm B}_{\rm H\,I}$
Q1017-2046A,B	1.08803±0.00044	19.87±0.09	1.08714±0.00053	19.79±0.12
Q1054+2733A,B	0.68153±0.00036	18.48±0.18	0.68350±0.00286	< 19.06
Q1349+1227A,B	1.23750±0.00026	20.90±0.02	1.24022±0.00083	21.37±0.05
Q1355-2257A,B	0.48183±0.00039	18.81±0.18	0.48153±0.00116	19.43±0.27
Q1355-2257A,B	0.70725± 0.00064	18.20±0.23	0.70534±0.00079	19.12±0.23

Note: The H I column densities $N_{\rm H\,I}$ are in units of cm^{-2}.

expected Lyα position for the redshift based on the Mg II lines seen in the unresolved SDSS spectrum. It is possible that this feature may not be the Lyα associated with the $z = 0.68$ Mg II absorber. Given the uncertainty in the detection of this feature in the noisy spectrum, we conservatively adopt an upper limit on the H I column density for this sight line. This upper limit was estimated from the 3σ sensitivity for the Lyα line and includes contributions to the equivalent width uncertainty from both the photon noise and continuum determination uncertainty, as well as assuming that the feature lies on the damping part of the curve of growth to obtain this conservative upper limit.

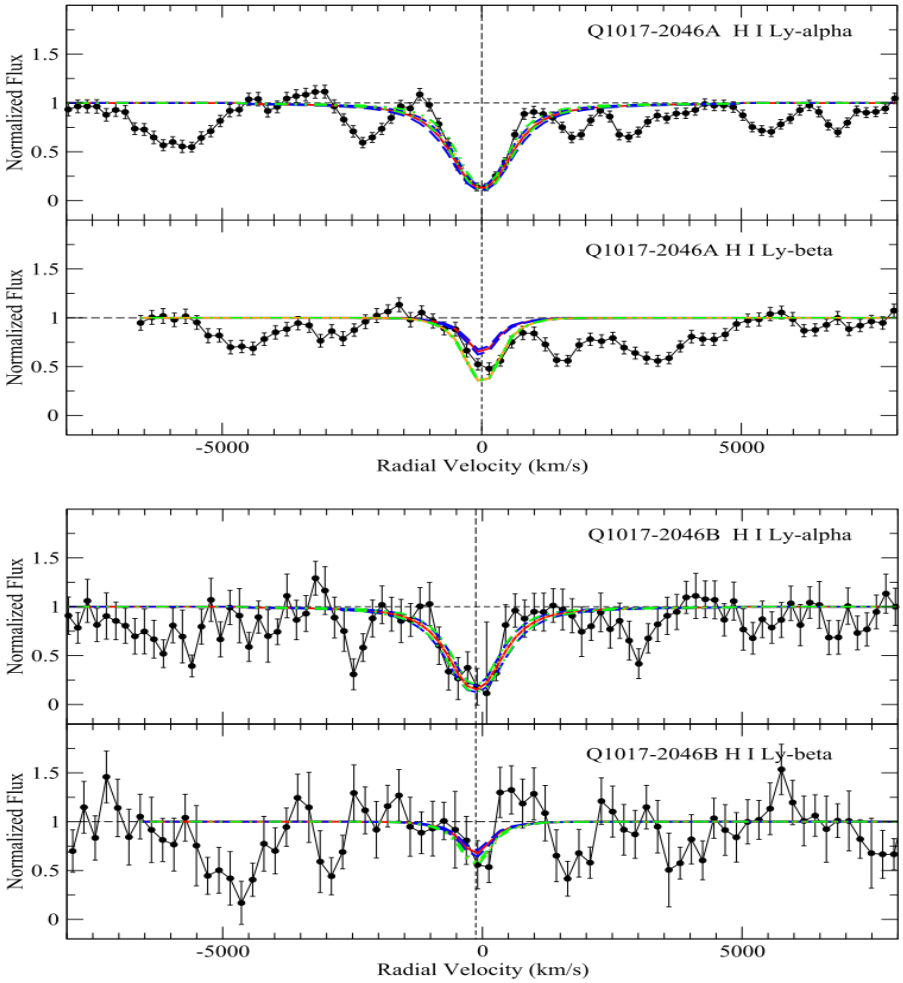

Figure 3.3 *HST* STIS G230L spectra of Q1017-2046A (top two panels) and Q1017-2046B (bottom two panels) showing velocity plots for the region near Lyα and Lyβ absorption with respect to $z = 1.08803$. The curves show the Voigt profiles (convolved with the instrumental profile) obtained by fitting Lyα and Lyβ together. Solid red curves show the fits for the minimum b-value considered, and dashed blue curves show profiles for the corresponding $\pm 1\sigma$ uncertainties in $N_{\rm H\,I}$. Orange and green curves show profiles for the best-fit and $\pm 1\sigma$ $N_{\rm H\,I}$ values, respectively, for the maximum b-value considered, in case the $N_{\rm H\,I}$ values for the minimum and maximum b-values differ by $\geq$0.02 dex. The horizontal dashed lines indicate the continuum levels. The vertical dashed lines indicate the positions of the components used in the fits.

To summarize, we adopt the H I column densities listed in Table 3.5. Follow-up spectra with higher S/N and higher resolution would help to obtain more definitive H I column densities. The highest H I column densities are found along the sight lines to Q1349+1227A, B.

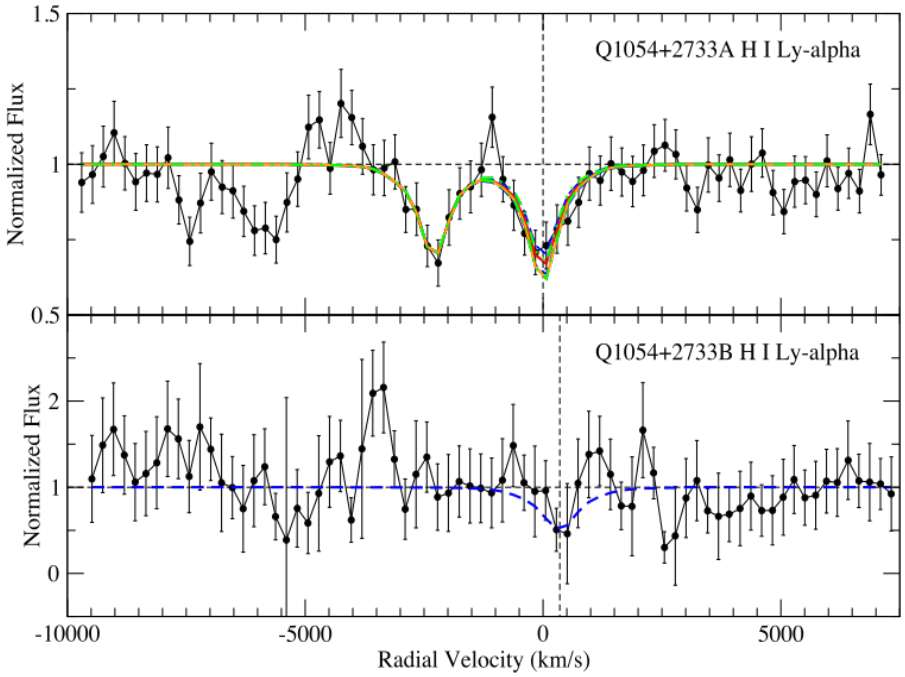

Figure 3.4 *HST* STIS G230L spectra for Q1054+2733A,B showing velocity plots for the region near Lyα absorption with respect to $z = 0.68153$. For Q1054+2733A, the red curve shows the best-fit Voigt profile for $b = 15$ along with another absorption feature (which may be H I Lyα at $z = 0.6687$ or Si III λ1206 at $z = 0.6815$, or a blend) not detected toward Q1054+2733B. The Lyβ region is too noisy and blended to give useful constraints. The horizontal dashed lines indicate the continuum levels. The vertical dashed lines indicate the positions of the components used in the fits. For Q1054+2733A, the difference between the dashed blue curves and the red curve is that the former show Voigt profiles corresponding to the $\pm1\sigma$ uncertainties in log $N_{\rm H\,I}$ for the minimum b-value considered for the $z = 0.6815$ absorber. The orange and green curves show the profiles for the best-fit and $\pm1\sigma$ $N_{\rm H\,I}$ values, respectively, for the maximum b-value considered. For Q1054+2733B, only a dashed blue curve corresponding to the adopted upper limit on the H I column density is shown.

3.3.2 Metal Lines

For the metal lines, where multiple lines of the same ion were covered by the data, they were used together to constrain the ionic column densities. The Doppler b-values and redshifts were tied together for all low ions (e.g., Si II, Fe II etc.). The total column densities were calculated by adding all the velocity components together. Furthermore, to ensure the reliability of the results, the column densities

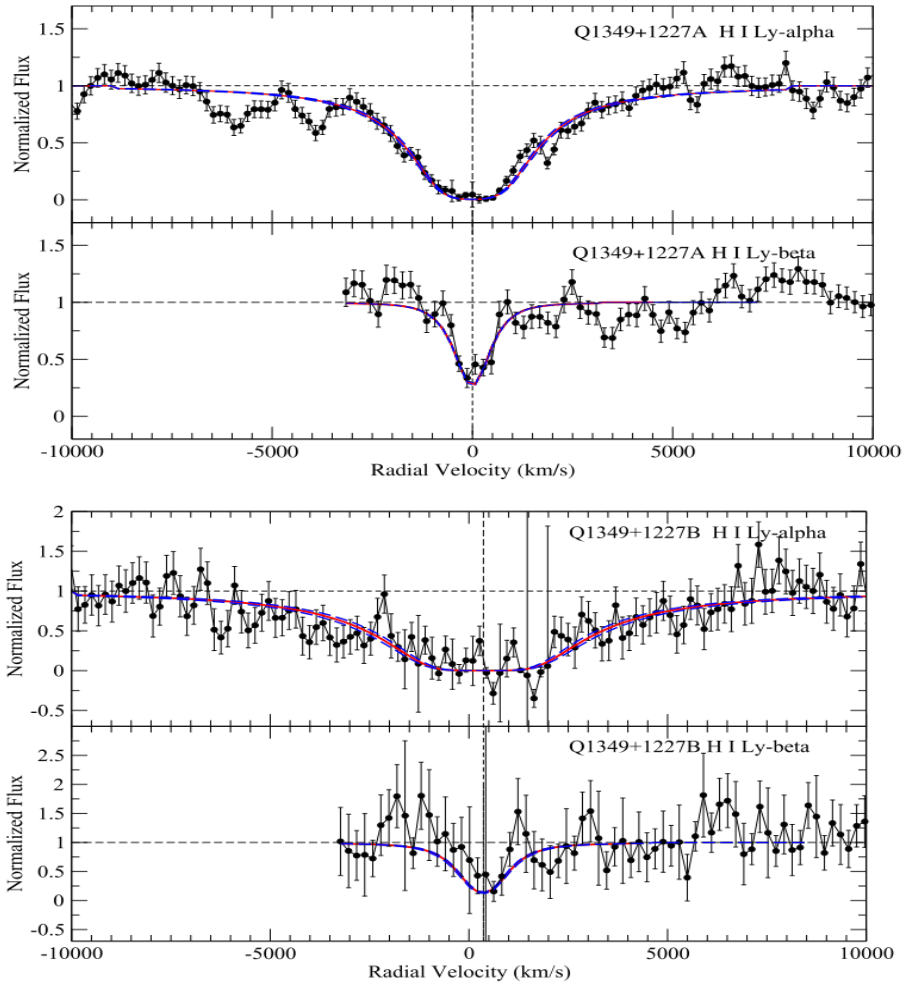

Figure 3.5 *HST* STIS G230L spectra showing velocity plots for the region near Lyman α and Lyβ absorption for Q1349+1227A (top two panels) and Q1349+1227B (bottom two panels) with respect to $z = 1.23750$. The red curves show the best-fit Voigt profiles obtained by fitting Lyα and Lyβ together for the full range of b-values considered. (There is no difference between the $N_{\rm H\,I}$ values obtained for the minimum and maximum b-values.) The dashed blue curves show Voigt profiles corresponding to the $\pm1\sigma$ uncertainties in log $N_{\rm H\,I}$. The Lyβ region for Q1349+1227B is very noisy, and ignoring it leads to very little change in the best-fit H I column density for this sight line. The horizontal dashed lines indicate the continuum levels. The vertical dashed lines indicate the positions of the components used in the fits.

of the unsaturated and unblended lines were also measured by the apparent optical depth method (AOD; Savage & Sembach 1991) and compared to the measurements from Voigt profile fitting. As another check of the `VPFIT` results, we also performed single-component curve-of-growth analyses for all available Fe II lines using both the

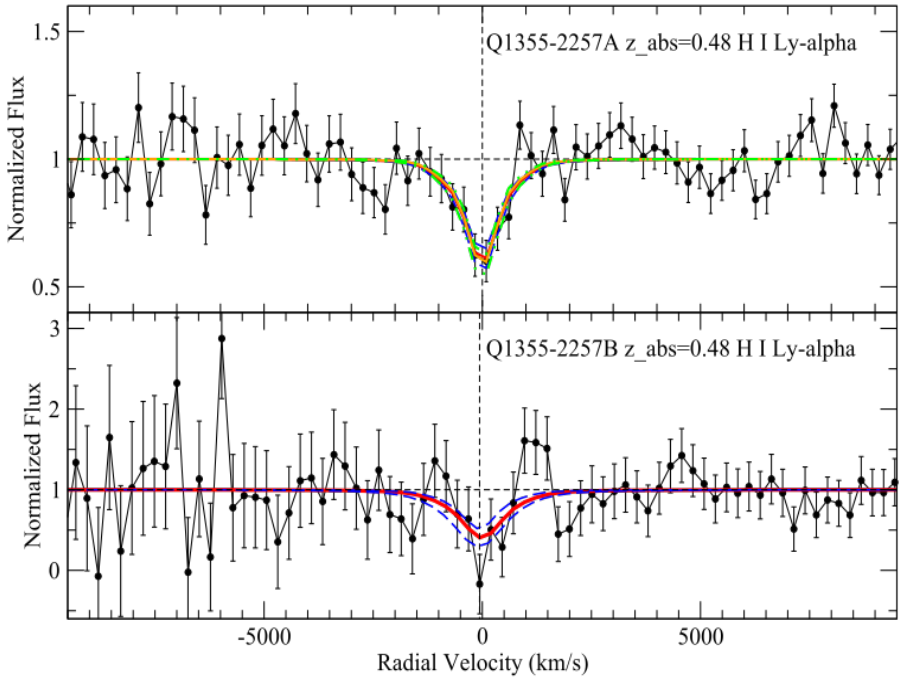

Figure 3.6 *HST* STIS G230L spectra of Q1355-2257A,B showing velocity plots for the region near Lyα absorption with respect to $z = 0.48183$. Red curves show the best-fit Voigt profiles for the minimum b-value considered, and dashed blue curves show Voigt profiles corresponding to the $\pm1\sigma$ uncertainties in log $N_{\rm H\,I}$. Orange and green curves show the corresponding best-fit and $\pm1\sigma$ curves, respectively, for the maximum b-value considered, in case the $N_{\rm H\,I}$ values for the minimum and maximum b-values differ by $\geq$0.02 dex. The horizontal dashed lines indicate the continuum levels. The vertical dashed lines indicate the positions of the components used in the fits.

Python package `linetools`[2], and a comparison of the observed data with theoretical curves-of-growth for a range of b-values. The Fe II column densities and effective b-values estimated from the curve-of-growth analyses agree closely with those estimated from `VPFIT`.

The uncertainties in the effective Doppler b-values listed in the tables are those estimated from `VPFIT`, and are typically $\lesssim 20\%$. Details about the estimation and reliability of parameter uncertainties in `VPFIT` can be found in the `VPFIT` manual (Carswell & Webb 2014). We independently checked these uncertainties using single-component

[2]http://linetools.readthedocs.io/en/latest/index.html

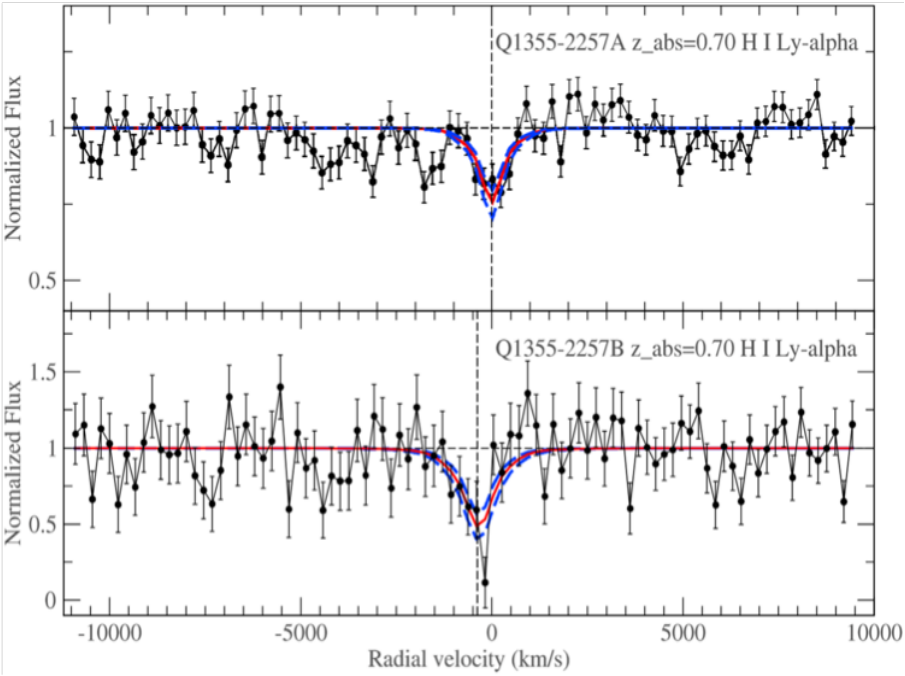

Figure 3.7 *HST* STIS G230L spectra of Q1355-2257A,B showing velocity plots for the region near Lyα absorption with respect to $z = 0.70721$. For both Q1355-2257A and Q1355-2257B, the red curves show the best-fit Voigt profiles for the minimum b-value considered, and the dashed blue curves show Voigt profiles corresponding to the $\pm 1\sigma$ uncertainties in log $N_{\rm H\,I}$. (No separate profiles are shown for the maximum b-value, since the $N_{\rm H\,I}$ values for the minimum and maximum b-value differ by < 0.02 dex for Q1355-2257B, and no b-value constraints are available for Q1355-2257A, where no metal lines are detected.) The horizontal dashed lines indicate the continuum levels. The vertical dashed lines indicate the positions of the components used in the fits.

curve-of-growth analyses for the available Fe II lines, and obtained uncertainties close to those returned by `VPFIT`, typically within 1-2 km s^{-1}. Additionally, we performed single-component curve-of-growth analyses for cleanly isolated individual components of the Fe II lines where possible, and once again obtained uncertainties close to those estimated from `VPFIT`. It is still possible that in some cases the uncertainties in the b-values may be underestimates. In any case, the metal column densities estimated from `VPFIT` show generally good agreement (within $\lesssim 1\sigma$) with the AOD values and the curve-of-growth estimates. Oscillator strengths from Cashman et al. (2017) and Morton (2003) were adopted for use in all metal-line column density measurements.

3.4 Results

Metal lines for a number of ions (e.g., Mg I, Mg II, Fe II, Si II, Al II, and/or Al III) were measured in the Magellan and SDSS spectra. Figures 3.8 − 3.15 show the profile fits to the metal lines in the absorbing systems.

3.4.1 Primary Absorption Systems

For Q1017-2046 and Q1355-2257, the resolved MagE spectra of images A and B allow profile fitting of the metal lines in each sight line. For Q1054+2733 and Q1349+1227, the unresolved SDSS spectra allow metal line fits for the combined A+B image. Tables 3.6 and 3.7 list the metal column density results from Voigt profile fitting for the $z = 1.09$ absorber toward Q1017-2046A and Q1017-2046B, respectively. Tables 3.8 and 3.9 list, for both of these sight lines, the total metal column densities (summed over all the detected velocity components) from the profile fits and the AOD method where available, based on the MagE data. Also listed are the corresponding element abundances derived from the metal and H I column densities. Tables 3.10 and 3.11 list the corresponding values obtained from the spatially unresolved Keck HIRES spectra of Q1017-2046A+B. While these values cannot be directly compared to the values for the individual sight lines from the MagE data, it is reassuring that the sum of the MagE values for Fe II column densities for sight lines A and B are consistent with the HIRES values for Q1017-2046A+B. There is a bigger difference for Mg II, which may be partly due to a higher degree of saturation. In any case, none of our discussion on abundance gradients in Section 3.5 is affected by these differences, since it is based on Fe II, for which both HIRES and MagE data give about the same total column density.

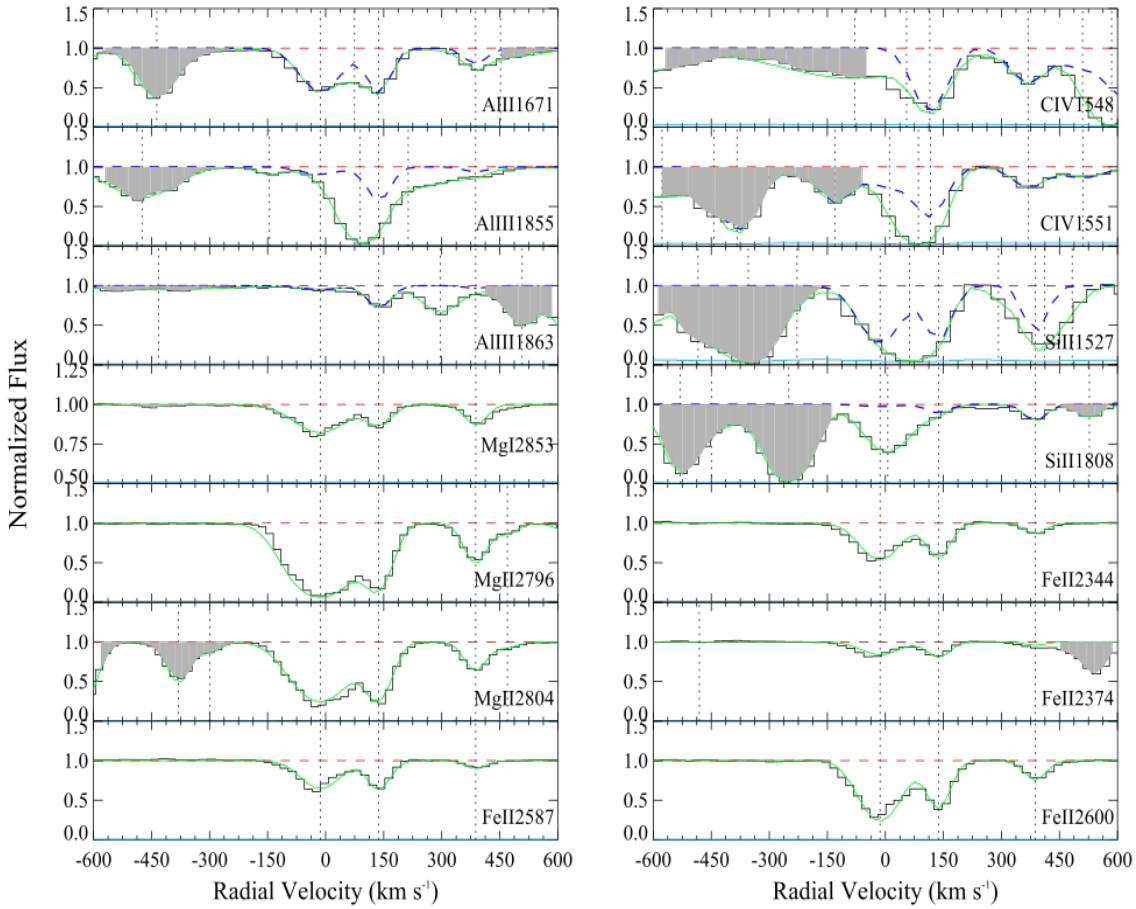

Figure 3.8 Velocity plots for the metal lines for the $z = 1.086$ system in the spectrum of Q1017-2046A taken with the Magellan MagE spectrograph. In each panel, the normalized data are shown in black, the solid green curve indicates the theoretical Voigt profile fit to the absorption feature, and the dashed red line shows the continuum level. For lines in the Lyman alpha forest, the dashed blue curve indicates the profile fit of the metal line absorption feature alone. The 1σ error values in the normalized flux are represented by the cyan curves near the bottom of each panel. Note that in a few panels with weak lines, if the normalized flux scale is shown starting at 0.5, the 1σ error arrays are offset by 0.5, so that they can be viewed in the same panels. The vertical dotted lines indicate the positions of the components that were used in the fit. Shaded regions indicate absorption unrelated to the line presented or regions of high noise.

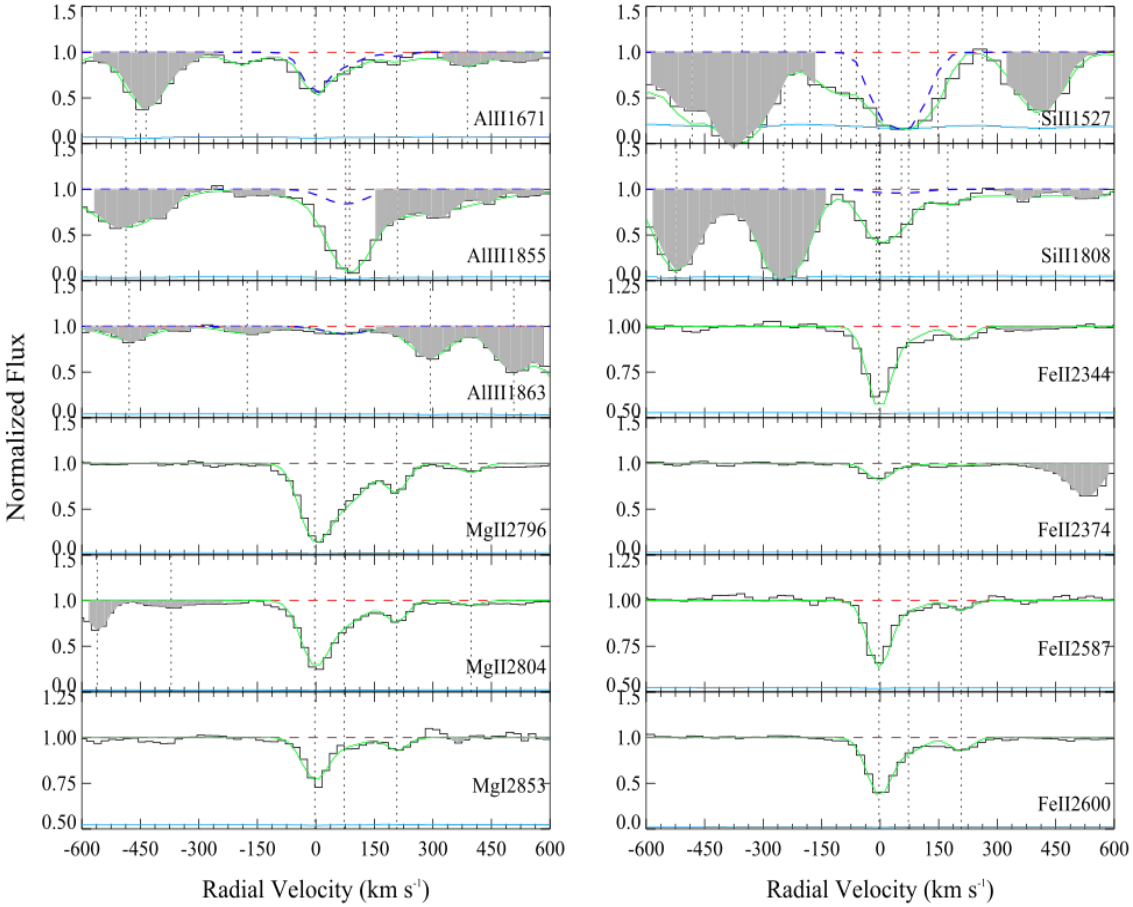

Figure 3.9 Same as Figure 3.8, but for metal lines in the $z = 1.0859$ system toward Q1017-2046B.

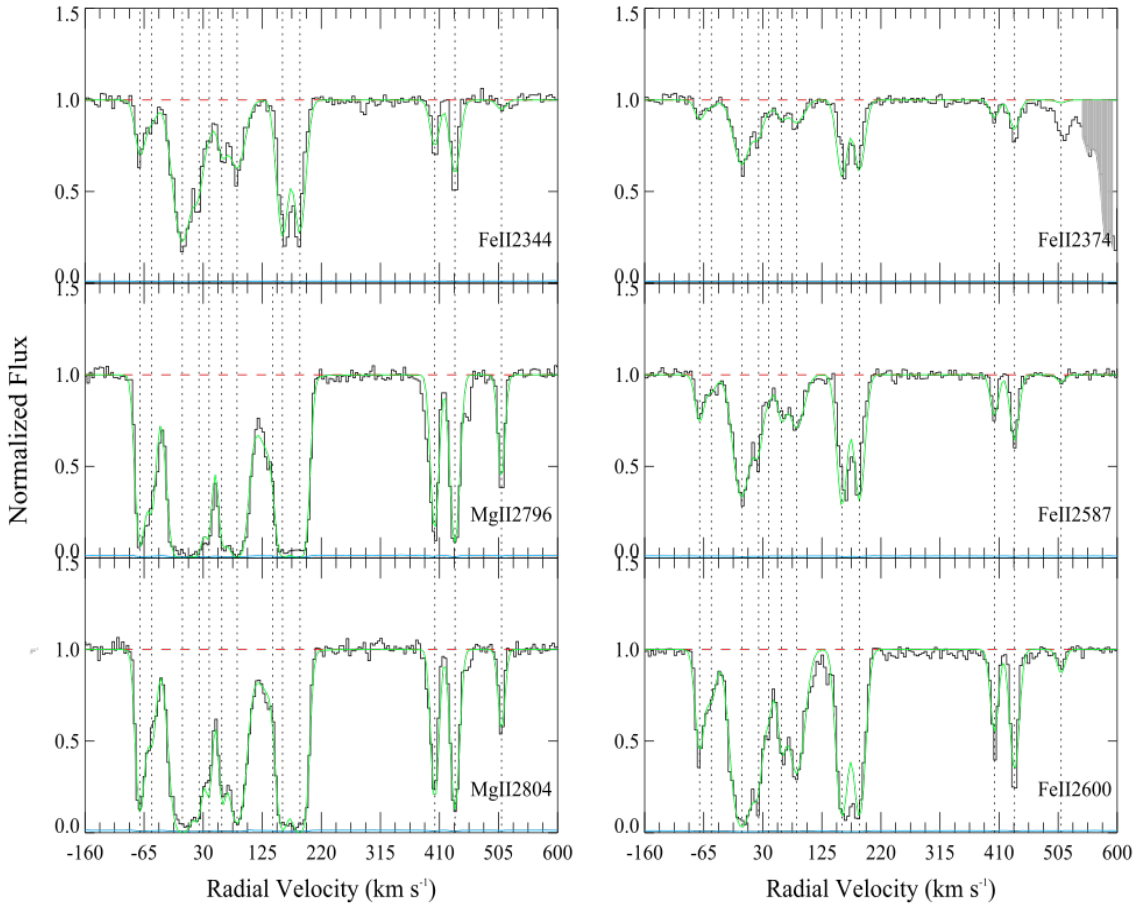

Figure 3.10 Velocity plots for the metal lines for the $z = 1.0859$ system in the spatially unresolved archival spectrum of Q1017-2046A+B obtained with the Keck HIRES spectrograph. In each panel, the normalized data are shown in black, the solid green curve indicates the theoretical Voigt profile fit to the absorption feature, and the dashed red line shows the continuum level. The 1σ error values in the normalized flux are represented by the cyan curves near the bottom of each panel. The vertical dotted lines indicate the positions of the components that were used in the fit. Shaded regions indicate absorption unrelated to the line presented or regions of high noise.

Table 3.6 Voigt Profile Fitting Results for Ions in the $z = 1.0859$ Absorber toward Q1017-2046A

z	$b_{\rm eff}$	log $N_{\rm Mg\ I}$	log $N_{\rm Mg\ II}$	log $N_{\rm Al\ II}$	log $N_{\rm Al\ III}$	log $N_{\rm Si\ II}$	log $N_{\rm Fe\ II}$
1.085905 ±0.000005	55.32 ± 0.92	12.39±0.04	14.01±0.01	13.12±0.07	12.64±0.32	14.45±0.16	14.03±0.01
1.086955 ±0.000005	16.30 ± 0.72	11.91±0.07	13.83±0.04	13.21±0.28	13.33±0.10	14.87±0.17	13.94±0.03
1.088699 ±0.000009	10.65 ± 1.69	11.90±0.10	13.26±0.06	12.44±0.44	12.27±0.55	15.26±0.09	13.20±0.05
1.089270 ±0.000049	10.00	...	12.40±0.09	...	...	...	...

z	$b_{\rm eff}$	log $N_{\rm C\ IV}$
1.086822 ±0.000016	36.00	14.41±0.05
1.088587 ±0.000028	42.69 ± 7.91	13.91±0.04
1.089569 ±0.000121	60.58 ± 19.68	13.69±0.15

Note: The effective Doppler parameter $b_{\rm eff}$ is in units of km s^{-1}; column density N is in units of cm^{-2}.

Table 3.7 Voigt Profile Fitting Results for Ions in the $z = 1.086$ Absorber toward Q1017-2046B

z	$b_{\rm eff}$	log $N_{\rm Mg\ I}$	log $N_{\rm Mg\ II}$	log $N_{\rm Si\ II}$	log $N_{\rm Fe\ II}$	log $N_{\rm Al\ II}$	log $N_{\rm Al\ III}$
1.085979±0.000006	18.07 ± 0.78	12.21±0.06	13.74±0.03	14.30±0.39	13.91±0.02	12.86±0.10	...
1.086504±0.000029	41.56 ± 2.91	11.68±0.20	13.22±0.03	14.54±0.17	12.99±0.05	12.32±0.19	...
1.087443±0.000015	8.00	11.63±0.21	13.08±0.07	...	12.91±0.07	11.65±0.78	...
1.088767±0.000058	11.00	...	12.24±0.10	...	...	...	...
1.086534±0.000091	62.79 ± 22.94	...	...	...	...	...	12.93±0.12

Note: The effective Doppler parameter $b_{\rm eff}$ is in units of km s^{-1}; column density N is in units of cm^{-2}.

Table 3.8 Total Column Densities for the $z = 1.086$ Absorber toward Q1017-2046A and Q1017-2046B

Ion	log N_A^{fit}(cm^{-2})	log N_A^{AOD}(cm^{-2})	log N_B^{fit}(cm^{-2})	log N_B^{AOD}(cm^{-2})
Mg I	12.61 ± 0.03	12.61 ± 0.02	12.40 ± 0.06	12.35 ± 0.03
Mg II	14.28 ± 0.02	14.23 ± 0.01	13.93 ± 0.02	13.83 ± 0.01
Al II	13.51 ± 0.15	...	12.99 ± 0.09	...
Al III	13.44 ± 0.10	...	12.93 ± 0.12	...
Si II	15.46 ± 0.08	...	14.74 ± 0.18	...
Fe II	14.32 ± 0.02	14.28±0.01	14.00 ± 0.02	13.97 ± 0.07
C IV	14.59 ± 0.04	...	...	...

Table 3.9 Metallicities for the $z = 1.086$ Absorber toward Q1017-2046A and B

Element	$[X/H]_A$	$[X/H]_B$
Mg	-1.18±0.09	-1.45±0.12
Al	-0.54±0.13	-0.98±0.14
Si	0.08±0.12	-0.56±0.21
Fe	-1.05±0.09	-1.29±0.12

Table 3.10 Voigt Profile Fitting Results for Ions in the $z = 1.086$ Absorber toward Q1017-2046A+B from unresolved *Keck* HIRES data

z	b_{eff} (km s^{-1})	log $N_{Mg\,II}$ (cm^{-2})	log $N_{Fe\,II}$ (cm^{-2})
1.085403±0.000007	4.60 ± 1.30	13.66±0.06	13.04±0.04
1.085534±0.000017	6.98 ± 4.38	12.77±0.02	12.59±0.06
1.085876±0.000004	15.47 ± 0.68	13.94±0.03	13.85±0.01
1.086063±0.000006	4.75 ± 1.03	13.35±0.08	13.28±0.04
1.086176±0.000010	3.89 ± 2.82	13.32±0.07	12.70±0.06
1.086317±0.000006	4.28 ± 1.33	13.24±0.06	12.99±0.06
1.086888±0.000067	32.74 ± 4.02	12.88±0.04	...
1.086489±0.000005	13.78 ± 1.12	13.57±0.02	13.30±0.02
1.086997±0.000008	6.68 ± 0.59	13.92±0.08	13.80±0.03
1.087192±0.000008	6.96 ± 0.57	14.82±0.07	13.75±0.02
1.088701±0.000004	3.16 ± 0.64	14.04±0.10	12.99±0.06
1.088927±0.000001	4.90 ± 0.58	13.52±0.05	13.25±0.04
1.089448±0.000020	3.02 ± 0.78	12.67±0.05	12.16±0.15

Table 3.11 Total Column Densities for the $z = 1.086$ Absorber toward Q1017-2046A+B from unresolved Keck HIRES data

Ion	log $N^{\rm fit}_{\rm A+B}$(cm^{-2})	log $N^{\rm AOD}_{\rm A+B}$(cm^{-2})
Mg II	15.05±0.04	14.37±0.01
Fe II	14.46±0.01	14.33±0.01

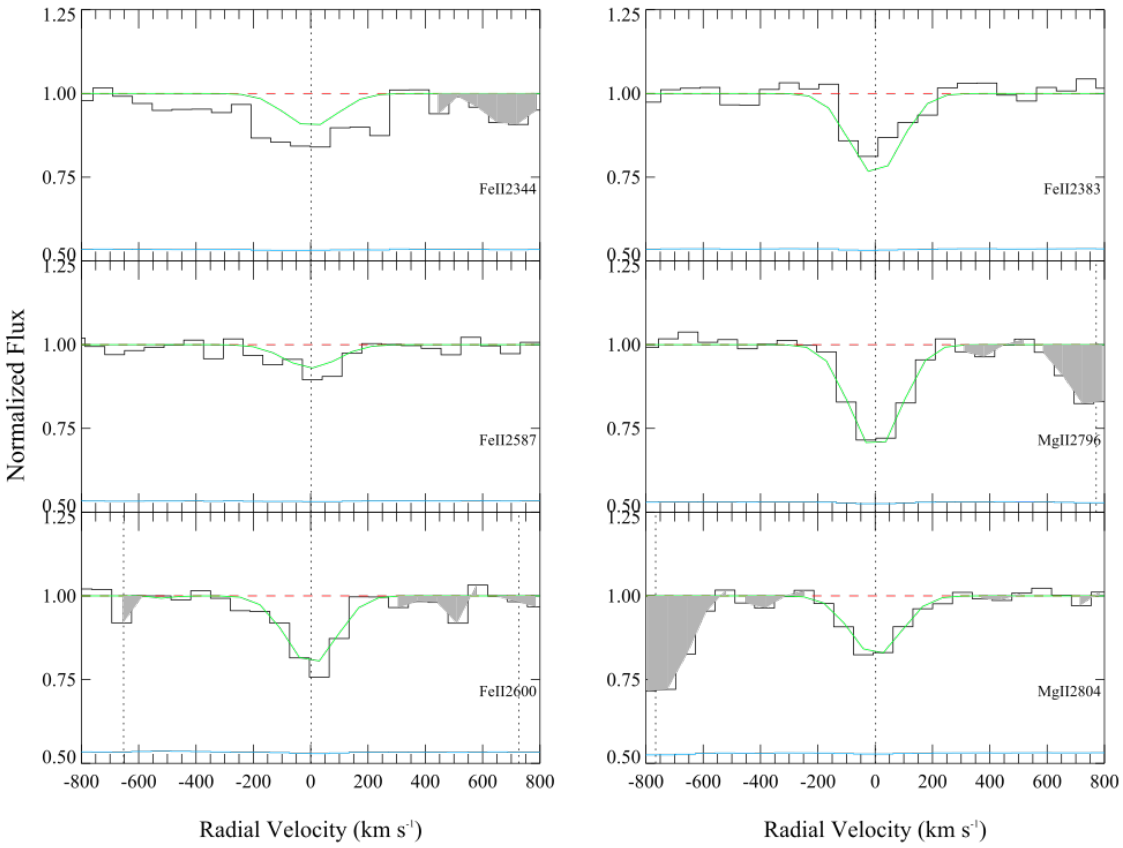

Figure 3.11 Velocity plots for the metal lines in the $z = 0.6794$ system in the SDSS spectrum of Q1054+2733. The two images of the quasar are not resolved at the SDSS resolution, and the spectrum shown is a superposition of the spectra along both sight lines. In each panel, the normalized data are shown in black, the solid green curve indicates the theoretical Voigt profile fit to the absorption feature, and the dashed red line shows the continuum level. The 1σ error values in the normalized flux are represented by the blue curves near the bottom of each panel. The vertical dotted lines indicate the positions of the components that were used in the fit. Shaded regions indicate absorption unrelated to the line presented.

Table 3.12 Voigt Profile Fitting Results for Ions in the $z = 0.6794$ Unresolved Absorber toward Q1054+2733A+B

z	$b_{\rm eff}$(km s^{-1})	log $N_{\rm Mg\ II}$(cm^{-2})	log $N_{\rm Fe\ II}$(cm^{-2})
0.679410±0.000029	68.59 ± 14.97	13.29±0.03	13.49±0.04

Table 3.13 Total Column Densities for the $z = 0.6794$ Unresolved Absorber toward Q1054+2733A+B

Ion	log $N^{\rm fit}$(cm^{-2})	log $N^{\rm AOD}$(cm^{-2})
Mg II	13.29±0.03	13.44±0.04
Fe II	13.49±0.04	13.50±0.04

Table 3.14 Metallicities for the $z = 0.6794$ Unresolved Absorber toward Q1054+2733A+B

Element	[X/H]
Mg	$>$ -1.02
Fe	$>$ -0.86

Note: Approximate mean abundance limits corresponding to the upper limit on the mean H I column density.

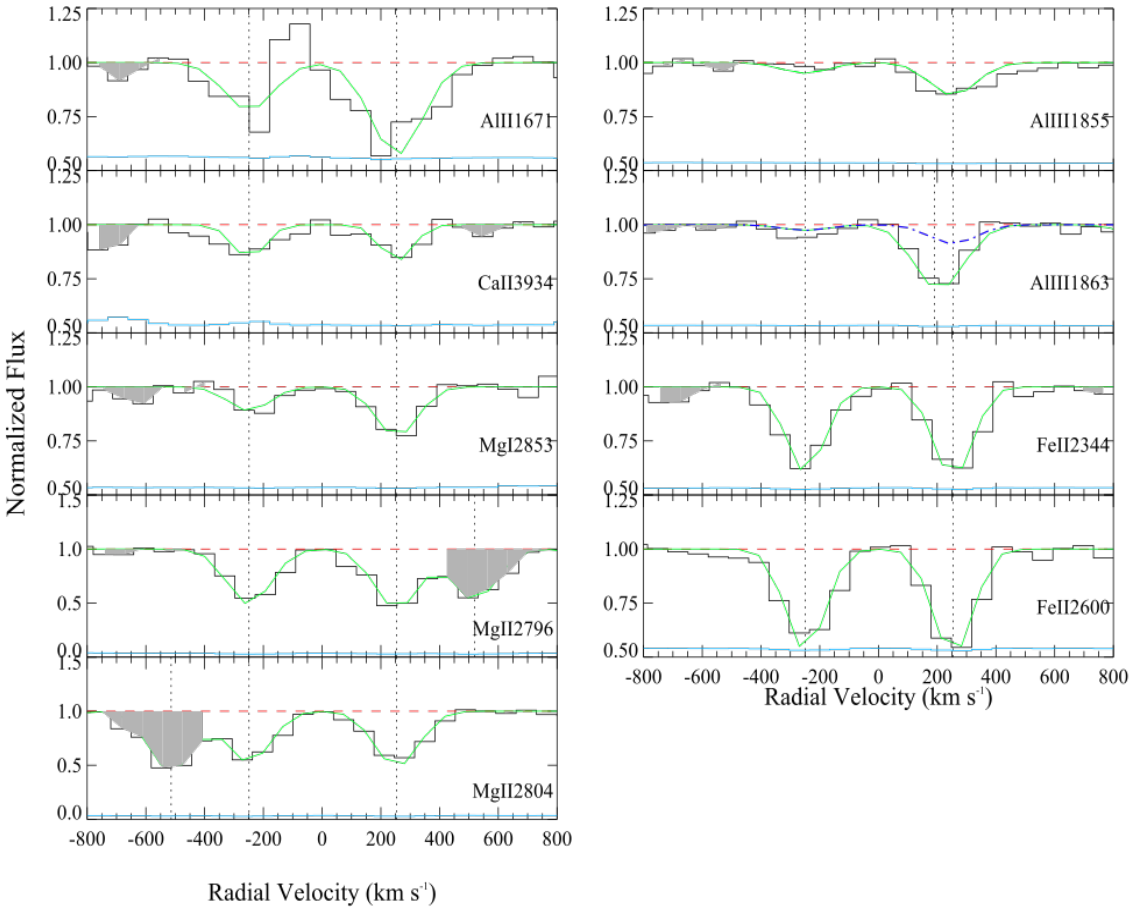

Figure 3.12 Same as Figure 3.11, but for the $z = 1.2366$ system in the unresolved SDSS spectrum of Q1349+1227. The dot-dashed blue curve in the Al III 1863 panel shows the contribution of Mg II 2796 at $z = 0.4913$ that is blended with the Al III 1863 line at $z = 1.2366$.

Table 3.15 Voigt Profile Fitting Results for Ions in the $z = 1.2366$ Unresolved Absorber toward Q1349+1227

z	$b_{\rm eff}$ (km s^{-1})	log $N_{\rm Mg\ I}$ (cm^{-2})	log $N_{\rm Mg\ II}$ (cm^{-2})	log $N_{\rm Al\ II}$ (cm^{-2})	log $N_{\rm Al\ III}$ (cm^{-2})	log $N_{\rm Ca\ II}$ (cm^{-2})	log $N_{\rm Fe\ II}$ (cm^{-2})
1.234744±0.000022	23.62±1.72	12.27±0.12	14.55±0.11	13.04±0.19	12.59±0.17	12.59±0.13	14.45±0.08
1.238496±0.000021	23.71±1.62	12.72±0.08	14.88±0.13	14.23±0.34	13.18±0.07	12.64±0.09	14.55±0.09

Table 3.16 Total Column Densities for the $z = 1.2366$ Unresolved Absorber toward Q1349+1227

Ion	log $N^{\rm fit}$ (cm^{-2})	log $N^{\rm AOD}$ (cm^{-2})
Mg I	12.85±0.07	12.59 ± 0.06
Mg II	15.05±0.09	...
Al II	14.25±0.32	...
Al III	13.28 ± 0.06	...
Ca II	12.91±0.08	12.80 ± 0.09
Fe II	14.80 ± 0.06	14.59 ± 0.05

Table 3.17 Metallicities for the $z = 1.2366$ Unresolved Absorber toward Q1349+1227

Element	[X/H]
Mg	-1.75±0.10
Al	-1.35±0.29
Ca	-2.74±0.10
Fe	-2.11± 0.06

Note: Approximate mean abundances corresponding to the mean H I column density.

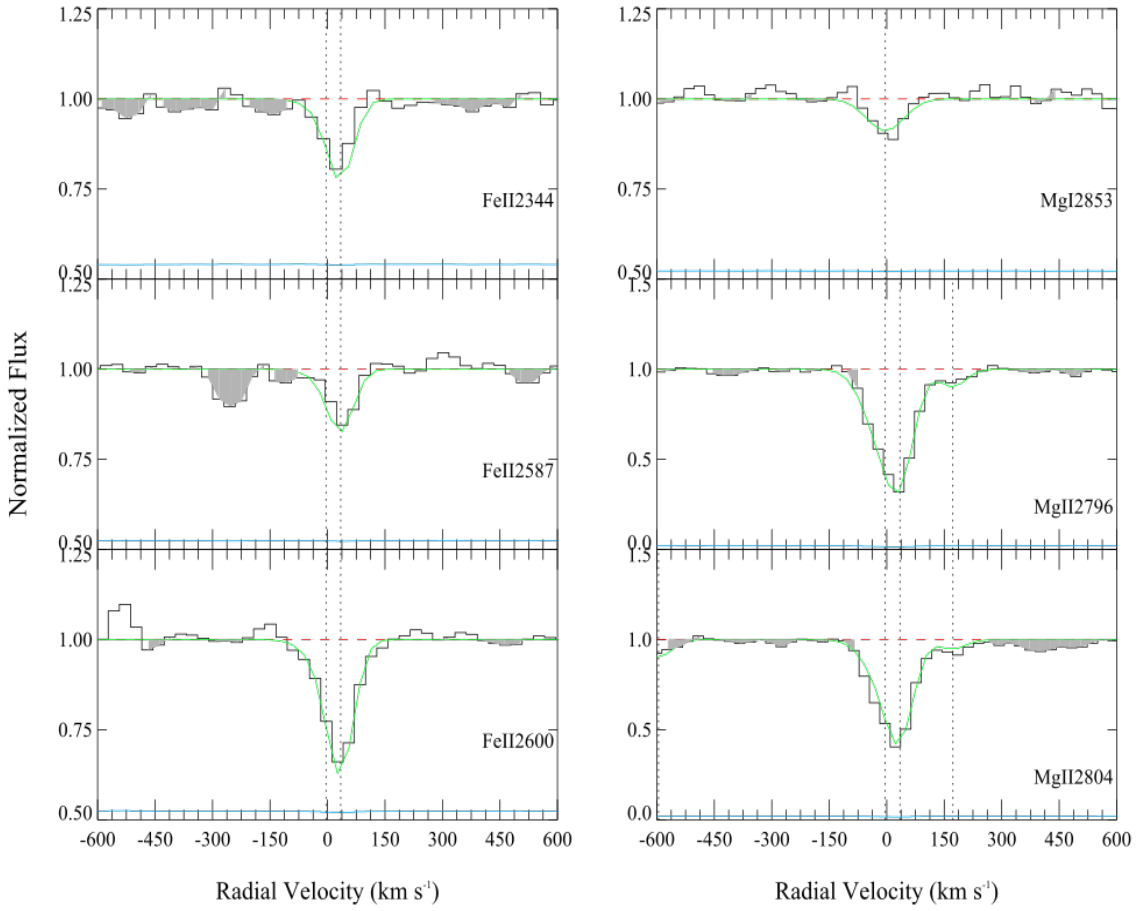

Figure 3.13 Same as Figure 3.8, but for metal lines in the $z = 0.4799$ system in the MagE spectrum of Q1355-2257A.

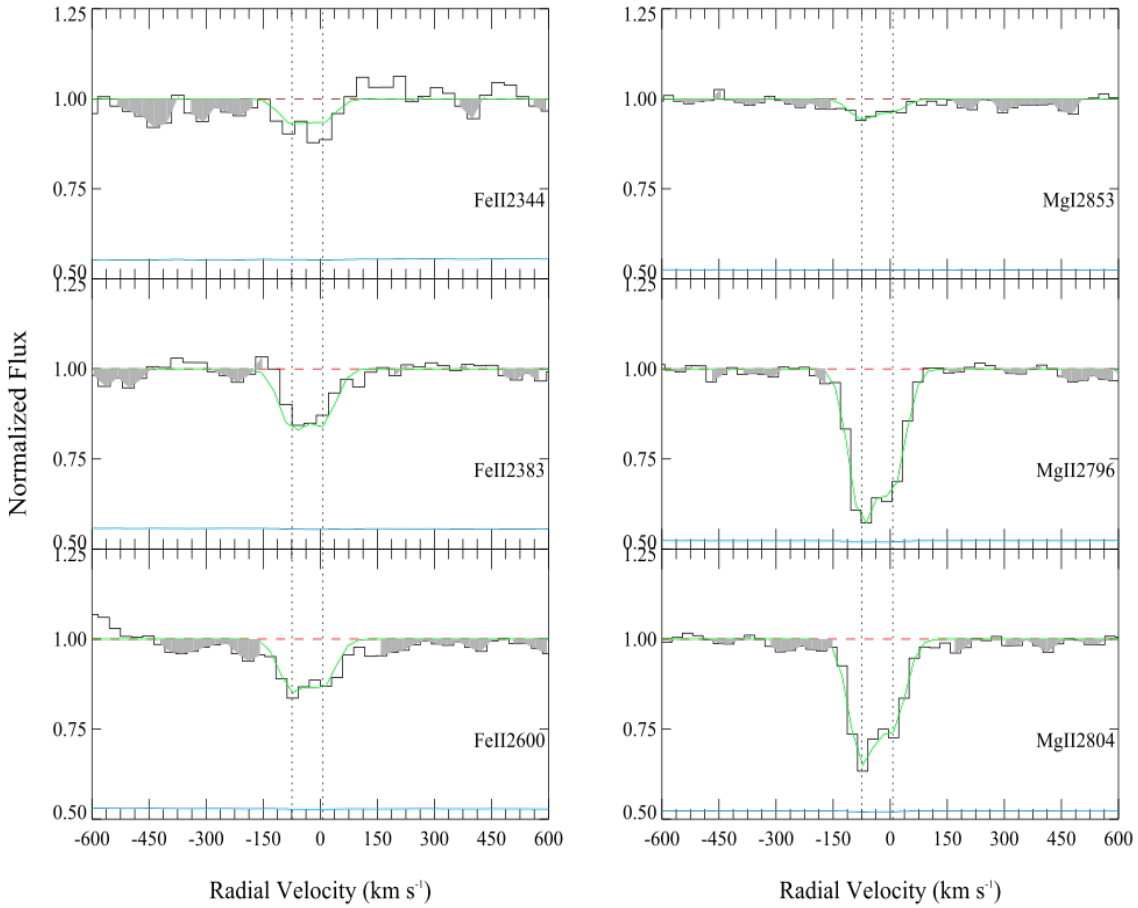

Figure 3.14 Same as Figure 3.8, but for metal lines in the $z = 0.4797$ system in the MagE spectrum of Q1355-2257B.

Table 3.18 Voigt Profile Fitting Results for Ions in the $z = 0.4799$ Absorber toward Q1355-2257A

z	$b_{\rm eff}$ (km s^{-1})	log $N_{\rm Mg\,I}$ (cm^{-2})	log $N_{\rm Mg\,II}$ (cm^{-2})	log $N_{\rm Fe\,II}$ (cm^{-2})
0.479971 ± 0.000006	13.43 ± 1.52	...	14.13 ± 0.08	13.45 ± 0.05
0.479781 ± 0.000021	51.33 ± 3.02	11.95 ± 0.06	13.20 ± 0.02	12.74 ± 0.12
0.480653 ± 0.000029	12.00	...	12.31 ± 0.06	...

Table 3.19 Voigt Profile Fitting Results for Ions in the $z = 0.4797$ Absorber toward Q1355-2257B

z	$b_{\rm eff}$ (km s^{-1})	log $N_{\rm Mg\,I}$ (cm^{-2})	log $N_{\rm Mg\,II}$ (cm^{-2})	log $N_{\rm Fe\,II}$ (cm^{-2})
0.479634 ± 0.000007	11.99 ± 1.12	11.59 ± 0.11	13.44 ± 0.03	12.96 ± 0.05
0.480035 ± 0.000009	10.26 ± 1.32	11.38 ± 0.17	13.20 ± 0.03	12.93 ± 0.05

Table 3.20 Total Column Densities for the $z \sim 0.48$ Absorbers toward Q1355-2257A and Q1355-2257B

Ion	log $N_{\rm A}^{\rm fit}$ (cm^{-2})	log $N_{\rm A}^{\rm AOD}$ (cm^{-2})	log $N_{\rm B}^{\rm fit}$ (cm^{-2})	log $N_{\rm B}^{\rm AOD}$ (cm^{-2})
Mg I	11.95 ± 0.06	11.87 ± 0.10	11.80 ± 0.10	11.63 ± 0.10
Mg II	14.18 ± 0.07	13.60 ± 0.02	13.64 ± 0.02	13.37 ± 0.02
Fe II	13.53 ± 0.05	13.42 ± 0.06	13.24 ± 0.04	13.19 ± 0.04

Table 3.21 Metallicities for the $z \sim 0.48$ absorbers toward Q1355-2257A and Q1355-2257B

Element	$[{\rm X/H}]_{\rm A}$	$[{\rm X/H}]_{\rm B}$
Mg	-0.22 ± 0.19	-1.38 ± 0.27
Fe	-0.78 ± 0.19	-1.69 ± 0.27

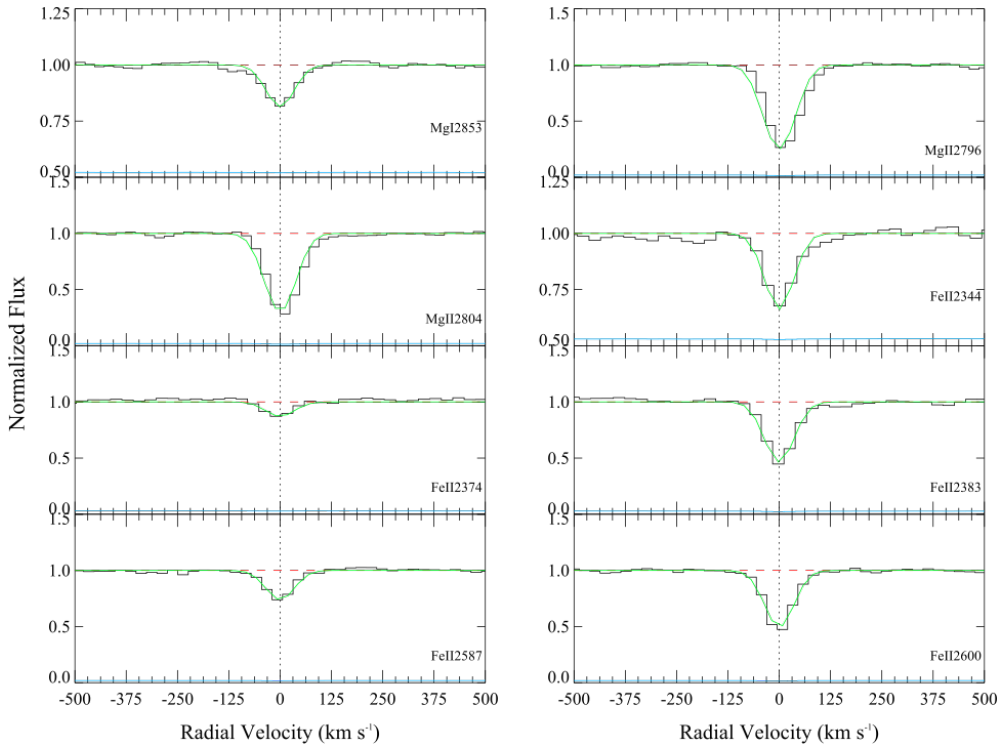

Figure 3.15 Same as Figure 3.8, but for metal lines in the $z = 0.7022$ system in the MagE spectrum of Q1355-2257B. No metal lines are detected toward Q1355-2257A.

Table 3.22 3σ Upper Limits for Ions in the $z = 0.7022$ Absorber toward Q1355-2257A

log $N_{\rm Mg\,I}$ (cm^{-2})	log $N_{\rm Mg\,II}$ (cm^{-2})	log $N_{\rm Fe\,II}$ (cm^{-2})
< 11.13	< 11.79	<12.00

Table 3.23 3σ Metallicity Upper Limits for the $z = 0.7022$ Absorber toward Q1355-2257A

Element	[X/H]
Mg	$<$ -1.92
Fe	$<$ -1.70

Table 3.24 Voigt Profile Fitting Results for Ions in the $z = 0.7022$ Absorber toward Q1355-2257B

z	$b_{\rm eff}$(km s^{-1})	log $N_{\rm Mg\,I}$(cm^{-2})	log $N_{\rm Mg\,II}$ (cm^{-2})	log $N_{\rm Fe\,II}$(cm^{-2})
0.702257 $\pm$0.0000046	18.30 $\pm$ 0.94	12.15 ± 0.04	14.40 ± 0.04	13.82 ± 0.02

Table 3.25 Metallicities for the $z = 0.7022$ Absorber toward Q1355-2257B

Element	[X/H]
Mg	-0.32 ± 0.24
Fe	-0.80 ± 0.23

We also note that, on degrading the Q1017-2046A+B HIRES data to the MagE resolution, we find column densities derived for the latter data to be within 0.02$-$0.05 dex of the values obtained from the original HIRES data. Thus, overall, we regard our metal column density estimates from the MagE data as reasonably robust. In the two cases where we do not have MagE or HIRES spectra and are forced to use SDSS

spectra (Q1054+2733A,B and Q1349+1227A,B), the metal lines are not resolved; in these cases, the AOD column densities are likely to be more accurate than the VPFIT estimates.

Tables 3.12 − 3.14 and Tables 3.15 − 3.17 list the metal column density and element abundance results for the unresolved images of Q1054+2733 and Q1349+1227, respectively. Tables 3.18 and 3.19 list the metal column density results from Voigt profile fitting for the $z = 0.48$ absorber toward Q1355-2257A and Q1355-2257B, respectively. Tables 3.20 and 3.21 list the total column densities, and the element abundances for both of these sight lines. Tables 3.24 and 3.25 list the metal column densities and element abundances for the $z = 0.70$ absorber toward Q1355-2257B. No metal lines are detected at $z = 0.70$ toward Q1355-2257A; Tables 3.22 and 3.23 list the corresponding 3σ upper limits on the metal column densities and on the abundances.

In all cases, the total abundances for the available elements (Tables 3.9, 3.14, 3.17, 3.21, 3.23) were derived from the total column densities for the respective elements, adopting solar photospheric abundances from Asplund et al. (2009) as the reference. Given the lack of coverage of higher metal ions, it is not possible to constrain the ionization parameter in the absorbing gas. However, we note that 6 of the 9 sight lines with detected H I and metal lines have a DLA or a sub-DLA with log $N_{\rm H\,I} \gtrsim$ 19.7, and are thus not expected to have significant ionization corrections.

3.4.2 Other Mg II Absorption Systems

In addition to the previously known Mg II absorbers mentioned in Section 3.2, weaker Mg II absorption systems were also detected in the available MagE/SDSS data. For Q1017-2046, a weak Mg II absorber at $z = 0.7952$ with identical Mg II column densities of log $\rm N_{Mg\,II} = 12.38 \pm 0.06$, but no Fe II detection was detected in both sight lines A and B. The *HST* STIS spectrum of Q1017-2046A shows no

H I absorption at $z = 0.7952$, but shows a weak absorption feature nearby. If this feature is H I Lyα at $z = 0.7987$, it may be associated with the Mg II absorber, given that the redshift difference ($\approx$ 585 km s^{-1}) is within 1 resolution element of STIS G230L. If this weak line is indeed H I Lyα, we can estimate a poorly constrained log $N_{\rm H\,I}$ value of $\approx 15.7 \pm 2.0$ assuming a Doppler b-value in the range of 10-30 km s^{-1} for the $z = 0.7987$ absorber toward Q1017-2046A. However, the corresponding H I Lyβ feature cannot be verified, because it lies in a region with very low quasar flux, owing to the Lyman limit break from the DLA at $z = 1.086$. The noisier *HST* STIS spectrum of Q1017-2046B shows no H I absorption at $z = 0.7952$, or anywhere within 1500 km s^{-1} of that redshift. Based on the S/N in the STIS spectrum of Q1017-2046B, we can place a 3σ upper limit on the equivalent width of the Lyα line at $z = 0.7952$ of $W < 0.91$ Å, which implies a 3σ upper limit on the H I column density of log $N_{\rm H\,I} \leq 18.19$ in this sight line.

For Q1349+1227, an Mg II absorber at $z = 0.4913$ was detected in the combined (unresolved) SDSS spectrum with log $N_{\rm Mg\,II} = 13.92 \pm 0.20$, with marginal detections of Ti II (log $N_{\rm Ti\,II} = 12.64 \pm 0.31$), and Fe II (log $N_{\rm Fe\,II} = 13.45 \pm 0.14$). The corresponding H I Lyα line lies in a very noisy part of the *HST* STIS spectrum (at wavelengths shorter than the Lyman limit for the DLA at $z = 1.2366$) and thus could not be measured in sight line A or B.

Interestingly, we also note that no metal lines were detected at the estimated lens redshift of $z = 0.23$ toward Q1054+2733 in the SDSS spectra. Likewise, no metal lines were detected at the estimated lens redshift of $z = 0.645$ in the SDSS spectrum of Q1349+1227. However, we note that the SDSS spectra are noisy, and we cannot rule out the presence of weak Mg II absorbers. These findings are consistent with other observations that also found that not all lenses produce strong absorption features (e.g., Rogerson & Hall 2012; Zahedy et al. 2016). For example, Zahedy et al. (2016) found that 1 of the 3 lens systems in their study (the quadruple lens for

HE 0405-1223, which arises in a group environment) shows no Mg II absorption along any of the 4 sight lines.

3.5 Discussion

We now discuss the implications of our results for comparing the H I and metal content between the individual sight lines in GLQ absorbers, keeping in mind that the derived column densities have the uncertainties discussed in Section 3.3 and Section 3.2.4.

3.5.1 H I Column Densities and their Differences between the Sight Lines

For the $z = 1.09$ absorber toward Q1017-2046A and Q1017-2046B, both the Lyα and Lyβ features were used in estimating the H I column densities. The Lyβ feature in the A sight line appears to be blended with another feature at a different redshift (possibly a Lyα forest line at a lower redshift.) The H I column densities derived are comparable along the two sight lines.

The H I column densities along the two sight lines for the $z = 0.68$ absorber toward Q1054+2733A,B cannot be compared exactly, since we can only place an upper limit on the H I column density along the B sight line owing to the much noisier spectrum. The Lyβ line at $z = 0.68$ is too noisy and blended in both sight lines to give useful constraints. Additionally, we detect a strong feature in Q1054+2733A, which may be H I Lyα at $z = 0.6687$, or Si III λ 1206 at $z = 0.6815$, or a blend. This feature is not seen in Q1054+2733B. This suggests that the cool gas in the $z = 0.6687$ absorber and/or the warm gas in the $z = 0.6815$ absorber detected toward Q1054+2733A has a transverse extent of $\lesssim$1.9 kpc.

For the $z = 1.24$ absorber toward Q1349+1227A and Q1349+1227B, we use both the Lyα and Lyβ lines in estimating the H I column densities. The Lyβ feature for this absorber toward Q1349+1227B may seem over-predicted for the estimated $N_{\rm H\,I}$

value, but the fit is consistent with the data within the high noise level present near this feature (see Figure 3.5). If this noisy Lyβ feature is excluded from the fit (i.e., if only the Lyα feature is used), there is little change to the H I column density derived (log $N_{\rm H\,I} = 21.39\pm0.05$ instead of 21.37 ± 0.05.) In either case, the best-fit H I column density appears to be higher along the B sight line than that along the A sight line by a factor of ~ 3.0.

For the $z = 0.48$ absorber toward Q1355-2257A,B, the H I column density is higher along the B sight line by 0.62 dex (a factor of ~ 4.2) compared to that in the A sight line. For the $z = 0.70$ absorber toward Q1355-2257A,B, the H I column density is higher along the B sight line by 0.92 dex (a factor of ~ 8.3) compared to that in the A sight line. For both of these absorbers, only Lyα lines were used in the fits, as the Lyβ lines were not covered by the HST STIS data.

Thus, there is a range in the variation of the H I column density across the few kpc distance between the two sight lines in the GLQ fields studied here, from almost no variation to variation by a factor of ~ 8. There is not a strong correlation between the difference in the H I column densities and the magnitude difference between the images; but this could be partly due to small number statistics. We further discuss our results together with others from the literature in Section 3.5.3.

3.5.2 Element Abundances and Abundance Gradients

We now describe our results for the Fe abundances [Fe/H] and the abundance gradients. The metallicity gradient is an average abundance gradient that shows how the abundance between the images would change per unit distance if the lens were considered to be uniform. We use [Fe/H] despite the fact that Fe is depleted on to dust grains simply because it is the most easily measured metal abundance in our data. We evaluate the [Fe/H] gradient from the difference in Fe abundances between the sight lines to the lensed quasar images and the difference in the impact parameters (in

kpc) of the sight lines relative to the lens galaxy center, i.e., Δ[Fe/H]/Δr = ([Fe/H]$_{\rm B}$ - [Fe/H]$_{\rm A}$)/($r_{\rm B}$ - $r_{\rm A}$).

For the z = 1.09 absorber toward Q1017-2046A,B (Figures 3.8, 3.9), given that sight line B is at a smaller impact parameter from the galaxy center than sight line A, it is interesting that the Fe abundance along sight line B is somewhat lower than that along sight line A. The Fe abundances along the two sight lines differ marginally by 0.24 $\pm$ 0.15 dex. Combining this with the impact parameters of the two sight lines (5.4 kpc and 1.5 kpc with respect to the galaxy center), we estimate an average abundance gradient of +0.063 $\pm$ 0.040 dex kpc^{-1}, i.e., a marginal inverted gradient compared to the negative abundance gradients seen in the Milky Way and nearby galaxies (e.g., $\sim$-0.01 to -0.09 dex kpc^{-1} in the Milky Way, Friel et al. 2002; Luck & Lambert 2011; Cheng et al. 2012; -0.043 dex kpc^{-1} in M101, Kennicutt et al. 2003; -0.027 $\pm$ 0.012 dex kpc^{-1} in M33, Rosolowsky & Simon 2008; -0.041$\pm$ 0.009 dex kpc^{-1} in nearby isolated spirals, Rupke et al. 2010).

For the z = 0.48 absorber toward Q1355-2257A,B (Figures 3.12, 3.13), the Fe abundance is lower along the B sight line by 0.91 $\pm$ 0.33 dex (a factor of $\sim$6). This is surprising if the lens galaxy is at z = 0.48, given that sight line B passes closer to the galaxy center (1.6 kpc) than sight line A 5.7 kpc). In this case, we estimate an average abundance gradient of +0.22 $\pm$ 0.08 dex kpc^{-1}, which is stronger and inverted compared to the abundance gradients seen in the Milky Way and nearby galaxies.

For the z = 0.70 absorber toward Q1355-2257A,B, metal lines are detected in sight line B (Figure 3.14), but no metal lines are detected in sight line A. The non-detection of the strongest Fe II line covered (Fe II λ 2383) implies a 3σ upper limit on the Fe II column density of log $N_{\rm Fe\,II}$ < 12.00, and hence an upper limit on the Fe abundance of [Fe/H] < -2.04. The Fe abundance is higher along the B sight line by > 1.24 dex (i.e., a factor of $\gtrsim$17). If the lens galaxy is at z = 0.70, the impact

parameters of the A and B sight lines are 6.9 kpc and 1.9 kpc, respectively, implying an average abundance gradient of < -0.25 dex kpc^{-1}. This abundance gradient is not inverted, but is much steeper compared to the abundance gradients seen in the Milky Way and nearby galaxies. On the other hand, such a steep metallicity gradient is consistent with the strongly negative metallicity gradients found in some galaxies at $z \sim 1-2$ (e.g., Yuan et al. 2011; Jones et al. 2013).

Given that the metallicity gradient in DLAs at $0.1 < z < 3.2$ is typically fairly weak (-0.022 ±0.004 dex; Christensen et al. 2014), one may wonder whether the steep abundance gradient in the $z = 0.70$ absorber toward Q1355-2257 A,B is a result of differing degrees of Fe depletion. However, this would require sight line A to be more dusty, even though the H I column density in sight line A is smaller than that in sight line B by a factor of ∼11. (We note, however, that Chen et al. 2013 reported a differential X-ray absorption between images A and B, with image A having stronger X-ray absorption by $\Delta N_{\rm H} = 4.0 \times 10^{20}$ cm^{-2}, which suggests the A sight line could be dustier.)

Thus, if the redshift of the lensing galaxy for Q1355-2257A,B is $z = 0.48$ as seems more likely to us (as explained in Section 3.5.3), it has a positive abundance gradient. If, however, the less likely value of $z = 0.70$ is in fact the correct redshift of the lens, it would have a negative abundance gradient. These different conclusions underscore the need for accurate determinations of the lens galaxy redshifts.

Overall, our observations suggest a mixture of both positive (inverted) and negative metallicity gradients. The inverted gradients are interesting, since such gradients have been suggested as evidence of inflowing metal-poor gas at high redshift (e.g., Cresci et al. 2010; Queyrel et al. 2012). Indeed, Queyrel et al. (2012) have suggested that such inverted gradients may be found in metal-poor galaxies. We note, however, that the gradient in the dust-corrected metallicity could be different from the gradient in [Fe/H]. Since the dust depletion of Fe in DLAs correlates with metallicity (e.g.,

Kulkarni et al. 2015), the sight line with higher [Fe/H] is likely to have a more severe dust depletion and thus a higher intrinsic (dust-corrected) metallicity, implying a steeper gradient (whether positive or negative). Indeed, in Q1017-2046A,B, the only case in our sample where we have measurements of Si (an element less depleted than Fe), the abundance of Si is higher than that of Fe by 1.13±0.15 dex in sight line A and by 0.73 ± 0.24 dex in sight line B. Furthermore, [Si/H] is lower in the B sight line by 0.64±0.24 dex, implying a [Si/H] gradient of +0.167±0.063 dex, which is steeper (and even more inverted) compared to the [Fe/H] gradient of +0.063±0.040. We also note that the abundance gradients depend on the H I column densities, whose accuracy is limited by the low spectral resolution of the STIS G230L spectra, as discussed in Section 3.3.1. Other sources of uncertainties in our estimates of abundance gradients come from the fact that they are based on only two sight lines through the galaxy, and that they involve the assumption of a uniform gradient.

Another way to estimate metallicity gradients in galaxies producing DLA/sub-DLAs is by comparison of emission and absorption metallicities: the emission typically comes from regions close to the galaxy center, while the absorption typically arises in regions further away. Integral field spectroscopic (IFS) observations allow the determination of emission-line metallicity (e.g., Péroux et al. 2011a, 2012, 2013). These studies also find a mixture of positive and negative metallicity gradients. Our results from GLQ sight lines are thus consistent with the IFS results. We compare our results with the IFS results and other studies of abundance gradients in more detail in Section 3.5.7.

3.5.3 Comparison with Other DLA/sub-DLA Absorbers toward GLQs

We now compare the absorbers studied here with absorbers toward other GLQs, where at least one of the multiple sight lines shows a DLA or a sub-DLA. Only a small number of other GLQs (HE1104-1805, HE 0512-3329, Q0957+561, H1413+117,

UM673, HE 0047-1756, SDSS J1442+4055) have measurements of H I column densities in such absorbers (Lopez et al. 1999; Lopez et al. 2005; Churchill et al. 2003; Monier et al. 2009; Cooke et al. 2010; Zahedy et al. 2017; and Krogager et al. 2018 respectively). Table 3.26 summarizes the sample including our own measurements. For HE 1104-1805, HE 0512-3329, Q0957+561, UM673, HE 0047-1756, and SDSS J1442+4055, measurements of metal line column densities also exist in the same absorbers. We therefore include these absorbers along with the absorbers studied here in our study of abundance variations in absorbers toward GLQs (those arising in the lens galaxies as well as other absorbers).

In the case of HE 1104-1805, Q0957+561, UM 673, and SDSS J1442+4055, the DLA/sub-DLAs reported in the literature are at redshifts considerably higher than the lens galaxy redshifts. For HE 0512-3329, while the lens redshift is not certain, the lens is likely to be the galaxy associated with the DLA at $z = 0.93$ (Gregg et al. 2000). Indeed, a DLA is detected along the sight lines of both HE 0512-3329A and HE 0512-3329B, separated by $0\farcs64$, with essentially identical H I column densities (log $N_{\rm H\,I} = 20.49 \pm 0.08$ and log $N_{\rm H\,I} = 20.47 \pm 0.08$, respectively, and this is likely to be the lensing galaxy (Lopez et al. 2005). Furthermore, Lopez et al. (2005) found some evidence of difference in metallicities ([Fe/H] $= -1.52 \pm 0.11$, [Mn/H] $= -1.44 \pm 0.09$ in sight line A and [Fe/H] > -1.32 dex, [Mn/H] $= -0.98 \pm 0.09$ in sight line B. For HE 0047-1756, a sub-DLA has been detected by Zahedy et al. (2017) at the redshift of the lens galaxy in both sight lines, separated by $1\farcs44$, with similar H I column densities (log $N_{\rm H\,I} = 19.7 \pm 0.1$ and log $N_{\rm H\,I} = 19.6^{+0.2}_{-0.3}$, respectively, for sight lines A and B). Fe II lines were also detected along both sight lines, implying abundances [Fe/H] of -0.59 ± 0.10 for HE 0047-1756A and -0.40 ± 0.26 for HE 0047-1756B. We therefore include the absorbers toward HE 0512-3329 and HE 0047-1756 along with the absorbers toward Q1017-2046 and Q1355-2257 in our examination of lens galaxy properties. Thus, our data (which provide H I and metal column densities for

2 lens galaxies) have doubled the sample of lens galaxies with measurements of H I column densities and element abundances along multiple sight lines. For the sake of definiteness, we assume the redshift of the lensing galaxy for Q1355-2257 to be 0.48 in the discussion below (but we also consider the alternative redshift of 0.70 in Section 3.5.2 and 3.5.6).

3.5.4 Transverse Separations

In a lensing geometry the light paths of lensed images at redshifts beyond the lens converge to the source, and therefore the intrinsic separation between the images gets smaller toward the source. When the absorber redshift is greater than or equal to the lens redshift, the transverse separation $l_{\rm AB,a}$ between the sight lines at the absorber redshift can be calculated as

$$l_{\rm AB,a} = \frac{D_{\rm aq}(1+z_{\rm l})\Delta\theta_{\rm AB}D_{\rm l}}{D_{\rm lq}(1+z_{\rm a})}, \tag{3.1}$$

where $D_{\rm l}$, $D_{\rm lq}$, and $D_{\rm aq}$ denote the angular diameter distances between the observer and the lens, the lens and the quasar, and the absorber and the quasar, respectively, and $\Delta\theta_{\rm AB}$ is the angular separation between quasar images A and B. It is worth noting that $D_{\rm aq} \neq D_{\rm q} - D_{\rm a}$, $D_{\rm lq} \neq D_{\rm q} - D_{\rm l}$, $D_{\rm aq} \neq -D_{\rm qa}$, and $D_{\rm lq} \neq -D_{\rm ql}$. Following Hogg (1999), which assumes a flat universe, we use

$$D_{12} = \frac{c}{H_0(1+z_2)} \int_{z_1}^{z_2} [\Omega_\Lambda + \Omega_{\rm m}(1+z)^3]^{-1/2}\, dz. \tag{3.2}$$

In the special case when the absorber is the lens itself, $l_{\rm AB,a} = \Delta\theta_{\rm AB}D_{\rm l}$. In the more typical case of $z_{\rm a} > z_{\rm l}$, the separation at the absorber redshift is smaller than that at the lens. Indeed, the closer the absorber is to the quasar, the smaller the separation probed at the absorber redshift.

3.5.5 Trends with Sight Line Separation and Quasar Image Brightness

Here we examine whether (a) the absolute differences in H I column densities, Fe II column densities and Fe abundances depend on the separation between the sight lines, and (b) whether these properties along the sight line to the fainter image are systematically smaller (or larger) compared to those along the sight line to the brighter image. We note that for non-lens absorbers, if the absorbing galaxy has not been imaged, it is not known how the sight line separation relates to the impact parameters, since this relation depends on the location of the galaxy center relative to the two sight lines. Nevertheless, even in such cases, it is of interest to examine whether and how absorber properties correlate with the sight line separation. Several past studies have examined whether equivalent width differences between the sight lines are correlated with the separations (e.g., Rauch et al. 2001; Ellison et al. 2004). For example, if the sight line separation is smaller than the absorber size, then one may expect that the smaller the separation, the smaller should be the column density difference. At large separations the trend may disappear as the separation exceeds the absorber size. Furthermore, one may expect the fainter sight line to have higher H I column density and metallicity if this sight line is obscured more due to a dustier absorbing region, although the lensing configuration also influences the relative brightness of the images. Generally, the magnification difference between images is minimized for symmetric lens configurations. A ballpark assessment of the magnification ratio can be estimated by comparing the angular separation between each pair of images and the lens center, where a ratio of 1 would indicate that the images are an equal angular distance from the lens galaxy. The approximate magnification ratios (smaller divided by the larger) are 0.3, 0.4, 0.1, and 0.3 for Q1017-2046, Q1054+2733, Q1349+1227, and Q1355-2257 respectively. These ratios suggest the lens configurations may be non-symmetric, and therefore a more careful study would be required to determine to what degree dust is also affecting the magnitude difference.

Figure 3.16(a) shows the absolute difference in the H I column densities $|\Delta \log N_{\rm H\,I}|$ vs. the transverse separation between the sight lines at the absorber redshift $l_{\rm AB,a}$ calculated using equations 4.2 and 4.3. A number of the points in Figure 3.16(a) are for absorbers along the sight lines toward a quadruple lens, and thus may not be independent of each other. Nevertheless, even if all the measurements are considered independent, no significant correlation is observed between $|\Delta \log N_{\rm H\,I}|$ and the sight line separation; we find a Spearman rank order correlation coefficient of $r_{\rm S}$ = 0.0726, and a 1-tailed probability of 0.372 for this occurring by chance. While some absorbers show $>$ 1 order of magnitude difference in H I column densities between the sight lines over separations >3 kpc, others show smaller differences (including some with essentially zero difference) for separations of 6-8 kpc. This suggests a wide variety of sizes in the H I extent of DLA/sub-DLAs in the entire range studied (0-8 kpc). It is possible that the sight lines are being probed by different galaxies; such a conclusion would be consistent with a similar conclusion by Ellison et al. (2007) based on observation of coincident DLAs on a scale of 100 kpc toward a binary quasar. Alternately, it may suggest a clumpy medium sampled randomly by a few sight line pairs.

Figure 3.16(b) shows the absolute difference in the Fe II column densities $|\Delta \log N_{\rm Fe\,II}|$ between the sight lines vs. the separation between the sight lines at the absorber redshift $l_{\rm AB,a}$. Not much correlation is seen here either, with a Spearman rank order correlation coefficient of -0.0476. Figure 3.16(c) shows the absolute difference in the Fe abundances $|\Delta$[Fe/H]$|$ between the sight lines vs. the separation between the sight lines at the absorber redshift. Once again, no significant correlation is evident, with a Spearman rank-order correlation coefficient of -0.156.

To examine differences between the sight lines toward the fainter and brighter images and the potential dependence of any such differences on the sight line separations, we now plot the actual differences (not their absolute values), i.e., the $N_{\rm H\,I}$,

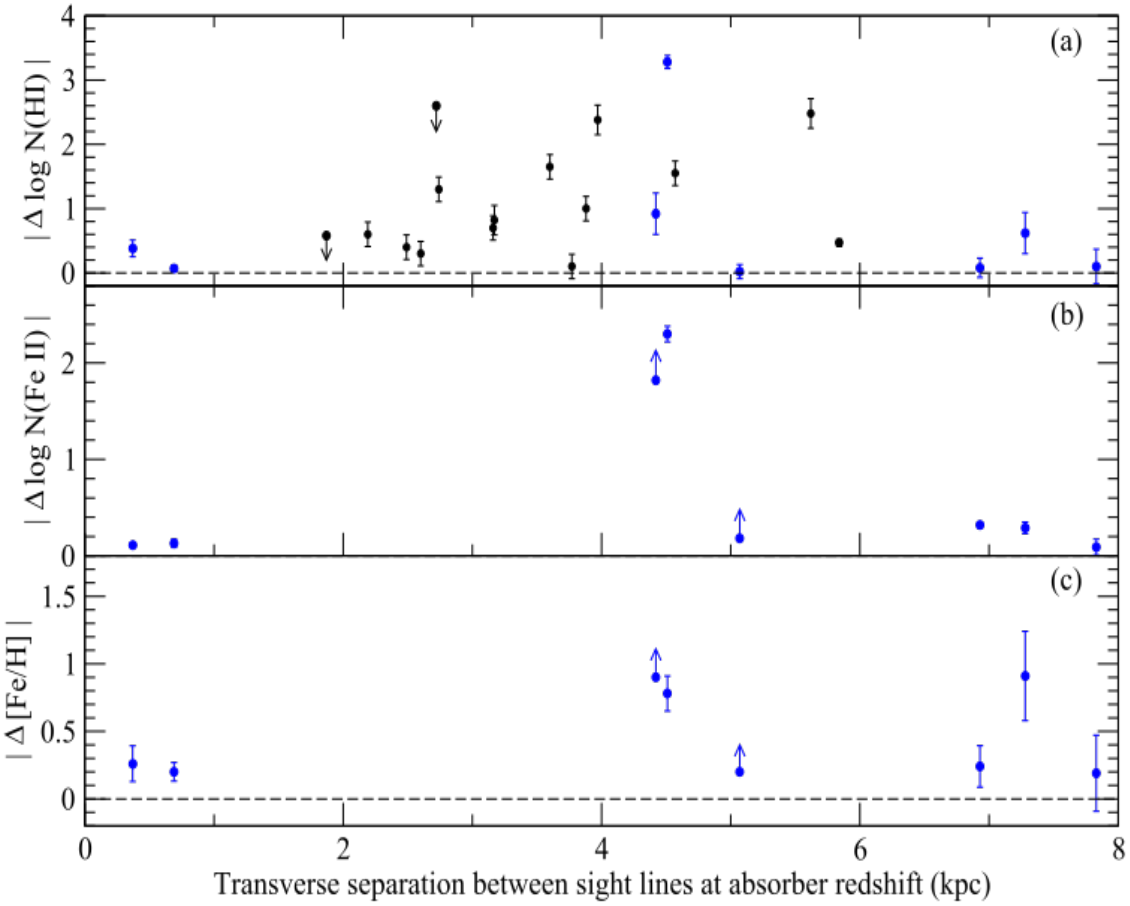

Figure 3.16 Absolute values of the differences (in dex) in (a) H I column densities, (b) Fe II column densities, and (c) Fe abundances between GLQ sight lines vs. the transverse separation between the sight lines at the absorber redshift. Blue symbols denote absorbers where measurements of both metal and H I column densities are available, while black symbols denote absorbers with measurements of only H I column densities.

$N_{\rm Fe\,II}$, and [Fe/H] values along the B (fainter) sight lines minus the corresponding quantities in the A (brighter) sight lines vs. the separations. (We note that if we plotted these differences as "A-B" differences instead of "B-A" differences, any trends seen with sight line separation would be reversed; but this would have no impact on any conclusions reached regarding the relative differences between the sight lines to the brighter images and the fainter images.)

Figure 3.17(a) shows the difference in the H I column densities $\Delta\log N_{\rm H\,I} = \log N^{\rm B}_{\rm H\,I}$ - $\log N^{\rm A}_{\rm H\,I}$ vs. the transverse separation between the sight lines at the absorber

redshift $l_{\rm AB,a}$. Once again, if all the measurements are considered independent, over the range of separations covered, there is not much correlation between $\Delta\log\ N_{\rm H\,I}$ and $l_{\rm AB,a}$, with a Spearman rank order correlation coefficient of $r_{\rm S}$ = -0.0148, and a 1-tailed probability of 0.472 for this occurring by chance. For 15 out of 23 cases, $\Delta\log\ N_{\rm H\,I} < 0$, i.e., the H I column density is lower along the fainter sight line compared to that along the brighter sight line. However, we caution that 12 of the 23 measurements are for two absorbers (6 points per absorber) along the sight lines toward a quadruple lens, and thus may not be independent of each other. If these 12 measurements are excluded, the fraction of cases showing $\Delta\log\ N_{\rm H\,I} < 0$ becomes smaller (6 out of 11), and the lack of correlation between Δ log $N_{\rm H\,I}$ and $l_{\rm AB,a}$ persists, with $r_{\rm S}$ = 0.109, and a 1-tailed probability of 0.374 for this occurring by chance.

Figure 3.17(b) shows the difference in the Fe II column densities between the sight lines vs. the separation between the sight lines at the absorber redshift. A wide range of differences in Fe II column densities are observed, from -2.3 dex to >1.8 dex. In general, the sight lines with larger Fe II differences are those with larger H I differences. There is not much correlation between the difference in Fe II column densities and the transverse separation, with a Spearman rank order correlation coefficient of $r_{\rm S}$ = -0.119.

Figure 3.17(c) shows the difference in the Fe abundances Δ[Fe/H] between the sight lines vs. the separation between the sight lines at the absorber redshift. While the sample is still small, there is a slight excess of cases where Δ[Fe/H] > 0, i.e., [Fe/H] is larger along the fainter sight line than along the brighter sight line. There is not much correlation between Δ[Fe/H] and the sight line separation, with a Spearman rank-order correlation coefficient of -0.524.

We note that the observation of lower $N_{\rm H\,I}$ values in fainter images for some GLQs may suggest that the faintness of the fainter images relative to the brighter images is not always caused by stronger obscuration in a more gas-rich and dust-

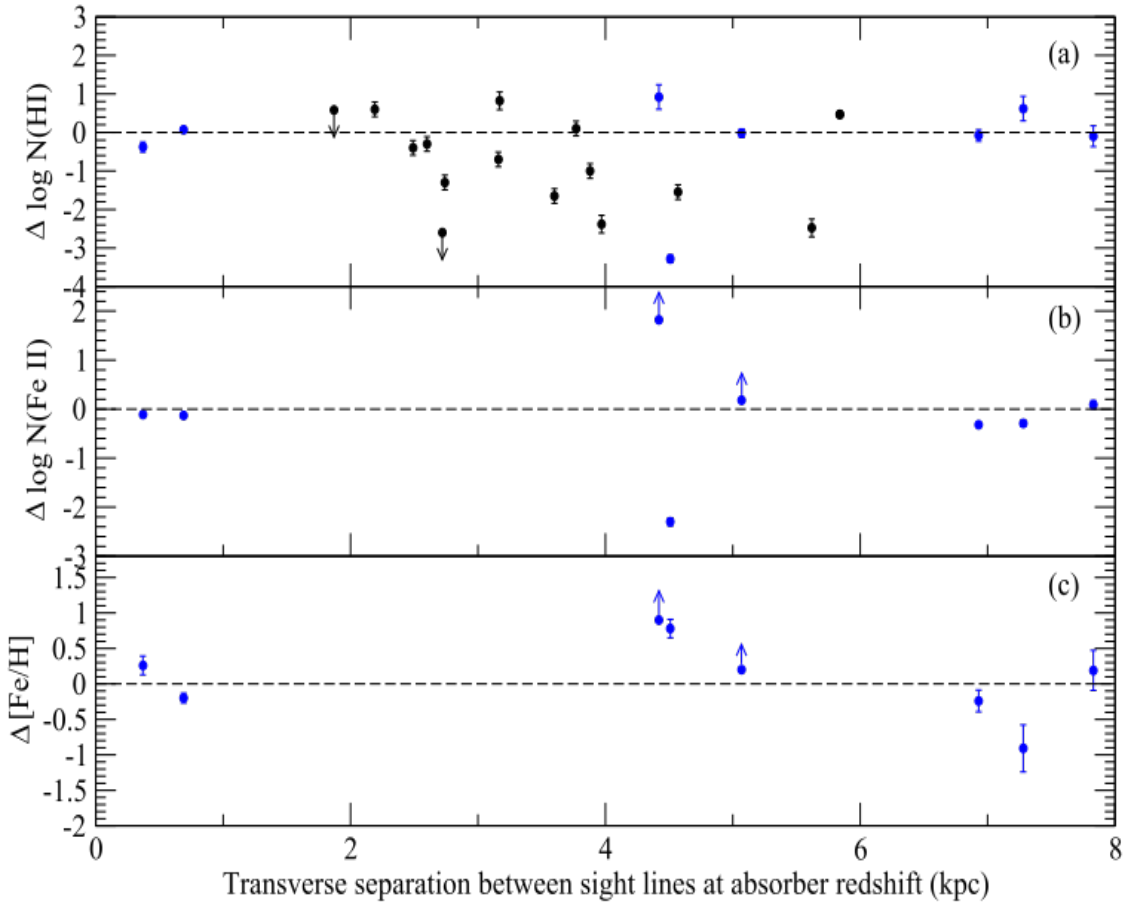

Figure 3.17 Differences (in dex) in (a) H I column densities, (b) Fe II column densities, and (c) Fe abundances between GLQ sight lines vs. the transverse separation between the sight lines at the absorber redshift. All differences are calculated by subtracting the quantities for the sight line toward the brighter image from those for the sight line toward the fainter image. Blue symbols denote absorbers where measurements of both metal and H I column densities are available, while black symbols denote absorbers with measurements of only H I column densities.

rich region along the sight line. In other words, obscuration along the sight line may play a smaller role than the lensing configuration in determining the relative image brightnesses. (We note, however, that the excess of lower $N_{\rm H\,I}$ systems seen in the present sample is driven by systems without metal abundance measurements. Measurements of abundances of volatile and refractory elements in these absorbers are essential to determine how the dust depletions in these lower $N_{\rm H\,I}$ absorbers compare with those in the higher $N_{\rm H\,I}$ absorbers.) Furthermore, a number of the available

H I measurements are for two absorbers along sight lines toward a quadruple lens, and therefore may not be independent of each other. Expanding the sample to a larger number of independent GLQ sight lines is essential to determine whether any statistically significant trend is present between H I column density difference and sight line separation.

3.5.6 Comparison with Other Abundance Gradient Measurements

We now examine the abundance gradients in GLQ absorbers at the lens redshifts with measurements of abundance gradients in other galaxies. In particular, we examine whether the abundance gradients show any trends with the abundances at the galaxy centers. The blue circles in Figure 3.18 show, for the GLQ absorbers at the lens redshifts, the [Fe/H] gradient in dex kpc^{-1} between the GLQ sight lines vs. the Fe abundance at the galaxy center estimated from the two measurements, assuming a uniform abundance gradient within the galaxy, i.e.

$$\left[\frac{Fe}{H}\right]_0 = \left[\frac{Fe}{H}\right]_{\rm A} - \frac{r_{\rm A}\Delta\left[\frac{Fe}{H}\right]}{\Delta r}. \tag{3.3}$$

Some GLQ absorbers appear to have positive (i.e., inverted) gradients, although the uncertainties are substantial.

For comparison, the green stars in Figure 3.18 show measurements of the abundance gradients inferred from long-slit spectroscopy or integral field spectroscopy (IFS) of absorption-selected galaxies at $0 < z < 2.4$ (primarily at $0.5 \lesssim z \lesssim 1$) foreground to quasars (Schulte-Ladbeck et al. 2004; Chen et al. 2005; Péroux et al. 2012, 2016, 2017; Rahmani et al. 2016; and references therein), plotted vs. the central emission-line abundance in the galaxy. We refer to these latter measurements as "QGP" (quasar-galaxy pair) measurements. For all QGPs, the oxygen abundance estimated from nebular emission lines for the galaxy is adopted as the central abundance. The majority of these QGP emission-line metallicities (from Péroux et al. 2012; Krogager et al. 2013; Kacprzak et al. 2014; many from Rahmani et al. 2016)

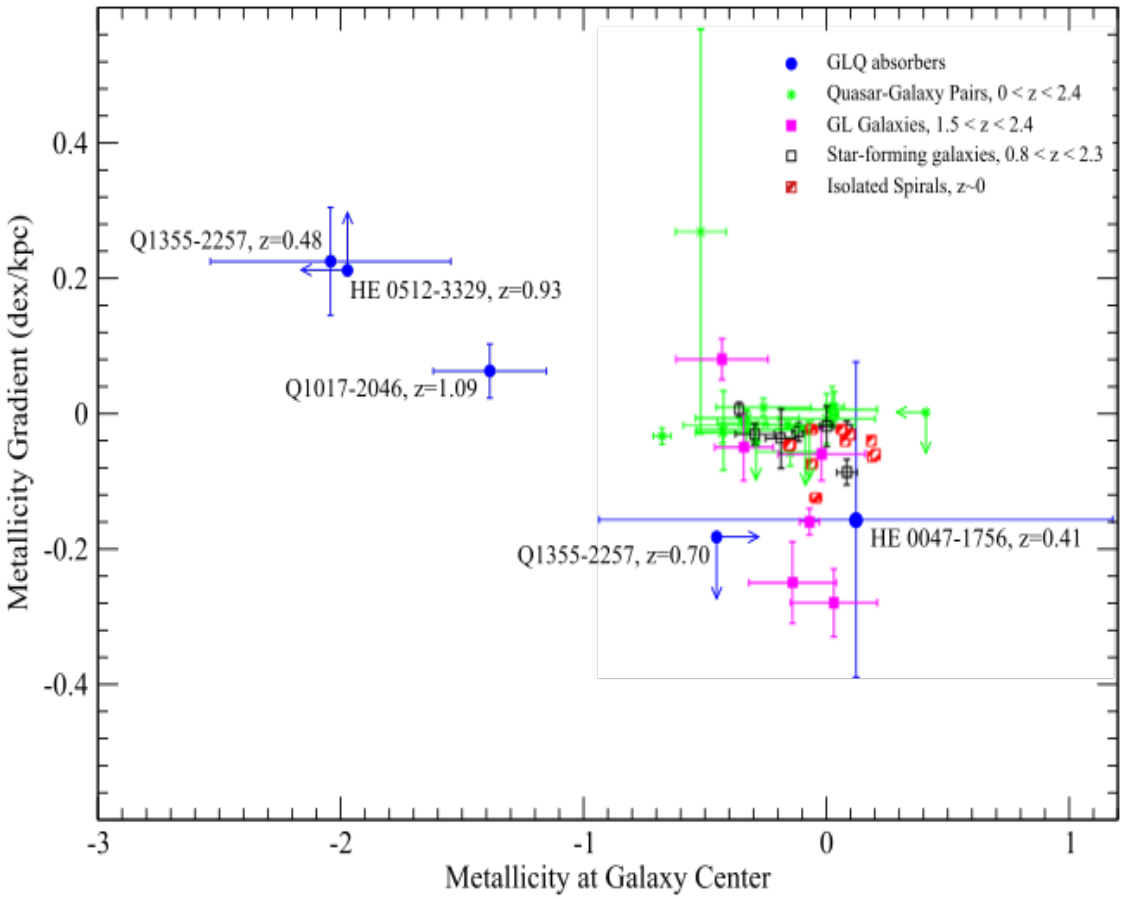

Figure 3.18 Metal abundance gradient in dex/kpc vs. abundance at the galaxy center for the GLQ absorbers with metal information, compared with measurements for quasar-galaxy pairs studied with integral field spectroscopy or long-slit spectroscopy, and with other measurements from the literature. The blue circles show the GLQ results for [Fe/H] in absorbers at lens redshifts. The green stars show [O/H] measurements from integral field spectroscopy or long-slit spectroscopy of quasar-galaxy pairs. The magenta squares show [O/H] values for arcs in gravitationally lensed galaxies. The black unfilled squares show [O/H] measurements for star-forming galaxies at $0.8 < z < 2.3$, and the red hatched squares show measurements for isolated spiral galaxies at $z \sim 0$. (See text for further details.)

are based on [N II]/Hα flux ratios and the calibration of Pettini & Pagel (2004; hereafter PP04). The measurement of Schulte-Ladbeck et al. 2004) is also based on [N II]/Hα, but uses the calibration of Denicolo et al. (2002; hereafter D02). The measurements from Chen et al. (2005), Straka et al. (2016), some from Rahmani et al. (2016), and Péroux et al. (2017) are based on the R_{23} index using the calibrations from Kobulnicky et al. (1999), who stated the 12 + log (O/H) vs. R_{23} relation of

Zaritsky et al. (1994; hereafter Z94) and parameterized the relation for 12 + log (O/H) as a function of R_{23} and log([O III]/[O II]) given in McGaugh et al. (1991; hereafter M91). The measurements from Fynbo et al. (2011, 2013) and Péroux et al. (2014) were based on the R_{23} index using the calibration from Kobulnicky & Kewley (2004; hereafter KK04).

Given that the different nebular line indices and/or calibrations can give significantly different metallicities, the prescriptions of Kewley & Ellison (2008) were used to convert the measurements based on D02, Z94, M91, and KK04 to the [N II]/Hα calibration of PP04 for consistency with the values from Péroux et al. (2012), Krogager et al. (2013), Kacprzak et al. (2014), and Rahmani et al. (2016). The emission-line metallicity values from Péroux et al. (2012) were adjusted slightly to account for the slightly different solar abundance of O adopted by us [12 + log $(O/H)_{\odot} = 8.69$ from Asplund et al. (2009), as opposed to 8.66 from Asplund et al. (2004) adopted by Péroux et al. (2012)]. For each QGP, the abundance gradient was estimated by comparing the central emission-line abundance thus derived to that in the absorber along the sight line to the background quasar. The uncertainties in the abundance gradients were calculated including the uncertainties in the re-calibrated emission-line metallicities, and the uncertainties in the absorption-line metallicities, but they do not include uncertainties in the impact parameters of the quasar sight lines relative to the galaxy centers, or the uncertainties in the fitting parameters for the relations converting the above-mentioned calibrations to the PP04 calibration from Kewley & Ellison (2008), since these uncertainties are not available.

Some of the QGP measurements show positive abundance gradients, although the majority of the QGP values appear to be nearly zero or negative. The magenta squares in Figure 3.18 show measurements from emission-line spectroscopy of arcs in gravitationally lensed galaxies at $1.5 < z < 2.4$ (Yuan et al. 2011; Jones et al. 2013, 2015). The remaining symbols show examples of other measurements from the liter-

ature: the black unfilled squares show the measurements for star-forming galaxies at $0.8 < z < 2.3$ from Swinbank et al. (2012), and the red hatched squares show measurements for isolated spiral galaxies at $z \sim 0$ from Rupke et al. (2010). The Rupke et al. (2010) measurements were based on the [N II]/[O II] diagnostic from Kewley & Dopita (2002), and were converted to the [N II]/Hα diagnostic with the PP04 calibration using the prescription in Kewley & Ellison (2008). The metallicity values from Swinbank et al. (2012) were based on [N II]/Hα with the PP04 calibration; so no corrections were needed for those.

The GLQ points (based on Fe/H) lie at systematically lower abundances than the QGP points (based on O/H), but this is likely an effect of depletion of Fe on dust grains, with possibly some contribution from α-enhancement of O relative to Fe. If the [Fe/H] values for GLQs were corrected for these effects, they would move to the right in Figure 3.18. As mentioned earlier, correction for dust depletion would also make the gradients steeper. For example, measurements of Si (an element less depleted than Fe) are available for both sight lines for one of our GLQs (Q1017-2046), and would give an estimated central Si abundance [Si/H] of -0.82 $\pm$ 0.36 dex and an abundance gradient of +0.167 $\pm$ 0.063 dex kpc^{-1}.

There may be an anti-correlation between the central abundance and the abundance gradient in the combined sample. The Spearman rank-order correlation coefficient for all the points plotted in Figure 3.18, treating the limits as detections, is $r_S = -0.379$, which is $\sim 3\sigma$ significant (a 1-tailed probability of 0.0039 of this correlation occurring purely by chance), if the lens redshift for Q1355-2257 is taken to be 0.48 rather than 0.70. This trend is consistent with a weak anti-correlation found by Queyrel et al. (2012) between the gradient and the global galaxy metallicity, and with the anti-correlation found by Belfiore et al. (2017) between the gradient and stellar mass (which in turn is correlated with the central metallicity). Indeed, the GLQ measurements extend to lower central metallicities a similar trend reported by

Jones et al. 2013 (see their Figure 8). If the lens redshift for Q1355-2257 is 0.70 rather than 0.48, the significance of the correlation becomes weaker (r_S = -0.279, with a 1-tailed probability of 0.0274 of this occurring purely by chance). Larger GLQ and QGP samples are needed to further assess the reality of such a trend. If such a trend exists, it could be caused by the infall of metal-poor intergalactic gas into the centers of the galaxies (e.g., Cresci et al. 2010; Queyrel et al. 2012), or due to central dilution resulting from mergers (e.g., Scudder et al. 2012; Ellison et al. 2013; Thorp et al. 2019). Of course, as mentioned earlier, our GLQ abundance gradient estimates are based on only 2 sight lines per galaxy, and are subject to assumptions about symmetry, dust depletion, etc., and also limited by the uncertainties in the lens galaxy redshifts and in the measurements of column densities. Despite these caveats and the small size of the GLQ sample, our findings demonstrate the potential for GLQs to offer constraints on metallicity gradients in distant galaxies. These constraints, if confirmed with larger samples (including GLQs with more than two lensed images), and with results from other techniques, may offer new insights into evolutionary processes such as gas accretion, star formation, and chemical enrichment in galaxies.

3.5.7 Masses of the Lensing Galaxies

One benefit of targeting gravitationally lensed galaxies is that analysis of the images of the background lensed object allows determination of the mass distribution in the lens. For early-type galaxies, the mass distribution is often assumed to be that of a singular isothermal sphere (SIS), given by $\rho \propto r^{-2}$ (e.g., Koopmans et al. 2009). In other words, the lens matter is assumed to behave as an ideal gas in thermal and hydrostatic equilibrium that is confined by a spherically symmetric gravitational potential. For the case of a galaxy lensing a quasar, the velocity dispersion of an SIS that would produce the observed quasar image separation $\Delta\theta$ is given by σ^2_{SIS} =

$c^2 D_{\rm q} \Delta\theta/(8\pi D_{\rm lq})$, where $D_{\rm q}$ and $D_{\rm lq}$ denote the angular diameter distances between the observer and the quasar, and between the lens and the quasar, respectively. For the lens galaxies toward Q1017-2046, Q1054+2733, Q1349+1227, and Q1355-2257, we estimate velocity dispersions of 190, 167, 318, and 194 km s^{-1}, respectively (which are comparable to the velocity dispersion of 192 km s^{-1} estimated for HE 0512-3329 by Wucknitz et al. 2003). These relatively large values support that lensing arises in early-type galaxies. The imaging of the lens galaxies reveals a Sersic index of 3.7 (Q1054+2733) and 1.7 (Q1349+1227; Kayo et al. 2010).

The mass of the lensing galaxy can be estimated from the astrometry of the quasar images relative to the lens galaxy, as $M = -c^2 \Delta\theta_{\rm AG} \Delta\theta_{\rm BG} D_{\rm q} D_{\rm l}/(4G D_{\rm lq})$, where $\Delta\theta_{\rm AG}$ and $\Delta\theta_{\rm BG}$ (which have opposite signs) are the angular separations of quasar images A and B from the lens (e.g., Schneider et al. 1992). For the lens redshifts adopted by us (including $z = 0.48$ for the Q1355-2257 lens), given the observed angular separations of the quasar images from the lens galaxies, we estimate masses log $(M/M_{\odot})$ of 10.80, 10.84, 10.82 and 11.02, respectively, for the lenses toward Q1017-2046, Q1355-2257, HE 0512-3329, and HE 0047-1756. The value for Q1355-2257 is consistent with the estimate of $5.0 \times 10^{10} M_{\odot}$ within the Einstein radius obtained by Morgan et al. (2003) assuming a lens redshift of $z = 0.55$. If the redshift of the lens toward Q1355-2257 is taken to be 0.70 instead of 0.48, the corresponding lens mass would be log $(M/M_{\odot})$ = 11.07. The estimate for HE 0512-3329 is consistent with the estimate of the mass enclosed within the Einstein radius of $M_{\rm E} = 6.8 \times 10^{10} M_{\odot}$ (Wucknitz et al. 2003). Finally, we note that the estimates of the masses of the lensing galaxies are subject to uncertainties in the redshifts of the lensing galaxies.

3.5.8 Constraining the Mass-Metallicity Relation for Lensing Galaxies

Measurements of metal abundances in the lens galaxy (from spectroscopy of the background quasar) along with the mass of the lens galaxy (from astrometry of the

lensed images) can, in principle, offer a powerful technique to constrain the mass-metallicity relation (MZR) for the lens galaxies. While the standard ways of estimating the MZR rely on stellar mass, the lensing galaxies allow determinations of the total mass.

Figure 3.20 shows a plot of [Fe/H] vs. the mass of the lens galaxy. Panel (a) shows the mean of the [Fe/H] values along the two sight lines, while panel (b) shows the [Fe/H] estimated to be at the galaxy center based on the measurements at the two sight lines, assuming a uniform gradient. The GLQ data points are the measurements for Q1017-2046, Q1355-2257, HE 0512-3329, and HE 0047-1756[3]. For Q1355-2257, we show both the possibilities for the lens redshift ($z = 0.48$ and $z = 0.70$). For comparison, the green stars in panel b show the dynamical masses (inferred from the maximum gas velocities) and emission-line metallicities (assumed to be the galaxy central metallicities) for absorber galaxies in quasar-galaxy pairs observed with integral field spectroscopy or long-slit spectroscopy (adopted from Chengalur & Kanekar 2002; Schulte-Ladbeck et al. 2004; Chen et al. 2005; Péroux et al. 2011b, 2012, 2014, 2016, 2017, Bouché et al. 2013, 2016; Fynbo et al. 2011, 2013; Krogager et al. 2013; Rahmani et al. 2016). The magenta squares in panel b show the corresponding measurements for gravitationally lensed galaxies at $1.5 < z < 2.4$ (Yuan et al. 2011; Jones et al. 2013). Despite the small number of measurements, it is interesting to compare the data with the metallicity vs. total mass relation for early-type galaxies. To this end, we show the dynamical mass vs. stellar metallicity relation for early-type SDSS galaxies from Galazzi et al. (2006), as a violet dashed curve in both panels of Figure 3.20. Also, for comparison, we show as an orange dashed-dotted curve the expected metallicity vs. total mass relation obtained by using the stellar mass to total (dynamical) mass relation for early-type galaxies $\log M_* = (0.93 \pm 0.02) \log$

[3]Using an SIS model would change the GLQ absorber points in Figures 3.20(a,b) minimally (by 0.01-0.17 dex in $\log M/M_\odot$) and would not change any of our conclusions.

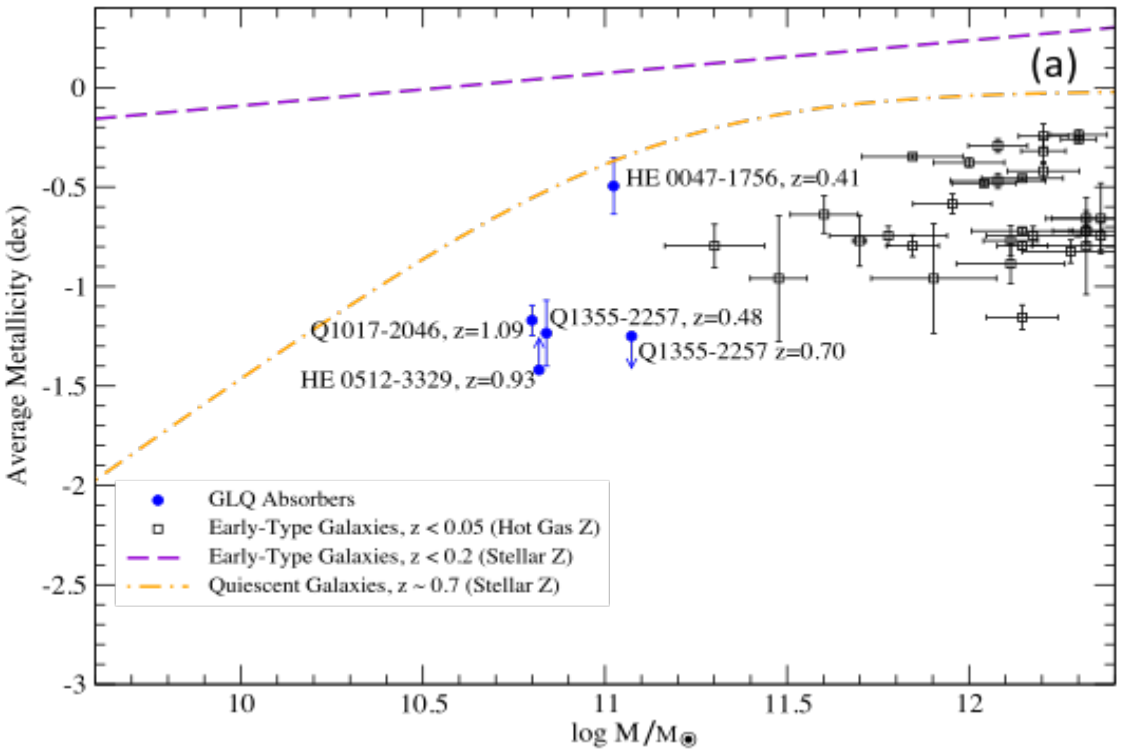

Figure 3.19 Mass-metallicity relation for GLQ absorbers compared with other measurements and/or expected trends. The blue circles show the measurements for GLQ absorbers at the lens redshift. GLQ data points show the mean Fe abundance of the two sight lines. For Q1355-2257, both possibilities for the lens galaxy redshift are shown. Black squares show the measurements for early-type galaxies at z<0.05 based on X-ray observations of hot gas. For reference, the total mass vs. stellar metallicity relations are shown for early-type galaxies at $z < 0.2$ (violet dashed curve), and for quiescent galaxies at $z \approx 0.7$ (orange dotted-dashed curve).

$M_{\rm dyn} + (0.09 \pm 0.20)$ from Ouellette et al. (2017), and the polynomial fit to the stellar mass vs. stellar metallicity relation for quiescent galaxies at $z = 0.7$ from Galazzi et al. (2014). The black squares show the measurements for individual early-type galaxies at $z < 0.05$ from X-ray measurements for hot gas (Babyk et al. 2018).

The measurements for QGPs and gravitationally lensed galaxies in Figure 3.20(b) lie relatively close to the expected trend for early-type galaxies. However, the GLQ points lie below the trend. Of course, the gas-phase measurements for GLQ absorbers could, in principle, differ from the stellar measurements; but it is interesting that the GLQ absorber measurements are lower than the gas-phase measurements for

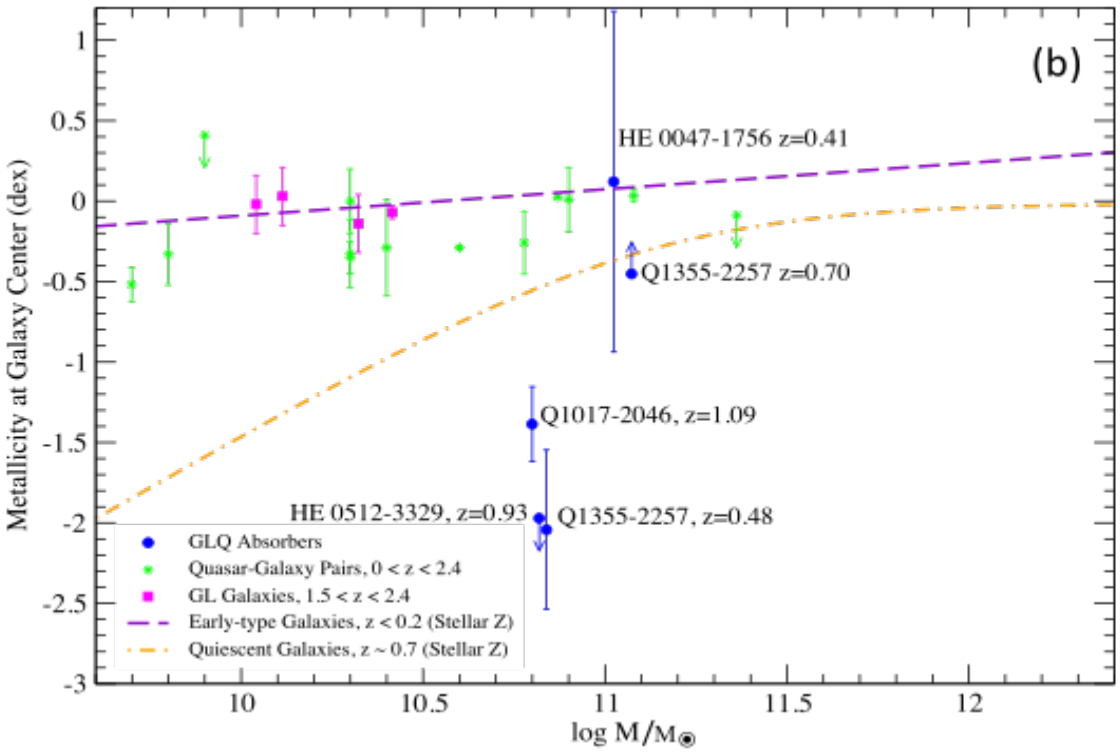

Figure 3.20 Mass-metallicity relation for GLQ absorbers compared with other measurements and/or expected trends. The blue circles show the measurements for GLQ absorbers at the lens redshift. GLQ data points in panel show the Fe abundance inferred to be at the galaxy center. For Q1355-2257, both possibilities for the lens galaxy redshift are shown. Green stars and magenta squares in panel show [O/H] measurements from emission-line spectroscopy for quasar-galaxy pairs at $0 < z < 2.4$, and for arcs in gravitationally lensed galaxies at $1.5 < z < 2.4$, respectively (see text for further details). For reference, the total mass vs. stellar metallicity relations are shown for early-type galaxies at $z < 0.2$ (violet dashed curve), and for quiescent galaxies at $z \approx 0.7$ (orange dotted-dashed curve).

QGPs and gravitationally lensed galaxies as well. One possible reason is that Fe is depleted onto dust grains, so [Fe/H] is lower than [O/H]. In the Milky Way, Fe is depleted on interstellar dust grains by > 1 to > 2 orders of magnitude in environments ranging from warm ISM to cool ISM (e.g., Savage & Sembach 1996; Jenkins 2009). Furthermore, O may be enhanced relative to Fe due to α-enhancement. Both of these effects together could substantially lower [Fe/H] compared to the true metallicity. Unfortunately, absorption-line measurements of elements that do not deplete much on interstellar dust grains (e.g., O, S, Zn) are currently not available for the lens

galaxy absorbers toward any of the GLQs. As mentioned earlier, measurements of Si (which is more depleted than O, S, Zn, but less depleted than Fe) are available for both sight lines for one of our GLQs (Q1017-2046). These measurements give an estimated central [Si/H] of -0.82 ± 0.36 dex and a mean [Si/H] of -0.24 ± 0.12 dex, which would put that galaxy somewhat closer to the expected trend for early-type galaxies. Some Fe depletion (possibly $\sim$ 0.5-0.6 dex) has also been suggested for HE 0047-1756 by Zahedy et al. (2017). It is thus plausible that, after correction for dust depletion and α-enhancement, the MZR for lens galaxies may be consistent with the expected trend for early-type galaxies and with the other measurements.

As seen in Figures 3.20(a) and 3.20(b), three of the observed lens galaxies have quite similar inferred masses (within 0.04 dex if the lens toward Q1355-2257 is at $z = 0.48$). The average [Fe/H] values for these systems differ by about 0.2 dex, but are consistent within the uncertainties. The differences are larger among the [Fe/H] values inferred for the galaxy centers, but so are the uncertainties in those values. These large uncertainties can be traced in part to the linear extrapolation made from the observed abundances for the two sight lines to the galaxy centers assuming a uniform gradient. (This effect is especially large when the impact parameters for the two sight lines are relatively close, e.g. for HE 0047-1756.) Additionally, the dispersion seen among the observed values in both panels could also be an effect of different levels of dust depletion and/or α-enhancement among the observed lens galaxies. Measurements of element abundances (especially for undepleted elements such as S, O, Zn) in many more GLQ (and QGP) absorbers based on high S/N spectra are essential to obtain tighter constraints on the mass-metallicity relation in absorption-selected galaxies.

Table 3.26 Absorbers with H I and/or Fe II Column Density Measurements toward GLQs

GLQ Sight Lines	z_{qso}	z_{lens}	z_{abs}	$l_{A,B,a}$ (kpc)	Δ log $N_{H\ I}$ (cm^{-2})	Δ log $N_{Fe\ II}$ (cm^{-2})	Δ[Fe/H]/Δr (cm^{-2})	[Fe/H]$_0$ (dex kpc^{-1})	Ref.[1]
Q1017-2046A,B	2.545	1.085	1.085	6.93	-0.08± 0.15	-0.32 ± 0.03	0.063± 0.040	-1.386±0.233	1
Q1355-2257A,B	1.373	0.48	0.48	7.28	0.62 ± 0.32	-0.29± 0.06	0.220± 0.080	-2.042± 0.495	1
Q1355-2257A,B	1.373	0.70	0.70	8.73	0.92± 0.32	> 1.82	< -0.182	> -0.452	1
Q0047-1756A,B	1.676	0.408	0.408	7.83	-0.1 ± 0.27	0.09 ± 0.082	-0.157 ± 0.233	0.121 ± 1.059	2
Q0512-3329A,B	1.587	0.933	0.933	5.07	-0.02 ± 0.11	> 0.18	> 0.217	< -1.972	3
Q1054+2733A,B	1.452	0.23	0.6794	1.87	< 0.58	NA	NA	NA	1
Q1349+1227A,B	1.722	0.645	1.2366	5.84	0.47 ± 0.05	NA	NA	NA	1
H1413+117A,B	2.551	1.0	1.44	3.17	0.82 ± 0.23	NA	NA	NA	4
H1413+117A,C	2.551	1.0	1.44	3.60	-1.65 ± 0.19	NA	NA	NA	4
H1413+117A,D	2.551	1.0	1.44	4.57	-1.55 ± 0.19	NA	NA	NA	4
H1413+117B,C	2.551	1.0	1.44	5.62	-2.48 ± 0.23	NA	NA	NA	4
H1413+117B,D	2.551	1.0	1.44	3.97	-2.38 ± 0.23	NA	NA	NA	4
H1413+117C,D	2.551	1.0	1.44	3.77	0.10 ± 0.19	NA	NA	NA	4
H1413+117A,B	2.551	1.0	1.66	2.19	0.60 ± 0.19	NA	NA	NA	4
H1413+117A,C	2.551	1.0	1.66	2.49	-0.40 ± 0.19	NA	NA	NA	4
H1413+117A,D	2.551	1.0	1.66	3.16	-0.70 ± 0.19	NA	NA	NA	4
H1413+117B,C	2.551	1.0	1.66	3.88	-1.00 ± 0.19	NA	NA	NA	4
H1413+117B,D	2.551	1.0	1.66	2.74	-1.30 ± 0.19	NA	NA	NA	4
H1413+117C,D	2.551	1.0	1.66	2.60	-0.30 ± 0.19	NA	NA	NA	4
Q0957+561A,B	1.414	0.36	1.391	0.37	-0.38 ± 0.13	-0.11 ± 0.019	NA	NA	5
Q1104-1805A,B	2.319	0.729	1.662	4.51	-3.28 ± 0.10	-2.30 ± 0.08	NA	NA	6
UM673A,B	2.743	0.493	1.626	2.72	< -2.6	NA	NA	NA	7
SDSS J1442+4055	2.590	0.284	1.946	0.69	0.07 ± 0.05	-0.13 ± 0.042	NA	NA	8

1. References: (1) Kulkarni et al. (2019) (2) Zahedy et al. (2017), (3) Lopez et al. (2005), (4) Monier et al. (2009), (5) Churchill et al. (2003), (6) Lopez et al. (1999), (7) Cooke et al. (2010), (8) Krogager et al. (2018).

Chapter 4

An in-depth Look at SBS 0909+532 AB

4.1 Introduction

Traditional quasar absorption line studies probe a single sight line through a galaxy, however, it is difficult to link the properties of an absorber to the galaxy host and surmise the galaxy's properties based on that single sight line. The use of gravitationally lensed quasars (GLQs) to probe foreground galaxies improves on the single sight line method as one has multiple sight lines to characterize the absorption regions of the galaxy. Using multiple sight lines has the advantage of studying variations in gas, dust, and structure to offer a unique transverse study of a galaxy. Locally, multiple sight lines have been successfully implemented to probe the ISM of the Milky Way (MW) and other nearby galaxies. Lauroesch et al. (2000) and Andrews et al. (2001) revealed turbulence-driven astronomical unit-scale variations in cold neutral gas structures traced by low column density Na I absorption lines along closely spaced stellar sight lines. Similarly, closely spaced sight lines toward GLQs can distinguish small-scale structure in the ISM of a lens galaxy. Additionally, any absorbers that exist between the lens and the background quasar are magnified by lensing, potentially revealing parsec to kiloparsec-scale structure depending on the location of the absorber.

Absorption line studies of lenses are not as common as non-lens absorbers due to the fact that most lenses lie at a redshift $z \lesssim 1$ and determining metallicities requires measurement of the H I column density, which requires UV spectroscopy (as does any

absorption line system with $z < 1.6$). Even though the opportunity to study lenses in the UV is rare due to limited access to instrumentation, it is a task worth pursuing, as analysis of GLQ images permit not only the determination of galaxy mass, but also abundance gradients within the galaxy. This is noteworthy as some lenses have shown positive or inverted gradients, i.e., gradients opposite to what is seen in the MW and other nearby galaxies (refer back to section 3.5.2).

Negative gradients can be understood as a result of "inside-out" evolution, in which the inner parts of galaxies form before and evolve faster than the outer parts (e.g., Ellison et al. 2018). A significant fraction of galaxies show shallow or flat gradients (e.g. Sánchez et al. 2014), and some high-redshift galaxies show positive gradients (e.g. Cresci et al. 2010; Queyrel et al. 2012; Troncoso et al. 2014). Even at $z \sim 0.02$ and $0.08 < z < 0.84$, ∼8-10% of galaxies show positive gradients (e.g., Pérez-Montero et al. 2016; Carton et al. 2018). Recent EAGLE simulations of disk galaxies at $z = 0$ find that a large fraction ($\approx 40\%$) of galaxies have positive gradients, and that these galaxies have significant star formation ∼1.5 Gyr before similar-M_* galaxies with negative gradients (Tissera et al. 2018). Positive gradients can be produced by inflows of metal-poor gas in central parts of galaxies, which can dilute their central metallicity, or by outflows of metal-rich gas that leave the central parts less metal rich than the outer parts, especially if the outflowing metal-rich gas falls back on the outer parts (e.g., Cresci et al. 2010; Troncoso et al. 2014). Infall of metal-poor gas, mergers, and/or outflows can also cause the anti-correlation between the gradient and metallicity or M_* that has been reported in several studies (e.g., Queyrel et al. 2012; Jones et al. 2013; Belfiore et al. 2017).

Previous lens galaxy imaging surveys suggest that the majority of lens galaxies are passively evolving normal early-type galaxies e.g., Keeton et al. 1998; Zahedy et al. 2016). Keeton et al. (1998) describes that lens galaxies are a biased sample, typically very massive galaxies, as massive galaxies are more likely to lens background objects.

This mass bias favors early-type galaxies, with late-type spiral galaxies expected to comprise only $10 - 20\%$ of all gravitational lenses. It has also been reported that approximately a third of nearby early-type ellipticals are not gas-poor, but contain large amounts of H I gas, despite being quiescent (e.g., recent 21 cm surveys by Grossi et al. 2009; Oosterloo et al. 2010; Serra et al. 2012; Young et al. 2014). Additionally, there are QSO absorption line studies of luminous red galaxies in which Mg II $\lambda\lambda$2796, 2803 has been detected at distances $\gtrsim$100 kpc (see Gauthier et al. 2010, 2009; Huang et al. 2016), suggesting that these halos are chemically enriched. This detection of enriched cool gas within passive galaxies raises questions as to what processes and mechanisms exist within the galaxy which keep the gas from cooling further and forming stars.

The mass bias in lensing studies can be advantageous, as studying variations within these lensing galaxies along sight lines to the multiple images can contribute significantly to what we know about the interstellar medium (ISM) of passively evolving elliptical galaxies. In a QSO absorption line study along multiple sight lines to three lensing galaxies, Zahedy et al. (2016) and Zahedy et al. (2017) reported that while the gas content varied amongst the lenses and within sight lines of the same lenses, supersolar [Fe/Mg] relative abundance patterns were observed in all sight lines which also had detections of cool gas. The high [Fe/Mg] ratios suggests a significant contribution from Type Ia supernovae (SNe Ia) to the chemical enrichment history of the inner ISM of these lenses. These observations support current theories that the presence of mature stellar populations could prevent further star formation from occurring in the reservoirs of chemically enriched cool gas due to a combination of injected energy from SNe Ia and winds from asymptotic giant branch stars (e.g., Conroy et al. 2015).

SBS 0909+532 is a well-studied doubly-imaged gravitationally lens system identified by Kochanek et al. (1997), who initially observed two images at $z_{QSO} = 1.377$

separated by 1.″1. Oscoz et al. (1997) were able to confirm the redshift of the source quasar, as well as the redshift of the reported Mg II absorption seen at $z = 0.83$. The lens redshift was later spectroscopically confirmed to be at $z = 0.8302 \pm 0.0001$ and the quasar's redshift was re-measured at $z = 1.3764 \pm 0.0003$ by Lubin et al. (2000), see Table 4.1.

Table 4.1 Physical characteristics of SBS 0909+532 AB

z_{QSO}	z_{lens}	Mag_A, Mag_B	$\Delta\theta_{AB}$ ($''$)	r_A (kpc)	r_B (kpc)	$l_{A,B}$ (kpc)
1.3764	0.8302	18.85, 15.65 (I)	1.17	3.154	5.744	8.4
$\pm$0.0003	$\pm$0.0001					

Lehár et al. (2000) conducted high angular resolution HST imaging and concluded that the lensing galaxy is, morphologically, a normal early-type galaxy with an extended dark matter halo with a large effective radius ($r_{eff} = 1.''58 \pm 0.''90$) and low surface brightness. Lubin et al. (2000) estimated the mass inside the Einstein ring to be 1.42×10^{11} $M_\odot$ h^{-1}. The core of the lens is observable in I-band imaging as a significant residual after the quasar images are subtracted, but it does not appear in the V-band. The local environment of the lensing galaxy consists of 3 nearby galaxies within ~200 kpc h^{-1}, 2 of which are within ~100 kpc h^{-1}.

The spectrum of the lens galaxy towards SBS 0909+532 shows an extinction curve produced by dust in the lens galaxy, the first optical extinction curve measurement at cosmological distances which matches the quality seen locally. However, there may be a unique link between the activity of a galaxy and the strength of the 2175 Å feature (Motta et al. 2002, Mediavilla et al. 2005) as passive galaxies are subjected to fewer shocks and processing by radiation, unlike the environments of starburst galaxies and AGNs.

What has been missing from the portrait of SBS 0909+532 is a description of the variation in metallicity and kinematic structure between the two sight line images. As many lens galaxies lie at $z < 1$, the hydrogen Lyman series lines fall in the UV portion

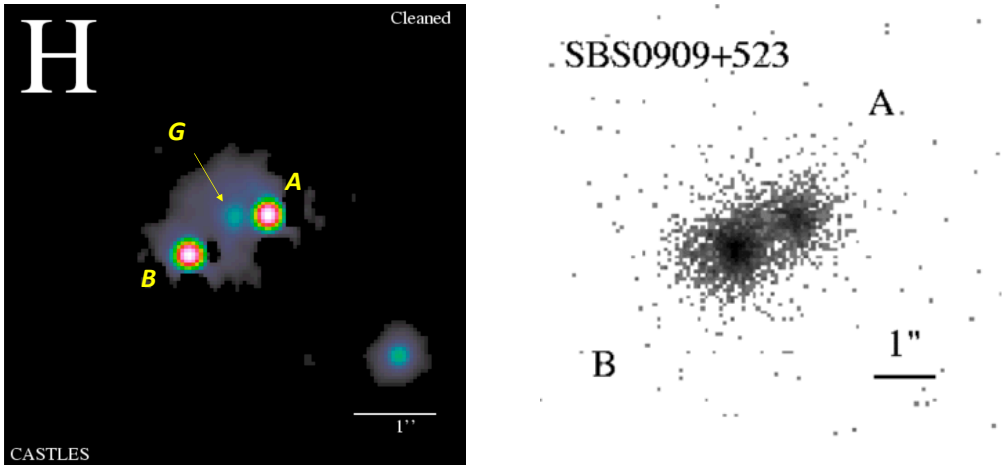

Figure 4.1 Left: HST image of SBS 0909+532 AB in the H-band from the CASTLeS Survey. The lensing galaxy is clearly visible in between the lensed images. Lehár et al. (2000) report an absorption-corrected optical flux ratio in the H-band of A/B = 1.12. Right: *Chandra* Observations of SBS 0909+523 AB from Dai & Kochanek (2009).

of the electromagnetic spectrum and are therefore only accessible to study with UV spectrographs onboard space-based telescopes. Therefore measurements of H I exist for only a handful of lenses, and this, in turn, means that metallicity measurements of lensing galaxies are also scarce. Thus our measurements provide a deeper probe into the environment of early-type lensing galaxies by providing multiple metallicity measurements at different impact parameters through the ISM of the lens galaxy. Only four other measurements of H I exist for lens galaxies (Q1017-2046 AB, Q1355-2257 AB, Kulkarni et al. 2019; Q0047-1756 AB, Zahedy et al. 2017; Q0512-3329 AB, Lopez et al. 2005; all lenses with redshift $0.48 < z < 1.1$) and three of the four lenses (Q1017-2046 AB, Q1355-2257 AB, Q0512-3329 AB) show a positive average metallicity gradient (or inverse gradient), where the metallicity is higher further from the center of the galaxy.

We used public archive *HST*-STIS UV absorption spectra and Keck HIRES optical spectra to study the unexplored difference in the chemical composition and kinematic structure of the lensing galaxy at $z = 0.83$ towards the double GLQ SBS 0909+532.

We report significant H I and metal column density differences at projected distances from the lens galaxy's center of $r_{\rm A} = 3.15$ and $r_{\rm B} = 5.74$ kpc on opposite sides of the lens in the inner ISM. We see much heavier H I and metal absorption in image B than in image A. We discuss the observed $N_{\rm Fe\,II}/N_{\rm Mg\,II}$ relative abundance pattern in SBS 0909+532 in comparison to the lenses Q1017-2046, Q1355-2257, Q0047-1756, and HE 0512-3329 from the literature. Furthermore, we report additional coincident Mg II absorption at a redshift of $z_{\rm abs} \sim 0.611$ along both lines of sight, see Table 4.2.

Table 4.2 Absorbers Along the Lines of Sight Towards SBS 0909+532

z	$W_{\rm A}^{2796}$ (Å)	$W_{\rm B}^{2796}$ (Å)	$l_{\rm A,B}$ (kpc)
0.611	0.15 ± 0.000675	0.35 ± 0.01	7.4
0.8302	0.09 ± 0.02	2.59 ± 0.52	8.4

This chapter is organized as follows. In section 4.2, we describe the archive observations and how the data were reduced. In section 4.3, we describe how the column density measurements and metallicities were determined for images A and B. In section 4.4, we show the results of our measurements. In section 4.5 we compare our results to similar studies from the literature. We adopt the cosmology $H_0 = 70$ km s^{-1} Mpc^{-1}, $\Omega_M = 0.3$, and $\Omega_\Lambda = 0.7$ throughout, unless specified otherwise.

4.2 Observations and Data Reduction

Spatially resolved spectra of SBS 0909+532 A and B were downloaded from the Keck Observatory archive. These data were obtained with the HIRES spectrograph on 1998 December 18 as part of program C140H (PI: W. Sargent). SBS 0909+532 was observed with *HST*-STIS (Space Telescope Imaging Spectrograph) on 2003 March 7 in both the optical and the UV using the CCD detector and the G430L and G230LB gratings with STIS during Cycle 11 as part of program GO-9380 (PI: E. Mediavilla). Details of these observations are found in Mediavilla et al. (2005).

4.2.1 *Keck* HIRES Observations and Data Reduction

Five 2700 s exposures were taken of image A and twelve 3000 s exposures were taken of image B. The extracted 1-dimensional spectra were binned in the spectral direction by two, and continuum-normalized spectra were produced using the `linetools` by fitting a spline function to the continuum of each quasar image. The wavelength coverage was ∼4300-6300 Å. The 1-dimensional spectra were inspected for gaps in data in the regions of interest and the spectra which had continuous data in the regions of interest were then co-added for each image.

4.2.2 *Hubble Space Telescope* STIS Observations and Data Reduction

The H I column density is needed to measure the gas metallicity. The lens galaxy at $z \sim 0.83$ results in the hydrogen Lyα line being redshifted to λ ∼2224.7 Å, which appears in the G230LB data. The reduced 2-dimensional G230LB data were examined to determine the locations of the traces of the two resolved quasar images, and were further processed using `IRAF` STSDAS X1D to extract the 1-dimensional spectra. Background subtraction, charge transfer efficiency correction, conversion to heliocentric wavelengths, and absolute flux calibration were also performed during the X1D task. The average wavelength dispersion was 1.37 Å per pixel, the average resolution was $\sim$ 500 km s^{-1}, and the S/N ratio per pixel is ∼30 in image A and ∼16 in image B in the regions of interest. As the flux levels between the exposures were consistent, the three exposures of A were combined with equal weighting. During the combination of exposures, gaps in spectral coverage due to bad pixels were recovered by replacing the pixel with the average flux value from the other two frames. The same procedure was performed for image B. The combined exposures of A and B were then continuum normalized using `linetools` by fitting a spline function in featureless spectral regions.

4.3 Absorption Line and Column Density Measurements

Where possible, two methods were used to measure column densities: the apparent optical depth (AOD) method (Savage & Sembach 1996) using the program `SPECP`[1] and Voigt profile fitting using `VPFIT` version 11.1. The atomic data utilized by `VPFIT` and `SPECP` were adopted from the compilations of Cashman et al. (2017) and Morton (2003) Atomic information on the specific transitions included in the fits is included in the notes under Table 4.3.

4.3.1 STIS H I Measurements

The only H I Lyman series line that could be used for estimating column densities was the H I Lyα line. Unfortunately, in both images the shorter wavelength Lyman series lines are either in regions of extreme noise or are severely blended with features at different redshifts (Lyα forest lines at lower redshifts and Milky Way interstellar medium lines). Although the column densities are unconstrained without higher order Lyman series lines (possibly within orders of magnitude), we determine values for log $N_{\rm H\,I}$ and emphasize that observations of SBS 0909+532 AB at higher resolution in the UV could remedy this situation. The column densities of the H I Lyα line for A and B were measured independently based on single component fits to the Lyα using `VPFIT`. The methods to obtain their H I column densities are described below.

4.3.2 SBS 0909+532 A

We find low H I absorption near $z_{\rm lens} = 0.83$ in the spectrum of SBS 0909+532 A. As can be seen in Figure 4.3, the H I Lyα feature spans a velocity range from ~ -600 to $+600$ km s^{-1}, and although it is broad and saturated, at this resolution it does not appear to be damped. Since in the saturated regime the value of $N_{\rm H\,I}$ depends sensitively on the b-value, we determine an upper limit to $N_{\rm H\,I}$ by considering a series

[1] `SPECP` was developed by D. Welty and J. Lauroesch.

of pair values of b and $N_{\rm H\,I}$, as described by Cooke et al. (2010), and find the lowest value of b (and thus highest value for $N_{\rm H\,I}$) for which the theoretical line profile shows the best fit to the data. This is done by fixing $N_{\rm H\,I}$ and allowing only b to vary using `VPFIT`. We began with $N_{\rm H\,I} = 20.38$ cm^{-2} (the measured column density for SBS 0909+532 B) and $b = 30$ km s^{-1} (the initial guess from the interactive program `RDGEN`[2]), and decreased $N_{\rm H\,I}$ in steps of 0.1 dex until we found a profile that showed the least disagreement with the data, which occurred for log $N_{\rm H\,I} = 18.18$ cm^{-2} and $b = 53.72$ km s^{-1}. As comparable fits can be achieved with higher values of b and lower values of $N_{\rm H\,I}$, we consider log $\rm N_{H\,I} \leq 18.18$ cm^{-2} to be an upper limit. The profile is shown in the top panel of Figure 4.2.

4.3.3 SBS 0909+532 B

There is significantly more H I absorption observed in sight line B than in sight line A. Given the low resolution of the G230LB data and the broad Lyα feature (see the bottom panel of Figure 4.2 and the right two panels in Figure 4.3) both the z and b-value for the single H I component was fixed to the redshift and b-value of the dominant metal line component observed in the high-resolution HIRES spectra and only log $N_{\rm H\,I}$ was allowed to vary using `VPFIT`.

Executing a χ^2 minimization analysis to determine damped and sub-damped H I column densities and uncertainties has historically given rise to unrealistically low uncertainties (see Prochaska et al. 2003b). Therefore, we created a series of Lyα profiles varying in steps of $\pm$0.1 dex from the resulting Voigt profile fit described in the paragraph above. Comparisons between the profiles were made for the wings and core of the component. For image B, it was determined that a $\pm$0.20 dex range from the Voigt profile fit of log $N_{\rm H\,I} = 20.38$ cm^{-2} gave the most consistency between the fitted profile and the flux within a 2σ buffer. Furthermore, to increase confidence

[2]See more about RDGEN at https://www.ast.cam.ac.uk/~rfc/

in the adopted log $N_{\rm H\,I}$ and its uncertainty, given the lower signal-to-noise and apparently damped nature of the absorption seen along the sight line to image B, we utilized a different technique (originally described by Rao & Turnshek 2000) to examine the possibility that additional uncertainty may have also arisen from subjective continuum placement. Our original "most likely" normalized continuum was shifted above and below by an offset per pixel from the 1σ error array of the flux data. Each offset spectrum was then renormalized and a Voigt profile was fitted again to the H I Lyα feature. The $+1\sigma$ continuum resulted in a column density log $N_{\rm H\,I} = 20.11\pm0.20$ cm^{-2}. The -1σ continuum resulted in a column density log $N_{\rm H\,I} = 20.55\pm0.25$ cm^{-2}. As the mean value of these high and low log $N_{\rm H\,I}$ values of 20.38 ± 0.33 cm^{-2} is within the range of the value determined from the initial fit, we chose to retain the initial log $N_{\rm H\,I}$ value of 20.38 cm^{-2} and the conservative ±0.20 dex uncertainty (see Table 4.4). The resulting profile is shown in the bottom panel of Figure 4.2.

The low resolution and signal-to-noise of the STIS spectra are such that column densities of metal species cannot be measured, as their absorption lines are only a few km s^{-1} wide, as shown in the multiple components of the Mg II and Fe II lines detected in the corresponding HIRES data (see Figure 4.4 and 4.5). Other potentially existing UV metals lines at the redshift of the lens are shown in Figure 4.3, however, obtaining higher resolution UV spectra is necessary to confirm the identity of these metal lines and to measure their column densities. Higher-resolution observations of the Fe II and Mg II lines would allow us to determine more accurate Mg and Fe abundances. Observations of other metal ions at high resolution would permit more accurate determinations of the ionization corrections using ion ratios besides the only ratio available to us (Mg II/Mg I). Measurements of the undepleted elements S and O would provide more robust determinations of the metallicity, and ion ratios such as Si II/S II or Si II/O I would allow improved dust depletion determinations.

Table 4.3 Component column densities in the $z_{\rm lens} = 0.83$ galaxy towards SBS 0909+532 A

z	b_{eff} km s^{-1}	log $N^a_{\rm H\,I}$ (cm^{-2})	log $N^b_{\rm Mg\,I}$ (cm^{-2})	log $N^c_{\rm Mg\,II}$ (cm^{-2})	log $N^d_{\rm Fe\,II}$ (cm^{-2})
0.830129±0.000005	6.20±1.11	$\leq$ 18.18	$\leq$ 10.59^e	11.90±0.04	12.08±0.04
0.830238±0.000004	6.81±1.01	...	...	12.00±0.04	12.06±0.07
0.830390±0.000006	3.75±2.02	...	...	11.58±0.09	11.88±0.09

(a) H I λ1215.6701: f-value = 0.4164, Palćhikov (1998)
(b) Mg I λ2852.964: f = 1.71, Froese Fischer et al. (2006)
(c) Mg II $\lambda\lambda$2796.352, 2803.531: f_{2796} = 0.613, f_{2803} = 0.306, Froese Fischer et al. (2006)
(d) Fe II $\lambda\lambda$2600.172, 2382.764, 2374.460: f_{2600} = 0.239, f_{2382} = 0.320, f_{2374} = 0.0313, Bergeson et al. (1996); Fe II λ2586.649: f_{2586} = 0.0717, Fuhr & Wiese (2006)
(e) There is a non-detection of Mg I λ2852, thus we calculated the 3σ upper limit to the column density from the 3σ observed frame equivalent width upper limit.

Table 4.4 Component column densities in the $z_{\rm lens} = 0.83$ galaxy towards SBS 0909+532 B

z	b_{eff} (km s^{-1})	log $N_{\rm H\,I}$ (cm^{-2})	log $N_{\rm Mg\,I}$ (cm^{-2})	log $N_{\rm Mg\,II}$ (cm^{-2})	log $N_{\rm Fe\,II}$ (cm^{-2})
0.82766±0.00001	11.14±1.04	...	11.27±0.21	12.47±0.03	12.45±0.06
0.82816±0.00001	10.61±0.46	...	11.55±0.11	12.90±0.02	12.89±0.03
0.82910±0.00001	28.14±0.52	...	12.12±0.05	13.64±0.01	13.71±0.01
0.83014±0.00001	21.67±0.61	...	12.05±0.05	13.57±0.02	13.38±0.02
0.83045±0.00002	19.02±0.92	...	12.15±0.04	13.67±0.03	13.67±0.02
0.83076±0.00001	16.31±0.50	20.38±0.20	12.84±0.03	14.14±0.03	14.29±0.02
0.83124±0.00002	16.18±1.81	...	11.27±0.22	12.51±0.04	12.43±0.08

4.3.4 *Keck* HIRES Metal Line Measurements

The only metal line transitions detected in the limited wavelength range of the available HIRES spectra were: Mg I λ2852; Mg II λ2796, 2803; and Fe II λ2374, 2382, 2586, 2600. Mg I λ2852 was not detected in image A, therefore we calculated the 3σ upper limit to the column density from the 3σ observed frame equivalent width upper limit assuming a linear curve of growth. We used `RDGEN` to select the velocity

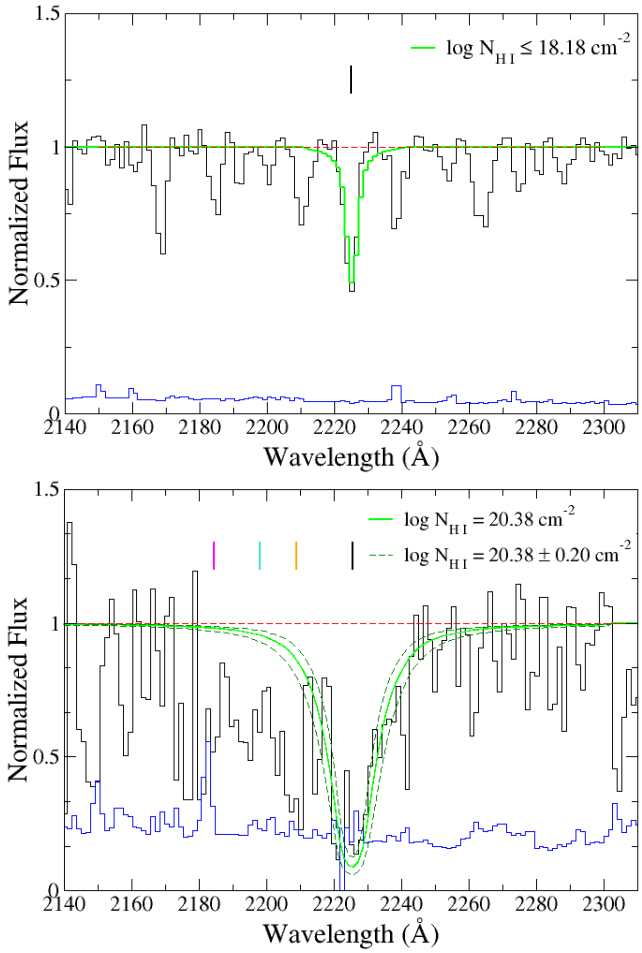

Figure 4.2 Plots of the H I Lyα line in the $z = 0.83$ lens galaxy in the *HST*-STIS spectrum of SBS 0909+532 AB in the same wavelength range for comparison. In each panel, the normalized data are shown in black, the dashed red line shows the continuum level, and the blue curve near the bottom shows the the 1σ error in the normalized flux. The solid green curve in each panel indicates the theoretical Voigt profile fit to the H I Lyα absorption feature. The thick black vertical dash indicates the position of the H I component that was used in the fit and for each fit it was fixed at the redshift of the dominant Fe II component identified in the corresponding HIRES spectrum (for image A, $z_{\rm H\,I,A} = 0.830129$; for B, $z_{\rm H\,I,B} = 0.830759$, see Tables 4.3 and 4.4). Left: The Voigt profile fit to the spectrum of SBS 0909+532 A showing the resulting upper limit to the column density with $b \approx 54$ km s^{-1}, see Section 4.3.2 for how this value was obtained. Right: The Voigt profile fit to the spectrum of SBS 0909+532 B. The dashed green curve above and below the fitted profile shows a ± 0.20 dex uncertainty in log $N_{\rm H\,I}$. The thick colored vertical dashes (magenta: Si II 1193 Å; cyan: N I 1200 Å; orange: Si III 1206 Å) indicate the positions (all at $z = 0.830759$) of metal lines that may be blended on the left wing of the H I feature at $z = 0.830759$.

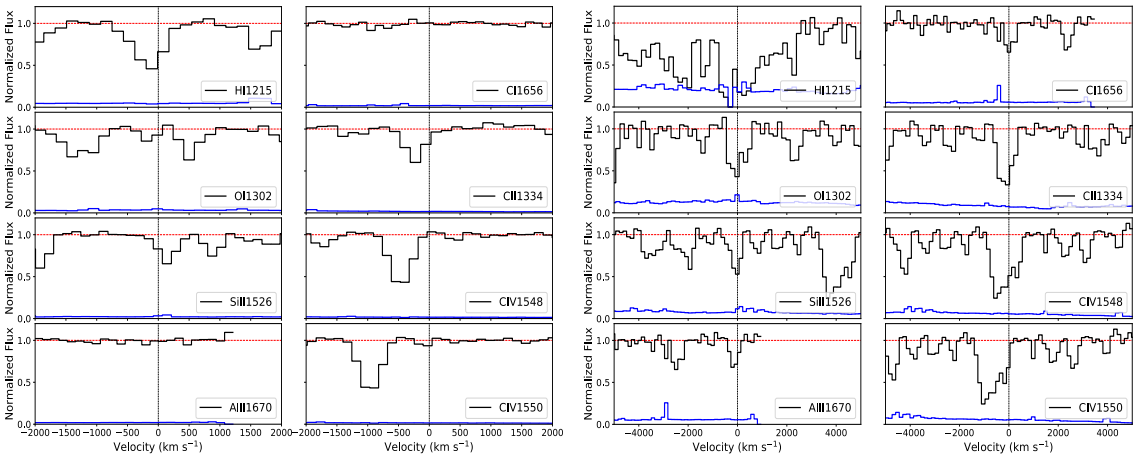

Figure 4.3 Velocity plots of potentially present metal lines compared with H I 1215 in STIS image B (right two panels) with the same lines for A (left two panels) included for comparison. There is no data at the red end of the panels for C I λ1656 and Al II λ1670 as this is the end of the available data from the STIS spectrum. Note that the C I or Al II transitions may not be present in image A.

ranges of the metal lines and to initially estimate their column densities. These resulting preliminary files were then input into `VPFIT` to determine the redshifts and b-values of the individual components. In image A, the absorbing region consists of 3 very weak components that span a total velocity range of $\sim$66 km s^{-1}, whereas the absorbing region in image B was fit with 7 components spanning a total velocity range of $\sim$650 km s^{-1}. For ions where multiple lines were detected, they were fit together to help constrain the ionic column densities. The redshifts and b-values were also tied together for ions of similar ionization stage. The total column densities for the individual ions are computed by adding all their constituent velocity components together. The results for these individual components can be seen in Tables 4.3 and 4.4 and fits to the profiles can be seen in Figures 4.4 and 4.5. The total column densities, as well as the comparable AOD measurements (for the detected lines) can be seen in Table 4.7.

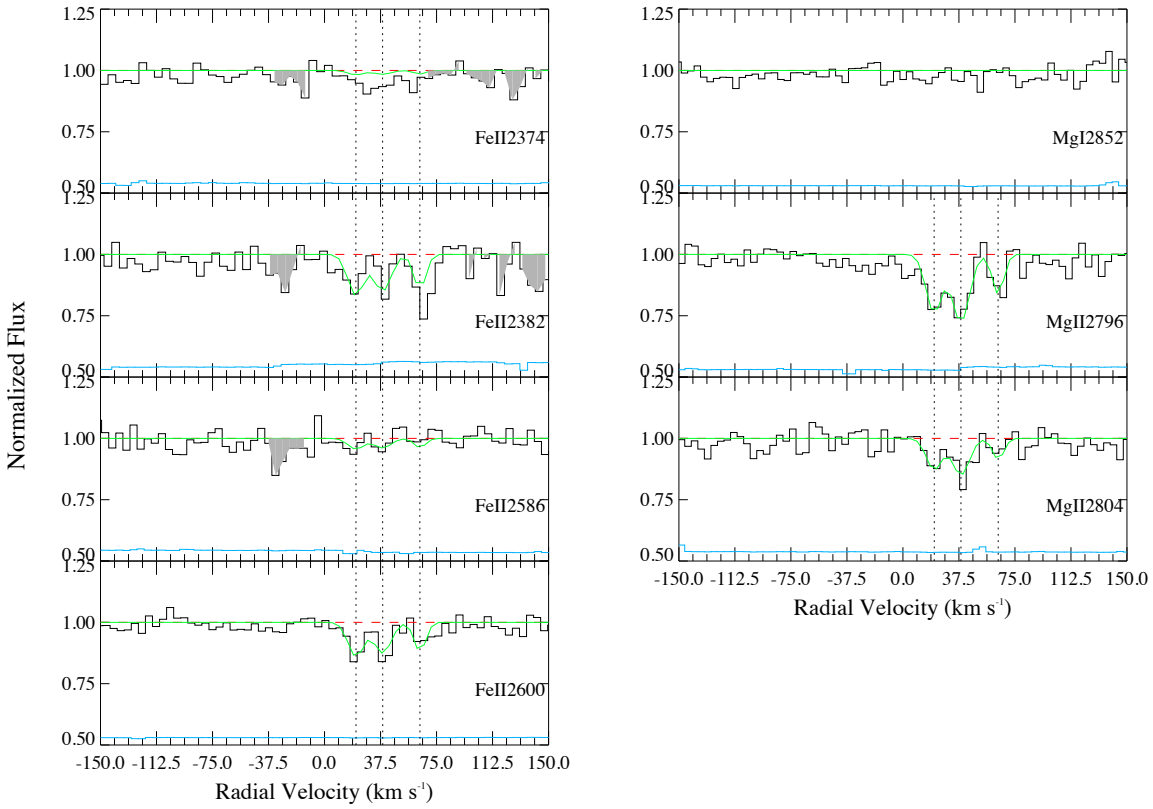

Figure 4.4 Velocity plots for the metal lines in the $z \sim 0.83$ lensing galaxy in the HIRES spectrum of SBS 0909+532 A. In each panel, the normalized data are shown in black, the solid green curve indicates the theoretical Voigt profile fit to the absorption features, and the dashed red line shows the continuum level. The 1σ error values in the normalized flux are represented by the blue curves near the bottom of each panel. The vertical dotted lines indicate the positions of the components that were used in the fit. Shaded regions indicate absorption unrelated to the presented line. As these lines show weaker absorption, the normalized flux scales are shown starting at 0.5 and the 1σ error arrays are offset by 0.5, so that they can be viewed in the same panels. Note that Mg I λ2852 was not detected in image A, but is included to facilitate comparison with its strong detection in image B, as shown in Figure 4.5.

4.4 Results

The redshifts, b-values, and column densities of each image's H I and metal line absorption components are summarized in Tables 4.3 and 4.4. The total column densities, calculated abundances, and overall average abundance gradients are summarized in Table 4.7. Following common practice, the abundances of each element

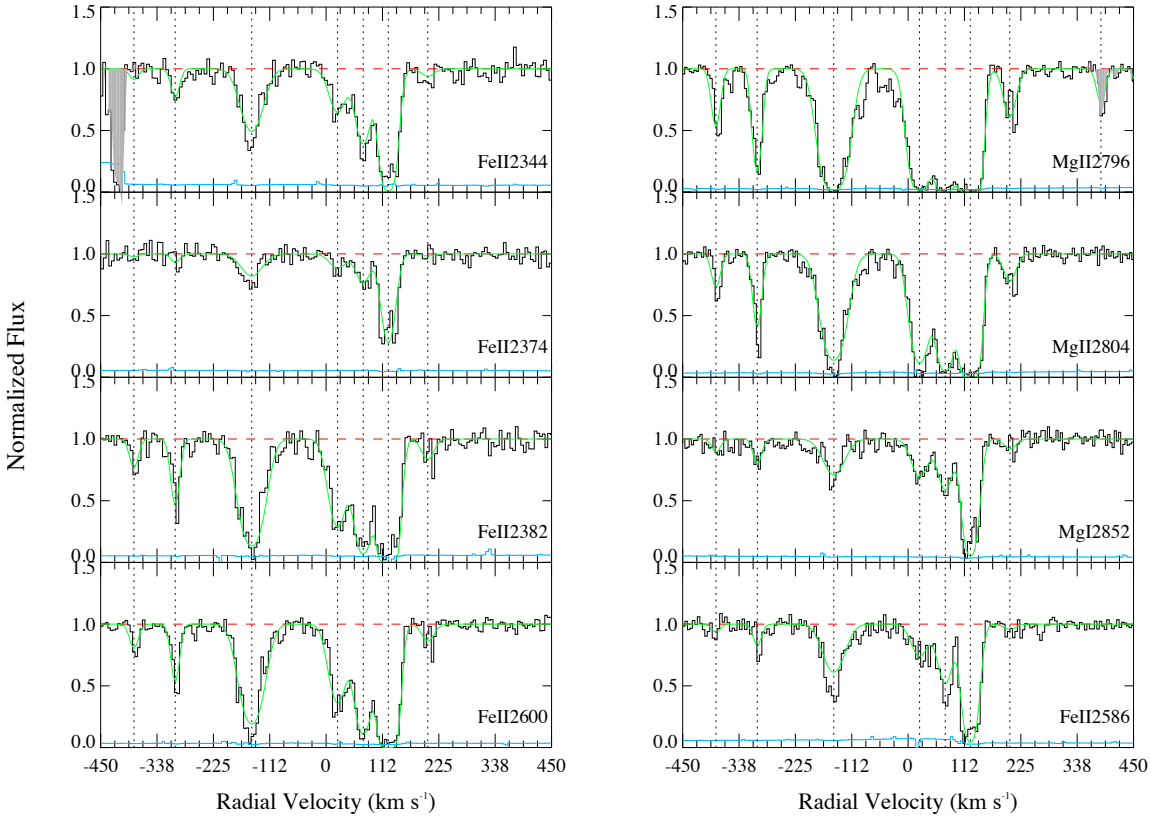

Figure 4.5 Velocity plots for the metal lines in the $z \sim 0.83$ lens galaxy in the HIRES spectrum of SBS 0909+532 B. Same as for Figure 4.4 but for SBS 0909+532 B.

X are defined as $[X/\mathrm{H}] = \log\,(N_X/N_{\mathrm{H\,I}}) - \log\,(X/\mathrm{H})_\odot$. Element abundances in the solar photosphere from Asplund et al. (2009) were used in these calculations.

4.4.1 Variations in the H I Column Density Between the Sight Lines

For the $z_{\mathrm{lens}} = 0.83$ absorber toward SBS 0909+532 AB, the H I column density is significantly higher along sight line B, by a factor of at least 2.20 dex (∼158 times higher). This suggests that the sight lines are not probing a spatially coherent region. This difference is interesting for two reasons. First, the separation between the sight lines is small, 1.11″ or 8.9 kpc at the redshift of the lens. This means that structural differences exist within this normal elliptical galaxy on scales less than 8.9 kpc. Secondly, the impact parameters (r) for sight lines A and B are $r_{\mathrm{A}} = 3.15$ kpc

and $r_{\rm B} = 5.74$ kpc, thus sight line B is oriented 1.8 times further away from the center of the lensing galaxy than sight line A. Thus, more H I exists further from the center of the galaxy, which could suggest that the region probed by sight line A at ∼3 kpc from the center of the galaxy is highly ionized. SBS 0909+532 AB was observed on 2006 December 17 with the Advanced CCD Imaging Spectrometer on board *Chandra* by Dai & Kochanek (2009). Similarly to what we observe, Dai & Kochanek (2009) also saw much more absorption in image B than in image A and measured $\Delta\log N_{\rm H,B-A} = 20.74^{+0.44}_{-0.22}$ dex between the sight lines. We consider the impact of ionization effects on our measurements for sight line A in Section 4.4.3.

4.4.2 Element Abundances and Abundance Gradients

Similarly, we see significantly more metal absorption in sight line B than in A (see Figures 4.4 and 4.5). In the limited wavelength range of the available HIRES spectra, Mg I λ2582; Mg II $\lambda\lambda$2796,2803; and Fe II $\lambda\lambda$2374,2382,2600 were detected in image B, while all the same lines were detected in image A except Mg I λ2582. In this case, the 3σ upper limit to the column density was calculated based on the 3σ observed frame equivalent width upper limit.

The metallicities were calculated for each sight line and are shown in Tables 4.3 and 4.4. The average abundance gradient is calculated from the difference in Fe abundances measured in the lensed images and the difference in the impact parameters as measured from the center of the lensing galaxy, i.e.,

$$\Delta[\mathrm{Fe/H}]/\Delta r = ([\mathrm{Fe/H}]_{\rm B} - [\mathrm{Fe/H}]_{\rm A})/(r_{\rm B} - r_{\rm A}). \quad (4.1)$$

This calculation shows how the abundance between the images would change per unit distance if the lens were considered to be uniform. Although Fe depletes readily on to dust grains, we use [Fe/H] to characterize the average abundance gradient because measurements of [Fe/H] exist for other lenses for comparison. Table 4.7 (presented at the end of the chapter) shows these results. For the upper limit $\log N_{\rm H\,I,A} \leq 18.18$

cm^{-2}, the resulting [Fe/H]$_{\rm A}$ is a lower limit and must be greater than or equal to -1.18 dex (or $\sim$3/50 Z$_\odot$), which constrains the average abundance gradient to be less than -0.07 dex kpc^{-1} between the two sight lines. Although this gradient is slightly higher than the range of metallicity gradients observed in the Milky Way and nearby galaxies, it is consistent with the upper end of this range.

4.4.3 Ionization Effects

The metallicities determined in each sight line were calculated assuming that the ion stages Fe II and Mg II, which are dominant in H I regions, can represent the total column density of that element in the LLS (sight line A) and the DLA (sight line B). This is likely a safe assumption in the case of the DLA, where the H I is expected to be self-shielding against photons capable of ionizing it ($h\nu > 13.6$ eV). However, the lower $N_{\rm H\,I}$ detected in sight line A could be an indication that the environment is highly ionized, therefore we investigate to what extent our results may be affected by ionization of the absorbing gas. Unfortunately, no higher ions have confirmed detections in either sight line.

We ran a suite of `CLOUDY` photoionization models using version 17.01 (Ferland et al. 2017) to determine the extent of ionization effects in both sight lines. We used the approximation that the absorption regions are plane-parallel slabs and included the cosmic microwave background at the redshift of the absorber and the extragalactic UV background from Khaire & Srianand (2019) at the redshift of the lens (KS18 in `CLOUDY`) as the radiation fields. Additionally, we included a cosmic ray background. The neutral hydrogen column densities were fixed to the estimated values measured from the STIS spectra listed in Table 4.7. The gas metallicities were fixed to the values obtained for Fe from the HIRES spectra ($\rm Z_{A,LLS} = 3/50\ Z_\odot$ and $\rm Z_{B,DLA} = 1/25\ Z_\odot$ for sight line A and sight line B respectively). The constraints on the number density $\log n_{\rm H}$ and the ionization parameter $\log U$ were estimated by comparing the value of

the only observed column density ratio of adjacent ions available, log ($N_{\rm Mg\,II}/N_{\rm Mg\,I}$), with the ratio calculated from the model over a range of hydrogen number densities from 10^{-3} to 10^{3} cm^{-3} (see Figure 4.6). The model estimates log $n_{\rm H}$ ≤ -2.59 cm^{-3} and log $U \geq -2.7$ and for sight line A and log $n_{\rm H} = 0.90$ cm^{-3} and log $U = -6$ for sight line B. We then estimate the Fe abundance of the gas by correcting the observed column density ratio by the predicted relative ionization fraction for the estimated log $n_{\rm H}$, i.e., log (Fe/H) = log ($N_{\rm Fe\,II}/N_{\rm H\,I}$) − log ($f_{\rm Fe^+}/f_{\rm H^0}$). If the relative ionization fraction is ~ 0, then the gas metallicity can be approximated directly from log ($N_{\rm Fe\,II}/N_{\rm H\,I}$), where then [Fe/H] $\approx$ log ($N_{\rm Fe\,II}/N_{\rm H\,I}$)− log (Fe/H)$_\odot$.

In sight line B, we obtain a relative ionization fraction correction between Fe^+ and H^0 of ($f_{\rm Fe^+}/f_{\rm H^0}$) ≈ 1, therefore we can estimate [Fe/H] directly from log ($N_{\rm Fe\,II}/N_{\rm H\,I}$) and we estimate [Fe/H] $= -1.36 \pm 0.20$. Dividing the observed log $N_{\rm H\,I}$ by the model value of log $n_{\rm H} = 0.9$ cm^{-3}, we estimate that the DLA absorbing region is ∼9.8 pc along the line of sight. In sight line A, we obtain log ($f_{\rm Fe^+}/f_{\rm H^0}$) = 0.15. After correcting log ($N_{\rm Fe\,II}/N_{\rm H\,I}$) by this amount, we adopt a new lower limit of [Fe/H] ≥ -1.33. This corrected metallicity results in a slightly higher upper limit gradient ≤ -0.02 dex kpc^{-1}. Interestingly, if we perform the gradient calculation with the corrected metallicity for A and the lower limit value of log $N_{\rm H\,I} = 20.18$ cm^{-2} is used, then the gradient has a positive upper limit ≤ 0.07 dex kpc^{-1}. Based on the model value of log $n_{\rm H}$ ≤ -2.59 cm^{-3} and the upper limit on the observed log $N_{\rm H\,I}$, we estimate that the LLS absorbing region is at most 0.2 kpc along the line of sight.

We note that these models are based on H I column densities derived from low resolution spectra as well as metal column densities of refractory elements. Higher resolution UV spectra would not only provide more robust H I column densities, but could potentially provide additional adjacent ion ratios to better constrain log $n_{\rm H}$ and the ionization fraction corrections. However, even with a model based on log $N_{\rm H\,I}$ from low resolution spectra, the results are consistent with the findings from the

Table 4.5 Results of Voigt Profile Fitting for Ions in the $z_{\rm abs} = 0.6116$ Mg II absorber along the sight line toward SBS 0909+532 A

z	$b_{\rm eff}$ (km s^{-1})	log $N^{a}_{\rm Mg\ I}$	log $N^{b}_{\rm Mg\ II}$
0.611367±0.000007	18.57±1.89	...	12.26±0.02
0.611601±0.000006	17.04±1.48	...	12.27±0.02
0.611845±0.000004	6.19±1.26	10.91±0.18	11.77±0.05
Total log $N_{\rm X,fit}$		10.91±0.18	12.63±0.01
Total log $N_{\rm X,AOD}$		...	12.59±0.04

(a) Mg I λ2852.964
(b) Mg II $\lambda\lambda$2796.352, 2803.531

photoionization studies of absorption line systems in QSO spectra from Bergeron & Stasińska (1986). They found that absence of Mg II in low log $N_{\rm H\ I}$ systems (< 17 cm^{-2}) only occurred for log $U > -2.82$ and log $n_{\rm H} < -1.96$, which is consistent with the results we see with the low upper limit on Mg II detected in absorption region in the LLS in sight line A.

4.4.4 An Mg II absorber at $z_{\rm abs} \approx 0.611$

While examining the HIRES spectrum of SBS 0909+532 AB for metal lines at the redshift of the lens, we found an Mg II absorption system in both sight lines with the dominant Mg II component at a redshift of $z_{\rm abs,A} = 0.6116$ and $z_{\rm abs,B} = 0.6114$. No other metal lines were detected at these redshifts. We then examined the STIS spectrum for corresponding H I absorption, however, none was seen due to extremely high noise at the blue end. We measure the Mg I, Mg II column densities using both `VPFIT`, and the AOD method where possible. The resulting Voigt profile fits are shown in Figure 4.7. The column densities for the individual components and the total column densities are listed in Tables 4.5 and 4.6.

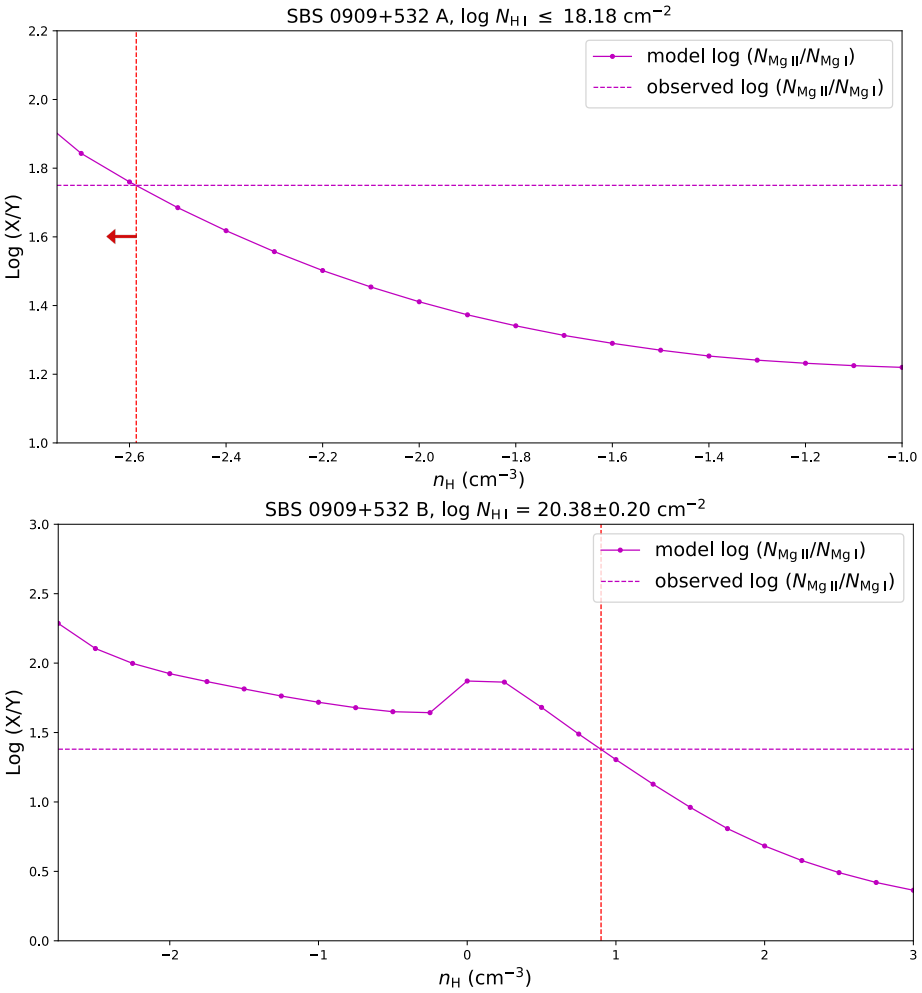

Figure 4.6 Estimated number densities for the two sight lines towards SBS 0909+532 AB using `CLOUDY` version 17.01. Top: Comparison of model log ($N_{\rm Mg\,II}/N_{\rm Mg\,I}$) over a range of log $n_{\rm H}$ values and the observed lower limit of log ($N_{\rm Mg\,II}/N_{\rm Mg\,I}$) $\geq$ 1.75 for the LLS (log $N_{\rm H\,I} \leq 18.18$ cm^{-2}) observed in the sight line to the lensed image SBS SBS 0909+532 A. We estimate log $n_{\rm H} \leq -2.59$ cm^{-3} and log $U \geq -2.7$. Bottom: Comparison of model log ($N_{\rm Mg\,II}/N_{\rm Mg\,I}$) over a range of log $n_{\rm H}$ values and the observed log ($N_{\rm Mg\,II}/N_{\rm Mg\,I}$) = 1.38 for the DLA (log $N_{\rm H\,I} = 20.38 \pm 0.20$ cm^{-2}) at $z = 0.83$ in the sight line to the lensed image SBS 0909+532 B. We estimate log $n_{\rm H} = 0.90$ cm^{-3} and log $U = -6$.

4.5 Discussion

Measurements of $N_{\rm H\,I}$, and therefore measurements of metallicities, have been performed for only four other lenses (Q1017-207AB, Q1355-2257 AB, Kulkarni et al. 2019; HE 0047-1756 AB, Zahedy et al. 2017; HE 0512-3329 AB, Lopez et al. 2005)

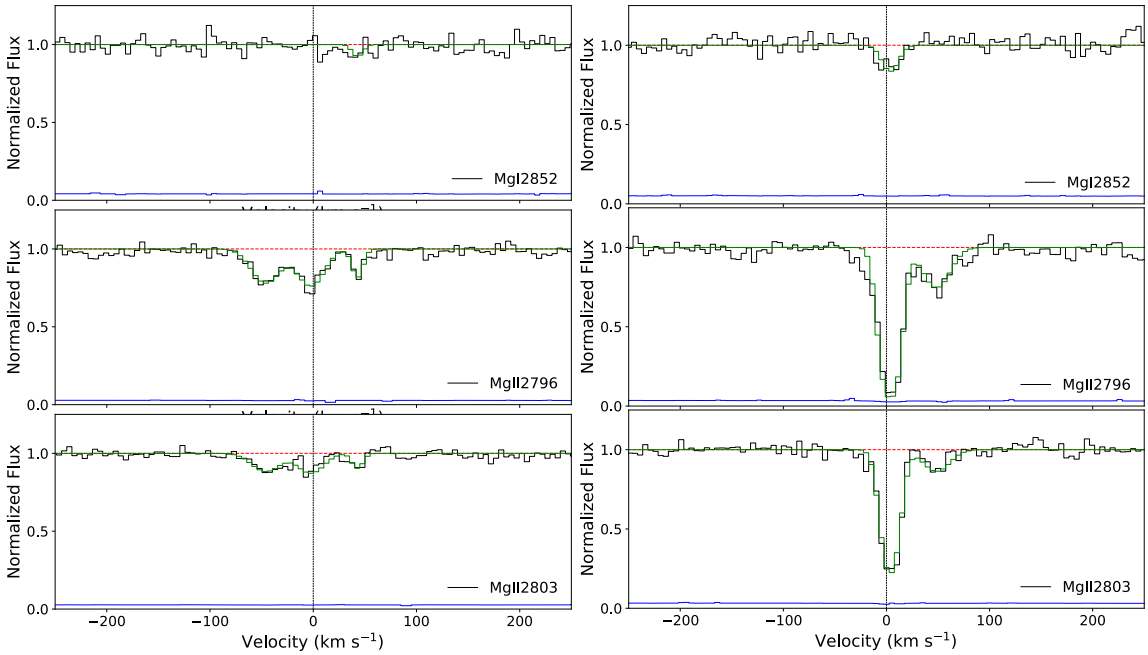

Figure 4.7 Voigt profile fits of the Mg II absorber detected at $z = 0.6116$ toward SBS 0909+532 A (left) and $z = 0.6114$ toward SBS 0909+532 B (right). In each panel, the normalized data are shown in black, the solid green curve indicates the theoretical Voigt profile fit to the absorption features, and the dashed red line shows the continuum level. The 1σ error values in the normalized flux are represented by the blue curves near the bottom of each panel.

Table 4.6 Results of Voigt Profile Fitting for Ions in the $z_{\rm abs} = 0.6114$ Mg II absorber along the sight line toward SBS 0909+532 B

z	$b_{\rm eff}$ (km s^{-1})	log $N^{a}_{\rm Mg\ I}$	log $N^{b}_{\rm Mg\ II}$
0.611433±0.000001	10.44±0.25	11.44±0.09	13.13±0.01
0.611675±0.000005	17.24±1.51	...	12.31±0.02
Total log $N_{\rm X,fit}$		11.44±0.09	13.19±0.01
Total log $N_{\rm X,AOD}$		11.61±0.08	13.18±0.02

(a) Mg I λ2852.964
(b) Mg II $\lambda\lambda$2796.352, 2803.531

along multiple sight lines through the lensing galaxy. Thus the measurements for the lens at $z = 0.83$ towards the two sight lines toward SBS 0909+532 AB adds important information to this small sample.

4.5.1 H I Absorption in Lenses

As SBS 0909+532 is a normal early-type galaxy, it is interesting that large differences in H I and metal column density are observed at such small impact parameters on either side of the galaxy. Sight line A, with an impact parameter $r_{\rm A} = 3.15$ kpc from the lensing galaxy, shows significantly less neutral hydrogen absorption than sight line B at an impact parameter $r_{\rm B} = 5.74$ kpc from the galaxy. The difference between log $N_{\rm H\,I,A} \leq 18.18$ cm^{-2} and log $N_{\rm H\,I,B} = 20.38 \pm 0.20$ cm^{-2} of at least 2.20 dex shows that the column density of neutral hydrogen drops by a factor of $\sim$160 over a transverse distance of 8.9 kpc. To compare the physical extent of the H I absorption and the scale over which it varies, we compute the fractional difference in log $N_{\rm H\,I}$ measured at the redshift of the lens along both lines of sight, (log $N_{\rm H\,I,X}$ − log $N_{\rm H\,I,Y}$)/log $N_{\rm H\,I,X}$, where sight line X has stronger H I absorption out of the two, and compare this difference to other lenses in Figure 4.8. In fact, SBS 0909+532 AB shows the largest fractional difference in $N_{\rm H\,I} \geq 0.99$ difference between log $N_{\rm H\,I,B}$ and log $N_{\rm H\,I,A}$) for the small sample of lenses for which measurements of $N_{\rm H\,I}$ exist. Three lenses show stronger spatial coherence with a fractional difference in log $N_{\rm H\,I} \leq 0.20$. The bars on the points show the maximum and minimum possible fractional difference given the range of uncertainty in log $N_{\rm H\,I}$. While such a large difference in H I absorption looks uncommon for albeit a small sample of lenses, it may not be uncommon amongst other non-lens absorbers. The orange diamonds in Figure 4.8 are measurements of the fractional difference between $N_{\rm H\,I}$ between sight lines of quasar absorption line systems (LLS, sub-DLAs, and DLAs) along the lines of sight to gravitationally lensed quasars, but are not the lenses themselves (see Kulkarni et al. 2019 for details on these absorption systems). The large range of possible fractional differences underscores the need for higher UV resolution spectra of these GLQs.

As mentioned in Section 4.4.1, Dai & Kochanek (2009) measured the differential X-ray absorption of the lensing galaxy at $z = 0.83$ in their effort to study the evolution

of the dust-to-gas ratio and also reported heavier $N_{\rm H}$ in image B than in image A with $\Delta\log N_{\rm H,B\text{-}A} = 20.74^{+0.44}_{-0.22}$. Hydrogen seen in ellipticals comes in multiple forms, predominately as X-ray emitting hot gas, perhaps from supernovae and stellar winds (e.g., Loewenstein et al. 1998, Mathews & Brighenti 2003, Pipino & Matteucci 2011). A large presence of hot hydrogen supports the idea that mature stellar populations could be what prevents reservoirs of chemically enriched cool gas from collapsing into furthering star formation in elliptical galaxies, due to a combination of injected energy from SNe Ia and winds from asymptotic giant branch stars. SBS 0909+532 also happens to reside in a group environment, with 3 nearby galaxies, 2 of which are within ∼100 kpc, that likely contribute tidal effects (Lehár et al. 2000). Thus we cannot rule out that past interactions between group members could have heated or tidally stripped cool gas from the inner regions of SBS 0909+532. As there is a large differential in both the presence of neutral gas and the amount of mass seen between images A and B given the small impact parameters on either side of the galaxy, it is possible that the galaxy's evolutionary history includes a mixed merger (e. g., a wet-dry merger).

4.5.2 Metal Absorption in Lenses

The lack of coherence between the two sight lines separated by 8.9 kpc is clearly seen in the metal absorption lines of the HIRES high resolution spectra in Figures 4.4 and 4.5 as well. The available archive spectra only covers the wavelength range from ∼4300-6300 Å and at the redshift of the lens $z = 0.83$ the metal lines detected are: Fe II $\lambda\lambda$2374, 2382, 2586, 2600; Mg II $\lambda\lambda$2796, 2802; and Mg I $\lambda\lambda$2852 (only in sight line B).

We also calculated the fractional difference in Fe II for all lenses in the small sample that also have H I measurements. These calculations are displayed alongside the H I fractional differences in Figure 4.8. SBS 0909+532 AB also shows the highest

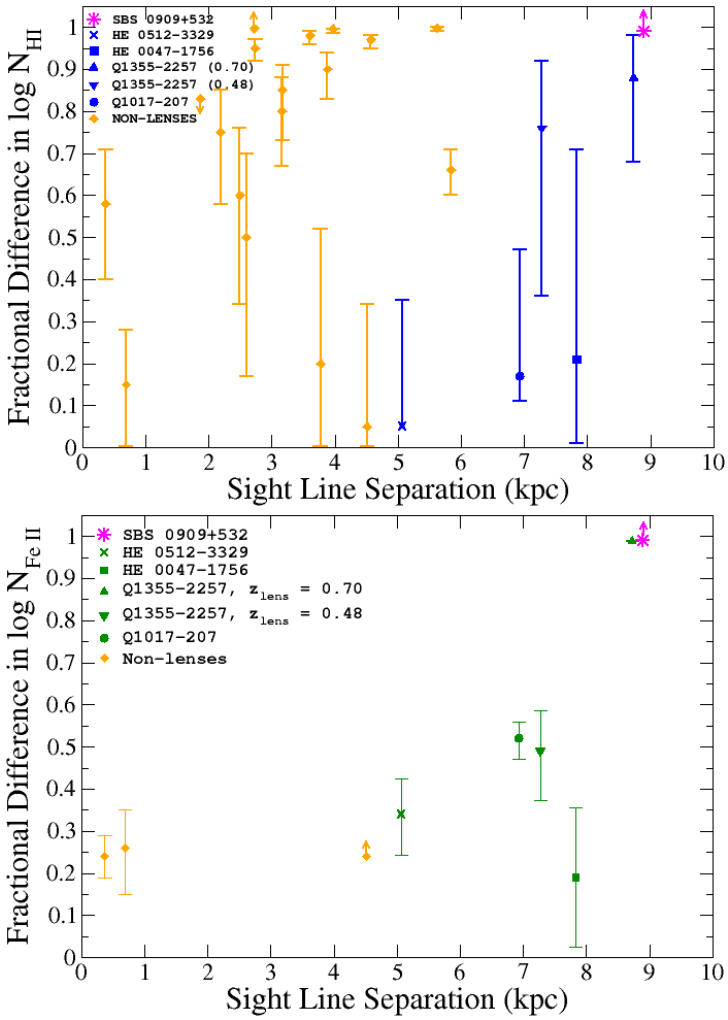

Figure 4.8 The fractional difference in log $N_{\rm H\,I}$ (top, in blue) and log $N_{\rm Fe\,II}$ (bottom, in green) for SBS 0909+532 AB, calculated as (log $N_{\rm X}$ − log $N_{\rm Y}$)/log $N_{\rm X}$, where sight line X has stronger absorption of the two. The orange diamonds in both figures are quasar absorption line systems (LLS, sub-DLAs, and DLAs) along the lines of sight to gravitationally lensed quasars, but are not the lenses themselves (see Table 26 in Kulkarni et al. 2019 for details on these absorption systems). The blue shapes are lenses for which H I has been measured. SBS 0909+532 AB, represented with a star, shows the highest H I fractional difference between lens sight lines. Only four other lenses to date have measurement of H I in all sight lines, and thus have computed H I fractional differences, however five are shown in the figure, as Q1355-2257 has two candidates for the lens at $z_{\rm lens} = 0.48$ and 0.70. Regardless, the H I fractional uncertainty for either lens redshift measurement is in the close range of $0.74 - 0.76$, but differs significantly for Fe II. The bars on the points show the maximum and minimum fractional difference possible given the uncertainty in log $N_{\rm X}$.

fractional difference in Fe II between lens sight lines in the sample of lenses. In fact, if the galaxy along the line of sight to Q1355-2257 at $z = 0.70$ is not the lens, then SBS 0909+532 is the only lens in the sample to show a fractional difference in Fe II above $\sim$0.50.

Of course, a relative deficit of Fe II can also be affected by differences in dust depletion, given that Fe is strongly depleted even in the warm Milky Way ISM. We were unable to consider the potential effects due to dust depletion as no other metal lines were detected.

4.5.3 The Transverse Separation and Mass of the Lens Galaxy

The transverse separation between the GLQ images was calculated for the absorber at $z_{abs} = 0.611$ and the lens at $z_{lens} = 0.8302$. In a lensing geometry, for redshifts beyond the lens, the light paths of the lens images converge to the source, thus the separation between the GLQ images becomes smaller closer to the source. For an absorber with a redshift greater than or equal to the lens redshift, the transverse separation l_{AB} between the sight lines is calculated as

$$l_{\rm AB} = \frac{D_{\rm aq}(1+z_{\rm l})\Delta\theta_{\rm AB}D_{\rm l}}{D_{\rm lq}(1+z_{\rm a})}, \tag{4.2}$$

where $D_{\rm l}$, $D_{\rm lq}$, and $D_{\rm aq}$ are the angular diameter distances between the observer and the lens, the lens and the quasar, and the absorber and the quasar, respectively, and $\Delta\theta_{\rm AB}$ is the angular separation between quasar images A and B. In the case when the absorber is the lens itself, i.e., $z_l = z_a$ and $D_{aq} = D_{lq}$, and Equation 4.2 simplifies to $l_{\rm AB} = \Delta\theta_{\rm AB}D_{\rm l}$.

The angular diameter distances in Equation 4.2 are calculated using

$$D_{12} = \frac{c}{H_0(1+z_2)}\int_{z_1}^{z_2}[\Omega_\Lambda + \Omega_{\rm m}(1+z)^3]^{-1/2}\,dz, \tag{4.3}$$

following Hogg (1999).

In addition to the unique transverse study of the lens and other absorbers that GLQs provide, analysis of the lensed images provides an opportunity to determine the mass and the mass distribution of the lens. The mass distribution for an early-type galaxy is presumed to be that of a singular isothermal sphere (SIS) given by $\rho \propto r^{-2}$ (e.g., Koopman et al. 2009), in which the lens matter behaves as an ideal gas in thermal and hydrostatic equilibrium confined by a spherically symmetric gravitational potential. The velocity dispersion of an SIS of a galaxy lensing a quasar that produces the observed lensed image separation $\Delta\theta$ is

$$\sigma_{SIS}^2 = \frac{c^2 D_q \Delta\theta}{8\pi D_{lq}}, \tag{4.4}$$

where D_q and D_{lq} are the same angular diameter distances between the observer and the quasar and the lens and the quasar that were calculated from Equation 4.3. We estimate a velocity dispersion of 258 km s^{-1} for SBS 0909+532. This value is comparable to the velocity dispersion from Oscoz et al. (1997) of 272 km s^{-1}.

We estimate the mass of the lens galaxy from the astrometry of the lensed images relative to the lens itself using

$$M = -\frac{c^2 \Delta\theta_{AG} \Delta\theta_{BG} D_q D_l}{4G D_{lq}}, \tag{4.5}$$

where $\Delta\theta_{AG}$ and $\Delta\theta_{BG}$ (with opposite signs) are the angular separations of lensed images A and B from the lens (e.g., Schneider et al. 1992). Given the angular separations and our calculated angular diameter distances, we estimate log $(M/M_\odot)$ = 11.3. Our value for the mass of the lens of SBS 0909+532 agrees with the estimate of log $(M/M_\odot) = 11.3$ within the Einstein radius by Lubin et al. (2000) who assumed the same lens redshift.

4.5.4 [Fe/Mg] Abundance Patterns

As mentioned in at the beginning of Chapter 4, Zahedy et al. (2016) and Zahedy et al. (2017) investigated [Fe/Mg] ratios in 3 lens galaxies along sight lines where

cool gas was detected to look for possible contributions to the chemical enrichment history of the inner ISM of lenses from SNe Ia. Mg II absorption traces cool, photoionized gas of $T \sim 10^4$ K (Bergeron & Stasińska 1986). Current theories suggest that a combination of injected energy from SNe Ia and winds from asymptotic giant branch stars from mature stellar populations could be responsible for quenching star formation in the reservoirs of chemically enriched cool gas in passive galaxies. Zahedy et al. (2017) reported that while the gas content varied amongst the lenses and within sight lines of the same lenses, supersolar [Fe/Mg] relative abundance patterns were observed in all sight lines which also had detections of cool gas. As each SNe Ia is estimated to contribute $\sim$0.7 $M_\odot$ of iron and $\lesssim$0.02 $M_\odot$ of magnesium (see Iwamoto et al. 1999), the high relative abundance pattern they observed suggests a significant contribution to the chemical enrichment of these lens galaxies from SNe Ia. Zahedy et al. (2017) also reported supersolar values of observed log $N_{\rm Fe\,II}/N_{\rm Mg\,II}$ using abundances adopted from Asplund et al. 2006 (log $({\rm Fe/Mg})_\odot > -0.08$) for most of the individual components detected in each sight line towards one of the lens galaxies in their sample. In both neutral and cool photoionized gas, Mg II and Fe II are the respective dominant ionization stages and the ratio $N_{\rm Fe\,II}/N_{\rm Mg\,II}$ should trace the total [Fe/Mg] abundance ratio. Thus each cloud of cool gas shows the supersolar relative abundance suggestive of a significant contribution from SNe Ia. Another factor that can affect the [Fe/Mg] ratio is that Fe depletes more strongly on dust grains than Mg. This would decrease [Fe/Mg], so the true [Fe/Mg] is even higher.

In the top panel of Figure 4.9 we show the observed log $N_{\rm Fe\,II}/N_{\rm Mg\,II}$ values for the individual components resolved in the HIRES spectra of SBS 0909+532 AB versus their velocity offset. All three resolved components in sight line A show a much higher log $N_{\rm Fe\,II}/N_{\rm Mg\,II}$ value than the typical solar abundance level of -0.10 from Asplund et al. (2009), although low H I and Mg II detections and photoionization modeling suggest that this sight line might not be probing cool gas. Only one of

the seven resolved components detected in sight line B shows a lower observed log $N_{\rm Fe\,II}/N_{\rm Mg\,II}$ value lower than the solar value. The reported effective radius $r_{\rm e}$ of the lensing galaxy is 12.01±6.84 kpc (Lubin et al. 2000) and therefore the impact parameters of the sight lines are $r_{\rm A} \approx 0.26\ r_e$ and $r_{\rm B} \approx 0.48\ r_e$. Thus the trend of supersolar relative abundance ratios seen in the cloud components in both sight line B at its low impact parameter suggests that the chemical enrichment in this inner region of the lens could be from SNe Ia.

Additionally, we plot the observed log $N_{\rm Fe\,II}/N_{\rm Mg\,II}$ values for the individual components resolved in the MagE spectra of both Q1017-207 AB and Q1355-2257 AB (see Figure 4.9 middle and bottom panels, both described in our recent work Kulkarni et al. 2019 and in Chapter 3). Q1017-207 AB is doubly imaged by a lens galaxy at $z_{\rm lens}$ = 1.086 with sight lines separated by l_{AB} = 6.9 kpc and log $N_{\rm H\,I,A}$ = 19.87±0.09 and log $N_{\rm H\,I,B}$ = 19.79±0.12. We observe supersolar values in three components in the sight line toward Q1017-207 A and two components in the sight line toward Q1017-207 B. 1355-2257 AB is doubly imaged by a lens galaxy at $z_{\rm lens}$ = 0.48 and l_{AB} = 7.3 kpc and log $N_{\rm H\,I,A}$ = 18.81 ± 0.18 and log $N_{\rm H\,I,B}$ = 19.43 ± 0.27. The red point shows an alternate value of log $N_{\rm Fe\,II}/N_{\rm Mg\,II}$ if the lens galaxy towards Q1355-2257 B is instead at redshift $z_{\rm lens}$ = 0.70, which is discussed in greater detail in Kulkarni et al. (2019). None of the components in the sight lines toward Q1355-2257 A or Q1355-2257 B at either redshift show a supersolar [Fe/Mg] ratio.

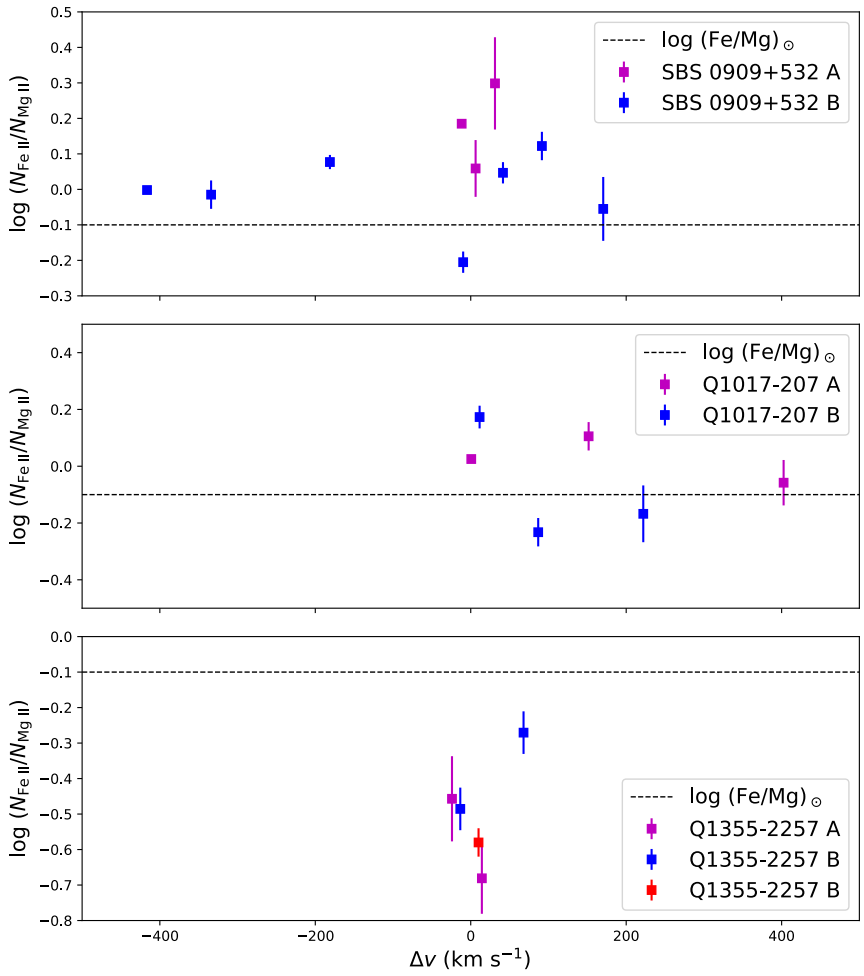

Figure 4.9 The observed column density ratio for $N_{\rm Fe\,II}/N_{\rm Mg\,II}$ for individual components versus their velocity offset from the center of the lensing galaxy for SBS 0909+532 AB. The dashed line is the solar ratio log $(\rm Fe/Mg)_\odot$ = -0.10 from Asplund et al. (2009). The error bars are the 1σ uncertainties for the calculated ratios. Additionally, we show the same plot for both Q1017-207 AB and Q1355-2257 AB, which we observed and reported on in Kulkarni et al. (2019). Top: SBS 0909+532 shows a supersolar value of log $N_{\rm Fe\,II}/N_{\rm Mg\,II}$ for all but one component in sight line B. Three components are resolved in the HIRES spectrum of image A. Seven components are resolved the HIRES spectrum of image B. Middle: Q1017-207 AB is doubly imaged by a lensing galaxy at $z_{\rm lens}$ = 1.0859 with sight lines separated by $l_{\rm AB}$ = 6.9 kpc and log $N_{\rm H\,I,A}$ = 19.87±0.09 and log $N_{\rm H\,I,B}$ = 19.79±0.12. Only one of the three resolved components in the MagE spectrum shows a supersolar value for log $N_{\rm Fe\,II}/N_{\rm Mg\,II}$ in sight line A. All three resolved components show a supersolar value for log $N_{\rm Fe\,II}/N_{\rm Mg\,II}$ in sight line B. Bottom: 1355-2257 AB is doubly imaged by a lensing galaxy at $z_{\rm lens}$ = 0.48 and $l_{\rm AB}$ = 7.3 kpc (log $N_{\rm H\,I,A}$ 18.81±0.18 = and log $N_{\rm H\,I,B}$ = 19.43±0.27). None of the components in the MagE spectrum along either sight line show a supersolar value for log $N_{\rm Fe\,II}/N_{\rm Mg\,II}$.

Table 4.7 Total Column Densities, Metallicities, and Gradients in the $z_{\rm lens} = 0.83$ galaxy

	SBS 0909+532 A			SBS 0909+532 B			
Ion	log $N_{\rm AOD}$	log $N_{\rm fit}$	[X/H]^a	log $N_{\rm AOD}$	log $N_{\rm fit}$	[X/H]	Δ[X/H]/Δr^b
Mg I	≤ 10.59	...	≥ -3.19	13.04±0.12	13.06±0.02	−2.91±0.20	...
Mg II	12.36±0.08	12.34±0.03	≥ -1.44	14.35±0.09	14.45±0.02	−1.53±0.20	...
Fe II	12.51±0.12	12.49±0.04	≥ -1.18	14.55±0.24	14.52±0.01	−1.36±0.20	≤ -0.07

(a) For sight line A, all metallicities calculated using log $N_{\rm H\,I} \leq 18.18$ cm^{-2}. See Section 4.3.2. For both sight line A and B, [Mg/H] is calculated from the total sum of log $N_{\rm Mg\,II}$ and log $N_{\rm Mg\,I}$.
(b) Average abundance gradient Δ[Fe/H]/$\Delta r =$ ([Fe/H]$_{\rm B}$ − [Fe/H]$_{\rm A}$)/($r_{\rm B}$ − $r_{\rm A}$) in dex kpc^{-1}.

Chapter 5

Creating an Atomic Survey

5.1 Atomic Spectroscopy

Atomic spectroscopy is fundamental to the study of a wide range of astrophysical environments. In the diffuse interstellar gas in the Milky Way, the atoms are often in the ground state, so that the resonant atomic transitions are of special interest. The vast majority of these atomic transitions lie in the ultraviolet. Space-based UV spectroscopy with a number of missions has made it possible to observe these interstellar transitions. Some of the earliest of these observations, carried out with the *Copernicus* mission led to fundamental discoveries such as the hot halo gas of the Milky Way (e.g., Rogerson et al. 1973; York 1974; Spitzer & Jenkins 1975). Subsequent missions such as the Far Ultraviolet Spectroscopic Explorer further extended the study of interstellar and intergalactic gas (e.g., Moos et al. 2000). The several generations of UV spectrographs on the Hubble Space Telescope have vastly increased the number of Galactic as well as extragalactic sight lines probed for their neutral or ionized gas. For example, these observations uncovered the existence and properties of low-redshift Lyman-α forest clouds, as well as the covering fractions, element abundances, temperatures, and kinematics of the circumgalactic medium (CGM) (e.g., Morris et al. 1991; Bahcall et al. 1993; Savage & Sembach 1996 and references therein; Kulkarni et al. 2005; Tumlinson et al. 2013; Lehner et al. 2013; Som et al. 2015; Werk et al. 2016). Naturally, these observations provide crucial constraints on models of galaxy evolution, including the effect of outflows and inflows. Furthermore, determinations

of relative element abundances in the interstellar medium (ISM) are important to understanding dust depletions and thus, indirectly, the composition of dust grains (e.g. Jenkins 2009 and references therein). Relative element abundances in distant galaxies offer crucial windows in understanding the cosmic evolution of dust, as well as the evolution of stellar nucleosynthetic processes. On a larger scale, observations of key ions in the intergalactic medium (IGM) offer rich insights into the physical conditions in the diffuse regions of the cosmic web, and the large-scale cosmic processes influencing it.

In view of the sweeping consequences of atomic spectroscopy for understanding the evolution of galaxies, ISM, CGM, and IGM, it is important to be able to derive accurate physical information from the spectra. This makes it essential to employ as accurate atomic data as possible in translating the spectroscopic measurements into determinations of physical quantities.

Thanks to the extensive efforts of numerous theoretical and experimental physicists, many improvements in the atomic data relevant for astrophysical spectroscopy have been happening in recent years. However, knowledge of many of these improvements often does not trickle down to the community of observational spectroscopists rapidly enough. For example, in the CGM/IGM community, the most commonly used reference for atomic data, by far, is Morton (2003). With the goal of making the latest improvements accessible to the community, we created a compilation of oscillator strengths for key transitions, including updates made since 2003. We focused in particular on the ions that have been measured in ISM/CGM/IGM studies for selected elements ranging from C to Pb. For each of the selected elements, we listed lines longward of the Hydrogen Lyman limit at 911.753 Å, since in this wavelength region, the bound-free H absorption does not contribute much to the ISM/CGM/IGM opacity. Atomic data for absorption lines shorter than 911.753 Å from the ground level can be found elsewhere, e.g. Verner et al. (1994), Kallman & Palmeri (2007).

5.2 General Terminology and Definitions

Throughout this paper, we focus on the electric dipole (E1) transitions. The absorption line corresponds to the transition between the lower level l and the upper level u, with level energies $E_{\rm l}$ and $E_{\rm u}$, respectively. The statistical weights ($g = 2J+1$, J being the total angular momentum of the state) of the lower and upper levels are denoted $g_{\rm l}$ and $g_{\rm u}$. In terms of the energy levels, the vacuum wavelength λ_{vac} of the transition is

$$\lambda_{vac} = hc/(E_{\rm u} - E_{\rm l}), \tag{5.1}$$

where h is Planck's constant, and c is the speed of light. The Einstein transition probability (in $\rm s^{-1}$) for spontaneous emission is denoted by $A_{\rm ul}$. The dimensionless absorption oscillator strength $f_{\rm lu}$ is related to the E1 transition probability $A_{\rm ul}$ by:

$$f_{\rm lu} = 1.49919 \times 10^{-16} \lambda_{vac}^2 g_{\rm u} A_{\rm ul}/g_{\rm l} \tag{5.2}$$

where λ_{vac} is in Å. The oscillator strengths compiled in this paper were obtained from either experimental techniques or theoretical calculations. In cases where oscillator strengths in both the length and velocity forms are available, we tabulate the length-form data as these are commonly used and more reliable.

In Table 5.1, we present the data for each ions species separately. These species and their ground levels are given in table subheaders. Table 5.1 lists the following information for each E1 line of interest:

1. Nuclear charge Z
2. Ion spectroscopic notation
3. Lower level
4. Upper level
5. Vacuum rest wavelength λ_{vac} in Å (where available)

6. Ritz wavelength λ_{Ritz} in Å

7. Lower level statistical weight $g_{\rm l}$

8. Upper level statistical weight $g_{\rm u}$

9. Absorption oscillator strength f

10. Logarithm of weighted oscillator strength, $\log(gf)$

11. Accuracy grade (uncertainty) of the oscillator strength f according to the NIST atomic spectra database (Kramida et al. 2016)

12. f-value data source

We wish to be as consistent as possible in selecting the lines presented in Table 5.1. Hence we need to explain a selection procedure for the tabulated lines. The following basic rules were followed for selecting data sources in our tables or providing any additional information.

1. For the species range, we consider elements with $6 \leq Z \leq 30$ and several other elements observed in the ISM, such as Ga, Ge, Kr, Pb. Usually we present data for a few of the lowest ionization stages. The selected ions have been observed in the ISM, CGM, and/or IGM.

2. We tabulate lines with wavelengths $\lambda_{vac} > 911.753$ Å. These are the vacuum wavelengths for all lines.

3. We give priority to the observed wavelength which we call λ_{vac} over the Ritz wavelength λ_{Ritz}. As a rule, the line wavelength source is the NIST database Kramida et al. 2016. We have represented the wavelengths from the NIST database to 3 decimal places.

4. We tabulate absorption lines originating from the ground level only. We do not tabulate lines originating from the excited levels of the ground configuration or the ground term even if their energies are just a few tenths of cm^{-1}, e.g. the C I, C II, N II ions.

5. We tabulate only those lines that have $f \geq 0.001$. We present no more than 3 significant figures for the f-values as we suppose that is enough to reflect their real accuracy.

6. Usually we tabulate f-values from the newest sources giving priority to the experimental data over the theoretical values. In the cases where new data are not significantly different from the older data, we choose to rely on the older data preferring the most advanced theoretical methods for data production. Those special cases will be mentioned in Section 5.3.

The accuracy grades of the tabulated oscillator strengths f were either derived from the original data sources or we tabulated the grades given in the NIST database by Kramida et al. (2016). For this reason, some of the lines do not have accuracy grades. In some cases, we were able to confidently assign an accuracy grade through careful comparative analysis. These instances and their justification are specifically documented within Section 5.3.

5.3 Comments and Assessment of Improved Data

In Table 5.1 wavelengths $\lambda_{\rm vac}$ are adopted from the NIST database (Kramida et al. 2016). Theoretical f-values $f_{\rm theor}$ are corrected for the inaccuracy in calculated level energies (or wavelengths $\lambda_{\rm theor}$ by adjusting them according to the observed values $\lambda_{\rm obs}$, see Lykins et al. (2015):

$$f_{\rm corr} = f_{\rm theor} \times (\lambda_{\rm theor}/\lambda_{\rm obs}). \tag{5.3}$$

A significant part of the new transition data are utilized from the theoretical calculation performed by Froese Fischer & Tachiev (2004), where multiconfiguration Hartree-Fock (MCHF) method was applied to determine the transition data for the neutrals and ions starting with the Beryllium isoelectronic sequence and finishing with the Argon isoelectronic sequence. The same MCHF approximation is applied to produce data for the Sodium to Argon isoelectronic sequences by Froese Fischer et al. (2006). This method is a reliable one producing high-accuracy results, and it is difficult to exceed their accuracy when dealing with large amounts of species. We tabulate transition data from the above sources for the species up to Argon complemented with data from other sources for the lines involving higher excited levels with $n > 4$. Another source of oscillator strength f-values for ions with $Z > 20$ is the data list of Kurucz (2016). This is an online data list, which is continuously updated with new results. We give the preference to their newer data as opposed to the older values given in the previous versions of this data list. We reference this source as Kurucz (2016) although in many cases data have been produced considerably earlier.

5.3.1 Carbon species

For neutral carbon and the species C II and C III, we tabulate theoretical data from the calculations of Froese Fischer and co-workers published in Froese Fischer (2006), Zatsarinny & Froese Fischer (2002), Tachiev & Froese Fischer (2001), and Froese Fischer & Tachiev (2004). These are very reliable data sources providing highly accurate radiative transition data. For two lines in the lithium-like C IV, which is outside the scope of the above-mentioned papers, we adopt data from Yan et al. (1998) having an accuracy grade of A. We performed an additional check for these two lines and calculated transition data using our own codes utilizing the Hartree-Fock (HF) and quasirelativistic (QR) approaches on a very extensive configuration-interaction (CI) wavefunction basis recently described by Kisielius et al. (2015). Our results

confirm the high accuracy of data from Yan et al. (1998); our calculated f-values agree within a few tenths of a percent.

5.3.2 Nitrogen species

Oscillator strengths are taken from Froese Fischer & Tachiev (2004) for the species N I, N II, and N III. The NIST database assigns them accuracy grades no worse than B. There is just one line in our investigated wavelength range in the N IV ion. It originates from the excited level $1s^2 2s2p\ ^3P_1$. But it is rather weak as it constitutes a spin-changing E1 transition. For the lithium-like ion N V we adopt data from Peach et al. (1988). For the N V lines, we performed an accuracy check because these data are coming from non-relativistic calculations. Our results, both in the length and velocity forms of the E1 transition operator, agree between themselves within 2% and do not deviate more than 0.5% from the results of Peach et al. (1988). This confirms a high accuracy grade of A assigned to oscillator strengths of the tabulated absorption lines in the N V ion.

5.3.3 Oxygen species

For the O I ion, data from Froese Fischer & Tachiev (2004) are adopted for the lines connecting the excited states $2s2p^3 3s$, 3d, and 4d. For other lines not covered by Froese Fischer & Tachiev (2004) we use data from Hibbert et al. (1991). This is the same source used by the NIST database, and the later investigation of Tayal (2009) just confirms the reliability and high accuracy of their data. Transition data from Tayal (2009) agree with oscillator strengths f of Hibbert et al. (1991) within 10%. We also tabulate oscillator strengths for two 2s – 2p transition lines in Li-like O VI determined by Peach et al. (1988). Likewise to the situation described in Sect 5.3.2, we have performed our own calculation and can confirm a high accuracy grade assigned to these data by the NIST team.

5.3.4 Sodium species

The oscillator strength f-values are taken from Froese Fischer et al. (2006) for the lines 3s – np, ($n = 3, 4$) and we retain the same accuracy grades as given by NIST. For the line 3s – 5p we adopt the oscillator strength value determined by applying the same MCHF approach B-spline method with non-orthogonal radial orbitals by Froese Fischer (2002). It was proved for neutral carbon by Zatsarinny & Froese Fischer (2002) that such an approach produces reliable results for the high-nl lines.

5.3.5 Magnesium species

For the lines representing resonance transitions from the ground $3s^2$ state to the excited 3s3p and 3s4p states of the Mg I ion, we use data from Froese Fischer et al. (2006) with accuracy grades of A and B+. For the transition to the 3s5p levels, more recent oscillator strength f data produced using a B-splines method within MCHF by Zatsarinny et al. (2009) are available, whereas for the lines representing transitions to highly excited 3snp levels ($6 \leq n \leq 8$) we adopt data of Chang & Tang (1990) as more recent data do not exist.

Oscillator strength values for Mg II are taken from Froese Fischer et al. (2006). The accuracy of the data for the 3s – 3p lines has a very high A+ grade. Meanwhile, although the lines 3s – np ($n > 3$) are in our investigated wavelength range ($\lambda_{\rm vac} > 911.753$), only the transition to the $2p^6 5p\ {}^2P^o_{3/2}$ level has $f \geq 0.001$ satisfying our selection criteria. Other lines fall short of that criteria although their fine-structure level unresolved oscillator strengths are within that range.

5.3.6 Aluminum species

We tabulate oscillator strength f values for three ions, Al I, Al II, and Al III. Here for the lines connecting the ground state with the lower $n = 3, 4$ levels, the theoretical data of Froese Fischer et al. (2006) are adopted. They have accuracy grades of B+

and A+. For the higher nl levels we list theoretical data from Mendoza et al. (1995), which were determined by non-relativistic R-matrix calculations. Furthermore, their data for fine-structure levels were derived from the multiplet values assuming a pure LS-coupling. Those data usually have rather poor accuracy grades, thus further data improvement can rectify this situation. For three lines of Al I we adopt experimental data of Vujnović et al. (2002) and Davidson et al. (1990) and assign an accuracy grade of B.

5.3.7 Silicon species

For the low-lying states of the $3s^2 3p4s$, $3s3p^3$, $3s^2 3p3d$ odd-parity configurations of Si I, we list f-values adopted from Froese Fischer et al. (2006). As we have mentioned before, these theoretical data are of high quality and reliability. It is necessary to admit here that these values differ noticeably from the previous oscillator strength values tabulated by Morton (2003). The case of the lines involving higher levels is more complicated. Some lines falling into our wavelength selection region are absent from the NIST database although their corresponding level energies are presented there, e.g. the lines at $\lambda_{\rm Ritz} = 1568.617$ Å, $\lambda_{\rm Ritz} = 1763.6614$ Å, and $\lambda_{\rm Ritz} = 1873.1032$ Å. The oscillator strength values for the first line and the line at $\lambda_{\rm Ritz} = 1589.173$ Å are derived from the non-relativistic R-matrix calculations of collision data for several Si-like ions of Nahar & Pradhan (1993), which we consider as being less accurate compared to the pure atomic structure calculations or the experimental results. The E1 transition data for the latter line are listed in Froese Fischer et al. (2006) although their $\log(gf)$ value of -2.16 differs noticeably from the experimental $\log(gf) = -2.57$ value from Smith et al. (1987). Additional experimental data for higher nl levels comes from the measurements of Smith et al. (1987) and from a critical compilation of Kelleher & Podobedova (2008).

Bautista et al. (2009) have produced a benchmark data set for the Si II ion by utilizing several theoretical approaches and experimental data to determine reliable recommended absorption oscillator strengths for the levels of the $3s3p^2$, $3s^23d$, and $3s^24s$ configurations. For the higher level of $3s^24d$ at 989.873 Å, we list the experimental f value of Curtis & Smith (1974), which is close to the theoretical value $f = 0.1849$ from Charro & Martin (2000), which also serves as a source for the $3s^25s$ level data. For the ions Si III and Si IV, we list oscillator strengths from Froese Fischer et al. (2006).

5.3.8 Phosphorus species

For the lines connecting the ground state $3s^23p^3\ {}^4S_{3/2}$ with the levels of ^{4}P term of the excited configuration $3s^23p^2(^3P)4s$ of P I, we adopt oscillator strengths from Froese Fischer et al. (2006). Unfortunately, that work does not list data for the transitions to the $3s^23p^2(^3P)3d\ {}^4P$ levels. Thus we resort to older theoretical data from Fawcett (1986). The f-values for the lines at $\lambda\lambda 1679.695, 1674.591, 1671.680$ given by Froese Fischer et al. (2006) differ significantly, at least by 2 orders of magnitude from the previous data of Fawcett (1986). Since the relative intensities for these three 3s – 3p lines given by the NIST database are similar to those of 3p – 4s lines at $\lambda\lambda 1787.656, 1782.838, 1774.951$, we believe the data from Fawcett (1986) given its D accuracy rating can be utilized for neutral phosphorus.

For the P II and P III lines we list data from Froese Fischer et al. (2006). Five more lines below 1153 Å (unlisted in the NIST database) are entered in Table 5.1 for P II. These lines originate from the absorption transitions from the ground level to the levels 3p4s and 3p4d. We derived their Ritz wavelengths using level energies listed by Kramida et al. (2016). The same process was performed for three P III lines below 999 Å. The source of the transition data chosen for the magnesium-like P IV and sodium-like P V is Froese Fischer et al. (2006).

5.3.9 Sulfur species

The main source of the data for the neutral Sulfur lines connecting the ground level $3s^2 3p^4\ ^3P_2$ with the levels of the excited 3d, 4d, 4s, 5s, 6s configurations are the theoretical results of Deb & Hibbert (2008). As in Deb & Hibbert (2006), the data from Deb & Hibbert (2008) agree very well with most lines from the results of the B-spline calculations by Zatsarinny & Bartschat (2006). They also are close to the data produced by Froese Fischer et al. (2006). Thus one has to be assured of high quality and reliability of the listed f-values. We include the line at $\lambda = 1474.5715\,\text{Å}$ even though its f-value is lower than our selection criterion $f \leq 0.001$ as other theoretical predictions put it above this criterion. The data from higher configurations with the valence 5d, 6d, 7s, and 8s electrons are taken from Biémont et al. (1998a). That set of f-values was deduced from a combination of laser lifetime measurements and theoretical branching ratios. For the lines with $\lambda < 1241\,\text{Å}$ that connect the ground state with the upper levels located above the first ionization limit at $83,559.1\,\text{cm}^{-1}$, we choose oscillator strengths from Deb & Hibbert (2008), with grades of C.

For the S II lines we list a data set from Kisielius et al. (2014). The authors concluded that their data are in good agreement with other theoretical data sets of Froese Fischer et al. (2006) and Tayal & Zatsarinny (2010). For the S III, S IV, and S VI lines we list data from Froese Fischer et al. (2006).

5.3.10 Chlorine species

The data for the Cl I lines are taken from the recent theoretical calculations of Oliver & Hibbert (2013). Their data accuracy grade is C+. For the two lines in Cl II and three lines of Cl III, we assume that the experimental data from Schectman et al. (2005) are the best source. The accuracy of their f-values is within 5% (or an accuracy grade of B+). We list an oscillator strength from Froese Fischer et al. (2006) for a single line of Cl IV.

5.3.11 Argon species

For the lines of Ar I and Ar II we recommend using oscillator strengths from Froese Fischer et al. (2006). One can safely assign the C+ accuracy grade to these data.

5.3.12 Potassium species

For the spectra of neutral K I we list four lines corresponding to the resonance 4p –4s and 5p – 4s transitions in the valence shell. The lines to the higher np levels are relatively weak and do not fall into our desired f-value range. The parameters of lines caused by the 4s – 4p transitions are determined by Wang et al. (1997). Their data agree very well with other high-accuracy measurements. They evaluate the accuracy of f-values as 0.2% (AAA accuracy grade). Data for the 4s – 5p lines are from the measurements of Shabanova & Khlyustalov (1985). Although their accuracy grade is unlisted, by comparing these data with the results of elaborated relativistic calculations of Migdalek & Kim (1998) we confidently assign them a grade of A.

5.3.13 Calcium species

The data for the λ4227.92 line are taken from the high-accuracy photoassociative measurements of Zinner et al. (2000), which produces reduced uncertainties compared to previous measurements. Their data have confirmed previous level-crossing measurements of Kluge & Sauter (1974). Recent theoretical values of Froese Fischer & Tachiev (2003) are also close (within error bars) to the above experimental data. The data for other resonance lines of neutral calcium are measured by Parkinson et al. (1976). They used the hook method to determine the gf values of the $4s^2$ – $4sn$p absorption lines. These data for most lines agree within 5% with other measurements, e.g. Ostrovskii & Penkin (1961), Shabanova (1963),and Mitchell (1975). The λ2722.450 line is the only exception, and here the differences are much higher. Even

though this line has an f-value below our cut-off level, we list it in our table. The list for Ca I contains lines up to $3p^6 4s13p$ while the transitions for higher Rydberg levels fall below our cut-off criterion of $f \geq 0.001$.

For the Ca II ion lines we recommend recently determined oscillator strengths from Safranova & Safranova (2011). Their calculations used a high-precision relativistic method where all single and double, and partially triple excitations of Dirac-Fock wavefunctions are included to all orders of perturbation theory. The authors estimate the relative uncertainties of their calculated oscillator strengths to be 0.9%.

5.3.14 Titanium species

The majority of the data for the Ti I lines come from the measurements of Lawler et al. (2013). They have used the previously measured radiative lifetimes combined with the branching fractions to yield absolute oscillator strengths. The data agree closely with the NIST data, therefore we consider it appropriate to assign them respective accuracy grades, which are no worse than B+. Some lines are missing in Lawler et al. (2013). For those lines we recommend the high-quality experimental data from Blackwell-Whitehead et al. (2006) or data from the earlier experiment of Smith & Kühne (1978).

For the Ti II ion lines we list data from the recent paper of Lundberg et al. (2016). The authors measured radiative level lifetimes and used the pseudo-relativistic Hartree-Fock method to determine oscillator strengths and theoretical lifetimes for the measured levels. Their data agree within 10% with the earlier theoretical data of Ruczkowski et al. (2014) and those from Pickering et al. (2001b). For the Ti III transition data we adopt the theoretical results of Raassen & Uylings (1997). They performed an orthogonal operator calculation for the electric dipole transition integrals by means of the multiconfiguration Dirac-Fock method including core polarization.

5.3.15 Chromium species

For the lines connecting the ground state of Cr I with the $n = 4$ levels, the data chosen were produced by Sobeck et al. (2007). The authors used branching fraction measurements from Fourier transform spectra in conjunction with radiative lifetimes to determine the transition probabilities. These data are assigned an accuracy grade of B. For the transitions to the $3d^5 5p$ levels we list data from Martin et al. (1988), which are given accuracy grades of C.

For the three lines above 2050 Å in Cr II, the recommended tabulated data are from the experimental work of Nilsson et al. (2006). The accuracy grade for their data is B+. For other lines of Cr II we tabulate theoretical data from Raassen & Uylings (1998) where oscillator strengths have been determined using the orthogonal operator technique. Five listed lines of Cr III are taken from Kurucz (2016).

5.3.16 Manganese species

For the manganese lines we adopt the experimental oscillator strength values from Blackwell-Whitehead et al. (2005, 2011). Their accuracy grade is B+ for the lines with $\lambda > 4000$ Å, and C+ for the lines below 3000 Å. Unfortunately, oscillator strengths for most Mn I lines listed in our table were not measured in the above experiments. For these lines we tabulate older data from Martin et al. (1988) or data from Kurucz (2016).

New data for some selected Mn II lines in Table 1 are listed from Den Hartog et al. (2011) who experimentally measure radiative lifetimes and branching fractions to derive transition probabilities and oscillator strengths. Other data come either from similar experimental work of Kling & Griesmann (2000) or from the configuration interaction calculations of Toner & Hibbert (2005).

5.3.17 Iron species

Lines for three iron ions are listed in Table 1. For lines with $\lambda > 2913$ Å our oscillator strength source is Blackwell et al. (1979), who measured absorption oscillator strengths and reported an accuracy of 0.5%. NIST assigns an accuracy grade of A for most of those lines. For the lines below 2913 Å our data come from the measurements of O'Brian et al. (1991). They employed time-resolved laser-induced fluorescence to measure radiative lifetimes and derived oscillator strengths by measuring branching fractions. Their accuracy grades are slightly worse compared to those of Blackwell et al. (1979). For the remaining lines below 2260 Å we list the data of Banfield & Huber (1973), who used the hook method to determine oscillator strengths in Fe I. Although the accuracy grade of their data is not as high, these oscillator strengths are substantially reliable.

Our main source for the Fe II lines above 2000 Å is the experimental data from Bergeson et al. (1996). The authors have measured branching ratios with a Fourier transform spectrometer and with a high-resolution grating spectrometer. The resulting measurements were used to derive transition probabilities for 56 lines. Another group of listed lines was theoretically studied by Raassen & Uylings (1998). Their accuracy grade is lower. These two sources are complemented by experimental oscillator strengths from Pickering et al. (2001a) and the critical compilation of Fuhr & Wiese (2006). For the Fe III ion line at 1122.5 Å we tabulate the theoretical oscillator strength from Deb & Hibbert (2009).

5.3.18 Cobalt species

Oscillator strengths for all but one of the Co I lines are taken from the recent measurements of Lawler et al. (2015). They derived oscillator strengths from experimental branching fractions combined with radiative lifetimes from laser induced fluorescence measurements. The NIST database assigns accuracy grades of B or B+

for their data. A rather weak line at λ2436 is taken from Cardon et al. (1982) where absolute oscillator strengths were determined using the hook method. Data for the Co II lines come from the calculations using the orthogonal operator technique by Raassen et al. (1998) and the measurements of Mullman et al. (1998). In general, the data for Co II have relatively low accuracy grades. For the lines of Co III we tabulate oscillator strengths from the Kurucz on-line data list (Kurucz, 2016).

5.3.19 Nickel species

For the Ni I lines we list oscillator strengths from new measurements of Wood et al. (2014) where f-values were determined by combining measured branching fractions and radiative lifetimes. Most of these data are assigned high accuracy grades (from B+ to B). Missing data are covered by the measured oscillator strengths obtained by the hook and absorption methods from Huber & Sandeman (1980). Their data accuracy evaluation is lower compared to that of Wood et al. (2014). NIST lists only a single line for transitions of Ni II. We tabulated oscillator strengths from the recent CI calculation of Cassidy et al. (2016). The authors state that it is difficult to provide a measure of the uncertainties for the large-scale CI calculations which would cover all transitions. Nevertheless they consider that their data are the best currently available and meet the accuracy demands for astrophysical applications. We do not assign any accuracy grades to these data although they can be considered as having an accuracy grade of B.

5.3.20 Copper species

The source of oscillator strength data for the resonance 4s – 4p lines in Cu I is a critical compilation of oscillator strengths for neutral ions by Doidge (1995). The data for the transitions 3d – 4p and 4s – 5p are adopted from Hannaford & McDonald (1978). The oscillator strengths were determined from atomic absorption

measurements of the radiation emitted from a copper hollow-cathode lamp. The oscillator strengths for the remaining lines 4s – np ($n \geq 6$) comes from the calculation of Çelik et al. (2015).

Three lines listed for Cu II originate from the transitions involving the ground level $3p^6 3d^{10}\,{}^1S_0$ and the levels with $J = 1$ from the configuration $3d^9 4p$. Their data source is either the theoretical data from Donnelly et al. (1999) or from the beam-foil experimental data of Brown et al. (2009), which were given an accuracy grade of B.

5.3.21 Zinc species

The oscillator strength for the $4s^2\,{}^1S_0$ – $4s4p\,{}^1P_0$ line of Zn I is taken from the Hanle-effect experiments of Kowalski & Träger (1976), which have confirmed the earlier level-crossing technique results of Lurio et al (1964). Later beam-foil spectroscopy measurements of Martinson et al. (1979) give very similar f-values ($f = 1.55 \pm 0.08$). These measurements are consistent with recent theoretical data, e.g. Froese Fischer & Zatsarinny (2007) and Głowacki & Migdałek (2006). For the λ1589 line we tabulate the oscillator strength from the line list of Kurucz (2016). The NIST database lists a rather strong line at λ1109.1 with no transition identification or Ritz wavelength. Analyzing the level list we can assume that this line originates from the transition 3d – 4p with $\lambda_{\rm Ritz} = 1108.316$ Å, although this wavelength noticeably differs from the measured one. That can be explained by the fact that the level $3d^9 4s^2 4p\,{}^3P^{\rm o}_1$ lies in the continuum, above the ionization limit.

Oscillator strengths for Zn II are taken from the quasi-relativistic calculations of Kisielius et al. (2015). Their data are consistent and agree with other theoretical data within a range of 10%.

5.3.22 Gallium species

Tabulated data for neutral gallium lines are from a new compilation of Shirai et al. (2007) with an unlisted line for the $4p_{1/2}$ – $7d_{3/2}$ transition data taken from the relativistic many-body perturbation theory calculation of Safranova et al. (2005). These two data sources tabulate oscillator strengths differing by approximately 10% for most of the listed lines. For λ1414 line of Ga II, we tabulate an oscillator strength from the low-energy beam-foil measurements of Andersen et al. (1979) which have 8% measurement errors (i.e., an accuracy grade of B). Later theoretical data confirm the reliability of the listed experimental data, see e.g. McElroy & Hibbert (2005), Jönsson et al. (2006), and Chi & Chou (2014). Oscillator strength values for two lines of the Ga III ion are from the compilation of Shirai et al. (2007).

5.3.23 Germanium species

There are no new reliable original oscillator strength data sources for the germanium species following Morton (2003) except for the compilation of Fuhr & Wiese (2005). For the Ge I lines we tabulate experimental oscillator strengths of Li et al. (1999). Their experiment measured natural level radiative lifetimes by employing time-resolved UV laser-induced fluorescence from a laser-produced plasma and determined branching fractions by an inductively coupled plasma emission spectrometry technique. The derived oscillator strengths have accuracy grades of B or B+. For the Ge II lines we list theoretical f-values from Biémont et al. (1998b). For the Ge III ion we list two $4s^2$ – 4s4p transition lines. The $^3P_1$ spin-forbidden line oscillator strength is tabulated from the empirical predictions of Curtis (1992). The resonance line f-value for the $^1P_1$ level was experimentally determined by Andersen et al. (1979) utilizing beam-foil spectroscopy. The oscillator strengths for Ge IV are adopted from the beam-foil measurements of Pinnington et al. (1981).

5.3.24 Krypton species

For the Kr I lines we tabulate experimental oscillator strengths from Chan et al. (1992). They measured photoabsorption f-values using the dipole (e, e) method. The oscillator strengths have accuracy grades of B or B+. The reliability of their data was confirmed by recent B-spline calculations of Zatsarinny & Bartschat (2009). The oscillator strengths for Kr II were derived from the selective pulsed monochromatized synchrotron radiation experiment of Lauer et al. (1999) where lifetimes of the $4s4p^6\,{}^2S_{1/2}$ states were measured. For the Kr VI line we list data from multiconfiguration Hartree-Fock relativistic calculation of Pagan et al. (1996) where adjustments were made to the electrostatic parameters in order to improve theoretical level energies and gf-values.

5.3.25 Lead species

We list data for the Pb II lines. The oscillator strength for the λ1682 line is adopted from Quinet et al. (2007) where transition probabilities were calculated in a relativistic multiconfiguration Dirac-Fock approach and the accuracy of the results was assessed by a new experimental determination of the radiative lifetime for the $7s_{1/2}$ level. Other listed data are from Safranova et al. (2005). The authors obtained radiative transition data using relativistic many-body perturbation theory. The remaining data for the $10s_{1/2}$ and $9d_{3/2}$ levels are adopted from the *ab initio* relativistic Hartree-Fock calculations of Colón & Alonso-Medina (2001).

Table 5.1 Line identifications, observed wavelengths $\lambda_{\rm vac}$ (Å), Ritz wavelengths $\lambda_{\rm Ritz}$ (Å), absorption oscillator strengths f and their accuracy grade for key transitions

Z	Ion	Lower level Upper level	$\lambda_{\rm vac}$	$\lambda_{\rm Ritz}$	$g_{\rm l}$	$g_{\rm u}$	f	$\log(gf)$	Grade	Source
6	C I	$2s^22p^2\ {}^3P_0$ $2s^22p3s\ {}^3P^o_1$	1656.928	1656.929	1	3	1.43E−1	−0.845	A	FF06
6	C I	$2s^22p^2\ {}^3P_0$ $2s2p^3\ {}^3D^o_1$	1560.310	1560.309	1	3	7.16E−2	−1.145	A	FF06
6	C I	$2s^22p^2\ {}^3P_0$ $2s2p^3\ {}^3P^o_1$		1328.834	1	3	5.80E−2	−1.236	B	FF06
6	C I	$2s^22p^2\ {}^3P_0$ $2s^22p4s\ {}^3P^o_1$		1280.135	1	3	2.61E−2	−1.583	B+	FF06
6	C I	$2s^22p^2\ {}^3P_0$ $2s^22p3d\ {}^3D^o_1$	1277.245	1277.245	1	3	9.22E−2	−1.035	A	FF06
6	C I	$2s^22p^2\ {}^3P_0$ $2s^22p5d\ {}^3D^o_1$	1157.910	1157.910	1	3	2.12E−2	−1.674		ZF02
6	C II	$2s^22p\ {}^2P^o_{1/2}$ $2s2p^2\ {}^2D_{3/2}$	1334.532	1334.532	2	4	1.29E−1	−0.589		FFT04
6	C II	$2s^22p\ {}^2P^o_{1/2}$ $2s2p^2\ {}^2S_{1/2}$	1036.337	1036.337	2	2	1.19E−1	−0.624		FFT04

Note: Table 5.1 is available in its entirety as a machine readable table in Appendix B.1. A portion is shown here to illustrate its content.

Note: An estimated accuracy grade is listed for each oscillator strength where available, indicated by a code letter as given below: AAA $\leq$ 0.3%; 0.3% $<$ AA $\leq$ 1%; 1% $<$ A+ $\leq$ 2%; 2% $<$ A $\leq$ 3%; 3% $<$ B+ $\leq$ 7%; 7% $<$ B $\leq$ 10%; 10% $<$ C+ $\leq$ 18%; 18% $<$ C $\leq$ 25%; 25% $<$ D+ $\leq$ 40%; 40% $<$ D $\leq$ 50%; E $>$ 50%.

5.4 Discussion

A complete version of Table 5.1 is available online in a machine-readable version. Please note that in the online machine-readable version, we used LaTeX encoding to tabulate the lower and upper levels in order to avoid any misrepresentations. Table 5.1 can also be obtained on request as a formatted PDF table from the authors (`Romualdas.Kisielius@tfai.vu.lt`). In the printed version of this paper we list just a few lines from the carbon species to facilitate understanding of the form and contents of our data list.

In Appendix A we explain the source abbreviations used in Table 5.1. For easier guidance we also tabulate the ion list from which oscillator strength values f were sourced.

Table 5.1 lists 576 transitions. For 400 of these transitions, we have listed updated oscillator strength determinations. Of these, 60 transitions, although listed either in Morton (2003) or in the NIST database Kramida et al. (2016), previously had no oscillator strength value reported. Figure 5.1 shows a comparison of the updated and former oscillator strengths. Table 5.2 compares updated oscillator strength values to their former values for 340 lines. For 171 of these transitions, the new f values are smaller than the old values, while for 157 transitions, the new f values are larger. The differences from the old values are usually smaller for the stronger transitions with $\log f \gtrsim -0.5$. The differences are ≥ 0.2 dex for $\approx 12\%$ of the lines, and $\gtrsim 0.1$ dex for $\approx 22\%$ of the lines.

A breakdown of the accuracy grades for all 576 oscillator strengths is given in Fig. 5.2. Approximately 37% of the oscillator strengths have an accuracy grade worse than 10%, while approximately 11% of the oscillator strengths have an accuracy grade worse than 25%. Figure 5.2 highlights the need for obtaining more accurate oscillator strength values for these, as well as for obtaining the accuracy grades for the 24% of the oscillator strengths that are currently without a grade.

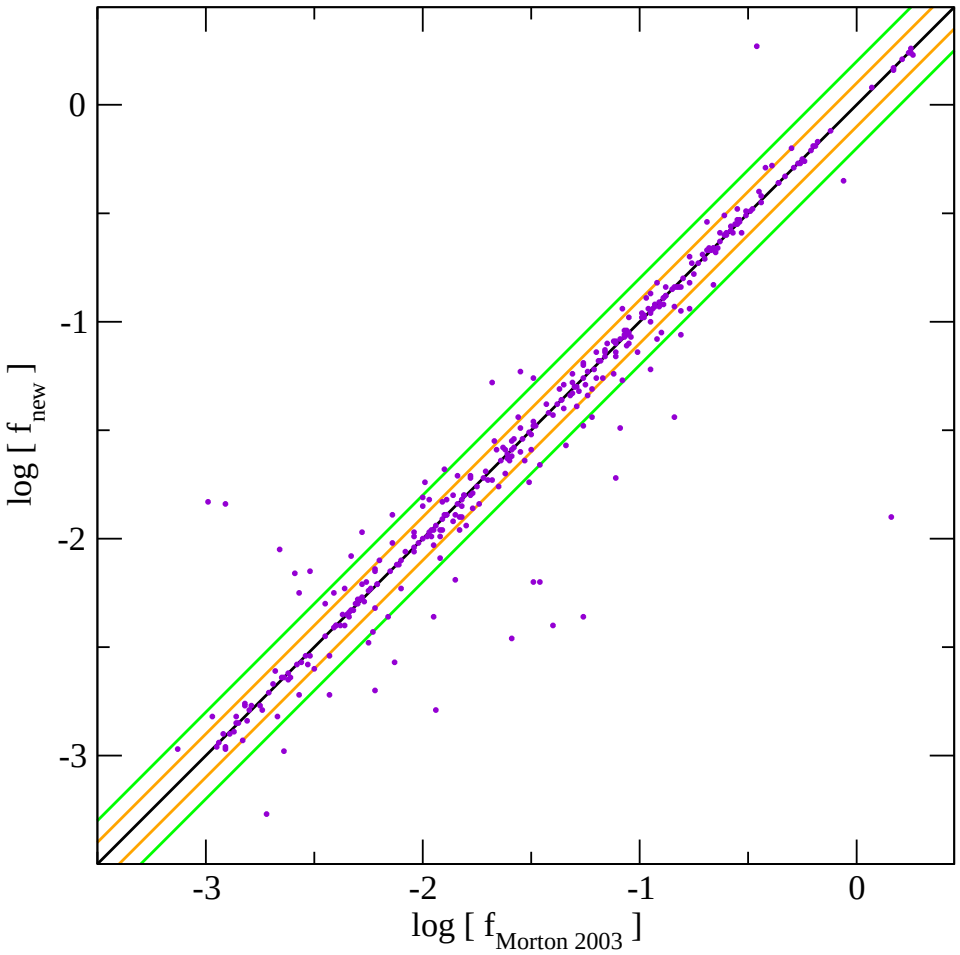

Figure 5.1 Comparison of the updated and former values of the oscillator strengths. The black line denotes a line of unit slope and zero intercept. The orange and green lines denote deviations of ±0.1 dex and ±0.2 dex, respectively, from the black line.

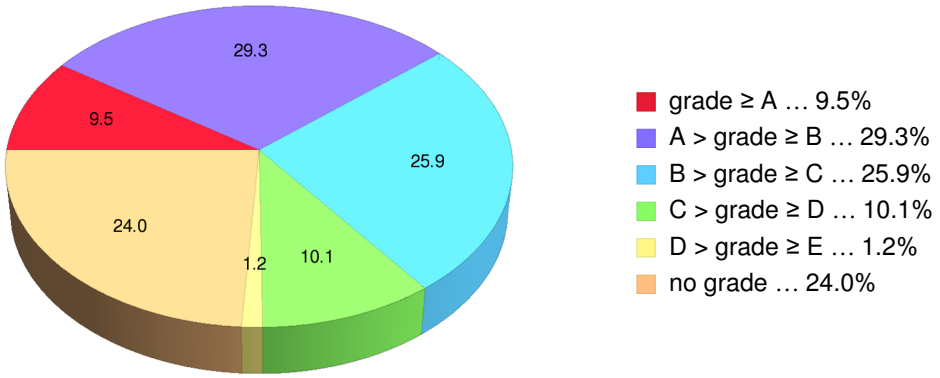

Figure 5.2 Statistical breakdown of accuracy grades of the 576 transitions in Table 5.1. An estimated accuracy grade is listed for each oscillator strength where available, indicated by the following code letters: A $\leq$ 3%; 3% $<$ B $\leq$ 10%; 10% $<$ C $\leq$ 25%; 25% $<$ D $\leq$ 50%; E $>$ 50%.

Table 5.2 Statistical Analysis of Change in Oscillator Strength

Δf	No. of lines	% lines
dex $\leq$ 0.05	198	58.2
0.05 $<$ dex $\leq$ 0.1	55	16.2
0.1 $<$ dex $\leq$ 0.2	35	10.3
0.2 $<$ dex $\leq$ 0.3	15	4.4
0.3 $<$ dex $\leq$ 0.4	6	1.8
dex $>$ 0.4	19	5.6
no change	12	3.5

Note: This table compares the former and current oscillator strength values for 340 lines. The remaining 236 lines were either newly tabulated by the authors or no improved update was found for the former value.

Chapter 6

Conclusions and Future Work

6.1 Galaxies Foreground to Gravitationally Lensed Quasars

We have measured absorption lines of H I as well as metals in 5 absorbers along multiple sight lines in 4 GLQs. Our data (which provide H I and metal column densities for 2 lens galaxies) have doubled the sample of lens galaxies with measurements ofH I column densities and metal abundances along multiple sight lines. Combining our data with the literature, we find no strong correlation between the absolute value of the difference in the H I column densities, Fe II column densities, or Fe abundances and the separation between the sight lines at the absorber redshift for separations of 0-8 kpc. Absorbers toward fainter GLQ images show lower $N_{\rm H\,I}$ compared to those toward brighter images in 15 out of 23 cases, potentially suggesting that dust obscuration along the sight line may play a smaller role than the lensing configuration in determining the relative image brightnesses; however, a number of the available H I measurements are for absorbers along sight lines toward a quadruple lens, and therefore may not be independent of each other. Expanding the sample to a larger number of independent GLQ sight lines is essential to determine whether any statistically significant trend is present between H I column density difference and sight line separation.

The abundance gradients inferred from some GLQ absorbers are positive (i.e., inverted). Combining our results with measurements for quasar-galaxy pairs studied with integral field spectroscopy or long-slit spectroscopy, and other measurements of

abundance gradients from the literature, we find a tentative anti-correlation between the abundance gradient and the central metallicity of the galaxy, with metal-poor galaxies showing more positive abundance gradients, and metal-rich galaxies showing negative abundance gradients. Combining the total masses inferred from the astrometry of the quasar images relative to the lens galaxies with the mean [Fe/H] measurements from the quasar spectroscopy, we find that the lens galaxies lie below the MZR expected for early-type galaxies at $z = 0.7$ and the measurements for QGPs and gravitationally lensed galaxies. This difference may be caused in part by dust depletion of Fe and possibly also α-enhancement of O relative to Fe.

Observations of more DLA/sub-DLAs toward other GLQs are essential to examine how common the trends suggested by our small sample are. It is especially necessary to cover GLQs with small separations in order to put further constraints on small-scale structure in the absorbing gas. Additionally, it is essential to obtain higher resolution and shorter-wavelength UV observations to cover the Lyman series lines in order to obtain accurate H I column densities. It is also essential to obtain abundances of elements that do not deplete much on dust grains (e.g., S, O, Zn). For lens galaxies at $z < 1$, the measurements of S, O, Zn will require observations with UV and blue-sensitive spectrographs. Combining such measurements of undepleted elements with measurements of depleted elements in the same sight lines will allow a direct determination of differences in dust depletion between the sight lines. Combining these results with existing differential extinction measurements in GLQ sight lines (e.g., Falco et al. 1999; Motta et al. 2002) will offer fresh insights into the spatial variations in sizes and chemical composition of interstellar dust grains in galaxies. Finally, as noted earlier, some of the lens redshifts are uncertain, which limits its estimates of their distances, transverse separations of the sight lines, abundance gradients etc. It is thus crucial to determine accurate lens galaxy redshifts in all GLQ cases. Future IFS observations of GLQ fields should enable such measurements

with high efficiency and provide additional constraints on the lens galaxy masses and kinematics.

6.2 Regarding SBS 0909+532 AB

We examined both *HST*-STIS UV spectra and *Keck* HIRES optical spectra of the images of the doubly lensed quasar SBS 0909+532 at $z_{\rm QSO} = 1.37$ to study the variations in neutral hydrogen and metal absorption lines of the lens galaxy, a massive normal elliptical, at $z_{\rm lens} = 0.83$. We show a large difference in the column densities of both neutral hydrogen and metals at impact parameters of $r_{\rm A}$ ~3.2 kpc (0.26 r_e) and $r_{\rm B}$ ~5.7 kpc (0.48 r_e) from the lens galaxy (r_e ~12 kpc). We measure log $N_{\rm H\,I,A} \leq$ 18.18 cm^{-2} and log $N_{\rm H\,I,B} = 20.38 \pm 0.20$ cm^{-2} in the STIS spectra and find that SBS 0909+532 AB shows the highest fractional difference (~0.99) in H I of lensing galaxies for which H I measurements exist. High ionization in the region probed by sight line A is likely responsible for these differences in H I. The iron abundance is low in both sight lines, [Fe/H] > -1.18 in image A and [Fe/H] $= -1.36$ in image B, but could be higher due to likely dust depletions for which we are unable to account, given the limited wavelength range of the optical spectra. We performed ionization models and adopt a new lower limit of [Fe/H] ≥ -1.33 for sight line sight line A. We compare our results with those from recent studies that suggest that SNe Ia make significant contributions to the chemical enrichment of the environment of such galaxies (e.g., Zahedy et al. 2016, Zahedy et al. 2017, and Mernier et al. 2017). We find that all but one cloud component in both sight lines shows a supersolar $N_{\rm Fe\,II}/N_{\rm Mg\,II}$ value. We also determine an upper limit to the average abundance gradient of ≤ -0.02 dex kpc^{-1} based on [Fe II/H I] and a sight line separation of 8.9 kpc, showing that the metallicity declines with radius for the present measurements. We would like to emphasize that higher resolution UV spectra of the individual images could place a firm value on log $N_{\rm H\,I}$ for sight line A and allow column densities of additional metals

of higher ionization stages to be measured. These measurements would permit a more robust determination of the metallicity and ionization corrections.

Robust measurements of both volatile and refractory elements will enable determination of the differences in dust depletions between the different sight lines. These differences, together with differential dust extinction curves and measurements of the 2175 Å bump (already available for SBS 0909+532 AB from Motta et al. 2002) will allow a detailed look at differences in dust structure and composition on kpc-scales. Increasing the samples of UV and optical high-resolution spectra for other gravitationally lensed quasar sight lines is also essential to understand how common the findings from SBS 0909+532 AB are. Measurements of metallicities, relative abundances, dust depletions, and ionization parameters along the lensed sight lines for a large sample will improve understanding of the spatial scales of processes important for galaxy evolution, e.g., chemical enrichment and heating of the ISM by Type Ia vs. Type II supernovae and the processing of dust grains.

6.3 Atomic Spectroscopy

We have encouraged all future studies of interstellar, circumgalactic, and intergalactic absorption lines to use the revised oscillator strengths compiled in Cashman et al. (2017), emphasizing that it is especially important for the $\sim 22\%$ of the lines where the improvements of > 0.1 dex are larger than the typically quoted measurement uncertainties in metal column densities (usually < 0.05 dex for non-saturated lines observed with state-of-the-art high-resolution spectrographs used for such studies, e.g., Keck High-resolution Spectrograph, VLT UV Echelle Spectrograph, Magellan Inamori Kyocera Echelle spectrograph).

In the future we would also like to confirm the oscillator strengths of the 43 transitions of C I, Si I, P II, S I, Cl I, Ti I, Ti II, Mn I, Mn II, Fe II, Kr I, and Pb II for which the differences in the oscillator strengths are $\gtrsim 0.2$ dex. Such improvements

in atomic data are crucial to obtain accurate element abundances in distant galaxies, which are needed to quantitatively test models of cosmic chemical evolution. Indeed, improved atomic data will be invaluable for accurately interpreting the large samples of spectra of high-redshift quasars, gamma-ray bursts, and star-forming galaxies that will be enabled by future extremely large telescopes.

The feedback from our 2017 compilation has been very positive. The recent paper from Boissé & Bergeron (2019) gives new experimental values of oscillator strengths for many important Ni II lines that we identified as needing improvement. Additionally, Rynkun et al. (2019) produced new theoretical data for P II lines which addresses some accuracy issues we raised over some of the transitions, and Brown et al. (2018) have produced a new and accurate experimental oscillator strength for the P II transition at λ1301.8. This is an example of the importance of improving communications between astronomers and the laboratory astrophysics community. We currently have a project designed to evaluate the new theoretical values from Rynkun et al. (2019). We are evaluating the effects that log $\Delta f_{P\,II}$, and the subsequent changes in log $N_{P\,II}$ they would produce, would have on ionization effects for a sample of DLAs and sub-DLAs. Ideally, we would produce experimental values for the uncertain P II lines from available high resolution spectra, but the transitions are rare. Currently there are no more than two transitions available in any archive spectra, rendering the COG method for determining f-values unreliable.

Bibliography

Abazajian, K. N., Adelman-McCarthy, J. K., Agüeros, M. A., et al. 2009, ApJS, 182, 543

Andersen, T., Eriksen, P., Poulsen, O., & Ramanujam, P. S. 1979, Phys. Rev. A, 20, 2621

Andrews, S. M., Meyer, D. M., & Lauroesch, J. T. 2001, ApJ, 552, L73

Asplund M., Grevesse N., Sauval A. J., Allende Prieto C., & Kiselman D. 2004, A&A, 417, 751

Asplund, M., Grevesse, N., & Jacques Sauval, A. 2006, NuPhA, 777, 1

Asplund, M., Grevesse, N., Sauval, A. J., et al. 2009, ARA&A, 47, 481

Babyk, I. V., McNamara, B. R., Nulsen, P. E. J. et al. 2018, ApJ, 857, 32

Bahcall, J. N., Bergeron, J., Boksenberg, A., et al. 1993, ApJS, 87, 1B

Ballester, P. 1992, ESO Conference and Workshop Proceedings, 41, 177

Banfield, F. P. & Huber, M. C. E. 1973, ApJ, 186, 335

Bautista, M. A., Quinet, P., Palmeri, P., et al. 2009, A&A, 508, 1527

Belfiore, F., Maiolino, R., Tremonti, C., et al. 2017, MNRAS, 469, 151

Berg, T. A. M., Ellison, S. L., Sánchez-Ramirez, R. et al. 2016, MNRAS, 463, 3021

Bergeron, J., & Stasińska, G. 1986, A&A, 169, 1

Bergeson S. D., Mullman K. L., Wickliffe M. E. et al. 1996 ApJ, 464, 1044

Biémont, E., Garnir, H. P., Federman, S. R., Li, Z. S., & Svanberg, S. 1998, ApJ, 502, 1010

Biémont, E., Morton, D. C., & Quinet, P. 1998, MNRAS, 297, 713

Black, J. H. 1987, Interstellar Processes, 731

Blackwell, D. E., Ibbetson, P. A., Petford, A. D., & Shallis, M. J. 1979, MNRAS, 186, 633

Blackwell-Whitehead, R. J., Xu, H. L., Pickering, J. C., Nave, G., & Lundberg, H. 2005, MNRAS, 361, 1281

Blackwell-Whitehead, R. J., Lundberg, H., Nave, G. et al. 2006, MNRAS, 373, 1603

Blackwell-Whitehead, R. J., Pavlenko, Y. V., Nave, G., et al. 2011, A&A, 525, A44

Boissé, P., & Bergeron, J. 2019, A&A, 622, A140

Bordoloi, R., Rigby, J. R., Tumlinson, J. et al. 2016, MNRAS, 458, 1891

Bowen, D. V., & Chelouche, D. 2011, ApJ, 727, 47

Brown, M. S., Alkhayat, R. B., Irving, R. E., et al. 2018, ApJ, 868, 42

Brown, M. S., Federman, S. R., Irving, R. E., Cheng, S., & Curtis, L. J. 2009, ApJ, 702, 880

Butler, K. & Zeippen, C. J. 1991, J. Phys. IV (France) 1, C1-141–C1-152

Cardon, B. L., Smith, P. L., Scalo, J. M., Testerman, L., & Whaling, W. 1982, ApJ, 260, 395

Carroll, B. W., & Ostlie, D. A. 2006, An introduction to modern astrophysics and cosmology / B. W. Carroll and D. A. Ostlie. 2nd edition. San Francisco: Pearson

Carswell, R. F., & Webb, J. K. 2014, VPFIT manual

Carton, D., Brinchmann, J., Contini, T., et al. 2018, MNRAS, 478, 4293

Cashman F. H., Kulkarni, V. P., Kisielius, R. et al. 2017, ApJS, 230, 1

Cassidy, C. M., Hibbert, A., & Ramsbottom, C. A. 2016, A&A, 587, A107

Çelik, G., Ateş, Ş., & Erol, E. 2015, Can. J. Phys., 93, 1015

Chan, W. F., Cooper, G., Guo, X., Burton, G. R., & Brion, C. E. 1992, Phys. Rev. A, 46, 149

Chang, T. N. & Tang, X. 1990, J. Quant. Spectrosc. Radiat. Transfer, 43, 207

Charro, E. & Martin, I. 2000, ApJS, 126, 551

Chen, H.-W., Kennicutt T. C., & Rauch M., 2005, ApJ, 620, 703

Chen, B., Dai, X., Kochanek, C. S., & Chartas, G. 2013, preprint, arXiv:astro-ph/1306.0008

Chen, H.-W., Gauthier, J.-R., Sharon, K., et al. 2014, MNRAS, 438, 1435

Cheng, J., Rockoski, C. M., Morrison, H., L. et al. 2012, ApJ, 746, 149

Chengalur, J. N., & Kanekar, N. 2002, A&A 388, 383

Chi, H.-C., & Chou, H.-S. 2014, J. Phys. B, 47, 055002

Christensen, L., Moller, P., Fynbo, J. P. U., & Zafar, T. 2014, MNRAS, 445, 225

Churchill, C.W., Mellon, R. R., Charlton, J. C., & Vogt, S. S. 2003, ApJ, 593,203

Colón, C. & Alonso-Medina, A. 2001, Can. J. Phys. 79, 999

Conroy, C., van Dokkum, P. G., & Kravtsov, A. 2015, ApJ, 803, 77

Cooke, R., Pettini, M., Steidel, C. C., et al. 2010, MNRAS, 409, 679

Cresci, G., Mannucci, F., Maiolino, R. et al. 2010, Nature, 467, 811

Curtis L. J. & Smith, W. H. 1974, Phys. Rev. A, 9, 1537

Curtis, L. J. 1992, J. Opt. Soc. Am. B, 9, 5

Dai, X., & Kochanek, C. S. 2009, ApJ, 692, 677

Davidson, M. D., Volten, H., & Dönszelmann, A. 1990, A&A, 238, 452

Deb, N. C. & Hibbert, A. 2006, J. Phys. B: At. Mol. Opt. Phys., 39, 4301

Deb, N. C. & Hibbert, A. 2008, At. Data Nucl. Data Tables 94, 561

Deb, N. C. & Hibbert, A. 2009, At. Data Nucl. Data Tables 95, 184

Den Hartog, E. A., Lawler, J. E., Sobeck, J. S., Sneden, C., & Cowan, J. J. 2011, ApJS, 194, 35

Denicoló, G., Terlevich, R., & Terlevich, E. 2002, MNRAS, 330, 69 (D02)

Dessauges-Zavadsky M., Ellison S. L., & Murphy M. T., 2009, MNRAS, 396, L61

Doidge, P. S. 1995, Spectrochim. Acta, Part B 50, 209

Donnelly, M. P. & Hibbert, A. 2001, MNRAS. Soc. 321, 247

Donnelly, M. P., Hibbert, A., & Bell, K. L. 1999, Phys. Scr. 59, 32

Eigenbrod, A., Courbin, F., Meylan, G., Vuissoz, C., & Magain, P. 2006, A&A, 451, 759

Eigenbrod, A., Courbin, F., & Meylan, G. 2007, A&A, 465, 51

Ellison, S., Ibata, R., Pettini, M. et al. 2004, A&A, 414, 79

Ellison, S., Hennawi, J. F., Martin, C. L., & Sommer-Larsen, J. 2007, MNRAS, 378, 801

Ellison, S. L. Mendel, J. T., Patton, D. R., & Scudder, J. M. 2013, MNRAS, 435, 3627

Ellison, S. L., Sánchez, S. F., Ibarra-Medel, H., et al. 2018, MNRAS, 474, 2039

Falco, E. E., Impey, C. D., Kochanek, C. S., et al. 1999, ApJ, 523, 617

Fawcett, B. C. 1986, At. Data Nucl. Data Tables, 35, 203

Ferland, G. J., Chatzikos, M., Guzmán, F., et al. 2017, RMxAA, 53, 385

Friel, E. D., Janes, K. A., Tavarez, M., et al. 2002, AJ, 124, 2693

Froese Fischer, C. & Tachiev, G. 2003, Phys. Rev. A 68, 012507

Froese Fischer, C. & Tachiev, G. 2004, At. Data Nucl. Data Tables, 87, 1

Frose Fischer, C., & Zatsarinny, O., 2007, Theor. Chem. Accounts, 118, 623

Froese Fischer C., Tachiev G. & Irimia A. 2006, ADNDT, 92, 607

Froese Fischer, C. 2002, MCHF/MCDHF Collection, http://nlte.nist.gov/MCHF/

Froese Fischer, C. 2006, J. Phys. B, 39, 2159

Fuhr, J. R. & Wiese, W. L. 2005, CRC Handbook of Chemistry and Physics, 86th Edition, 10-93–10-155

Fuhr, J. R. & Wiese, W. L. 2006, JPCRD, 35, 1669

Fynbo J. P. U., Ledoux, C., Noterdaeme, P. et al. 2011, MNRAS, 413, 2481

Fynbo, J. P. U., Geier, S. J., Christensen, L., et al. 2013, MNRAS, 436, 361

Głowacki, L., & Migdałek, J. 2006, J. Phys. B 39, 1721

Gallazzi, A., Charlot, S., Brinchmann, J., & White, S. D. M. 2006, MNRAS, 370, 1106

Gallazzi, A., Bell, E. F., Zibetti, S., Brinchmann, J., & Kelson, D. D. 2014, ApJ, 788, 72

Gauthier, J.-R., Chen, H.-W., & Tinker, J. L. 2009, ApJ, 702, 50

Gauthier, J.-R., Chen, H.-W., & Tinker, J. L. 2010, ApJ, 716, 1263

Green, P. J., Myers, A. D., Barkhouse, W. A. et al. 2011, ApJ, 743, 81

Gregg, M. D., Wisotzki, L., Becker, R. H., et al. 2000, AJ, 119, 2535

Grossi, M., di Serego Alighieri, S., Giovanardi, C., et al. 2009, A&A, 498, 407

Hannaford, P. & McDonald, D. C. 1978, J. Phys. B 11, 1177

Hennawi, J., F. et al. 2006, AJ, 131, 1

Hibbert, A., Biémont, E., Godefroid, M. & Vaeck, N. 1991, J. Phys. B, 24, 3943

Hogg, D. W. 1999, e-print, arXiv:astro-ph/9905116

Huang, Y.-H., Chen, H.-W., Johnson, S. D., et al. 2016, MNRAS, 455, 1713

Huber, M. C. E. & Sandeman, R. J. 1980, A&A, 86, 95

Iwamoto, K., Brachwitz, F., Nomoto, K., et al. 1999, ApJS, 125, 439

Jönsson P., Andersson, M., Sabel, H., & Brage, T. 2006, J. Phys. B: At. Mol. Opt. Phys., 39, 1813

Jenkins, E. B., Bowen, D. V., Tripp, T. M., et al. 2005, ApJ, 623, 767

Jenkins, E. B. 2009, ApJ, 700, 1299

Jones, T., Ellis, R. S., Richard, J., & Julilo, E. 2013, ApJ, 765, 48

Jones, T., Schmidt, K. B., Treu, T., et al. 2015, AJ, 149, 107

Joye, W. A., & Mandel, E. 2003, Astronomical Society of the Pacific Conference Series, Vol. 295, Astronomical Data Analysis Software and Systems XII, ed. H. E. Payne, R. I. Jedrzejewski, & R. N. Hook, 489

Kacprzak G. G., Martin, C. L., Bouché, N. et al., 2014, ApJL, 792, L12

Kallman, T. R., & Palmeri, P. 2007, RvMP, 79, 79

Kayo, I., Inada, N., Oguri, M. et al. 2010, AJ, 139, 1614

Keeton, C. R., Kochanek, C. S., & Falco, E. E. 1998, ApJ, 509, 561

Kelleher D. E. & Podobedova, L. I. 2008, J. Phys. Chem. Ref. Data, 37, 1285

Kennicutt, R. C., Jr, Bresolin, F., & Garnett, D. R. 2003, ApJ, 591, 801

Kewley, L. J., & Dopita, M. A. 2002, ApJS, 142, 35 (KD02)

Kewley, L. J., & Ellison, S. L. 2008, ApJ, 681, 1183

Khaire, V., & Srianand, R. 2019, MNRAS, 484, 4174

Kisielius, R., Kulkarni V. P., Ferland, G. J., Bogdanovich P., & Lykins M. L. 2014, ApJ, 780, 76

Kisielius R., Kulkarni V. P., Ferland G. J., et al. 2015, ApJ, 804, 76

Kling, R. & Griesmann, U. 2000, ApJ, 531, 1173

Kluge, H.J. & Sauter, H. 1974, Z. Physik 270, 295

Kobulnicky H. A., & Kewley L. J., 2004, ApJ, 617, 240 (KK04)

Kobulnicky H. A., Kennicutt Jr. R. C., & Pizagno J. L., 1999, ApJ, 514, 544 (K99)

Kochanek, C. S. , Falco, E. E., Impey, C. D. et al. 2000, ApJ, 543, 131

Kochanek, C. S., Falco, E. E., Schild, R., et al. 1997, ApJ, 479, 678

Koopmans, L. V. E., Bolton, A., Treu, T., et al. 2009, ApJ, 703, L51

Kowalski, J., & Träger, F. 1976, Z Physik A, 278, 1

Kramida, A., Ralchenko, Yu., Reader, J., and NIST ASD Team (2015). NIST Atomic Spectra Database (ver. 5.3), [Online]. Available: http://physics.nist.gov/asd [2017, April 8]. National Institute of Standards and Technology, Gaithersburg, MD

Krogager, J.-K., Fynbo, J. P. U., Ledoux, C. et al. 2013, MNRAS, 433, 3091

Krogager, J.-K., Noterdaeme, P., O'Meara, J. M. et al. 2018, A&A, 619, A142

Kulkarni, V. P., Fall, S. M., Lauroesch, J. T. et al. 2005, ApJ, 618, 68

Kulkarni, V. P., Fall, S. M., Lauroesch, J. T. et al. 2005, ApJ, 618, 68

Kulkarni, V. P., Khare, P., Péroux, C. et al. 2007, ApJ, 661, 88

Kulkarni, V. P., Khare, P., Som, D., et al. 2010, NewA, 15, 735

Kulkarni, V. P., Som, D., Morrison, S., et al. 2015, ApJ, 815, 24

Kulkarni, V. P., Cashman, F. H., Lopez, S., et al. 2019, ApJ, 886, 83

Kurucz, R. L. 2016, http://kurucz.harvard.edu/atoms.html [December 29, 2016]

Lauer, S., Liebel, H., Vollweiler, F., et al. 1999, J. Phys. B, 32, 2015

Lauroesch, J. T., Meyer, D. M., & Blades, J. C. 2000, ApJ, 543, L43

Lawler, J. E., Guzman, A., Wood, M. P., Sneden, C., & Cowan, J. J. 2013, ApJS, 205, 11

Lawler, J. E., Sneden, C., & Cowan, J. J. 2015, ApJS, 220, 13

Lehár, J., Falco, E. E., Kochanek, C. S., et al. 2000, ApJ, 536, 584

Lehner, N., Howk, J. C., Tripp, T. M., et al. 2013, ApJ, 770, 138

Li, Z.-S., Norin, J., Persson, A., et al. 1999, Phys. Rev. A, 60, 198

Lopez, S., Reimers, D., Rauch, M., Sargent, W. L. W., & Smette, A. 1999, ApJ, 513, 598

Lopez, S., Reimers, D., Gregg, M. D., et al. 2005, ApJ, 626, 767

Lopez, S., Ellison, S., D'Odorico, S., & Kim, T.-S. 2007, A&A, 469, 61

Lopez, S., Tejos, N., Ledoux, C., et al. 2018, Nature, 554, 493

Loewenstein, M., Hayashida, K., Toneri, T., et al. 1998, ApJ, 497, 681

Lubin, L. M., Fassnacht, C. D., Readhead, A. C. S., et al. 2000, AJ, 119, 451

Luck, R. E., & Lambert, D. L. 2011, AJ, 142, 136

Lundberg, H., Hartman, H., L. Engström, L., et al. 2016, MNRAS, 460, 356

Lurio, A., DeZafra, R. L., Goshen, R. J. 1964, Phys. Rev. A, 134, 1198

Lykins, M. L., Ferland, G. J., Kisielius R., et al. 2015, ApJ, 807, 118

Madau, P., & Dickinson, M. 2014, ARAA, 52, 415

Martin, G. A., Fuhr, J. R., & Wiese, W. L. 1988, J. Phys. Chem. Ref. Data 17, Suppl. 3

Martinson, I., L. J. Curtis, L. J., Huldt, S. 1979, Phys. Scripta, 19, 17

Mathews, W. G., & Brighenti, F. 2003, ARA&A, 41, 191

Meiring, J. D., Lauroesch, J. T., Kulkarni, V. P., et al. 2007, MNRAS, 376, 557

Meiring, J. D., Kulkarni, V. P., Lauroesch, J. T., et al. 2008, MNRAS, 384, 1015

Meiring, J. D., Kulkarni, V. P., Lauroesch, J. T., et al. 2009, MNRAS, 393, 1513

Meiring, J. D., Lauroesch, J. T., Kulkarni, V. P., et al. 2009, MNRAS, 397, 2037

McClure-Griffiths, N. M. 2010, ASPC, 438, 133

McElroy, T., & Hibbert, A. 2005, Phys. Scripta, 71, 479

McGaugh S., 1991, ApJ, 380, 140

Mediavilla, E., Muñoz, J. A., Kochanek, C. S. et al. 2005, ApJ, 691, 749

Mendoza, C., Eissner, W., Le Dourneuf, M., & Zeippen, C. J. 1995, TOPBASE Opacity Project

Mernier, F., de Plaa, J., Kaastra, J. S., et al. 2017, A&A, 603, A80

Michalitsianos, A. G., Dolan, J. F., Kazanas, D., et al. 1997, ApJ, 474, 598

Migdalek, J., & Kim, Y.-K. 1998, J. Phys. B, 31, 1947

Mitchell, C. J. 1975, J. Phys. B, 8, 25

Monier, E. M., Turnshek, D. A., & Rao, S. 2009, MNRAS, 397, 943

Monier, E. M., Turnshek, D. A., & Lupie, O. L. 1998, ApJ, 496, 177

Moos, H. W., Cash, W. C., Cowie, L. L., et al. 2000, ApJ, 538, L1

Morgan, N. D., Gregg, M. D., Wisotzki, L. et al. 2003, AJ, 126, 696

Morris, S. L., Weymann, R. J., Savage, B. D., & Gilliland, R. L. 1991, ApJ, 377, L21

Morton D. C. 2003, ApJS, 149, 205

Motta, V., Mediavilla, E., Muñoz, J. A., et al. 2002, ApJ, 574, 719

Mullman, K. L., Lawler, J. E., Zsargó, J., & Federman, S. R. 1998, ApJ, 500, 1064

Nahar, S. N. & Pradhan, A. K. 1993, J. Phys. B, 26, 1109

Neeleman, M., Prochaska, J. X., Ribaudo, J., et al. 2016, ApJ, 818, 113

Nestor, D. B., Pettini, M., Hewett, P. C., et al. 2008, MNRAS, 390, 1670

Nilsson, H., Ljung, G., Lundberg, H., & Nielsen, K. E. 2006, A&A, 445, 1165

O'Brian, T. R., Wickliffe, M. E., Lawler, J. E., Whaling, W., & Brault, J. W. 1991, J. Opt. Soc. Am. B 8, 1185

Ofek, E. O., Maoz, D., Rix, H.-W., Kochanek, C. S., & Falco, E. E. 2006, ApJ, 641, 70

Oliver, P. & Hibbert, A. 2013, At. Data Nucl. Data Tables 99, 459

Oosterloo, T., Morganti, R., Crocker, A., et al. 2010, MNRAS, 409, 500

Oscoz, A., Serra-Ricart, M., Mediavilla, E., et al. 1997, ApJL, 491, L7

Ostrovskii, Yu. I. & Penkin, N. P. 1961, Opt. Spektrosk. 10(4), 429

Ouellette, N. N.-Q. et al. 2017, ApJ, 843, 74

Pei, Y. C., Fall, S. M., & Hauser, M. G. 1999, ApJ, 522, 604

Péroux, C., Dessauges-Zavadsky, M., D'Odorico, S., Kim, T.-S., & McMahon, R. G. 2003, MNRAS, 345, 480

Péroux, C., Meiring, J. D., Kulkarni, V. P., et al. 2006, MNRAS, 372, 369

Péroux, C., Bouché, N., Kulkarni, V. P., York, D. G., & Vladilo, G. 2011a, MNRAS, 410, 2237

Péroux, C., Bouché, N., Kulkarni, V. P., York, D. G., & Vladilo, G. 2011b, MNRAS, 410, 2251

Péroux, C., Bouché, N., Kulkarni, V. P., York, D. G., & Vladilo, G. 2012, MNRAS, 419, 3060

Péroux, C., Bouché, N., Kulkarni, V. P., & York, D. G. 2013, MNRAS, 436, 2650

Péroux, C., Kulkarni, V. P., & York, D. G. 2014, MNRAS, 437, 3144

Péroux, C., Quiret, S., Rahmani, H., et al. 2016, MNRAS, 457, 903

Péroux, C., Rahmani, H., Quiret, S., et al. 2017, MNRAS, 464, 2053

Péroux, C., Rahmani, H., Arrigoni Battaia, F., et al. 2018, MNRAS, 479, L50

Pagan, C. J. B., Raineri, M., Bredice, F., et al. 1996, J. Quant. Spectrosc. Rad. Transfer, 55, 163

Palćhikov, V. G. 1998, Phys. Scr., 57, 581

Parkinson, W. H., Reeves E. M., Tomkins, F. S. 1976, J. Phys. B, 9, 157

Peach, G., Saraph, H. E. & Seaton, M. J. 1988, J. Phys. B, 21, 3669

Pérez-Montero, E., García-Benito, R., Vílchez, J. M., et al. 2016, A&A, 595, A62

Petitjean, P., Webb, J. K., Rauch, M., et al. 1993, MNRAS, 262, 499

Pettini, M., Rix, S. A., Steidel, C. C., et al. 2002, ApJ, 569, 742

Pettini, M. 2004, Cosmochemistry. The Melting Pot of the Elements, 257

Pettini, M. & Pagel, B. E. J. 2004, MNRAS, 348, L59

Pettini, M. 2006, in 'The Fabulous Destiny of Galaxies: Bridging Past and Present', eds. V. Le Brun et al. (arXiv:astro-ph/0603066)

Pickering, J. C., Johansson, S., & Smith, P. L. 2001, A&A, 377, 361

Pickering, J. C., Thorne, A. P., & Perez, R. 2001, ApJS, 132, 403

Pinnington, E. H., Bahr, J. L., & Irwin, D. J. G. 1981, Phys. Lett., 84A, 247

Pipino, A., & Matteucci, F. 2011, A&A, 530, A98

Popping, G., Somerville, R. S., & Trager, S. C. 2014, MNRAS, 442, 2398

Poudel, S., Kulkarni, V. P., Cashman, F. H., et al. 2019, MNRAS, 2603

Prochaska J. X., Gawiser E., Wolfe A. M., et al. 2003b, ApJ, 147, 227

Prochaska, J. X., Wolfe, A. M., Howk, J. C., et al. 2007, ApJS, 171, 29

Prochaska, J. X., & Wolfe, A. M. 2009, ApJ, 696, 1543

Queyrel J. et al., 2012, A&A, 539, 93

Quider, A. M., Nestor, D. B., Turnshek, D. A., et al. 2011, AJ, 141, 137

Quinet, P., Biémont, E., Palmeri, P., & Xu, H. L. 2007, J. Phys. B 40, 1705

Quiret, S., Péroux, C., Zafar, T., et al. 2016, MNRAS, 458, 4074

Raassen, A. J. J. & Uylings, P. H. M. 1997, A&AS, 123, 147

Raassen, A. J. J. & Uylings, P. H. M. 1998, J. Phys. B, 31, 2137

Raassen, A. J. J., Pickering, J. C., & Uylings, P. H. M. 1998, A&AS, 130, 541

Rafelski, M., Wolfe, A. M., Prochaska, J. X., Neeleman, M., & Mendez, A. J. 2012, ApJ, 755, 89

Rafelski, M., Neeleman, M., Fumagalli, M., et al. 2014, ApJL, 782, L29

Rahmani, H., Péroux, C., Turnshek, D. A., et al. 2016, MNRAS, 463, 980

Rao, S. M. & Turnshek, D. A. 2000, ApJ, 130, 1

Rao, S. M., Turnshek, D. A., & Nestor, D. B. 2006, ApJ, 636, 610

Rauch, M., Miralda-Escudé, J., Sargent, W. L. W., et al. 1997, ApJ, 489, 7

Rauch, M., Sargent, W. L. W., & Barlow, T. A. 1999, ApJ, 515, 500

Rauch, M., Sargent, W. L. W., & Barlow, T. A. 2001, ApJ, 554, 823

Remy, M., Claeskens, J.-F., Surdej, J., et al. 1998, NewA, 3, 379

Riediger, R., Petitjean, P., & Mucket, J. P. 1998, A&A, 329, 30

Rogerson, J. A., & Hall, P. B. 2012, MNRAS, 421, 971

Rogerson, J. B., Spitzer, L., Drake, J. F., et al. 1973, ApJ, 181, L97

Rosolowsky, E., & Simon, J. D. 2008, ApJ, 675, 1213

Rubin, K. H. R., Prochaska, J. X., Koo, D. C., et al. 2010, ApJ, 712, 574

Rubin, K. H. R., Diamond-Stanic, A. M., Coil, A. L., et al. 2018a, ApJ, 853, 95

Rubin, K. H. R., O'Meara, J. M., Cooksey, K. L., et al. 2018b, ApJ, 859, 146

Ruczkowski, J., Elantkowska, M., & Dembczyński, J. 2014, J. Quant. Spectrosc. Radiat. Transfer 149, 168

Rupke, D. S. N., Kewley, L. J., & Chien, L.-H. 2010, ApJ, 723, 1255

Rynkun, P., Radžiūtė, L., Gaigalas, G., et al. 2019, A&A, 622, A167

Safronova, M. S., & Safronova, U. I. 2011, Phys. Rev. A 83, 012503

Safronova, U. I., Cowan, T. R., & Safronova, M. S. 2006, J. Phys. B: At. Mol. Opt. Phys. 39, 749

Safronova, M. S., Safronova, U. I., & Johnson, W. R. 2005, Phys. Rev. A 71, 052506

Sánchez, S. F., Rosales-Ortega, F. F., Iglesias-Páramo, J., et al. 2014, A&A, 563, A49

Savage, B. D., & Sembach, K. R. 1991, ApJ, 379, 245

Savage, B. D. & Sembach, K. R. 1996, ARA&A, 34, 279

Schectman, R. M., Federman, S. R., Brown, M., et. al. 2005, ApJ, 621, 1159

Schneider, P., Ehlers, J., & Falco, E. E. 1992, Gravitational Lenses (Berlin: Springer)

Schulte-Ladbeck, R. E., Rao, S. M., Drozdovsky, I. O., Turnshek, D. A., & Pettini, M. 2004, ApJ, 600, 613

Scudder, J. M., Ellison, S. L., Torrey, P, Patton, D. R., & Mendel, J. T. 2012, MNRAS, 426, 549

Serra, P., Oosterloo, T., Morganti, R., et al. 2012, MNRAS, 422, 1835

Shabanova, L. N. & Khlyustalov, A. N. 1985, Opt. Spectrosc. 59, 123

Shabanova, N. L. 1963, Opt. Spektrosk. 15(6), 828

Shirai, T., Reader, J., Kramida, A. E., & Sugar, J. 2007, J. Phys. Chem. Ref. Data 36, 509

Siegel, W., Migdalek, J., & Kim, Y.-K. 1998, At. Data Nucl. Data Tables 68, 303

Smette, A., Surdej, J., Shaver, P. A., et al. 1992, ApJ, 389, 39

Smith, P. L. & Kühne, M. 1978, Proc. R. Soc. London, Ser. A 362, 263

Smith, P. L., Huber, M. C. E., Tozzi, G. P., et al. 1987, ApJ, 322, 573

Sobeck, J. S., Lawler, J. E., & Sneden, C. 2007, ApJ, 667, 1267

Som, D., Kulkarni, V. P., Meiring, J., et al. 2013, MNRAS, 435, 1469

Som, D., Kulkarni, V. P., Meiring, J., et al. 2015, ApJ, 806, 25

Somerville, R. S., Primack, J. R., & Faber, S. M. 2001, MNRAS, 320, 504

Spangler, S. R. 2001, SSRev, 99, 261

Spitzer, L., & Jenkins, E. B. 1975, ARA&A, 13, 133

Straka, L. A., Johnson, S., York, D. G. et al. 2016, MNRAS, 458, 3760

Surdej, J., Claeskens, J.-F., Remy, M., et al. 1997, A&A, 327, L1

Swinbank A. M., Sobral D., Smail I., et al. 2012, MNRAS, 426, 935

Tachiev, G., & Froese Fischer, C. 2001, Can. J. Phys., 79, 955

Tayal, S. S. & Zatsarinny, O. 2010, ApJSS, 188, 32

Tayal, S. S. 2009, Phys. Scr. 79, 015303

Thorp, M. D., Ellison, S. L., Simard, L., Sánchez, S. F., & Antonio, B. 2019, MNRAS, 482, L55

Tissera, P. B., Machado, R. E. G., Carollo, D., et al. 2018, MNRAS, 473, 1656

Toner, A. & Hibbert, A. 2005, MNRAS, 361, 673

Troncoso, P., Maiolino, R., Sommariva, V., et al. 2014, A&A, 563, A58

Tumlinson, J., Thom, C., Werk, J. K., et al. 2013, ApJ, 777, 59

Verner, D. A., Barthel, P. D., & Tytler, D. 1994, A&AS, 108, 287

Vujnović, V., Blagoev, K., Fürböck, C., Neger, T., & Jäger, H. 2002, A&A, 388, 704

Wang, H., Li, J., Wang, X. T., et al. 1997, Phys. Rev. A 55, R1569

Werk, J. K., Prochaska, J. X., Cantalupo, S. et al. 2016, ApJ, 833, 54

Wolfe, A. M., Turnshek, D. A., Smith, L. J., & Cohen, R. D. 1986, ApJS, 61, 249

Wood, M. P., Lawler, J. E. Sneden, C., & Cowan, J. J. 2014, ApJS, 211, 20

Wucknitz, O., Wisotzki, L., Lopez, S., & Gregg, M. D. 2003, A&A, 405, 445

Yan, Z.-C., Tambasco, M., & Drake, G. W. F. 1998, Phys. Rev. A, 57, 1652

York, D. G., Adelman, J., Anderson, J. E., Jr., et al. 2000, AJ, 120, 1579

York, D. G. 1974, ApJ, 193, L127

Young, L. M., Scott, N., Serra, P., et al. 2014, MNRAS, 444, 3408

Yuan, T.-T., Kewley, L. J., Swinbank, A. M., et al. 2011, ApJL, 732, L14

Zafar, T., Péroux, C., Popping, A., et al. 2013, A&A, 556, 141

Zahedy, F. S., Chen, H.-W., Rauch, M., et al. 2016, MNRAS, 458, 2423

Zahedy, F. S., Chen, H.-W., Rauch, M., et al. 2017, ApJL, 846, L29

Zaritsky, D., Kennicutt, R. C., & Huchra, J. P. 1994, ApJ, 420, 87

Zatsarinny, O. & Bartschat, K. 2006, J. Phys. B: At. Mol. Opt. Phys., 39, 2861

Zatsarinny, O. & Bartschat, K. 2009, Phys. Scr. T134, 014020

Zatsarinny, O. & Froese Fischer, C. 2002, J. Phys. B, 35, 4669

Zatsarinny, O., Bartschat, K., Gedeon, S., et al. 2009, Phys. Rev. A, 79, 052709

Zinner, G., Binnewies, T., Riehle, F., & Tiemann E. 2000, Phys. Rev. Lett. 85, 2292

Appendix A

References Abbreviated in Table 5.1

Abbreviation	Citation	Ion
AEP79	Andersen et al. 1979	Ga II; Ge III
BFI09	Brown et al. 2009	Cu II
BGF98	Biémont et al. 1998	S I
BH73	Banfield & Huber 1973	Fe I
BIP79	Blackwell et al. 1979	Fe I
BLN06	Blackwell-Whitehead et al. 2006	Ti I
BMQ98	Biémont et al. 1998	Ge II
BMW96	Bergeson et al. 1996	Fe II
BPN11	Blackwell-Whitehead et al. 2011	Mn I
BQP09	Bautista et al. 2009	Si II
BXP05	Blackwell-Whitehead et al. 2005	Mn I
BZ91	Butler & Zeippen 1991	O I
C92	Curtis 1992	Ge III
CAE15	Çelik et al. 2015	Cu I
CAM01	Colón & Alonso-Medina 2001	Pb II
CCG92	Chan et al. 1992	Kr I
CHR16	Cassidy et al. 2016	Ni II
CM00	Charro & Martín 2000	Si II
CS74	Curtis & Smith 1974	Si II
CSS82	Cardon et al. 1982	Co I
CT90	Chang & Tang 1990	Mg I
D95	Doidge 1995	Cu I
DH01	Donnelly & Hibbert 2001	Fe II
DH08	Deb & Hibbert 2008	S I
DH09	Deb & Hibbert 2009	Fe III
DHB99	Donnelly et al. 1999	Cu II
DHL11	Den Hartog et al. 2011	Mn II
DVD90	Davidson et al. 1990	Al I
F86	Fawcett 1986	P I
FF02	Froese Fischer 2002	Na I
FF06	Froese Fischer 2006	C I
FFT04	Froese Fischer & Tachiev 2004	C II, III; N I, II, III; O I

Abbreviation	Citation	Ion
FFT06	Froese Fischer et al. 2006	Na I; Mg I, II; Al I, II, III; Si I, III, IV; P I, II, III, IV, V; S III, IV, VI; Cl IV; Ar I, II
FW06	Fuhr & Wiese 2006	Fe II
HBG91	Hibbert et al. 1991	O I
HM78	Hannaford & McDonald 1978	Cu I
HS80	Huber & Sandeman 1980	Ni I
K16	Kurucz 2016	Fe II, Cr III, Mn I, Co III, Zn I
KG00	Kling & Griesmann 2000	Mn II
KKF14	Kisielius et al. 2014	S II
KKF15	Kisielius et al. 2015	Zn II
KP08	Kelleher & Podobedova 2008	Si I
KT76	Kowalski & Träger 1976	Zn I
LGW13	Lawler et al. 2013	Ti I
LHE16	Lundberg et al. 2016	Ti II
LLV99	Lauer et al. 1998	Kr II
LNP99	Li et al. 1999	Ge I
LSC15	Lawler et al. 2015	Co I
MEL95	Mendoza et al. 1995	Al I
MFW88	Martin et al. 1988	Cr I, Mn I
MLZ98	Mullman et al. 1998	Co II
NLL06	Nilsson et al. 2006	Cr II
NP93	Nahar & Pradhan 1993	Si I
OH13	Oliver & Hibbert 2013	Cl I
OWL91	O'Brian et al. 1991	Fe I
PBI81	Pinnington et al. 1981	Ge IV
PJS01	Pickering et al. 2001	Fe II
PRB96	Pagan et al. 1996	Kr VI
PRT76	Parkinson et al. 1976	Ca I
PSS88	Peach et al. 1988	N V, O VI
QBP07	Quinet et al. 2007	Pb II
RPU98	Raassen et al. 1998	Co II
RU97	Raassen & Uylings 1997	Ti III
RU98	Raassen & Uylings 1998	Cr II, Fe II
SFB05	Schectman et al. 2005	Cl II, III
SHT87	Smith et al. 1987	Si I
SK78	Smith & Kühne 1978	Ti I
SK85	Shabanova & Khlyustalov 1985	K I
SLS07	Sobeck et al. 2007	Cr I
SMK98	Siegel et al. 1998	Mg II
SRK07	Shirai et al. 2007	Ga I, III
SS11	Safronova & Safronova 2011	Ca II
SSJ05	Safronova et al. 2005	Pb II
TH05	Toner & Hibbert 2005	Mn II

Abbreviation	Citation	Ion
VBF02	Vujnović et al. 2002	Al I
WLS14	Wood et al. 2014	Ni I
WWW97	Wang et al. 1997	K I
YTD98	Yan et al. 1998	C IV
ZB09	Zatsarinny & Bartschat 2009	Kr I
ZBG09	Zatsarinny et al. 2009	Mg I
ZBR00	Zinner et al. 2000	Ca I
ZF02	Zatsarinny & Froese Fischer 2002	C I

Appendix B

Data for key transitions

This appendix gives the line identifications, observed wavelengths $\lambda_{\rm vac}$ (Å), Ritz wavelengths $\lambda_{\rm Ritz}$ (Å), absorption oscillator strengths f, and the accuracy grades (column label Acc) for key transitions important in absorption line studies of the ISM, CGM, and IGM. It is also the full version of Table 5.1. The reference source for the atomic data is in the column labeled Ref. The complete references, organized by code can be found in Appendix A. Vacuum wavelengths with precision greater than four decimal places have been truncated to four decimal places because of space restrictions. The full wavelengths are available in the machine readable table in the electronic form of Cashman et al. (2017).

Z	Ion	Upper level	$\lambda_{\rm vac}$ (Å)	$\lambda_{\rm Ritz}$ (Å)	$g_{\rm l}$	$g_{\rm u}$	f	$\log(gf)$	Acc	Ref
6	C I	lower level 2s^2^2p^2^ ^3^P__0__								
6	C I	2s^2^2p3s ^3^P^o^__1__	1656.928	1656.929	1	3	1.43E-01	-0.845	A	FF06
6	C I	2s2p^3^ ^3^D^o^__1__	1560.31	1560.309	1	3	7.16E-02	-1.145	A	FF06
6	C I	2s2p^3^ ^3^P^o^__1__		1328.834	1	3	5.80E-02	-1.236	B	FF06
6	C I	2s^2^2p4s ^3^P^o^__1__		1280.135	1	3	2.61E-02	-1.583	B+	FF06
6	C I	2s^2^2p3d ^3^D^o^__1__	1277.245	1277.245	1	3	9.22E-02	-1.035	A	FF06
6	C I	2s^2^2p4s ^1^P^o^__1__		1276.483	1	3	3.69E-03	-2.433	C+	FF06

Z	Ion	Upper level	λ_{vac} (Å)	λ_{Ritz} (Å)	g_l	g_u	f	$\log(gf)$	Acc	Ref
6	C I	2s^2^2p3d ^3^P^o^_1_		1260.735	1	3	4.07E-02	-1.39	B	FF06
6	C I	2s^2^2p5s ^3^P^o^_1_		1193.995	1	3	1.25E-02	-1.903		ZF02
6	C I	2s^2^2p4d ^3^D^o^_1_	1193.031	1193.031	1	3	4.09E-02	-1.388	B+	ZF02
6	C I	2s^2^2p5s ^1^P^o^_1_		1192.218	1	3	1.37E-03	-2.863		ZF02
6	C I	2s^2^2p4d ^3^P^o^_1_		1188.833	1	3	1.24E-02	-1.907		ZF02
6	C I	2s^2^2p6s ^3^P^o^_1_		1158.324	1	3	6.56E-03	-2.183		ZF02
6	C I	2s^2^2p5d ^3^D^o^_1_	1157.91	1157.91	1	3	2.12E-02	-1.674		ZF02
6	C I	2s^2^2p5d ^3^P^o^_1_		1155.809	1	3	4.93E-03	-2.307		ZF02
6	C I	2s^2^2p7s ^3^P^o^_1_		1140.01	1	3	3.57E-03	-2.447		ZF02
6	C I	2s^2^2p6d ^3^D^o^_1_		1139.792	1	3	1.23E-02	-1.91		ZF02
6	C I	2s^2^2p6d ^3^P^o^_1_		1138.383	1	3	2.41E-03	-2.618		ZF02
6	C I	2s^2^2p8s ^3^P^o^_1_		1129.317	1	3	1.99E-03	-2.701		ZF02
6	C I	2s^2^2p7d ^3^D^o^_1_		1129.196	1	3	7.72E-03	-2.112		ZF02
6	C I	2s^2^2p7d ^1^P^o^_1_		1128.171	1	3	1.05E-03	-2.979		ZF02
6	C I	2s^2^2p7d ^3^P^o^_1_		1128.075	1	3	1.36E-03	-2.866		ZF02
6	C I	2s^2^2p9s ^3^P^o^_1_		1122.518	1	3	1.15E-03	-2.939		ZF02
6	C I	2s^2^2p8d ^3^D^o^_1_		1122.438	1	3	5.12E-03	-2.291		ZF02
6	C I	2s^2^2p9d ^3^D^o^_1_		1117.865	1	3	3.55E-03	-2.45		ZF02
6	C II	lower level 2s^2^2p ^2^P^o^_1/2_								
6	C II	2s2p^2^ ^2^D_3/2_	1334.532	1334.532	2	4	1.29E-01	-0.589		FFT04
6	C II	2s2p^2^ ^2^S_1/2_	1036.337	1036.337	2	2	1.19E-01	-0.624		FFT04
6	C III	lower level 1s^2^2s^2^ ^1^S_0_								
6	C III	1s^2^2s2p ^1^P^o^_1_	977.03	977.02	1	3	7.58E-01	-0.121		FFT04
6	C IV	lower level 1s^2^2s ^2^S_1/2_								
6	C IV	1s^2^2p ^2^P^o^_1/2_	1550.774	1550.772	2	2	9.48E-02	-0.722	A	YTD98
6	C IV	1s^2^2p ^2^P^o^_3/2_	1548.202	1548.187	2	4	1.90E-01	-0.42	A	YTD98
7	N I	lower level 2s^2^2p^3^ ^4^S^o^_3/2_								
7	N I	2s^2^2p^2^(^3^P)3s ^4^P_1/2_	1200.71	1200.71	4	2	4.32E-02	-0.762	A	FFT04
7	N I	2s^2^2p^2^(^3^P)3s ^4^P_3/2_	1200.223	1200.223	4	4	8.69E-02	-0.459	A	FFT04
7	N I	2s^2^2p^2^(^3^P)3s ^4^P_5/2_	1199.55	1199.55	4	6	1.32E-01	-0.278	A	FFT04

Z	Ion	Upper level	$\lambda_{\rm vac}$ (Å)	$\lambda_{\rm Ritz}$ (Å)	$g_{\rm l}$	$g_{\rm u}$	f	$\log(gf)$	Acc	Ref
7	N I	2s2p^4^ ^4^P_5/2_	1134.98	1134.98	4	6	4.16E-02	-0.779	B	FFT04
7	N I	2s2p^4^ ^4^P_3/2_	1134.415	1134.415	4	4	2.87E-02	-0.941	B	FFT04
7	N I	2s2p^4^ ^4^P_1/2_	1134.165	1134.165	4	2	1.46E-02	-1.234	B	FFT04
7	N I	2s^2^2p^2^(^3^P)4s ^4^P_1/2_	965.041	965.041	4	2	3.86E-03	-1.812	A	FFT04
7	N I	2s^2^2p^2^(^3^P)4s ^4^P_3/2_	964.626	964.626	4	4	7.90E-03	-1.5	A	FFT04
7	N I	2s^2^2p^2^(^3^P)4s ^4^P_5/2_	963.99	963.99	4	6	1.24E-02	-1.304	A	FFT04
7	N I	2s^2^2p^2^(^3^P)3d ^2^F_5/2_		954.104	4	6	4.00E-03	-1.796	B+	FFT04
7	N I	2s^2^2p^2^(^3^P)3d ^4^P_5/2_	953.97	953.97	4	6	3.31E-02	-0.879	B	FFT04
7	N I	2s^2^2p^2^(^3^P)3d ^4^P_3/2_	953.655	953.655	4	4	2.47E-02	-1.005	B	FFT04
7	N I	2s^2^2p^2^(^3^P)3d ^4^P_1/2_	953.415	953.415	4	2	1.29E-02	-1.286	B	FFT04
7	N I	2s^2^2p^2^(^3^P)3d ^4^D_3/2_		952.415	4	4	1.97E-03	-2.103	B	FFT04
7	N I	2s^2^2p^2^(^3^P)3d ^4^D_5/2_		952.303	4	6	2.29E-03	-2.039	B	FFT04
7	N II	lower level 2s^2^2p^2^ ^3^P_0_								
7	N II	2s2p^3^ ^3^D^o^_1_	1083.99	1083.99	1	3	1.11E-01	-0.956	A	FFT04
7	N II	2s2p^3^ ^3^P^o^_1_	915.612	915.612	1	3	1.59E-01	-0.798	A	FFT04
7	N III	lower level 2s^2^2p ^2^P^o^_1/2_								
7	N III	2s2p^2^ ^2^D_3/2_	989.79	989.799	2	4	1.23E-01	-0.609	B	FFT04
7	N V	lower level 1s^2^2s ^2^S_1/2_								
7	N V	1s^2^2p ^2^P^o^_1/2_	1242.804	1242.804	2	2	7.77E-02	-0.809	A	PSS88
7	N V	1s^2^2p ^2^P^o^_3/2_	1238.821	1238.821	2	4	1.56E-01	-0.505	A	PSS88
8	O I	lower level 2s^2^2p^4^ ^3^P_2_								
8	O I	2s^2^2p^3^(^4^S)3s ^3^S^o^_1_	1302.168	1302.168	5	3	4.80E-02	-0.62		FFT04
8	O I	2s^2^2p^3^(^4^S)4s ^3^S^o^_1_	1039.23	1039.23	5	3	9.07E-03	-1.343		FFT04
8	O I	2s^2^2p^3^(^4^S)3d ^3^D^o^_2_	1025.762	1025.763	5	5	2.91E-03	-1.837		FFT04
8	O I	2s^2^2p^3^(^4^S)3d ^3^D^o^_3_	1025.762	1025.762	5	7	1.63E-02	-1.088		FFT04
8	O I	2s^2^2p^3^(^2^D)3s ^3^D^o^_3_	988.773	988.773	5	7	4.64E-02	-0.635	B	HBG91
8	O I	2s^2^2p^3^(^2^D)3s ^3^D^o^_2_		988.655	5	5	8.46E-03	-1.374	B	HBG91
8	O I	2s^2^2p^3^(^4^S)5s ^3^S^o^_1_	976.448	976.448	5	3	3.31E-03	-1.781	C+	BZ91
8	O I	2s^2^2p^3^(^4^S)4d ^3^D^o^_3_	971.738	971.738	5	7	1.16E-02	-1.237	C+	HBG91
8	O I	2s^2^2p^3^(^4^S)4d ^3^D^o^_2_	971.738	971.738	5	5	2.07E-03	-1.986	C+	HBG91

Z	Ion	Upper level	$\lambda_{\rm vac}$ (Å)	$\lambda_{\rm Ritz}$ (Å)	$g_{\rm l}$	$g_{\rm u}$	f	$\log(gf)$	Acc	Ref
8	O I	2s^2^2p^3^(^4^S)6s ^3^S^o^_1_		950.885	5	3	1.58E-03	-2.103	C	BZ91
8	O I	2s^2^2p^3^(^4^S)5d ^3^D^o^_3_	948.686	948.686	5	7	5.31E-03	-1.576	C+	BZ91
8	O I	2s^2^2p^3^(^4^S)6d ^3^D^o^_3_		936.629	5	7	3.06E-03	-1.816	C+	BZ91
8	O I	2s^2^2p^3^(^4^S)7d ^3^D^o^_3_		929.517	5	7	1.92E-03	-2.017	C	BZ91
8	O I	2s^2^2p^3^(^4^S)8d ^3^D^o^_3_		924.95	5	7	1.30E-03	-2.188	C	BZ91
8	O VI	lower level 1s^2^2s ^2^S_1/2_								
8	O VI	1s^2^2p ^2^P^o^_1/2_		1037.613	2	2	6.60E-02	-0.879	A	PSS88
8	O VI	1s^2^2p ^2^P^o^_3/2_		1031.912	2	4	1.33E-01	-0.576	A	PSS88
11	Na I	lower level 2p^6^3s ^2^S_1/2_								
11	Na I	2p^6^3p ^2^P^o^_1/2_	5897.5581	5897.558	2	2	3.24E-01	-0.188	AA	FFT06
11	Na I	2p^6^3p ^2^P^o^_3/2_	5891.5833	5891.583	2	4	6.50E-01	0.114	AA	FFT06
11	Na I	2p^6^4p ^2^P^o^_1/2_	3303.93	3303.93	2	2	4.32E-03	-2.063	B+	FFT06
11	Na I	2p^6^4p ^2^P^o^_3/2_	3303.32	3303.319	2	4	8.80E-03	-1.754	A	FFT06
11	Na I	2p^6^5p ^2^P^o^_3/2_	2853.649	2853.649	2	4	1.28E-03	-2.592	B+	FF02
12	Mg I	lower level 2p^6^3s^2^ ^1^S_0_								
12	Mg I	2p^6^3s3p ^1^P^o^_1_	2852.965	2852.964	1	3	1.71E+00	0.233	A	FFT06
12	Mg I	2p^6^3s4p ^1^P^o^_1_	2026.477	2026.477	1	3	1.13E-01	-0.947	B+	FFT06
12	Mg I	2p^6^3s5p ^1^P^o^_1_	1827.934	1827.935	1	3	2.60E-02	-1.585	B	ZBG09
12	Mg I	2p^6^3s6p ^1^P^o^_1_	1747.794	1747.794	1	3	9.10E-03	-2.041	C+	CT90
12	Mg I	2p^6^3s7p ^1^P^o^_1_	1707.061	1707.061	1	3	4.30E-03	-2.367	D+	CT90
12	Mg I	2p^6^3s8p ^1^P^o^_1_	1683.412	1683.412	1	3	2.40E-03	-2.62	D+	CT90
12	Mg II	lower level 2p^6^3s ^2^S_1/2_								
12	Mg II	2p^6^3p ^2^P^o^_1/2_	2803.53	2803.531	2	2	3.06E-01	-0.214	A+	FFT06
12	Mg II	2p^6^3p ^2^P^o^_3/2_	2796.352	2796.352	2	4	6.13E-01	0.089	A+	FFT06
12	Mg II	2p^6^5p ^2^P^o^_3/2_	1025.962	1025.968	2	4	1.08E-03	-2.666	B	SMK98
13	Al I	lower level 3s^2^3p ^2^P^o^_1/2_								
13	Al I	3s^2^4s ^2^S_1/2_	3945.1222	3945.122	2	2	1.16E-01	-0.636	B+	FFT06
13	Al I	3s^2^3d ^2^D_3/2_	3083.0481	3083.046	2	4	1.65E-01	-0.482	B+	FFT06
13	Al I	3s^2^5s ^2^S_1/2_	2653.274	2653.265	2	2	1.50E-02	-1.523	B	VBF02
13	Al I	3s^2^nd y ^2^D_3/2_	2568.754	2568.752	2	4	3.80E-02	-1.119	B	DVD90

Z	Ion	Upper level	$\lambda_{\rm vac}$ (Å)	$\lambda_{\rm Ritz}$ (Å)	$g_{\rm l}$	$g_{\rm u}$	f	$\log(gf)$	Acc	Ref
13	Al I	3s^2^6s ^2^S_1/2_	2372.794	2372.794	2	2	4.86E-03	-2.012	C	MEL95
13	Al I	3s^2^4d ^2^D_3/2_	2367.775	2367.775	2	4	1.28E-01	-0.592	C+	MEL95
13	Al I	3s^2^5d ^2^D_3/2_	2264.162	2264.165	2	4	1.05E-01	-0.678	B	DVD90
13	Al I	3s^2^7s ^2^S_1/2_	2258.698	2258.706	2	2	2.88E-03	-2.239	C	MEL95
13	Al I	3s^2^6d ^2^D_3/2_	2205.348	2205.355	2	4	6.37E-02	-0.895	C+	MEL95
13	Al I	3s^2^8s ^2^S_1/2_	2199.837	2199.869	2	2	1.27E-03	-2.595	C	MEL95
13	Al I	3s^2^7d ^2^D_3/2_	2169.485	2169.507	2	4	4.18E-02	-1.078	C	MEL95
13	Al I	3s^2^8d ^2^D_3/2_	2146.231	2146.23	2	4	2.85E-02	-1.244	C	MEL95
13	Al I	3s^2^9d ^2^D_3/2_	2130.335	2130.335	2	4	2.07E-02	-1.383	C	MEL95
13	Al I	3s^2^10d ^2^D_3/2_	2118.982	2118.986	2	4	1.39E-02	-1.557	C	MEL95
13	Al II	lower level 2p^6^3s^2^ ^1^S_0_								
13	Al II	3s3p ^1^P^o^_1_	1670.7867	1670.787	1	3	1.74E+00	0.241	A+	FFT06
13	Al III	lower level 2p^6^3s ^2^S_1/2_								
13	Al III	2p^6^3p ^2^P^o^_1/2_	1862.7895	1862.79	2	2	2.79E-01	-0.253	A+	FFT06
13	Al III	2p^6^3p ^2^P^o^_3/2_	1854.7164	1854.716	2	4	5.61E-01	0.05	A+	FFT06
14	Si I	lower level 3s^2^3p^2^ ^3^P_0_								
14	Si I	3s^2^3p4s ^3^P^o^_1_	2515.08	2515.073	1	3	2.17E-01	-0.664	B	FFT06
14	Si I	3s^2^3p4s ^1^P^o^_1_	2439.51	2439.507	1	3	1.50E-03	-2.824	C	FFT06
14	Si I	3s3p^3^ ^3^D^o^_1_	2208.67	2208.667	1	3	4.61E-02	-1.336	B	FFT06
14	Si I	3s^2^3p3d ^3^P^o^_1_		1977.598	1	3	4.67E-02	-1.33	B	FFT06
14	Si I	3s^2^3p3d ^1^P^o^_1_		1873.103	1	3	6.92E-03	-2.16	C	FFT06
14	Si I	3s^2^3p3d ^3^D^o^_1_	1845.51	1845.52	1	3	2.58E-01	-0.589	C+	FFT06
14	Si I	3s^2^3p5s ^3^P^o^_1_	1841.15	1841.152	1	3	2.29E-02	-1.64	D	SHT87
14	Si I	3s^2^3p4d ^3^P^o^_1_		1763.661	1	3	8.13E-03	-2.09	D	SHT87
14	Si I	3s^2^3p4d ^1^P^o^_1_	1700.63	1700.636	1	3	3.98E-02	-1.4	D+	SHT87
14	Si I	3s^2^3p4d ^3^D^o^_1_	1693.29	1693.293	1	3	8.71E-02	-1.06	D+	SHT87
14	Si I	3s^2^3pnd a ^3^P^o^_1_	1666.37	1666.376	1	3	2.19E-02	-1.66	D	SHT87
14	Si I	3s^2^3p5d ^3^D^o^_1_	1625.71	1625.705	1	3	8.51E-02	-1.07	E	KP08
14	Si I	3s^2^3p6d ^3^D^o^_1_		1589.173	1	3	5.04E-02	-1.298	E	KP08
14	Si I	3s^2^3p7d ^3^D^o^_1_		1568.617	1	3	3.18E-02	-1.498	E	NP93

Z	Ion	Upper level	λ_{vac} (Å)	λ_{Ritz} (Å)	g_l	g_u	f	log(gf)	Acc	Ref
14	Si II	lower level 3s^2^3p ^2^P^o^_1/2_								
14	Si II	3s3p^2^ ^2^D_3/2_	1808	1808.013	2	4	2.45E-03	-2.31	C+	BQP09
14	Si II	3s^2^4s ^2^S_1/2_	1526.72	1526.707	2	2	1.44E-01	-0.54	B	BQP09
14	Si II	3s3p^2^ ^2^S_1/2_	1304.37	1304.37	2	2	9.10E-02	-0.74	B	BQP09
14	Si II	3s^2^3d ^2^D_3/2_	1260.42	1260.422	2	4	1.20E+00	0.38	B+	BQP09
14	Si II	3s3p^2^ ^2^P_1/2_	1193.28	1193.29	2	2	5.44E-01	0.037	B+	BQP09
14	Si II	3s3p^2^ ^2^P_3/2_	1190.42	1190.416	2	4	2.56E-01	-0.29	B	BQP09
14	Si II	3s^2^5s ^2^S_1/2_	1020.7	1020.699	2	2	1.39E-02	-1.556	D	CM00
14	Si II	3s^2^4d ^2^D_3/2_	989.87	989.873	2	4	2.00E-01	-0.398	C+	CS74
14	Si III	lower level 2p^6^3s^2^ ^1^S_0_								
14	Si III	3s3p ^1^P^o^_1_	1206.51	1206.5	1	3	1.61E+00	0.206	A	FFT06
14	Si IV	lower level 2p^6^3s ^2^S_1/2_								
14	Si IV	2p^6^3p ^2^P^o^_1/2_	1402.77	1402.77	2	2	2.54E-01	-0.293	A+	FFT06
14	Si IV	2p^6^3p ^2^P^o^_3/2_	1393.76	1393.755	2	4	5.13E-01	0.011	A+	FFT06
15	P I	lower level 3s^2^3p^3^ ^4^S^o^_3/2_								
15	P I	3s^2^3p^2^(^3^P)4s ^4^P_1/2_	1787.656	1787.648	4	2	4.93E-02	-0.705	B	FFT06
15	P I	3s^2^3p^2^(^3^P)4s ^4^P_3/2_	1782.838	1782.829	4	4	9.90E-02	-0.402	B	FFT06
15	P I	3s^2^3p^2^(^3^P)4s ^4^P_5/2_	1774.951	1774.949	4	6	1.50E-01	-0.223	B	FFT06
15	P I	3s3p^4^ ^4^P_5/2_	1679.695	1679.697	4	6	5.36E-02	-0.669	D	F86
15	P I	3s3p^4^ ^4^P_3/2_	1674.591	1674.595	4	4	3.25E-02	-0.886	D	F86
15	P I	3s3p^4^ ^4^P_1/2_	1671.68	1671.671	4	2	1.56E-02	-1.205	D	F86
15	P I	3s^2^3p^2^(^3^P)3d ^4^P_5/2_		1381.476	4	6	3.16E-01	0.102		F86
15	P I	3s^2^3p^2^(^3^P)3d ^4^P_3/2_		1379.428	4	4	2.19E-01	-0.057		F86
15	P I	3s^2^3p^2^(^3^P)3d ^4^P_1/2_		1377.073	4	2	1.10E-01	-0.357		F86
15	P II	lower level 3s^2^3p^2^ ^3^P_0_								
15	P II	3s3p^3^ ^3^D^o^_1_	1532.51	1532.533	1	3	7.01E-03	-2.155		FFT06
15	P II	3s3p^3^ ^3^P^o^_1_	1301.87	1301.874	1	3	2.11E-02	-1.676		FFT06
15	P II	3s^2^3p4s ^3^P^o^_1_		1152.818	1	3	2.53E-01	-0.596		FFT06
15	P II	3s^2^3p4s ^1^P^o^_1_		1124.945	1	3	2.28E-03	-2.643		FFT06
15	P II	3s^2^3p3d ^1^P^o^_1_		972.779	1	3	5.20E-02	-1.284		FFT06

Z	Ion	Upper level	$\lambda_{\rm vac}$ (Å)	$\lambda_{\rm Ritz}$ (Å)	$g_{\rm l}$	$g_{\rm u}$	f	$\log(gf)$	Acc	Ref
15	P II	3s^2^3p3d ^3^P^o^_1_		963.801	1	3	1.27E-02	-1.895		FFT06
15	P II	3s^2^3p3d ^3^D^o^_1_		961.041	1	3	1.86E+00	0.27		FFT06
15	P III	lower level 3s^2^3p ^2^P^o^_1/2_								
15	P III	3s3p^2^ ^2^D_3/2_	1334.808	1334.813	2	4	3.20E-02	-1.193		FFT06
15	P III	3s3p^2^ ^2^S_1/2_		998	2	2	1.33E-01	-0.574		FFT06
15	P III	3s3p^2^ ^2^P_1/2_		917.118	2	2	5.28E-01	0.024		FFT06
15	P III	3s3p^2^ ^2^P_3/2_		913.968	2	4	2.87E-01	-0.241		FFT06
15	P IV	lower level 2p^6^3s^2^ ^1^S_0_								
15	P IV	3s3p ^1^P^o^_1_	950.655	950.657	1	3	1.47E+00	0.168	B	FFT06
15	P V	lower level 2p^6^3s ^2^S_1/2_								
15	P V	2p^6^3p ^2^P^o^_1/2_	1128.01	1128.008	2	2	2.33E-01	-0.332	C	FFT06
15	P V	2p^6^3p ^2^P^o^_3/2_	1117.98	1117.977	2	4	4.71E-01	-0.026	C	FFT06
16	S I	lower level 3s^2^3p^4^ ^3^P_2_								
16	S I	3s^2^3p^3^(^4^S)4s ^3^S^o^_1_	1807.3108	1807.311	5	3	8.55E-02	-0.369	C+	DH08
16	S I	3s^2^3p^3^(^2^D)4s ^3^D^o_1	1474.5715	1474.571	5	3	9.91E-04	-2.305	D+	DH08
16	S I	3s^2^3p^3^(^2^D)4s ^3^D^o^_2_	1474.38	1474.379	5	5	1.26E-02	-1.201	C	DH08
16	S I	3s^2^3p^3^(^2^D)4s ^3^D^o^_3_	1473.9948	1473.994	5	7	5.33E-02	-0.574	C+	DH08
16	S I	3s^2^3p^3^(^4^S)3d ^5^D^o^_3_		1472.971	5	7	1.13E-02	-1.248	D+	DH08
16	S I	3s^2^3p^3^(^4^S)3d ^3^D^o^_1_	1425.219	1425.219	5	3	1.17E-03	-2.233	D+	DH08
16	S I	3s^2^3p^3^(^4^S)3d ^3^D^o^_2_		1425.188	5	5	1.73E-02	-1.063	C	DH08
16	S I	3s^2^3p^3^(^4^S)3d ^3^D^o^_3_	1425.0301	1425.03	5	7	8.95E-02	-0.349	C+	DH08
16	S I	3s^2^3p^3^(^4^S)5s ^3^S^o^_1_	1401.5136	1401.514	5	3	1.51E-02	-1.122	C	DH08
16	S I	3s^2^3p^3^(^4^S)4d ^3^D^o^_2_	1316.6183	1316.615	5	5	1.07E-02	-1.272	C	DH08
16	S I	3s^2^3p^3^(^4^S)4d ^3^D^o^_3_	1316.5423	1316.543	5	7	5.84E-02	-0.535	C	DH08
16	S I	3s^2^3p^3^(^4^S)6s ^3^S^o^_1_	1303.4295	1303.43	5	3	5.85E-03	-1.534	D+	DH08
16	S I	3s^2^3p^3^(^2^P)4s ^3^P^o^_1_	1296.1738	1296.174	5	3	2.59E-02	-0.888	C	DH08
16	S I	3s^2^3p^3^(^2^P)4s ^3^P^o^_2_	1295.6526	1295.653	5	5	7.74E-02	-0.412	C+	DH08
16	S I	3s^2^3p^3^(^4^S)5d ^3^D^o^_2_	1270.7821	1270.787	5	5	1.62E-03	-2.092	D+	BGF98
16	S I	3s^2^3p^3^(^4^S)5d ^3^D^o^_3_	1270.7821	1270.78	5	7	8.61E-03	-1.366	C	BGF98
16	S I	3s^2^3p^3^(^4^S)7s ^3^S^o^_1_	1262.8596	1262.86	5	3	2.12E-03	-1.975	D+	BGF98

Z	Ion	Upper level	λ_{vac} (Å)	λ_{Ritz} (Å)	g_l	g_u	f	$\log(gf)$	Acc	Ref
16	S I	3s^2^3p^3^(^4^S)6d ^3^D^o^_3_	1247.16	1247.16	5	7	4.43E-03	-1.655	D+	BGF98
16	S I	3s^2^3p^3^(^4^S)8s ^3^S^o^_1_	1241.905	1241.905	5	3	1.69E-03	-2.073	D+	BGF98
16	S I	3s^2^3p^3^(^2^D)3d ^3^D^o^_2_		1191.895	5	5	1.31E-02	-1.184	C	DH08
16	S I	3s^2^3p^3^(^2^D)3d ^3^D^o^_3_		1191.895	5	7	8.02E-02	-0.397	C	DH08
16	S I	3s^2^3p^3^(^2^D)3d ^3^S^o^_1_		1170.549	5	3	9.33E-03	-1.331	C	DH08
16	S I	3s^2^3p^3^(^2^D)5s ^3^D^o^_3_		1167.134	5	7	1.60E-02	-1.097	C	DH08
16	S I	3s^2^3p^3^(^2^D)5s ^3^D^o^_2_		1167.134	5	5	3.44E-03	-1.764	C	DH08
16	S I	3s^2^3p^3^(^2^D)3d ^3^P^o^_1_		1156.276	5	3	4.58E-03	-1.64	C	DH08
16	S I	3s^2^3p^3^(^2^D)3d ^3^P^o^_2_		1156.026	5	5	9.13E-03	-1.341	C	DH08
16	S I	3s^2^3p^3^(^2^D)4d ^3^D^o^_3_		1103.753	5	7	4.73E-03	-1.626	C	DH08
16	S I	3s^2^3p^3^(^2^D)4d ^3^S^o^_1_		1096.611	5	3	3.42E-02	-0.767	C	DH08
16	S I	3s^2^3p^3^(^2^D)6s ^3^D^o^_3_		1094.331	5	7	4.53E-03	-1.645	C	DH08
16	S I	3s^2^3p^3^(^2^D)4d ^3^P^o^_1_		1093.063	5	3	4.16E-03	-1.682	C	DH08
16	S I	3s^2^3p^3^(^2^D)4d ^3^P^o^_2_		1092.669	5	5	1.54E-02	-1.114	C	DH08
16	S I	3s^2^3p^3^(^2^P)3d ^3^D^o^_3_		1061.797	5	7	5.54E-03	-1.558	C	DH08
16	S I	3s^2^3p^3^(^2^P)3d ^3^P^o^_2_		1059.535	5	5	3.67E-02	-0.736	C	DH08
16	S I	3s^2^3p^3^(^2^P)3d ^3^P^o^_1_		1059.535	5	3	1.46E-02	-1.137	C	DH08
16	S I	3s^2^3p^3^(^2^P)5s ^3^P^o^_1_		1050.332	5	3	4.39E-03	-1.659	C	DH08
16	S II	lower level 3s^2^3p^3^ ^4^S^o^_3/2_								
16	S II	3s3p^4^ ^4^P_5/2_	1259.518	1259.519	4	6	1.57E-02	-1.203		KKF14
16	S II	3s3p^4^ ^4^P_3/2_	1253.805	1253.811	4	4	1.04E-02	-1.383		KKF14
16	S II	3s3p^4^ ^4^P_1/2_	1250.578	1250.584	4	2	5.15E-03	-1.686		KKF14
16	S II	3s^2^3p^2^(^3^P)4s ^4^P_1/2_	912.735	912.736	4	2	6.95E-02	-0.556		KKF14
16	S II	3s^2^3p^2^(^3^P)4s ^4^P_3/2_		910.484	4	4	1.40E-01	-0.252		KKF14
16	S II	3s^2^3p^2^(^3^P)4s ^4^P_5/2_		906.885	4	6	2.12E-01	-0.071		KKF14
16	S III	lower level 3s^2^3p^2^ ^3^P_0_								
16	S III	3s3p^3^ ^3^D^o^_1_	1190.206	1190.203	1	3	2.63E-02	-1.58		FFT06
16	S III	3s3p^3^ ^3^P^o^_1_	1012.504	1012.495	1	3	4.41E-02	-1.355		FFT06
16	S IV	lower level 3s^2^3p ^2^P^o^_1/2_								
16	S IV	3s3p^2^ ^2^D_3/2_	1062.656	1062.664	2	4	5.25E-02	-0.979		FFT06

Z	Ion	Upper level	$\lambda_{\rm vac}$ (Å)	$\lambda_{\rm Ritz}$ (Å)	$g_{\rm l}$	$g_{\rm u}$	f	$\log(gf)$	Acc	Ref
16	S VI	lower level 2p^6^3s ^2^S_1/2_								
16	S VI	2p^6^3p ^2^P^o^_1/2_	944.525	944.523	2	2	2.15E-01	-0.367	AA	FFT06
16	S VI	2p^6^3p ^2^P^o^_3/2_	933.376	933.378	2	4	4.36E-01	-0.06	AA	FFT06
17	Cl I	lower level 3s^2^3p^5^ ^2^P^o^_3/2_								
17	Cl I	3s^2^3p^4^(^3^P)4s ^4^P_3/2_	1379.528	1379.528	4	4	2.69E-03	-1.969	C+	OH13
17	Cl I	3s^2^3p^4^(^3^P)4s ^2^P_3/2_	1347.24	1347.24	4	4	1.45E-01	-0.236	C+	OH13
17	Cl I	3s^2^3p^4^(^3^P)4s ^2^P_1/2_	1335.726	1335.726	4	2	3.01E-02	-0.919	C+	OH13
17	Cl I	3s^2^3p^4^(^1^D)4s ^2^D_5/2_	1188.774	1188.774	4	6	8.02E-02	-0.494	C+	OH13
17	Cl I	3s^2^3p^4^(^1^D)4s ^2^D_3/2_		1188.751	4	4	6.31E-03	-1.598	C+	OH13
17	Cl I	3s^2^3p^4^(^3^P)3d ^4^F_5/2_		1101.936	4	6	4.35E-03	-1.76	C+	OH13
17	Cl I	3s^2^3p^4^(^3^P)3d ^4^F_3/2_		1099.523	4	4	1.63E-03	-2.185	C+	OH13
17	Cl I	3s^2^3p^4^(^3^P)5s ^4^P_5/2_		1094.769	4	6	2.23E-03	-2.049	C+	OH13
17	Cl I	3s^2^3p^4^(^3^P)3d ^4^P_3/2_		1092.437	4	4	1.04E-03	-2.38	C+	OH13
17	Cl I	3s^2^3p^4^(^3^P)3d ^4^P_5/2_		1090.982	4	6	1.50E-02	-1.223	C+	OH13
17	Cl I	3s^2^3p^4^(^3^P)5s ^2^P_3/2_		1090.739	4	4	1.07E-02	-1.37	C+	OH13
17	Cl I	3s^2^3p^4^(^3^P)3d ^2^F_5/2_		1088.059	4	6	3.22E-02	-0.89	C+	OH13
17	Cl I	3s^2^3p^4^(^3^P)3d ^2^P_3/2_		1084.667	4	4	6.37E-03	-1.594	C+	OH13
17	Cl I	3s^2^3p^4^(^3^P)5s ^2^P_1/2_		1079.882	4	2	4.38E-03	-1.756	C+	OH13
17	Cl I	3s^2^3p^4^(^1^S)4s ^2^S_1/2_		1004.678	4	2	4.43E-02	-0.752	C+	OH13
17	Cl II	lower level 3s^2^3p^4^ ^3^P_2_								
17	Cl II	3s3p^5^ ^3^P^o^_2_	1071.036	1071.036	5	5	1.42E-02	-1.149	B+	SFB05
17	Cl II	3s3p^5^ ^3^P^o^_1_	1063.831	1063.831	5	3	4.96E-03	-1.606	B+	SFB05
17	Cl III	lower level 3s^2^3p^3^ ^4^S^o^_3/2_								
17	Cl III	3s3p4(3P) ^4^P_5/2_	1015.02	1015.019	4	6	2.85E-02	-0.943	B+	SFB05
17	Cl III	3s3p4(3P) ^4^P_3/2_	1008.78	1008.762	4	4	1.93E-02	-1.112	B+	SFB05
17	Cl III	3s3p4(3P) ^4^P_1/2_	1005.28	1005.275	4	2	9.60E-03	-1.416	B+	SFB05
17	Cl IV	lower level 3s^2^3p^2^ ^3^P_0_								
17	Cl IV	3s3p^3^ ^3^D^o^_1_	973.21	973.217	1	3	3.94E-02	-1.405	C+	FFT06
18	Ar I	lower level 3s^2^3p^6^ ^1^S_0_								
18	Ar I	3s^2^3p^5^(^2^P)4s ^3^P^o^_1_	1066.66	1066.66	1	3	5.48E-02	-1.261	C+	FFT06

Z	Ion	Upper level	$\lambda_{\rm vac}$ (Å)	$\lambda_{\rm Ritz}$ (Å)	$g_{\rm l}$	$g_{\rm u}$	f	$\log(gf)$	Acc	Ref
18	Ar I	3s^2^3p^5^(^2^P)4s ^1^P^o^_1_	1048.22	1048.22	1	3	2.64E-01	-0.578	C+	FFT06
18	Ar II	lower level 3s^2^3p^5^ ^2^P^o^_3/2_								
18	Ar II	3s3p^6^ ^2^S_1/2_	919.781	919.781	4	2	1.03E-02	-1.387	C+	FFT06
19	K I	lower level 3p^6^4s ^2^S_1/2_								
19	K I	3p^6^4p ^2^P^o^_1/2_	7701.0835	7701.084	2	2	3.33E-01	-0.176	AAA	WWW97
19	K I	3p^6^4p ^2^P^o^_3/2_	7667.0089	7667.009	2	4	6.70E-01	0.127	AAA	WWW97
19	K I	3p^6^5p ^2^P^o^_1/2_	4048.351	4048.357	2	2	2.63E-03	-2.279	A	SK85
19	K I	3p^6^5p ^2^P^o^_3/2_	4045.279	4045.285	2	4	5.69E-03	-1.944	A	SK85
20	Ca I	lower level 3p^6^4s^2^ ^1^S_0_								
20	Ca I	3p^6^4s4p ^1^P^o^_1_	4227.92	4227.918	1	3	1.74E+00	0.243	AA	ZBR00
20	Ca I	3p^6^4s5p ^1^P^o^_1_	2722.46	2722.45	1	3	9.12E-04	-3.04	C	PRT76
20	Ca I	3p^6^4s6p ^1^P^o^_1_	2399.29	2399.289	1	3	4.07E-02	-1.39	C+	PRT76
20	Ca I	3p^6^4snp w ^1^P^o^_1_	2276.16	2276.169	1	3	6.61E-02	-1.18	C+	PRT76
20	Ca I	3p^6^4s7p ^1^P^o^_1_	2201.42	2201.414	1	3	3.24E-02	-1.49	C+	PRT76
20	Ca I	3p^6^4s8p ^1^P^o^_1_	2151.48	2151.472	1	3	1.23E-02	-1.91	C+	PRT76
20	Ca I	3p^6^4s9p ^1^P^o^_1_		2119.346	1	3	5.50E-03	-2.26	C+	PRT76
20	Ca I	3p^6^4s10p ^1^P^o^_1_		2098.103	1	3	3.23E-03	-2.49	C+	PRT76
20	Ca I	3p^6^4s11p ^1^P^o^_1_		2083.442	1	3	2.04E-03	-2.69	C+	PRT76
20	Ca I	3p^6^4s12p ^1^P^o^_1_		2072.946	1	3	1.38E-03	-2.86	C+	PRT76
20	Ca II	lower level 3p^6^4s ^2^S_1/2_								
20	Ca II	3p^6^4p ^2^P^o^_1/2_	3969.59	3969.592	2	2	3.21E-01	-0.192	AA	SS11
20	Ca II	3p^6^4p ^2^P^o^_3/2_	3934.77	3934.777	2	4	6.49E-01	0.113	AA	SS11
20	Ti I	lower level 3d^2^4s^2^ a ^3^F_2_								
20	Ti I	3d^2^(^3^F)4s4p(^3^P) z ^3^F^o^_2_	5175.181	5175.184	5	5	1.74E-02	-1.06	B+	LGW13
22	Ti I	3d^2^(^3^F)4s4p(^3^P) z ^3^F^o^_3_	5148.911	5148.912	5	7	2.30E-03	-1.94	B+	LGW13
22	Ti I	3d^2^(^3^F)4s4p(^3^P) z ^3^D^o^_1_	5015.585	5015.585	5	3	1.21E-02	-1.22	B+	LGW13
22	Ti I	3d^2^(^3^F)4s4p(^3^P) z ^3^D^o^_2_	4998.487	4998.491	5	5	1.70E-03	-2.07	B+	LGW13
22	Ti I	3d^2^(^3^F)4s4p(^3^P) z ^3^G^o^_3_	4657.772	4657.773	5	7	1.03E-02	-1.29	C+	BLN06
22	Ti I	3d^2^(^3^P)4s4p(^3^P) z ^5^S^o^_2_	3983.607	3983.608	5	5	1.10E-02	-1.26	B+	LGW13
22	Ti I	3d^2^(^3^F)4s4p(^1^P) y ^3^F^o^_2_	3982.8878	3982.888	5	5	1.07E-01	-0.27	B+	LGW13

Z	Ion	Upper level	$\lambda_{\rm vac}$ (Å)	$\lambda_{\rm Ritz}$ (Å)	$g_{\rm l}$	$g_{\rm u}$	f	$\log(gf)$	Acc	Ref
22	Ti I	3dˆ2ˆ(ˆ3ˆF)4s4p(ˆ1ˆP) yˆ3ˆFˆoˆ_3_	3963.9721	3963.972	5	7	1.59E-02	-1.1	C+	LGW13
22	Ti I	3dˆ3ˆ(ˆ4ˆF)4p yˆ3ˆDˆoˆ_1_	3949.7884	3949.788	5	3	7.96E-02	-0.4	B+	LGW13
22	Ti I	3dˆ3ˆ(ˆ4ˆF)4p yˆ3ˆDˆoˆ_2_	3930.9867	3930.986	5	5	2.05E-02	-0.99	B+	LGW13
22	Ti I	3dˆ2ˆ(ˆ1ˆD)4s4p(ˆ3ˆP) ˆ3ˆPˆoˆ_2_	3922.533	3922.533	5	5	5.90E-03	-1.53	B+	LGW13
22	Ti I	3dˆ2ˆ(ˆ1ˆD)4s4p(ˆ3ˆP) ˆ3ˆPˆoˆ_1_	3915.8464	3915.843	5	3	1.10E-03	-2.24	C	SK78
22	Ti I	3dˆ3ˆ(ˆ4ˆF)4p yˆ3ˆDˆoˆ_3_	3899.5931	3899.593	5	7	1.26E-03	-2.2	B+	LGW13
22	Ti I	3dˆ2ˆ(ˆ3ˆP)4s4p(ˆ3ˆP) ˆ5ˆDˆoˆ_2_	3891.0526	3891.053	5	5	1.20E-03	-2.24	C	SK78
22	Ti I	3dˆ2ˆ(ˆ1ˆD)4s4p(ˆ3ˆP) xˆ3ˆFˆoˆ_2_	3730.8672	3730.867	5	5	1.05E-01	-0.28	B+	LGW13
22	Ti I	3dˆ2ˆ(ˆ1ˆD)4s4p(ˆ3ˆP) xˆ3ˆFˆoˆ_3_	3718.449	3718.449	5	7	1.29E-02	-1.19	B+	LGW13
22	Ti I	3dˆ2ˆ(ˆ1ˆD)4s4p(ˆ3ˆP) xˆ3ˆDˆoˆ_1_	3655.6311	3655.631	5	3	1.10E-02	-1.26	B+	LGW13
22	Ti I	3dˆ2ˆ(ˆ1ˆD)4s4p(ˆ3ˆP) xˆ3ˆDˆoˆ_2_	3647.235	3647.235	5	5	4.80E-03	-1.62	B+	LGW13
22	Ti I	3dˆ2ˆ(ˆ1ˆD)4s4p(ˆ3ˆP) xˆ3ˆDˆoˆ_3_	3639.0019	3639.002	5	7	2.00E-03	-2	B+	LGW13
22	Ti I	3dˆ2ˆ(ˆ3ˆF)4s4p(ˆ1ˆP) yˆ3ˆGˆoˆ_3_	3636.4987	3636.498	5	7	2.52E-01	0.1	B+	LGW13
22	Ti I	3dˆ2ˆ(ˆ3ˆF)4s4p(ˆ1ˆP) wˆ3ˆDˆoˆ_1_	3371.4026	3371.402	5	3	7.96E-02	-0.4	B+	LGW13
22	Ti I	3dˆ2ˆ(ˆ3ˆF)4s4p(ˆ1ˆP) wˆ3ˆDˆoˆ_2_	3359.2362	3359.236	5	5	1.10E-02	-1.26	B+	LGW13
22	Ti I	3dˆ2ˆ(ˆ1ˆG)4s4p(ˆ3ˆP) xˆ3ˆGˆoˆ_3_	3342.8349	3342.834	5	7	1.87E-01	-0.03	B+	LGW13
22	Ti I	3dˆ3ˆ(ˆ4ˆF)4p wˆ3ˆGˆoˆ_3_	3187.3724	3187.372	5	7	2.05E-01	0.01	B+	LGW13
22	Ti I	3dˆ3ˆ(ˆ4ˆF)4p wˆ3ˆFˆoˆ_2_	2971.246	2971.25	5	5	9.35E-03	-1.33	B	LGW13
22	Ti I	3dˆ2ˆ(ˆ1ˆG)4s4p(ˆ3ˆP) vˆ3ˆFˆoˆ_2_	2942.8552	2942.851	5	5	1.45E-01	-0.14	B+	LGW13
22	Ti I	3dˆ2ˆ(ˆ1ˆG)4s4p(ˆ3ˆP) vˆ3ˆFˆoˆ_3_	2934.386	2934.392	5	7	1.87E-02	-1.03	B	LGW13
22	Ti I	3dˆ3ˆ(ˆ2ˆG)4p vˆ3ˆGˆoˆ_3_	2662.751	2662.757	5	7	1.26E-02	-1.2	C+	LGW13
22	Ti I	3d4sˆ2ˆ4p xˆ1ˆFˆoˆ_3_	2657.977	2657.979	5	7	4.70E-03	-1.62	C	SK78
22	Ti I	3dˆ2ˆ(ˆ3ˆP)4s4p(ˆ1ˆP) uˆ3ˆDˆoˆ_1_	2641.874	2641.882	5	3	1.21E-01	-0.22	B+	LGW13
22	Ti I	3dˆ2ˆ(ˆ3ˆP)4s4p(ˆ1ˆP) uˆ3ˆDˆoˆ_2_	2633.196	2633.201	5	5	2.58E-02	-0.89	B+	LGW13
22	Ti I	3dˆ3ˆ(ˆ2ˆG)4p tˆ3ˆFˆoˆ_2_	2600.681	2600.692	5	5	6.93E-02	-0.46	C+	LGW13
22	Ti I	3dˆ3ˆ(ˆ2ˆG)4p tˆ3ˆFˆoˆ_3_	2594.416	2594.416	5	7	8.34E-03	-1.38	B	LGW13
22	Ti I	3dˆ3ˆ(ˆ2ˆ_2_D)4p sˆ3ˆDˆoˆ_1_	2521.3	2521.3	5	3	2.30E-02	-0.94	B	LGW13
22	Ti I	3dˆ3ˆ(ˆ2ˆ_2_D)4p sˆ3ˆDˆoˆ_2_	2519.783	2519.783	5	5	3.90E-03	-1.71	C	LGW13
22	Ti I	3dˆ3ˆ(ˆ2ˆH)4p ˆ3ˆGˆoˆ_3_	2428.951	2428.953	5	7	3.64E-03	-1.74	C	LGW13
22	Ti I	3d4sˆ2ˆ4p sˆ3ˆFˆoˆ_2_	2419.097	2419.097	5	5	1.10E-02	-1.28	C	SK78

Z	Ion	Upper level	$\lambda_{\rm vac}$ (Å)	$\lambda_{\rm Ritz}$ (Å)	$g_{\rm l}$	$g_{\rm u}$	f	$\log(gf)$	Acc	Ref
22	Ti I	3dˆ2ˆ4s(ˆ4ˆF)5p r ˆ3ˆFˆoˆ_2_	2300.566	2300.567	5	5	5.50E-02	-0.56	C	SK78
22	Ti I	3dˆ2ˆ4s(ˆ4ˆF)5p ˆ3ˆGˆoˆ_3_	2264.716	2264.719	5	7	2.50E-02	-0.91	D	SK78
22	Ti II	lower level 3dˆ2ˆ(ˆ3ˆF)4s a ˆ4ˆF_3/2_								
22	Ti II	3dˆ2ˆ(ˆ3ˆF)4p z ˆ4ˆGˆoˆ_5/2_	3384.73	3384.73	4	6	3.96E-01	0.2	B+	LHE16
22	Ti II	3dˆ2ˆ(ˆ3ˆF)4p z ˆ4ˆFˆoˆ_3/2_	3242.9180	3242.918	4	4	2.56E-01	0.01	B+	LHE16
22	Ti II	3dˆ2ˆ(ˆ3ˆF)4p z ˆ4ˆFˆoˆ_5/2_	3230.1217	3230.122	4	6	7.38E-02	-0.53	B+	LHE16
22	Ti II	3dˆ2ˆ(ˆ3ˆF)4p z ˆ2ˆFˆoˆ_5/2_	3204.357	3204.357	4	6	1.90E-03	-2.12	B+	LHE16
22	Ti II	3dˆ2ˆ(ˆ3ˆF)4p z ˆ2ˆDˆoˆ_3/2_	3148.9479	3148.948	4	4	1.14E-02	-1.34	C	LHE16
22	Ti II	3dˆ2ˆ(ˆ3ˆF)4p z ˆ4ˆDˆoˆ_1/2_	3073.8629	3073.863	4	2	1.51E-01	-0.22	B+	LHE16
22	Ti II	3dˆ2ˆ(ˆ3ˆF)4p z ˆ4ˆDˆoˆ_3/2_	3067.2375	3067.238	4	4	5.73E-02	-0.64	B+	LHE16
22	Ti II	3dˆ3ˆ(ˆ3ˆF)4p z ˆ4ˆDˆoˆ_5/2_	3058.2819	3058.282	4	6	3.96E-03	-1.8	B+	LHE16
22	Ti II	3dˆ2ˆ(ˆ3ˆP)4p y ˆ4ˆDˆoˆ_1/2_	2479.53	2479.525	4	2	1.31E-03	-2.28		LHE16
22	Ti II	3d(ˆ2ˆD)4s4p(ˆ3ˆP) ˆ4ˆFˆoˆ_3/2_	1910.9538	1910.954	4	4	7.21E-02	-0.54	A	LHE16
22	Ti II	3d(ˆ2ˆD)4s4p(ˆ3ˆP) ˆ4ˆDˆoˆ_1/2_	1910.6123	1910.612	4	2	1.04E-01	-0.38	A’	LHE16
22	Ti III	lower level 3pˆ6ˆ3dˆ2ˆ ˆ3ˆF_2_								
22	Ti III	3pˆ6ˆ3d4p ˆ1ˆDˆoˆ_2_	1329.837	1329.819	5	5	1.65E-03	-2.083		RU97
22	Ti III	3pˆ6ˆ3d4p ˆ3ˆDˆoˆ_1_	1298.659	1298.697	5	3	9.64E-02	-0.317		RU97
22	Ti III	3pˆ6ˆ3d4p ˆ3ˆDˆoˆ_2_	1295.883	1295.884	5	5	4.18E-02	-0.68		RU97
22	Ti III	3pˆ6ˆ3d4p ˆ3ˆFˆoˆ_2_	1291.622	1291.625	5	5	2.65E-02	-0.878		RU97
22	Ti III	3pˆ6ˆ3d4p ˆ3ˆDˆoˆ_3_		1291.582	5	7	2.67E-03	-1.874		RU97
22	Ti III	3pˆ6ˆ3d4p ˆ3ˆFˆoˆ_3_	1286.228	1286.233	5	7	4.37E-03	-1.661		RU97
24	Cr I	lower level 3dˆ5ˆ(ˆ6ˆS)4s a ˆ7ˆS_3_								
24	Cr I	3dˆ5ˆ(ˆ6ˆS)4p z ˆ7ˆPˆoˆ_2_	4290.9376	4290.924	7	5	6.09E-02	-0.37	B	SLS07
24	Cr I	3dˆ5ˆ(ˆ6ˆS)4p z ˆ7ˆPˆoˆ_3_	4276.0147	4276	7	7	8.61E-02	-0.22	B	SLS07
24	Cr I	3dˆ5ˆ(ˆ6ˆS)4p z ˆ7ˆPˆoˆ_4_	4255.5493	4255.534	7	9	1.16E-01	-0.09	B	SLS07
24	Cr I	3dˆ4ˆ(ˆ5ˆD)4s4p(ˆ3ˆP) y ˆ7ˆPˆoˆ_2_	3606.3731	3606.357	7	5	2.11E-01	0.17	B	SLS07
24	Cr I	3dˆ4ˆ(ˆ5ˆD)4s4p(ˆ3ˆP) y ˆ7ˆPˆoˆ_3_	3594.5275	3594.511	7	7	2.92E-01	0.308	B	SLS07
24	Cr I	3dˆ4ˆ(ˆ5ˆD)4s4p(ˆ3ˆP) y ˆ7ˆPˆoˆ_4_	3579.7254	3579.708	7	9	3.76E-01	0.42	B	SLS07
24	Cr I	3dˆ5ˆ(ˆ6ˆS)5p x ˆ7ˆPˆoˆ_2_	2367.5387	2367.539	7	5	4.14E-03	-1.538	C	MFW88
24	Cr I	3dˆ5ˆ(ˆ6ˆS)5p x ˆ7ˆPˆoˆ_3_	2366.6417	2366.642	7	7	4.62E-03	-1.49	C	MFW88

Z	Ion	Upper level	$\lambda_{\rm vac}$ (Å)	$\lambda_{\rm Ritz}$ (Å)	$g_{\rm l}$	$g_{\rm u}$	f	$\log(gf)$	Acc	Ref
24	Cr I	3d^5^(^6^S)5p x ^7^P^o^_4_	2365.45	2365.454	7	9	5.72E-03	-1.398	C	MFW88
24	Cr I	3d^5^(^6^S)6p w ^7^P^o^_4_	2095.67	2095.594	7	9	1.02E-03	-2.148	C	MFW88
24	Cr II	lower level 3p^6^3d^5^ a ^6^S_5/2_								
24	Cr II	3d^4^(^5^D)4p z ^6^P^o^_3/2_	2066.1638	2066.164	6	4	5.01E-02	-0.522	B+	NLL06
24	Cr II	3d^4^(^5^D)4p z ^6^P^o^_5/2_	2062.2359	2062.236	6	6	8.13E-02	-0.312	B+	NLL06
24	Cr II	3d^4^(^5^D)4p z ^6^P^o^_7/2_	2056.2568	2056.257	6	8	1.09E-01	-0.186	B+	NLL06
24	Cr II	3d^4^(^5^D)4p z ^4^P^o^_3/2_	2040.5729	2040.573	6	4	1.47E-03	-2.056		RU98
24	Cr II	3d^4^(^5^D)4p z ^6^P^o^_5/2_	2026.2712	2026.271	6	6	1.30E-03	-2.109		RU98
24	Cr II	3d^4^(^5^D)5p ^4^P^o^_3/2_		1066.776	6	4	5.21E-03	-1.505		RU98
24	Cr II	3d^4^(^5^D)5p ^4^P^o^_5/2_		1064.124	6	6	7.98E-03	-1.32		RU98
24	Cr II	3d^4^(^5^D)5p ^6^P^o^_7/2_		1059.732	6	8	1.09E-02	-1.185		RU98
24	Cr II	3d^3^(^4^P)4s4p(^3^P) x ^6^D^o^_7_		1058.732	6	8	1.69E-03	-1.995		RU98
24	Cr II	3d^4^(^5^D)4f ^4^P^o^_5/2_		951.273	6	6	1.10E-03	-2.181		RU98
24	Cr II	3d^4^4f ^6^P^o^_7/2_		950.81	6	8	2.68E-02	-0.793		RU98
24	Cr II	3d^4^(^5^D)4f ^6^H^o^_7/2_		950.594	6	8	7.28E-03	-1.36		RU98
24	Cr II	3d^4^(^5^D)4f ^6^G^o^_3/2_		948.688	6	4	4.84E-03	-1.537		RU98
24	Cr II	3d^4^(^5^D)4f ^6^D^o^_7/2_		948.586	6	8	3.40E-03	-1.691		RU98
24	Cr II	3d^4^(^5^D)4f ^6^G^o^_5/2_		948.422	6	6	6.02E-03	-1.442		RU98
24	Cr II	3d^4^(^5^D)4f ^4^D^o^_5/2_		947.578	6	6	1.04E-03	-2.204		RU98
24	Cr II	3d^4^(^5^D)4f ^6^F^o^_3/2_		947.174	6	4	1.62E-03	-2.013		RU98
24	Cr II	3d^4^(^5^D)4f ^6^D^o^_5/2_		947.011	6	6	5.22E-03	-1.504		RU98
24	Cr II	3d^4^(^5^D)4f ^6^G^o^_3/2_		946.885	6	4	2.97E-03	-1.749		RU98
24	Cr III	lower level 3p^6^3d^4^ ^5^D_0_								
24	Cr III	3d^3^(^4^F)4p ^5^F^o^_1_		1040.059	1	3	1.19E-01	-0.925		K16
24	Cr III	3d^3^(^4^F)4p ^5^D^o^_1_		1033.341	1	3	6.64E-02	-1.178		K16
24	Cr III	3d^3^(^4^F)4p ^3^D^o^_1_		1030.109	1	3	7.24E-02	-1.14		K16
24	Cr III	3d^3^(^4^P)4p ^5^P^o^_1_		923.789	1	3	8.41E-02	-1.075		K16
24	Cr III	3d^3^(^4^P)4p ^5^D^o^_1_		918.579	1	3	6.14E-03	-2.212		K16
25	Mn I	lower level 3d^5^(^6^S)4s^2^ a ^6^S_5/2_								
25	Mn I	3d^5^(^6^S)4s4p(^3^P) z ^6^P^o^_3/2_	4035.63	4035.623	6	4	2.41E-02	-0.84	B+	BPN11

Z	Ion	Upper level	$\lambda_{\rm vac}$ (Å)	$\lambda_{\rm Ritz}$ (Å)	$g_{\rm l}$	$g_{\rm u}$	f	$\log(gf)$	Acc	Ref
25	Mn I	3d^5^(^6^S)4s4p(^3^P) z ^6^P^o^_5/2_	4034.21	4034.202	6	6	3.73E-02	-0.65	B+	BPN11
25	Mn I	3d^5^(^6^S)4s4p(^3^P) z ^6^P^o^_7/2_	4031.9	4031.892	6	8	5.15E-02	-0.51	B+	BPN11
25	Mn I	3d^5^(^6^S)4s4p(^1^P) y ^6^P^o^_3/2_	2801.89	2801.907	6	4	2.90E-01	0.24	C	MFW88
25	Mn I	3d^5^(^6^S)4s4p(^1^P) y ^6^P^o^_5/2_	2799.09	2799.094	6	6	4.19E-01	0.4	C	MFW88
25	Mn I	3d^5^(^6^S)4s4p(^1^P) y ^6^P^o^_7/2_	2795.64	2795.641	6	8	5.65E-01	0.53	C	MFW88
25	Mn I	3d^6^(^5^D)4p x ^6^P^o^_7/2_		2222.523	6	8	1.91E-02	-0.94	C+	BXP05
25	Mn I	3d^6^(^5^D)4p x ^6^P^o^_5/2_		2214.54	6	6	4.38E-03	-1.58	C+	BXP05
25	Mn I	3d^6^(^5^D)4p x ^6^P^o^_3/2_		2209.497	6	4	6.34E-03	-1.42	C+	BXP05
25	Mn I	3d^5^4s(^7^S)5p w ^6^P^o^_7/2_		2110.256	6	8	5.65E-03	-1.47	C+	BXP05
25	Mn I	3d^5^4s(^7^S)5p w ^6^P^o^_3/2_		2092.819	6	4	8.95E-03	-1.27	C+	BXP05
25	Mn I	3d^5^(^4^P)4s4p(^3^P) v ^6^P^o^_7/2_		2004.49	6	8	3.60E-02	-0.665		K16
25	Mn I	3d^5^(^4^P)4s4p(^3^P) v ^6^P^o^_5/2_		1999.5	6	6	2.72E-02	-0.788		K16
25	Mn I	3d^5^(^4^P)4s4p(^3^P) v ^6^P^o^_3/2_		1996.047	6	4	1.83E-02	-0.96		K16
25	Mn I	3d^5^4s(^7^S)6p t ^6^P^o^_7/2_		1877.545	6	8	1.53E-03	-2.037		K16
25	Mn I	3d^5^4s(^5^S)5p s ^6^P^o^_3/2_		1785.813	6	4	7.16E-03	-1.367		K16
25	Mn I	3d^5^4s(^5^S)5p s ^6^P^o^_5/2_		1785.453	6	6	1.08E-02	-1.187		K16
25	Mn I	3d^5^4s(^5^S)5p s ^6^P^o^_7/2_		1785.312	6	8	1.47E-02	-1.056		K16
25	Mn II	lower level 3d^5^(^6^S)4s a ^7^S_3_								
25	Mn II	3d^5^(^6^S)4p z ^7^P^o^_2_	2606.4587	2606.459	7	5	1.96E-01	0.137	A+	DHL11
25	Mn II	3d^5^(^6^S)4p z ^7^P^o^_3_	2594.4966	2594.497	7	7	2.79E-01	0.29	A+	DHL11
25	Mn II	3d^5^(^6^S)4p z ^7^P^o^_4_	2576.8752	2576.875	7	9	3.58E-01	0.399	A+	DHL11
25	Mn II	3d^5^(^6^S)4p z ^5^P^o^_3_	2305.712	2305.713	7	7	1.16E-03	-2.09	C+	KG00
25	Mn II	3d^4^(^5^D)4s4p(^3^P) y ^7^P^o^_2_	1201.124	1201.115	7	5	8.30E-02	-0.23	C+	TH05
25	Mn II	3d^4^(^5^D)4s4p(^3^P) y ^7^P^o^_3_	1199.38	1199.389	7	7	1.16E-01	-0.09	C+	TH05
25	Mn II	3d^4^(^5^D)4s4p(^3^P) y ^7^P^o^_4_	1197.17	1197.182	7	9	1.48E-01	0.02	C+	TH05
25	Mn II	3d^5^(^6^S)5p x ^7^P^o^_2_	1164.21	1164.206	7	5	8.30E-03	-1.24	C	TH05
25	Mn II	3d^5^(^6^S)5p x ^7^P^o^_3_	1163.32	1163.323	7	7	1.30E-02	-1.05	C	TH05
25	Mn II	3d^5^(^6^S)5p x ^7^P^o^_4_	1162.02	1162.012	7	9	1.80E-02	-0.9	C	TH05
26	Fe I	lower level 3d^6^4s^2^ a ^5^D_4_								
26	Fe I	3d^6^(^5^D)4s4p(^3^P) z ^5^D^o^_4_	3861.0055	3861.006	9	9	2.17E-02	-0.71	A	BIP79

Z	Ion	Upper level	$\lambda_{\rm vac}$ (Å)	$\lambda_{\rm Ritz}$ (Å)	$g_{\rm l}$	$g_{\rm u}$	f	$\log(gf)$	Acc	Ref
26	Fe I	3dˆ6ˆ(ˆ5ˆD)4s4p(ˆ3ˆP) z ˆ5ˆDˆo_3_	3825.5287	3825.529	9	7	4.83E-03	-1.362	A	BIP79
26	Fe I	3dˆ6ˆ(ˆ5ˆD)4s4p(ˆ3ˆP) z ˆ5ˆFˆo_5_	3720.9926	3720.993	9	11	4.11E-02	-0.432	A	BIP79
26	Fe I	3dˆ6ˆ(ˆ5ˆD)4s4p(ˆ3ˆP) z ˆ5ˆFˆo_4_	3680.9608	3680.961	9	9	2.80E-03	-1.599	A	BIP79
26	Fe I	3dˆ6ˆ(ˆ5ˆD)4s4p(ˆ3ˆP) z ˆ5ˆPˆo_3_	3441.5918	3441.592	9	7	2.36E-02	-0.673	B	BIP79
26	Fe I	3dˆ7ˆ(ˆ4ˆF)4p y ˆ5ˆDˆo_4_	3021.5186	3021.519	9	9	1.04E-01	-0.029	B	BIP79
26	Fe I	3dˆ7ˆ(ˆ4ˆF)4p y ˆ5ˆDˆo_3_	2984.44	2984.44	9	7	2.90E-02	-0.583	A	BIP79
26	Fe I	3dˆ7ˆ(ˆ4ˆF)4p y ˆ5ˆFˆo_5_	2967.7644	2967.764	9	11	4.38E-02	-0.404	A	BIP79
26	Fe I	3dˆ7ˆ(ˆ4ˆF)4p y ˆ5ˆFˆo_4_	2937.7622	2937.762	9	9	1.81E-02	-0.788	C+	BIP79
26	Fe I	3dˆ7ˆ(ˆ4ˆF)4p y ˆ5ˆFˆo_3_	2913.0099	2913.01	9	7	2.58E-03	-1.634	D	BIP79
26	Fe I	3dˆ7ˆ(ˆ4ˆF)4p z ˆ5ˆGˆo_5_	2875.0155	2875.016	9	11	1.41E-03	-1.897	B	OWL91
26	Fe I	3dˆ6ˆ(ˆ5ˆD)4s4p(ˆ1ˆP) y ˆ5ˆPˆo_3_	2719.8328	2719.833	9	7	1.22E-01	0.042	B+	OWL91
26	Fe I	3dˆ6ˆ(ˆ5ˆD)4s4p(ˆ1ˆP) x ˆ5ˆDˆo_4_	2523.6082	2523.608	9	9	2.03E-01	0.262	B	OWL91
26	Fe I	3dˆ6ˆ(ˆ5ˆD)4s4p(ˆ1ˆP) x ˆ5ˆDˆo_3-	2501.8857	2501.886	9	7	4.93E-02	-0.353	C+	OWL91
26	Fe I	3dˆ5ˆ(ˆ6ˆS)4sˆ2ˆ4p y ˆ7ˆPˆo_3_	2487.1229	2487.123	9	7	2.22E-03	-1.699	B+	OWL91
26	Fe I	3dˆ6ˆ(ˆ5ˆD)4s4p(ˆ1ˆP) x ˆ5ˆFˆo_5_	2484.0204	2484.021	9	11	5.43E-01	0.689	B	OWL91
26	Fe I	3dˆ5ˆ(ˆ6ˆS)4sˆ2ˆ4p y ˆ7ˆPˆo_4_	2473.904	2473.904	9	9	2.52E-03	-1.644	B+	OWL91
26	Fe I	3dˆ6ˆ(ˆ5ˆD)4s4p(1P) x ˆ5ˆFˆo_4_	2463.3921	2463.392	9	9	5.32E-02	-0.32	C+	OWL91
26	Fe I	3dˆ6ˆ(ˆ5ˆD)4s4p(1P) x ˆ5ˆFˆo_3_	2448.4508	2448.451	9	7	2.31E-03	-1.683	D+	OWL91
26	Fe I	3dˆ6ˆ(ˆ3ˆP)4s4p(3P) w ˆ5ˆDˆo_4_	2298.8767	2298.877	9	9	2.45E-02	-0.657	D+	OWL91
26	Fe I	3dˆ6ˆ(ˆ3ˆP)4s4p(3P) w ˆ5ˆDˆo_3_	2276.7288	2276.729	9	7	7.55E-03	-1.168	D+	OWL91
26	Fe I	3dˆ6ˆ(ˆ3ˆF)4s4p(3P) w ˆ5ˆFˆo_5_	2260.2096	2260.21	9	11	5.29E-03	-1.322	B+	OWL91
26	Fe I	3dˆ7ˆ(ˆ4ˆP)4p w ˆ5ˆPˆo_3_	2167.4532	2167.453	9	7	1.50E-01	0.13	D+	BH73
26	Fe I	3dˆ7ˆ(ˆ4ˆP)4p u ˆ5ˆDˆo_3_	2139.2666	2139.267	9	7	1.50E-03	-1.87	D+	BH73
26	Fe I	3dˆ6ˆ(ˆ3ˆF)4s4p(ˆ3ˆP) x ˆ3ˆFˆo_4_	2132.69	2132.69	9	9	5.20E-03	-1.33	C+	BH73
26	Fe I	3dˆ6ˆ4s(ˆ6ˆD)5p u ˆ5ˆFˆo_3_	1937.2683	1937.268	9	7	9.50E-03	-1.07	C+	BH73
26	Fe I	3dˆ6ˆ4s(ˆ6ˆD)5p u ˆ5ˆPˆo_3_	1934.535	1934.535	9	7	1.10E-02	-1	C+	BH73
26	Fe II	lower level 3dˆ6ˆ(ˆ5ˆD)4s a ˆ6ˆD_9/2_								
26	Fe II	3dˆ6ˆ(ˆ5ˆD)4p z ˆ6ˆDˆo_9/2_	2600.1721	2600.172	10	10	2.39E-01	0.378	B+	BMW96
26	Fe II	3dˆ6ˆ(ˆ5ˆD)4p z ˆ6ˆDˆo_7/2_	2586.6494	2586.649	10	8	7.17E-02	-0.144	B+	FW06
26	Fe II	3dˆ6ˆ(ˆ5ˆD)4p z ˆ6ˆFˆo_11/2_	2382.7639	2382.764	10	12	3.20E-01	0.505	B+	BMW96

Z	Ion	Upper level	$\lambda_{\rm vac}$ (Å)	$\lambda_{\rm Ritz}$ (Å)	$g_{\rm l}$	$g_{\rm u}$	f	$\log(gf)$	Acc	Ref
26	Fe II	3dˆ6ˆ(ˆ5ˆD)4p z ˆ6ˆFˆoˆ_9/2_	2374.4601	2374.46	10	10	3.13E-02	-0.504	B+	BMW96
26	Fe II	3dˆ6ˆ(ˆ5ˆD)4p z ˆ6ˆPˆoˆ_7/2_	2344.2127	2344.213	10	8	1.14E-01	0.057	A+	BMW96
26	Fe II	3dˆ6ˆ(ˆ5ˆD)4p z ˆ4ˆFˆoˆ_9/2_	2260.7791	2260.779	10	10	2.44E-03	-1.61	B	BMW96
26	Fe II	3dˆ6ˆ(ˆ5ˆD)4p z ˆ4ˆDˆoˆ_7/2_	2249.8752	2249.875	10	8	1.82E-03	-1.74	B	BMW96
26	Fe II	3dˆ6ˆ(a ˆ3ˆF)4p y ˆ3ˆFˆoˆ_7/2_	1611.197	1611.2	10	8	1.40E-03	-1.86	C	PJS01
26	Fe II	3dˆ5ˆ(ˆ6ˆS)4s4p(3P) y ˆ6ˆPˆoˆ_7/2_	1608.4508	1608.451	10	8	5.91E-02	-0.228	A	FW06
26	Fe II	3dˆ5ˆ(ˆ6ˆS)4s4p(1P) x ˆ6ˆPˆoˆ_7/2_	1260.525	1260.536	10	8	2.00E-02	-0.7	D+	RU98
26	Fe II	3dˆ5ˆ(ˆ4ˆG)4s4p(3P) y ˆ6ˆFˆoˆ_11/2_	1144.926	1144.939	10	12	8.30E-02	-0.08	B	DH01
26	Fe II	3dˆ5ˆ(ˆ4ˆG)4s4p(3P) y ˆ6ˆFˆoˆ_9/2_	1143.22	1143.226	10	10	1.90E-02	-0.72	D+	RU98
26	Fe II	3dˆ5ˆ(ˆ4ˆG)4s4p(3P) y ˆ6ˆFˆoˆ_7/2_	1142.361	1142.366	10	8	4.00E-03	-1.4	D+	RU98
26	Fe II	3dˆ5ˆ(ˆ4ˆP)4s4p(3P) ˆ6ˆDˆoˆ_7/2_	1133.662	1133.665	10	8	4.70E-03	-1.33	D+	RU98
26	Fe II	3dˆ6ˆ(ˆ5ˆD)5p ˆ6ˆDˆoˆ_9/2_	1127.099	1127.098	10	10	1.10E-03	-1.9	D	RU98
26	Fe II	3dˆ6ˆ(ˆ5ˆD)5p ˆ6ˆDˆoˆ_7/2_	1125.442	1125.448	10	8	1.60E-02	-0.81	D+	RU98
26	Fe II	3dˆ5ˆ(ˆ4ˆP)4s4p(ˆ3ˆP) ˆ6ˆPˆoˆ_7/2_	1121.967	1121.975	10	8	2.90E-02	-0.54	D+	RU98
26	Fe II	3dˆ6ˆ(ˆ5ˆD)5p ˆ6ˆFˆoˆ_11/2_	1112.046	1112.048	10	12	4.50E-03	-1.35	D+	RU98
26	Fe II	3dˆ6ˆ(ˆ5ˆD)5p ˆ6ˆPˆoˆ_7/2_	1096.871	1096.877	10	8	3.30E-02	-0.49	D+	RU98
26	Fe II	3dˆ5ˆ(ˆ4ˆD)4s4p(ˆ3ˆP) ˆ6ˆFˆoˆ_9/2_	1083.42	1083.42	10	10	2.80E-03	-1.6	D	RU98
26	Fe II	3dˆ5ˆ(ˆ4ˆD)4s4p(ˆ3ˆP) ˆ6ˆFˆoˆ_11/2_	1081.872	1081.875	10	12	1.30E-02	-0.9	D+	RU98
26	Fe II	3dˆ5ˆ(ˆ4ˆD)4s4p(ˆ3ˆP) ˆ6ˆDˆoˆ_7/2_	1063.97	1063.972	10	8	4.70E-03	-1.32	D+	RU98
26	Fe II	3dˆ5ˆ(ˆ4ˆD)4s4p(ˆ3ˆP) ˆ6ˆDˆoˆ_9/2_	1063.17	1063.177	10	10	5.50E-02	-0.26	D+	RU98
26	Fe II	3dˆ5ˆ(ˆ4ˆG)4s4p(ˆ3ˆP) w ˆ4ˆGˆoˆ_9/2_	1062.15	1062.153	10	10	2.90E-03	-1.5	D	RU98
26	Fe II	3dˆ5ˆ(ˆ4ˆD)4s4p(ˆ3ˆP) 6Pˆoˆ_7/2_	1055.258	1055.262	10	8	6.10E-03	-1.21	D+	RU98
26	Fe II	3dˆ6ˆ(ˆ5ˆD)6p ˆ6ˆDˆoˆ_9/2_	940.193	940.192	10	10	1.44E-02	-0.843		K16
26	Fe II	3dˆ5ˆ(ˆ4ˆF)4s4p(ˆ3ˆP) ˆ6ˆFˆoˆ_11/2_	937.651	937.651	10	12	7.00E-03	-1.2	E	RU98
26	Fe II	3dˆ6ˆ(ˆ5ˆD)6p ˆ6ˆFˆoˆ_11/2_	935.517	935.517	10	12	3.48E-03	-1.458		K16
26	Fe II	3dˆ5ˆ(ˆ2ˆF)4s4p(ˆ3ˆP) ˆ4ˆDˆoˆ_7/2_	926.898	926.897	10	8	3.30E-03	-1.5	D	RU98
26	Fe II	3dˆ5ˆ(ˆ4ˆF)4s4p(ˆ3ˆP) ˆ6ˆDˆoˆ_9/2_	926.204	926.212	10	10	3.30E-02	-0.5	E	RU98
26	Fe II	3dˆ5ˆ(ˆ4ˆF)4s4p(ˆ3ˆP) ˆ6ˆDˆoˆ_7/2_	923.878	923.878	10	8	2.90E-03	-1.5	D	RU98
26	Fe III	lower level 3pˆ6ˆ3dˆ6ˆ ˆ5ˆD_4_								
26	Fe III	3dˆ5ˆ(ˆ6ˆS)4p ˆ5ˆPˆoˆ_3_		1122.524	9	7	6.42E-02	-0.238		DH09

Z	Ion	Upper level	$\lambda_{\rm vac}$ (Å)	$\lambda_{\rm Ritz}$ (Å)	$g_{\rm l}$	$g_{\rm u}$	f	$\log(gf)$	Acc	Ref
27	Co I	lower level 3p^6^3d^7^4s^2^ a ^4^F_9/2_								
27	Co I	3d^7^(^4^F)4s4p(^3^P) z ^4^F^o^_9/2_	3527.86	3527.852	10	10	2.57E-02	-0.59	B+	LSC15
27	Co I	3d^7^(^4^F)4s4p(^3^P) z ^4^F^o^_7/2_		3474.965	10	8	3.98E-03	-1.4	B+	LSC15
27	Co I	3d^7^(^4^F)4s4p(^3^P) z ^4^G^o^_11/2_	3466.79	3466.779	10	12	2.29E-02	-0.64	B+	LSC15
27	Co I	3d^7^(^4^F)4s4p(^3^P) z ^4^D^o^_7/2_	3413.61	3413.608	10	8	1.95E-02	-0.71	B+	LSC15
27	Co I	3d^8^(^3^F)4p y ^4^D^o^_7/2_		3122.317	10	8	2.63E-03	-1.58	B	LSC15
27	Co I	3d^8^(^3^F)4p y ^4^G^o^_11/2_		3083.508	10	12	4.57E-03	-1.34	B+	LSC15
27	Co I	3d^8^(^3^F)4p y ^4^F^o^_9/2_	3044.89	3044.883	10	10	2.82E-02	-0.55	B+	LSC15
27	Co I	3d^8^(^3^F)4p y ^4^F^o^_7/2_		3014.467	10	8	1.45E-03	-1.84	B	LSC15
27	Co I	3d^8^(^3^F)4p y ^2^G^o^_9/2_	2990.46	2990.456	10	10	5.25E-03	-1.28	B+	LSC15
27	Co I	3d^8^(^3^F)4p y ^4^G^o^_7/2_	2988.03	2988.029	10	8	5.37E-03	-1.27	B	LSC15
27	Co I	3d^7^(^4^F)4s4p(^1^P) x ^4^D^o^_7/2_	2522.12	2522.122	10	8	2.19E-01	0.34	B+	LSC15
27	Co I	3d^7^(^4^P)4s4p(^3^P) ^6^P^o^_7/2_		2436.562	10	8	1.35E-03	-1.87	D	CSS82
27	Co I	3d^7^(^4^F)4s4p(^1^P) x ^4^F^o^_9/2_	2425.67	2425.668	10	10	3.31E-01	0.52	B	LSC15
27	Co I	3d^7^(^4^F)4s4p(^1^P) x ^4^G^o^_11/2_	2407.98	2407.983	10	12	5.13E-01	0.71	B	LSC15
27	Co I	3d^7^(^4^F)4s4p(^1^P) x ^4^F^o^_7/2_	2385.59	2385.586	10	8	1.91E-02	-0.72	B	LSC15
27	Co I	3d^7^(^4^F)4s4p(^1^P) x ^4^G^o^_9/2_		2365.782	10	10	1.51E-02	-0.82	B+	LSC15
27	Co I	3d^7^(^2^G)4s4p(^3^P) w ^4^F^o^_9/2_	2309.73	2309.718	10	10	5.13E-02	-0.29	B+	LSC15
27	Co I	3d^8^(^1^D)4p x ^2^F^o^_7/2_		2295.936	10	8	1.58E-02	-0.8	B+	LSC15
27	Co II	lower level 3p^6^3d^8^ a ^3^F_4_								
27	Co II	3d^7^(^4^F)4p z ^5^G^o^_5_	2112.1176	2112.118	9	11	1.52E-03	-1.863	D	RPU98
27	Co II	3d^7^(^4^F)4p z ^3^G^o^_5_	2059.4756	2059.476	9	11	7.51E-03	-1.17	B	RPU98
27	Co II	3d^7^(^4^F)4p z ^3^G^o^_4_	2026.4120	2026.412	9	9	1.25E-02	-0.95	C+	RPU98
27	Co II	3d^7^(^4^F)4p z ^3^F^o^_4_	2012.1663	2012.166	9	9	3.68E-02	-0.48	B+	MCL98
27	Co II	3d^7^(^4^F)4p z ^3^D^o^_3_	1941.2852	1941.285	9	7	3.40E-02	-0.514	B	MLZ98
27	Co II	3d^7^(^2^G)4p z ^3^H^o^_5_	1579.6	1579.612	9	11	1.00E-03	-2	E	RPU98
27	Co II	3d^7^(^2^G)4p y ^3^F^o^_4_	1574.5503	1574.551	9	9	2.50E-02	-0.648	B	MLZ98
27	Co II	3d^7^(^4^P)4p y ^3^D^o^_3_	1572.6492	1572.649	9	7	1.20E-02	-0.967	B	MLZ98
27	Co II	3d^7^(^2^G)4p z ^3^H^o^_4_	1567.5767	1567.577	9	9	7.00E-03	-1.19	D	RPU98
27	Co II	3d^7^(^2^G)4p y ^3^F^o^_3_	1553.759	1553.759	9	7	3.70E-03	-1.48	D	RPU98

Z	Ion	Upper level	λ_{vac} (Å)	λ_{Ritz} (Å)	g_l	g_u	f	log(gf)	Acc	Ref
27	Co II	3dˆ7ˆ(ˆ2ˆG)4p z ˆ1ˆGˆoˆ_4_	1552.7625	1552.762	9	9	1.16E-02	-0.981	B	MLZ98
27	Co II	3dˆ7ˆ(ˆ2ˆG)4p y ˆ3ˆGˆoˆ_5_	1547.9445	1547.945	9	11	1.11E-02	-1	D	RPU98
27	Co II	3dˆ7ˆ(ˆ2ˆG)4p z ˆ1ˆHˆoˆ_5_	1539.456	1539.469	9	11	1.90E-03	-1.766	D	RPU98
27	Co II	3dˆ7ˆ(ˆ2ˆG)4p y ˆ3ˆGˆoˆ_4_	1534.813	1534.824	9	9	2.33E-03	-1.678	D	RPU98
27	Co II	3dˆ7ˆ(ˆ2ˆG)4p z ˆ1ˆFˆoˆ_3_	1514.74	1514.746	9	7	1.12E-03	-1.998	D	RPU98
27	Co II	3dˆ7ˆ(ˆ2ˆP)4p x ˆ3ˆDˆoˆ_3_	1480.9545	1480.954	9	7	1.19E-02	-0.97	B	MLZ98
27	Co II	3dˆ7ˆ(ˆ2ˆH)4p x ˆ3ˆGˆoˆ_5_	1466.212	1466.211	9	11	3.10E-02	-0.554	B	MLZ98
27	Co II	3dˆ7ˆ(ˆ2ˆ_2_D)4p w ˆ3ˆDˆoˆ_3_	1448.0178	1448.018	9	7	7.90E-03	-1.148	D+	MLZ98
27	Co II	3dˆ7ˆ(ˆ2ˆ_2_D)4p x ˆ3ˆFˆoˆ_4_	1424.778	1424.786	9	9	1.09E-02	-1.008	D	RPU98
27	Co II	3dˆ7ˆ(ˆ2ˆF)4p w ˆ3ˆFˆoˆ_4_		1188.486	9	9	2.31E-03	-1.682		RPU98
27	Co II	3dˆ7ˆ(ˆ2ˆF)4p v ˆ3ˆDˆoˆ_3_	1187.413	1187.413	9	7	7.43E-03	-1.18	D	RPU98
27	Co II	3dˆ7ˆ(ˆ4ˆF)5p ˆ3ˆFˆoˆ_4_		1030.26	9	9	8.55E-03	-1.114		RPU98
27	Co II	3dˆ7ˆ(ˆ4ˆF)5p ˆ3ˆDˆoˆ_3_		1025.679	9	7	2.51E-03	-1.646		RPU98
27	Co II	3dˆ7ˆ(ˆ4ˆF)5p ˆ3ˆGˆoˆ_4_		1023.489	9	9	1.37E-03	-1.909		RPU98
27	Co II	3dˆ7ˆ(ˆ4ˆF)5p ˆ3ˆFˆoˆ_3_	1020.757	1020.745	9	7	3.39E-03	-1.52	D	RPU98
27	Co III	lower level 3pˆ6ˆ3dˆ7ˆ a ˆ4ˆF_9/2_								
27	Co III	3dˆ6ˆ(ˆ5ˆD)4p z ˆ6ˆFˆoˆ_9/2_	967.237	967.24	10	10	1.07E-03	-1.97	E	K16
27	Co III	3dˆ6ˆ(ˆ5ˆD)4p z ˆ6ˆFˆoˆ_7/2_	966.162	966.165	10	8	1.10E-03	-1.958		K16
27	Co III	3dˆ6ˆ(ˆ5ˆD)4p z ˆ6ˆPˆoˆ_7/2_	952.297	952.297	10	8	5.90E-03	-1.229	D+	K16
27	Co III	3dˆ6ˆ(ˆ5ˆD)4p z ˆ4ˆDˆoˆ_7/2_	939.068	939.061	10	8	8.85E-02	-0.053	C	K16
27	Co III	3dˆ6ˆ(ˆ5ˆD)4p z ˆ4ˆFˆoˆ_9/2_	936.634	936.637	10	10	4.58E-02	-0.339	D+	K16
27	Co III	3dˆ6ˆ(ˆ5ˆD)4p z ˆ4ˆFˆoˆ_7/2_	929.971	929.972	10	8	1.02E-02	-0.991	D+	K16
28	Ni I	lower level 3dˆ8ˆ(ˆ3ˆF)4sˆ2ˆ ˆ3ˆF_4_								
28	Ni I	3dˆ8ˆ(ˆ3ˆF)4s4p(ˆ3ˆP) ˆ5ˆFˆoˆ_4_	3438.27	3438.262	9	9	7.10E-03	-1.2	B+	WLS14
28	Ni I	3dˆ9ˆ(ˆ2ˆD)4p ˆ3ˆFˆoˆ_4_	3392.02	3392.016	9	9	9.90E-03	-1.05	B+	WLS14
28	Ni I	3dˆ9ˆ(ˆ2ˆD)4p ˆ3ˆDˆoˆ_3_	3370.54	3370.531	9	7	2.32E-02	-0.68	B+	WLS14
28	Ni I	3dˆ8ˆ(ˆ3ˆF)4s4p(ˆ3ˆP) ˆ3ˆGˆoˆ_5_	3233.89	3233.867	9	11	1.06E-02	-1.02	B+	WLS14
28	Ni I	3dˆ9ˆ(ˆ2ˆD)4p ˆ1ˆFˆoˆ_3_	3222.58	3222.581	9	7	1.50E-03	-1.87	B+	WLS14
28	Ni I	3dˆ8ˆ(ˆ3ˆF)4s4p(ˆ3ˆP) ˆ3ˆFˆoˆ_4_	3032.75	3032.75	9	9	1.72E-03	-1.81	B+	WLS14
28	Ni I	3dˆ8ˆ(ˆ3ˆF)4s4p(ˆ3ˆP) ˆ3ˆFˆoˆ_3_	3020.02	3020.022	9	7	5.20E-03	-1.33	B+	WLS14

Z	Ion	Upper level	λ_{vac} (Å)	λ_{Ritz} (Å)	g_l	g_u	f	$\log(gf)$	Acc	Ref
28	Ni I	3d^8^(^3^F)4s4p(^3^P) ^3^D^o^_3_	2985	2985.002	9	7	3.51E-03	-1.5	B+	WLS14
28	Ni I	3d^8^(^3^P)4s4p(^3^P) ^5^P^o^_3_	2477.62	2477.624	9	7	1.64E-03	-1.83	B+	WLS14
28	Ni I	3d^8^(^1^D)4s4p(^3^P) ^3^F^o^_4_	2348.24	2348.233	9	9	1.46E-02	-0.88	B+	WLS14
28	Ni I	3d^8^(^1^D)4s4p(^3^P) ^3^D^o^_3_	2346.26	2346.261	9	7	1.46E-01	0.12	B+	WLS14
28	Ni I	3d^8^(^1^D)4s4p(^3^P) ^3^F^o^_3_		2338.205	9	7	3.68E-02	-0.48	B+	WLS14
28	Ni I	3d^8^(^3^F)4s4p(^1^P) ^3^G^o^_5_	2320.74	2320.747	9	11	6.85E-01	0.79	C	HS80
28	Ni I	3d^8^(^3^F)4s4p(^1^P) ^3^F^o^_4_		2311.672	9	9	3.85E-01	0.54	B	WLS14
28	Ni I	3d^8^(^3^F)4s4p(^1^P) ^3^D^o^_3_	2290.69	2290.69	9	7	1.28E-01	0.06	B	WLS14
28	Ni I	3d^8^(^3^P)4s4p(^3^P) ^5^D^o^_3_		2262.131	9	7	5.44E-03	-1.31	C	HS80
28	Ni I	3d^8^(^3^F)4s4p(^1^P) ^3^G^o^_4_		2256.577	9	9	1.37E-03	-1.91	B	WLS14
28	Ni I	3d^8^(^3^P)4s4p(^3^P) ^o^_4_		2255.498	9	9	7.30E-03	-1.18	C	HS80
28	Ni I	3d^8^(^3^P)4s4p(^3^P) ^3^D^o^_3_		2126.298	9	7	1.89E-03	-1.77	B+	WLS14
28	Ni I	3d^9^(^2^D)5p ^3^F^o^_4_		2052.731	9	9	6.11E-03	-1.26	C	HS80
28	Ni I	3d^9^(^2^D)5p ^3^D^o^_3_		2027.241	9	7	1.16E-02	-0.981	C	HS80
28	Ni I	3d^9^(^2^D)5p ^3^F^o^_3_		1994.304	9	7	2.67E-03	-1.62	C	HS80
28	Ni I	3d^8^(^1^G)4s4p(^3^P)^3^F^o^_4_		1968.919	9	9	2.60E-03	-1.63	C	HS80
28	Ni II	lower level 3p^6^3d^9^ ^2^D_5/2_								
28	Ni II	3d^8^(^3^F)4p ^4^F^o^_7/2_		1804.473	6	8	5.39E-03	-1.49		CHR16
28	Ni II	3d^8^(^3^F)4p ^2^G^o^_7/2_		1773.949	6	8	4.79E-03	-1.542		CHR16
28	Ni II	3d^8^(^3^F)4p ^2^F^o^_7/2_		1751.91	6	8	3.61E-02	-0.664		CHR16
28	Ni II	3d^8^(^3^F)4p ^2^D^o^_5/2_		1741.553	6	6	4.88E-02	-0.533		CHR16
28	Ni II	3d^8^(^3^F)4p ^2^F^o^_5/2_		1709.604	6	6	5.51E-02	-0.481		CHR16
28	Ni II	3d^8^(^3^F)4p ^2^D^o^_3/2_		1703.412	6	4	7.26E-03	-1.361		CHR16
28	Ni II	3d^8^(^3^P)4p ^4^P^o^_5/2_		1502.148	6	6	9.45E-03	-1.246		CHR16
28	Ni II	3d^8^(^1^D)4p ^2^F^o^_5/2_		1477.222	6	6	1.25E-03	-2.125		CHR16
28	Ni II	3d^8^(^1^D)4p ^2^F^o^_7/2_		1467.756	6	8	1.55E-02	-1.032		CHR16
28	Ni II	3d^8^(^1^D)4p ^2^D^o^_3/2_		1467.259	6	4	8.03E-03	-1.317		CHR16
28	Ni II	3d^8^(^1^D)4p ^2^D^o^_5/2_		1454.842	6	6	3.47E-02	-0.682		CHR16
28	Ni II	3d^8^(^3^P)4p ^4^D^o^_5/2_		1415.72	6	6	2.54E-03	-1.817		CHR16
28	Ni II	3d^8^(^3^P)4p ^4^D^o^_3/2_		1414.292	6	4	1.13E-03	-2.169		CHR16

Z	Ion	Upper level	$\lambda_{\rm vac}$ (Å)	$\lambda_{\rm Ritz}$ (Å)	$g_{\rm l}$	$g_{\rm u}$	f	$\log(gf)$	Acc	Ref
28	Ni II	3d^8^(^3^P)4p ^4^D^o^_7/2_		1412.866	6	8	4.99E-03	-1.524		CHR16
28	Ni II	3d^8^(^3^P)4p ^2^D^o^_5/2_		1393.324	6	6	1.42E-02	-1.07		CHR16
28	Ni II	3d^8^(^3^P)4p ^4^P^o^_3/2_		1370.132	6	4	8.11E-02	-0.313		CHR16
28	Ni II	3d^8^(^3^P)4p ^4^S^o^_3/2_		1345.878	6	4	7.67E-03	-1.337		CHR16
28	Ni II	3d^8^(^1^G)4p ^2^F^o^_7/2_		1317.217	6	8	8.18E-02	-0.309		CHR16
28	Ni II	3d^8^(^1^G)4p ^2^F^o^_5/2_		1308.866	6	6	3.28E-03	-1.706		CHR16
28	Ni II	3d^8^(^1^S)4p ^2^P^o^_3/2_		993.542	6	4	8.17E-03	-1.31		CHR16
29	Cu I	lower level 3p^6^3d^10^4s ^2^S_1/2_								
29	Cu I	3d^10^4p ^2^P^o^_1/2_	3274.901	3274.896	2	2	2.21E-01	-0.354	AA	D95
29	Cu I	3d^10^4p ^2^P^o^_3/2_	3248.477	3248.473	2	4	4.41E-01	-0.054	AA	D95
29	Cu I	3d^9^4s4p(^3^P) ^4^P^o^_3/2_	2492.898	2492.895	2	4	5.20E-03	-1.983	B	HM78
29	Cu I	3d^9^4s4p(^3^P) ^4^P^o^_1/2_	2442.377	2442.373	2	2	1.80E-03	-2.44	B	HM78
29	Cu I	3d^9^4s4p(^3^P) ^4^D^o^_3/2_	2244.961	2244.963	2	4	2.80E-03	-2.252	C+	HM78
29	Cu I	3d^9^4s4p(^3^P) ^4^D^o^_1/2_	2226.389	2226.394	2	2	3.30E-02	-1.18	C+	HM78
29	Cu I	3d^9^4s4p(^3^P) ^2^P^o^_1/2_	2182.403	2182.408	2	2	7.10E-02	-0.848	C+	HM78
29	Cu I	3d^9^4s4p(^3^P) ^2^P^o^_3/2_	2179.626	2179.631	2	4	1.30E-01	-0.585	C+	HM78
29	Cu I	3d^9^4s4p(^3^P) ^o^_3/2_	2165.773	2165.773	2	4	7.70E-02	-0.812	C+	HM78
29	Cu I	3d^10^5p ^2^P^o^_3/2_	2024.99	2024.991	2	4	1.20E-02	-1.62	B	HM78
29	Cu I	3d^10^5p ^2^P^o^_1/2_	2024.979	2024.978	2	2	6.00E-03	-1.921	B	HM78
29	Cu I	3d^10^7p ^2^P^o^_3/2_	1725.668	1725.668	2	4	2.43E-03	-2.313	C+	CAE15
29	Cu I	3d^10^8p ^2^P^o^_3/2_	1687.053	1687.052	2	4	1.32E-03	-2.578	C+	CAE15
29	Cu I	3d^10^10p ^2^P^o^_1/2_	1650.133	1650.133	2	2	2.13E-03	-2.371	C+	CAE15
29	Cu II	lower level 3p^6^3d^10^ ^1^S_0_								
29	Cu II	3d^9^(^2^D)4p ^3^P^o^_1_		1472.395	1	3	2.17E-02	-1.663		DHB99
29	Cu II	3d^9^(^2^D)4p ^3^D^o^_1_		1367.951	1	3	1.79E-01	-0.747		DHB99
29	Cu II	3d^9^(^2^D)4p ^1^P^o^_1_		1358.773	1	3	2.73E-01	-0.564	B	BFI09
30	Zn I	lower level 3p^6^3d^10^4s^2^ ^1^S_0_								
30	Zn I	3d^10^4s(^2^S)4p ^1^P^o^_1_		2139.248	1	3	1.46E+00	0.164	A	KT76
30	Zn I	3d^10^4s(^2^S)5p ^1^P^o^_1_		1589.561	1	3	1.36E-01	-0.865		K16
30	Zn I	3d^9^4s^2^4p ^3^P^o^_1_	1109.1	1108.316	1	3	3.67E-02	-1.435		K16

Z	Ion	Upper level	$\lambda_{\rm vac}$ (Å)	$\lambda_{\rm Ritz}$ (Å)	$g_{\rm l}$	$g_{\rm u}$	f	$\log(gf)$	Acc	Ref
30	Zn II	lower level 3p^6^3d^10^4s ^2^S_1/2_								
30	Zn II	3d^10^4p ^2^P^o^_1/2_		2062.66	2	2	3.09E-01	-0.209		KKF15
30	Zn II	3d^10^4p ^2^P^o^_3/2_		2026.137	2	4	6.30E-01	0.1		KKF15
30	Zn II	3d^10^5p ^2^P^o^_1/2_		986.524	2	2	1.54E-03	-2.511		KKF15
30	Zn II	3d^10^5p ^2^P^o^_3/2_		984.141	2	4	2.46E-03	-2.308		KKF15
30	Zn II	3d^9^(^2^D)4s4p(^3^P) ^4^P^o^_3/2_		949.463	2	4	4.75E-03	-2.022		KKF15
30	Zn II	3d^9^(^2^D)4s4p(^3^P) ^4^P^o^_1/2_		938.713	2	2	1.83E-03	-2.438		KKF15
31	Ga I	lower level 3d^10^4s^2^4p ^2^P^o^_1/2_								
31	Ga I	4s^2^5s ^2^S_1/2_	4034.124	4034.124	2	2	1.18E-01	-0.627	C	SRK07
31	Ga I	4s^2^4d ^2^D_3/2_	2875.078	2875.078	2	4	2.90E-01	-0.237	C	SRK07
31	Ga I	4s^2^6s ^2^S_1/2_	2660.664	2660.652	2	2	1.29E-02	-1.59	C	SRK07
31	Ga I	4s^2^5d ^2^D_3/2_	2450.82	2450.809	2	4	5.01E-02	-0.999	C	SRK07
31	Ga I	4s^2^7s ^2^S_1/2_	2372.01	2371.986	2	2	4.70E-03	-2.03	C	SRK07
31	Ga I	4s^2^6d ^2^D_3/2_	2294.9	2294.888	2	4	1.10E-02	-1.66	C	SRK07
31	Ga I	4s^2^8s ^2^S_1/2_	2255.733	2255.693	2	2	2.40E-03	-2.32	C	SRK07
31	Ga I	4s^2^7d ^2^D_3/2_	2218.73	2218.685	2	4	1.20E-02	-1.319		SCS06
31	Ga I	4s^2^9s ^2^S_1/2_		2196.032	2	2	1.40E-03	-2.55	C	SRK07
31	Ga II	lower level 3p^6^3d^10^4s^2^ ^1^S_0_								
31	Ga II	4s(^2^S)4p ^1^P^o^_1_	1414.401	1414.399	1	3	1.84E+00	0.276	B	AEP79
31	Ga III	lower level 3p^6^3d^10^4s ^2^S_1/2_								
31	Ga III	3d^10^4p ^2^P^o^_1/2_	1534.462	1534.462	2	2	2.62E-01	-0.281	C	SRK07
31	Ga III	3d^10^4p ^2^P^o^_3/2_	1495.045	1495.045	2	4	5.40E-01	0.033	C	SRK07
32	Ge I	lower level 4s^2^4p^2^ ^3^P_0_								
32	Ge I	4s^2^4p5s ^3^P^o^_1_	2652.3577	2652.358	1	3	2.19E-01	-0.66	B	LNP99
32	Ge I	4s^2^4p5s ^1^P^o^_1_	2498.7156	2498.716	1	3	3.09E-02	-1.51	B+	LNP99
32	Ge I	4s^2^4p4d ^3^D^o^_1_	2042.3676	2042.368	1	3	2.95E-01	-0.53	B	LNP99
32	Ge I	4s^2^4p4d ^3^P^o^_1_	1934.0483	1934.048	1	3	1.15E-02	-1.94	B+	LNP99
32	Ge II	lower level 4s^2^4p ^2^P^o^_1/2_								
32	Ge II	4s^2^5s ^2^S_1/2_	1602.4864	1602.486	2	2	1.44E-01	-0.54		BMQ98
32	Ge II	4s^2^4d ^2^D_3/2_	1237.058	1237.059	2	4	1.23E+00	0.39		BMQ98

Z	Ion	Upper level	λ_{vac} (Å)	λ_{Ritz} (Å)	g_l	g_u	f	$\log(gf)$	Acc	Ref
32	Ge II	4s4p^2^ ^2^S_1/2_	1164.273	1164.272	2	2	2.81E-01	-0.25		BMQ98
32	Ge II	4s4p^2^ ^2^P_1/2_	1098.71	1098.706	2	2	5.48E-01	0.04		BMQ98
32	Ge II	4s4p^2^ ^2^P_3/2_	1085.513	1085.509	2	4	3.01E-01	-0.22		BMQ98
32	Ge II	4s^2^6s ^2^S_1/2_	1055.0252	1055.026	2	2	2.56E-02	-1.29		BMQ98
32	Ge II	4s^2^5d ^2^D_3/2_	999.1009	999.101	2	4	2.56E-01	-0.29		BMQ98
32	Ge III	lower level 3p^6^3d^10^4s^2^ ^1^S_0_								
32	Ge III	4s4p ^3^P^o^_1_	1600.09	1600.001	1	3	1.17E-03	-2.931		C92
32	Ge III	4s4p ^1^P^o^_1_	1088.45	1088.463	1	3	1.84E+00	0.264	C+	AEP79
32	Ge IV	lower level 3d^10^4s ^2^S_1/2_								
32	Ge IV	3d^10^4p ^2^P^o^_1/2_	1229.81	1229.84	2	2	2.49E-01	-0.303		PBI81
32	Ge IV	3d^10^4p ^2^P^o^_3/2_	1188.99	1189.028	2	4	5.17E-01	0.015		PBI81
36	Kr I	lower level 4s^2^4p^6^ ^1^S_0_								
36	Kr I	4s^2^4p^5^(^2^P_3/2_)5s ^2^[3/2]^o^_1_	1235.838	1235.838	1	3	2.14E-01	-0.67	B+	CCG92
36	Kr I	4s^2^4p^5^(^2^P_1/2_)5s ^2^[1/2]^o^_1_	1164.867	1164.867	1	3	1.93E-01	-0.714	B+	CCG92
36	Kr I	4s^2^4p^5^(^2^P_3/2_)4d ^2^[1/2]^o^_1_	1030.022	1030.023	1	3	5.30E-03	-2.276	B+	CCG92
36	Kr I	4s^2^4p^5^(^2^P_3/2_)4d ^2^[3/2]^o^_1_	1003.55	1003.55	1	3	8.24E-02	-1.084	B	CCG92
36	Kr I	4s^2^4p^5^(^2^P_3/2_)6s ^2^[3/2]^o^_1_	1001.0606	1001.061	1	3	1.54E-01	-0.812	B	CCG92
36	Kr I	4s^2^4p^5^(^2^P_3/2_)5d ^2^[1/2]^o^_1_	963.3745	963.375	1	3	1.40E-02	-1.854	B	CCG92
36	Kr I	4s^2^4p^5^(^2^P_1/2_)4d ^2^[3/2]^o^_1_	953.403	953.404	1	3	4.35E-02	-1.362	B	CCG92
36	Kr I	4s^2^4p^5^(^2^P_1/2_)6s ^2^[1/2]^o^_1_	951.055	951.056	1	3	1.05E-02	-1.979	B	CCG92
36	Kr I	4s^2^4p^5^(^2^P_3/2_)5d ^2^[3/2]^o^_1_	946.536	946.536	1	3	6.10E-02	-1.215	B	CCG92
36	Kr I	4s^2^4p^5^(^2^P_3/2_)7s ^2^[3/2]^o^_1_	945.441	945.441	1	3	1.13E-01	-0.947	B	CCG92
36	Kr I	4s^2^4p^5^(^2^P_3/2_)6d ^2^[1/2]^o^_1_	928.71	928.711	1	3	1.50E-03	-2.824	B	CCG92
36	Kr I	4s^2^4p^5^(^2^P_3/2_)6d ^2^[3/2]^o^_1_	923.712	923.713	1	3	4.39E-02	-1.358	B	CCG92
36	Kr I	4s^2^4p^5^(^2^P_3/2_)8s ^2^[3/2]^o^_1_	922.738	922.739	1	3	2.03E-02	-1.693	B	CCG92
36	Kr II	lower level 4s^2^4p^5^ ^2^P^o^_3/2_								
36	Kr II	4s4p^6^ ^2^S_1/2_	917.427	917.428	4	2	1.43E-03	-2.241	AA	LLV99
36	Kr VI	lower level 4s^2^4p ^2^P^o^_1/2_								
36	Kr VI	4s4p^2^ ^4^P_1/2_	927.34	927.334	2	2	1.90E-03	-2.42		PRB96
82	Pb II	lower level 5d^10^6s^2^6p ^2^P^o^_1/2_								

Z	Ion	Upper level	$\lambda_{\rm vac}$ (Å)	$\lambda_{\rm Ritz}$ (Å)	$g_{\rm l}$	$g_{\rm u}$	f	$\log(gf)$	Acc	Ref
82	Pb II	6s^2^7s ^2^S_1/2_	1682.15	1682.127	2	2	1.17E-01	-0.632	C+	QBP07
82	Pb II	6s^2^6d ^2^D_3/2_	1433.96	1433.906	2	4	4.52E-01	-0.044		SSJ05
82	Pb II	6s^2^8s ^2^S_1/2_	1121.36	1121.325	2	2	1.86E-02	-1.43		SSJ05
82	Pb II	6s^2^7d ^2^D_3/2_	1060.66	1060.619	2	4	3.64E-02	-1.138		SSJ05
82	Pb II	6s^2^9s ^2^S_1/2_	986.71	986.721	2	2	2.68E-03	-2.271		SSJ05
82	Pb II	6s^2^8d ^2^D_3/2_	967.23	967.174	2	4	3.97E-03	-2.1		SSJ05
82	Pb II	6s^2^10s ^2^S_1/2_	926.44	926.535	2	2	5.62E-03	-1.949		CAM01
82	Pb II	6s^2^9d ^2^D_3/2_		915.273	2	4	2.89E-02	-1.239		CAM01